TABLE OF CONTENTS

List of Figures		vii	1/A11
List of Tables		x	1/A14
Nomenclature		xi	1/B1
I.	INTRODUCTION	1	1/B4
II.	TEST FACILITY, INSTRUMENTATION, AND PROCEDURES	3	1/B6
A.	Test Facility Description	3	1/B7
B.	Test Configurations	4	
C.	Instrumentation	5	1/B8
D.	Data Acquisition and Reduction	5	
E.	Facility Calibration	6	1/B9
III.	STRUCTURE-BORNE NOISE TRANSFER FUNCTIONS TESTS	8	1/B11
A.	Narrow Band Data	8	
B.	Peak One-Third Octave Data	11	1/B14
C.	Isolator Relative Performance	11	
D.	System Linearity	12	1/C1
E.	Engine Mount Damping Effectiveness	13	1/C2
F.	Fuselage Tail Cone Isolation	13	
IV.	ANALYTICAL MODEL	15	1/C4
A.	Model Concept	15	
B.	Component Representation	15	
1.	Engine As a Rigid Body	15	
2.	Vibration Isolators	17	1/C6
3.	Engine Mount Structure	20	1/C9
4.	Aircraft Fuselage and Interior Response	22	1/C11
C.	Component Coupling Procedures	25	1/C14
D.	Coupled Model Normal Mode Response	30	1/D5

TABLE OF CONTENTS (CONTINUED)

V.	COMPARISON OF ANALYTICAL AND EXPERIMENTAL RESULTS	34	1/D9
	A. Narrow Band Spectra	34	1/D10
	B. One-Third Octave Spectra	35	
VI.	MODEL PARAMETER SENSITIVITY STUDY	36	1/D11
	A. Engine Mount Parameters	36	1/D12
	B. Isolator Properties	37	
VII.	CONCLUSIONS AND RECOMMENDATIONS	39	1/D14
REFERENCES	. . . . .	41	1/E2

JUN 3 0 1981

NAS1.26:3427
not mailed
7/8/81

NASA Contractor Report 3427

COMPLETED
ORIGINAL

Engine Isolation for Structural-Borne Interior Noise Reduction in a General Aviation Aircraft

James F. Unruh and Dennis C. Scheidt

CONTRACT NAS1-14861
MAY 1981

NASA

Engine Isolation for Structural-Borne Interior Noise Reduction in a General Aviation Aircraft

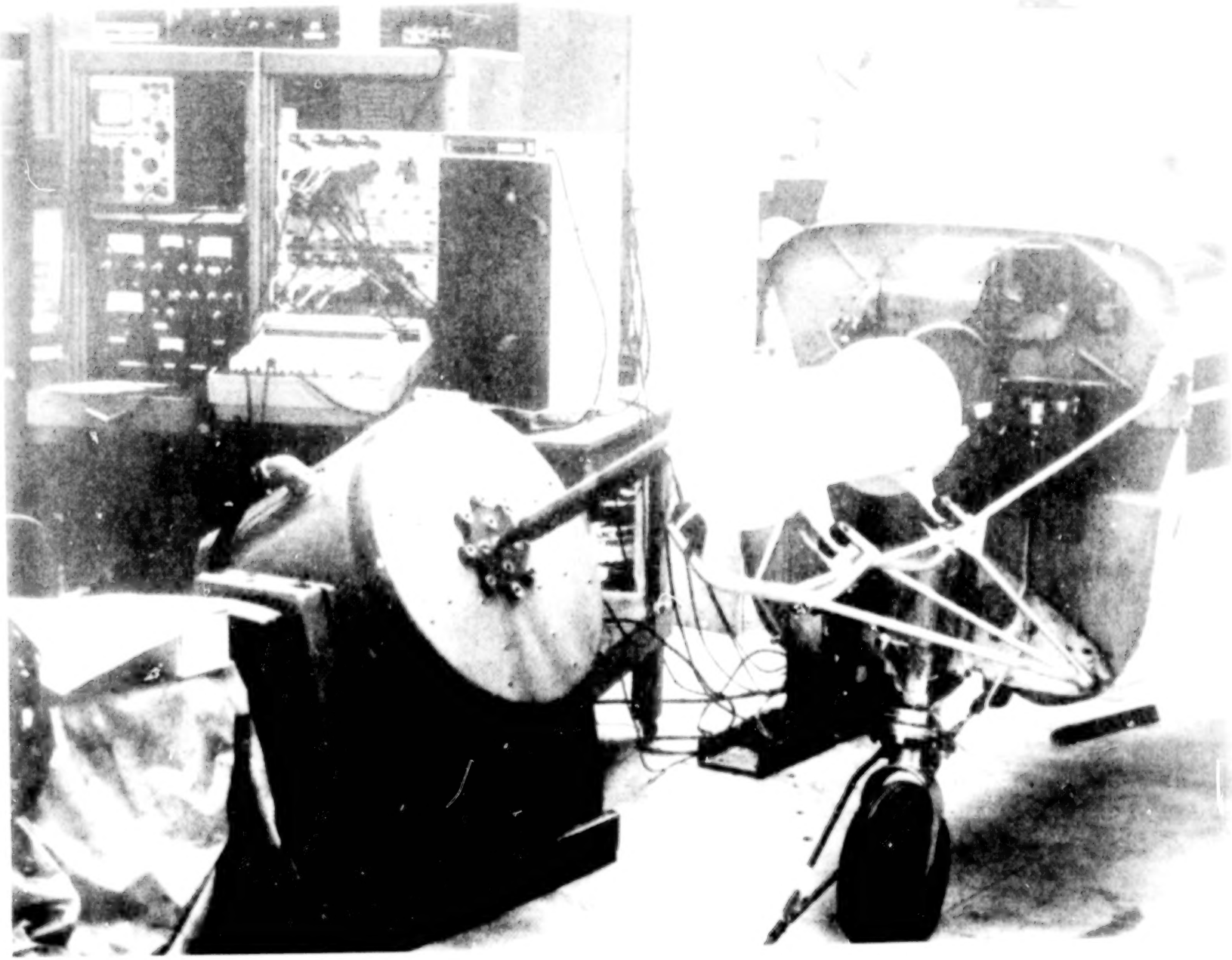

NASA Contractor Report 3427

Engine Isolation for Structural-Borne Interior Noise Reduction in a General Aviation Aircraft

James F. Unruh and Dennis C. Scheidt
Southwest Research Institute
San Antonio, Texas

Prepared for
Langley Research Center
under Contract NAS1-14861

National Aeronautics
and Space Administration

**Scientific and Technical
Information Branch**

1981

Blank Page

TABLE OF CONTENTS

List of Figures vii

List of Tables x

Nomenclature xi

I. INTRODUCTION 1

II. TEST FACILITY, INSTRUMENTATION, AND PROCEDURES 3

A. Test Facility Description 3
B. Test Configurations 4
C. Instrumentation 5
D. Data Acquisition and Reduction 5
E. Facility Calibration 6

III. STRUCTURE-BORNE NOISE TRANSFER FUNCTIONS TESTS 8

A. Narrow Band Data 8
B. Peak One-Third Octave Data 11
C. Isolator Relative Performance 11
D. System Linearity 12
E. Engine Mount Damping Effectiveness 13
F. Fuselage Tail Cone Isolation 13

IV. ANALYTICAL MODEL 15

A. Model Concept 15
B. Component Representation 15

1. Engine As a Rigid Body 15
2. Vibration Isolators 17
3. Engine Mount Structure 20
4. Aircraft Fuselage and Interior Response 22

C. Component Coupling Procedures 25
D. Coupled Model Normal Mode Response 30

TABLE OF CONTENTS (CONTINUED)

V. COMPARISON OF ANALYTICAL AND EXPERIMENTAL RESULTS 44

A. Narrow Band Spectra 44
B. One-Third Octave Spectra 57

VI. MODEL PARAMETER SENSITIVITY STUDY 66

A. Engine Mount Parameters 66
B. Isolator Properties 67

VII. CONCLUSIONS AND RECOMMENDATIONS 69

REFERENCES 71

LIST OF FIGURES

Figure No.		
1	Structure-Borne Noise Equals Airborne Noise	61
2	Sketch of the Rigid Engine Design	62
3	Vibration Isolators and Attachment Lugs	63
4	Excitation Configurations for Transfer Function Tests .	64
5	Rigid Engine and Test Setup	65
6	Instrumentation and Data Acquisition System for Isolator Transfer Function Tests	66
7	Facility Noise Floor, SPL at P1 Shaker Detached with 0.05 G Excitation	67
8	Measured Transfer Function Spectra, Load Case #2, Isolated Configuration B1, Ref. 89 N rms	68
9	Measured Transfer Function Spectra, Load Case #3, Isolator Configuration B1, Ref. 89 N rms	74
10	Measured Transfer Function Spectra, Load Case #2, Isolator Configuration OA, Ref. 89 N rms	78
11	Measured Transfer Function Spectra, Load Case #2, Isolator Configuration AA, Ref. 89 N rms	82
12	Measured Interior Noise Transmission, Ref. 89 N rms . .	86
13	Measured Interior Noise Transmission, Ref. 89 N rms . .	88
14	Measured One-Third Octave Peak SPL Transfer Function Response at P1; Load Case #2; Ref. 89 N rms	90
15	Measured One-Third Octave Peak SPL Transfer Function Response at P1; Load Case #3; Ref. 89 N rms	91
16	SPL at P1 Based on Engine Running Data; 2160 rpm and Transfer Functions from Load Case #2 Excitation	92
17	SPL at P1 Based on Engine Running Data; 2160 rpm and Transfer Functions from Load Case #3 Excitation	93
18	Check on Linearity Transfer Function Spectra, Load Case #3, Isolator Configuration AA	94
19	Measured Peak SPL Transfer Function Response at P1; Load Case #3; Isolator Configuration AA, Ref. 178 N rms . . .	98
20	Measured SPL Transfer Function Spectra; Load Case #3; Response P1, Ref. 89 N rms	99
21	Engine Rigid Body and Coupling Degrees of Freedom . . .	100
22	Vibration Isolator Degrees of Freedom	101

LIST OF FIGURES (CONT.)

Figure No.		
23	Engine Mount Structure with Coupling Degrees of Freedom and Strut Identification	102
24	Cessna Model 172 Engine Mount Free-Free Normal Mode Frequencies	103
25	Firewall Degrees of Freedom Notation at the Engine Attach Points	104
26	Random Noise Input Force Spectrum F_{X1}	105
27	Fuselage Driving Point Inertance at X1	106
28	Fuselage Driving Point Inertance at X4	108
29	Driving Point Inertance - Engine Mount Lower Attach Points	109
30	Fuselage Transfer Inertance - Comparison for Reciprocity	111
31	Fuselage Sound Pressure Level Transfer Function, Input at X1	113
32	Predicted Transfer Function Spectra, Load Case #2, Isolator Configuration R1, Ref. 89 N rms	115
33	Predicted Transfer Function Spectra, Load Case #3, Isolator Configuration R1, Ref. 89 N rms	121
34	Predicted Transfer Function Spectra, Load Case #2, Isolator Configuration OA, Ref. 89 N rms	125
35	Predicted Transfer Function Spectra, Load Case #2, Isolator Configuration AA, Ref. 89 N rms	129
36	Comparison of Narrow Band SPL Transfer Function Spectra, Load Case #2, Response P2, Ref. 89 N rms	133
37	Comparison of Narrow Band SPL Transfer Function Spectra, Load Case #3, Response P1, Ref. 89 N rms	136
38	Comparison of One-Third Octave Peak SPL Transfer Function Spectra at P1, Load Case #2, Ref. 89 N rms	139
39	Comparison of One-Third Octave Peak SPL Transfer Function Spectra at P1, Load Case #3, Ref. 89 N rms	142
40	Effect of Engine Mount Lug Stiffness on Transfer Function Spectra at P1, Ref. 89 N rms	145
41	Effect of Variation in Engine Mount Parameters on Transfer Function Spectra at P1, Load Case #2, Ref. 89 N rms	147

LIST OF FIGURES (CONT.)

Figure No.

42 Effect of Isolator Stiffness Variation on SPL Transfer Function Spectrum at P1, Load Case #2, Configuration AA, Ref. 89 N rms 148

43 Effect of Isolator Damping Variation on SPL Transfer Function Spectra P1, Load Case #2, Configuration AA, Ref. 89 N rms 149

44 Effect of Isolator Stiffness Variation on Transfer Function Spectra at P1, Load Case #2, Ref. 89 N rms . . 150

45 Effect of Isolator Stiffness Variation on Transfer Function Spectra at P1, Load Case #3, Ref. 89 N rms . . 151

LIST OF TABLES

Table No.

1 Rigid Engine Mass Properties 41

2 Isolator Static Mechanical Properties 43

3 Noise and Vibration Data Acquisition Specification for Isolator Performance Tests 45

4 Test Schedule 47

5 Measured One-Third Octave Peak SPL Transfer Functions at Microphone Position P1; Ref. 89 N rms 48

6 Measured One-Third Octave Peak SPL Transfer Functions at Microphone Position P1; Ref. 89 N rms 49

7 Measured Engine Alone-Interior Sensed One-Third Octave SPL at MIR 50

8 Isolator Performance Comparisons; OASPL at P1 Based on Engine Running Data 51

9 Engine Mount Free-Free Normal Mode Frequencies 52

10 Engine Mount Normal Mode Selection Bands 53

11 Data Specification - Fuselage Impedance and Noise Transmission Tests 53

12 Model #1 - Predicted Engine Support Frequencies for Various Isolators 54

13 Model #2 Fuselage Stiffness Variation, Isolator Configuration B1, 30 Elastic Modes, Predicted Frequencies, Hz 55

14 Model #2 Mode Convergence, Isolator Configuration B1, Fuselage Stiffness - 1.13×10^8 N/m Predicted Frequencies, Hz 56

15 Model #2 Mode Convergence, Isolator Configuration B1, Fuselage Stiffness 1.13×10^8 N/m Predicted Frequencies, Hz 57

16 Model #2, Predicted Resonant Frequencies, Hz Fuselage Stiffness 1.13×10^8 N/m, 30 Elastic Modes . . 58

17 Model #2 Resonant Frequencies for all Prediction Bands, Configuration AA Isolators, Fuselage Stiffness 1.13×10^8 N/m 59

18 Load Case Force Vectors 60

NOMENCLATURE

a_x	engine c.g. longitudinal acceleration
a_y	engine c.g. lateral acceleration
a_z	engine c.g. vertical acceleration
g	gravity units
i	complex number $\sqrt{-1}$, also index
k_a	isolator complex axial stiffness
k_f	fuselage ground springs
k_r	isolator complex radial stiffness
q_e	engine mount elastic mode degree of freedom
q_r	engine mount rigid body degree of freedom
C^*_{S2}	fuselage inertance matrix
F_R	forces applied to engine c.g.
F_{S1}	attach point nodal forces associated with X_{S1}
F'_{S1}	attach point nodal forces associated with X'_{S1}
F_{S2}	nodal forces associated with X_{S2}
F'_{S2}	attach point nodal forces associated with X'_{S2}
I	unity diagonal matrix
I_{xx}	engine roll inertia
I_{yy}	engine pitch inertia
I_{zz}	engine yaw inertia
K	stiffness matrix, in general
K^*_{S2}	fuselage dynamic stiffness matrix
M	mass matrix, in general
M_M	engine mount rigid body mass matrix
M_R	rigid engine mass matrix
M^*_{S2}	fuselage apparent mass matrix

P^{*}_{S2}	firewall force excitation to cabin SPL transfer function matrix
Q_e	engine mount elastic mode eigenvectors
Q_R	engine mount rigid body eigenvectors
T_{cg}	engine c.g. to isolator rigid body transformation
W	engine weight
X,Y,Z	Cartesian coordinates
X_I	engine mount interior nodal degrees of freedom
R	engine c.g. degrees of freedom
X'_{S1}	engine to isolator degrees of freedom set
X_{S1}	engine mount to isolator degrees of freedom set
X_{S2}	fuselage degrees of freedom
X'_{S2}	engine mount to fuselage degrees of freedom set
β	engine mount critical damping ratio
δ^i	switch, denoting ± 1
γ	ratio of disturbing frequency f_d to system natural frequency f_n
η	material loss factor
$\theta_x, \theta_y, \theta_z$	angular rotations about the Cartesian coordinates
ω	circular frequency
ω_e	engine mount free-free normal mode circular frequency
$\dot{}$	superscript denoting differentiation with respect to time
$\ddot{}$	superscript denoting two differentiations with respect to time

BLANK

PAGE

I. INTRODUCTION

Over the past few years considerable attention has been given to the reduction of interior noise in general aviation aircraft (ref. 1-14). A majority of the literature in this area has concentrated on reduction of the airborne source by investigating methods for increasing sidewall transmission loss or reducing the propeller signature (ref. 15-22). The twin engine aircraft has been the major subject of the above referenced work due to the geometric location of the propeller plane, being in close proximity to the fuselage sidewall. In single engine general aviation aircraft the structure-borne noise component produced by engine vibrarions has been shown to be a major source of interior noise (ref. 23). The interior noise spectra shown in Figure 1 is taken from data presented in Reference 23 wherein ground tests of a Cessna Model 172 aircraft were carried out using an engine attached/detached test technique to determine the engine induced structure-borne noise contribution. As can be seen by the data given in Figure 1, engine induced structure-borne noise has significant components up through the 1600 Hz band. For the referenced data which was taken at an engine speed of 2160 rpm the fundamental propeller tone, is in the 63 Hz band, and establishes the major low frequency component. Responses in the 500 to 1250 Hz bands establish the major mid-frequency contributions.

Improved engine vibration isolation would appear to be a viable noise control measure for the reduction of the structure-borne noise in the single engine aircraft. However effective application of any noise control measure requires predictive procedures for screening candidate materials and test procedures for verifying the choice of a particular control measure. To this end an experimental and analytical program was undertaken to develop the necessary test and analysis procedures to investigate engine vibration isolation treatment for reduced interior noise transmission. The specific objectives of the program were to:

1) develop a laboratory based test procedure to simulate engine induced structure-borne noise transmission

2) test a range of candidate isolators for relative performance data and basic data for analytical model correlation

3) develop an analytical model for isolator design evaluation.

The approach to this program was to develop a laboratory based test facility employing the Cessna Model 172 aircraft used in previous studies, and described in Reference 23. A picture of the facility is shown in the frontispiece. By direct excitation of a rigid engine, via an electrodynamic shaker, transfer function data in the form of interior sound pressure level response for a given force input could be obtained for candidate noise control measures. A series of isolators, including a rigid baseline set were tested and relative comparisons were made between measured transfer functions. Due to the lack of predictive procedures for the higher frequency range of interest in this study, the development of the analytical model required empirical characterization of the aircraft aft of the firewall. Forward of the firewall finite element structural analysis and dynamic modeling procedures were used to model the various components. Coupling procedures then were used to combine the various component representations. Comparisons of predicted to measured results for the various isolator sets were made to verify the analytical model and to point out the modeling detail necessary to insure adequate analytical representation.

Use of trade names or names of manufacturers in this report does not constitute an official endorsement of such products or manufacturers, either expressed or implied, by the National Aeronautics and Space Administration.

II. TEST FACILITY, INSTRUMENTATION, AND PROCEDURES

A. Test Facility Description

The 1963 Cessna model 172 single engine aircraft used in the previously referenced source identification ground tests was also employed for the present investigation. In the previous studies engine attached/detached tests were carried out to determine the structure-borne noise component. The structure-borne noise levels were determined by subtracting the airborne noise, which was obtained during the engine detached tests, from the engine attached spectra. The subtraction of the airborne component worked quite well since both source components were of near equal strength. However, it was realized that if moderate reductions in structure-borne noise were obtained, the engine running test facility would not yield accurate measures of the structure-borne noise levels. Effectively the engine attached and engine detached spectrum would for the most part appear identical. This was the major reason for developing a laboratory based test facility. The simulation of engine excitation would be supplied by electrodynamic shaker excitation applied to the engine. After preliminary laboratory tests it was felt that shaker excitation of the engine could be harmful to the engine bearings unless the propeller was continuously rotated during the tests. It was also desirable to have well defined engine mass properties for development of the analytical model and a mechanically convenient means of varying engine isolator properties. For these reasons a rigid engine mass was designed for the laboratory test facility.

The rigid engine mass properties were designed to meet the major mass properties of the actual engine which were determined from a series of static weight measurements to determine the engine center of gravity and a series of swing tests to measure principal inertias. In Table 1, the actual engine measured mass properties and the rigid engine design calculated mass properties are listed. It was felt that the primary engine mass properties would be the engine weight, center of gravity location, and I_{XX} or roll inertia. Obtaining these mass properties would allow simulation of the primary engine dynamic loads, namely thrust and torque oscillations.

A sketch of the rigid engine design is given in Figure 2. The design allowed direct use of the existing engine mount frame and the incorporation of a series of engine vibration isolators with varying mechanical properties in addition to the original equipment isolators. A photograph of one of the original Lord Kinematics H-3006-1 vibration isolators and a Barry Controls Series 22002 vibration isolator is given in Figure 3 along with the forward section of the engine mount structure. The original equipment isolator was adapted to the dummy engine via a pair of ring collars to pick up engine loads in the axial direction. A rigid (steel) set of isolators, duplicating the Series 22002 dimensions, were also manufactured to provide a baseline configuration. The static isolator properties were obtained from the manufacturer's product literature (ref. 24-25) and are listed in Table 2 for comparison. For the purposes of maintaining numerical stability in the solution procedures, to be discussed in Section IV, the "rigid" isolator stiffness was set to a finite value. The baseline values for the material loss factor (η) for the isolators were taken to be 0.10; specific loss factor data were not given in the product literature.

The wings, empennage and interior trim were removed from the test aircraft during previous investigations. For the majority of the tests conducted during the present investigation a 1.27 cm plywood bulkhead was installed at Body Station 108 which separated the cabin area from the fuselage aft tail cone. This bulkhead replaced the standard interior trim which was a thin plastic panel with molded stiffeners. Outside of the installation of the relatively rigid bulkhead, the cabin interior was void of all trim items. In this configuration the cabin was most sensitive to structure-borne noise transmission and provided a maximum signal to noise ratio for the acoustically untreated laboratory environment.

B. Test Configurations

Engine excitation was provided by a 7100 N Unholtz Dickie electrodynamic shaker which could be attached directly to the rigid engine. The attach points are shown in Figure 2. The resulting loading configurations are shown in Figure 4. Load Case 1 represents primarily a yaw type loading,

Load Case 2 allows for simulation of engine torque oscillations and Load Case 3 thrust/pitch oscillations. In Figure 5 the facility is shown in the Load Case 2 configuration. In addition to the three load configurations, four isolator configurations were incorporated into the facility; R1 - a set of rigid isolators, OA - Lord Kinematics H-3006-1 original equipment isolators, EA - a set of Barry Controls 22002-5 hard rubber isolators, and AA - a set of Barry Controls 22002-1 soft rubber isolators. Reference is again made to Table 2 for their relative stiffnesses.

C. Instrumentation

The rigid engine was instrumented with three accelerometers located at the engine center of gravity. Access for the triaxial accelerometer arrangement is shown in Figure 2. A load cell was also attached directly to the engine at the shaker attach points to provide for input force control. Three microphones were located within the aircraft cabin; P1 at the pilot's right ear position, P2 at the copilot's left ear position, and P3 mid-cabin at the passenger's ear level. A list of the specific transducers used during the tests is given in the data acquisition specification in Table 3.

D. Data Acquisition and Reduction

A Spectral Dynamics (SD) 105 amplitude servo/monitor was driven by a SD 104A-5 sweep oscillator to provide a constant harmonic input force. The oscillator was swept from 10 Hz up through 1000 Hz at a rate of 2 Hz/second. This was the fastest sweep rate possible without loss of peak response in the low frequency region. To record transfer function data a d.c. signal proportional to frequency, taken from the sweep oscillator, was used to drive the X-axes of two Hewlett-Package Z-Y analog recorders. Via a switching network one of the engine accelerometer signals and one of the interior microphone signals were input into a Spectral Dynamics dual channel tracking filter set on a 5.0 Hz bandwidth. The tracking filter was driven by the sweep oscillator. The outputs of the tracking filter were routed to the Y axis of the X-Y

recorders. In this manner direct transfer function plots of two of the transducer signals could be obtained in a single sweep. A Nicolet Scientific MINI-UBIQUITOUS 444A fast fourier transform (FFT) computing spectrum analyzer was used to record one-third octave peak SPL responses of the interior microphones. The sweep data were recorded on an Ampex model PR2230 14-channel FM intermediate band magnetic tape. The channel assignment is given in Table 3. A schematic of the instrumentation and data acquisition system used during the isolator transfer function tests is shown in Figure 6.

A majority of the transfer function data were recorded at an input level of 89 N rms. Several runs were made at 178 N rms to check for system linearity. The sound pressure level data presented herein are referenced to $p_r = 2 \times 10^{-5}$ N/m^2 and defined in the usual way by

$$SPL = 10 \times \log_{10}\left(\frac{p_{rms}}{p_r}\right)^2 .$$

Acceleration data are presented as acceleration levels referenced to $a_r = 1.0$ g where g = 9.807 m/s^2 and are defined by

$$AL = 10 \times \log_{10}\left(\frac{a_{rms}}{a_r}\right)^2 .$$

E. Facility Calibration

Calibration of the instrumentation used in the test facility was carried out in the usual manner. The accelerometers were calibrated against a Kistler model 808K/561T accelerometer which is traceable to NBS Standards. A B&K sound level calibrator type 4230 (94 dB @ 1000 Hz) was used to calibrate the interior microphones. The load cell was calibrated using a known mass under controlled excitation. Facility background noise during the test established the microphone instrumentation noise floor. In Figure 7 a plot of the sound pressure level at microphone P1 is given for the case where the shaker was detached from the dummy engine, however the shaker was driven at a 0.05 g excitation to

simulate expected shaker radiated noise. When comparing noise floor data given in Figure 7 to the isolator transfer function data, to be presented in the following section, it can be seen that sufficient signal to noise levels exist to record meaningful data throughout the frequency range of interest. The noise floor for the rigid engine c.g. mounted accelerometers were on the order of 25 dB below the measured on axis responses. Maximum error in controlling the shaker drive signals was less than 0.5 dB (4.4N for a 89 N drive force).

III. STRUCTURE-BORNE NOISE TRANSFER FUNCTION TESTS

The simulated engine induced structure-borne noise tests results obtained during the program were used for two purposes: First to obtain a relative measure of the structure-borne noise isolation capability of several engine vibration isolator's with varying static stiffness properties. Second, and of major importance, was to generate basic data to verify a mathematical model of the structure-borne noise transmission phenomena. The model would then be used as a tool for improved isolator design evaluation.

Each of the four isolator configurations listed in Table 2 were subjected to 89 N rms shaker excitation in each of the three excitation configurations shown in Figure 4. In addition to these runs several additional runs were made at the increased excitation level of 178 N rms to provide a check on the linearity of the system. Data were also obtained with the bulkhead at B.S. 108 removed to obtain a measure of tail cone isolation provided by the bulkhead. During one additional run the four lower engine mount struts were held hand tight to obtain a qualitative measure of the importance of these components to the transmission phenomena. The run schedule used during the transfer function tests is given in Table 4.

Due to similarities in excitation and resulting responses between Load Case #1 and Load Case #2 configurations and for the sake of brevity, Load Case #1 data have been intentionally omitted from the following discussions. Likewise, the performance of the hard rubber isolators, configuration EA, was very similar to that of the original equipment isolators, OA, and therefore emphasis has been placed on comparisons of the R1, OA, and AA isolator configurations.

A. Narrow Band Data

Typical narrow band (5 Hz) transfer function data are represented by the complete set of spectra shown in Figure 8. While these spectra are for Load Case #2 excitation of the rigid isolators, configuration R1, they

serve to point out several general characteristics of all the recorded data. As can be seen, the interior noise spectra are rich in narrow band response. The SPL spectra at the various interior locations exhibit only minor variations from position to position and thus any one of the microphone responses would serve to represent the cabin noise spectra. The Load Case #2 excitation (ref. Figure 4) effectively applies a set of forces to engine c.g. in the Y-Z plane and torque about the X-axis. For a shaker excitation of 89 N rms the resultant c.g. forces are F_y = 77.8 N rms and F_z = 43.1 N rms. With an engine design weight of 170 kg the estimated engine c.g. acceleration levels away from resonant responses, are calculated to be a_y = -26.6 dB and a_z = -31.72 dB (r_e 1.0 g). These estimated levels are indicated on the corresponding acceleration spectra in Figure 8 and agree very well with the measured levels. The relatively high acceleration response along the X-axis is attributed to X-Z axis dynamic coupling.

Similar measured response data are shown in Figure 9 for Load Case #3 type excitation. For this case excitation is in the X-Z plane directed through the engine c.g. The estimated c.g. accelerations are again noted on the spectra and again agree well with the measured data. The acceleration spectra show two distinct engine rigid body coupled longitudinal-vertical resonant responses at 23 Hz and 76 Hz. Due to X-Z coupling these resonances also appear in the Load Case #2 data of Figure 8. A strong elastic mode resonance at 970 Hz is also easily identified in the spectra. The response is primarily engine vertical bending. These engine resonances are clearly identified in the interior noise spectra. The interior SPL's for Load Case #3 are dominated in the lower frequency region by the engine rigid body responses. The corresponding SPL responses for the Load Case #2 excitation are not so distinct due to the higher level of other low frequency content in the spectra.

The relative structure-borne noise transmission isolation performance of the original equipment isolators, OA, as compared to the rigid isolators R1 can be obtained by comparison of the SPL response at P1 in Figure 10 to the SPL response given in Figure 8. A similar comparison/evaluation can be

made for the lowest frequency isolators, configuration AA, by examination of the transfer function data given in Figure 11. The original equipment isolators appear to function well in the 50 to 100 Hz range, thereafter a plateau is reached until the influence of the 970 Hz engine resonance begins to increase the transmission. Similar trends are found for the softer isolators, AA, with somewhat increased performance over that of the original equipment isolators. The leveling off of the isolation performance in the higher frequencies is not at all expected based on simple single degree of freedom isolation analysis (ref. 25). It is well known that elastomeric materials exhibit frequency dependent properties (ref. 26-29) and to what extent this behavior may be responsible for the observed response is addressed with the aid of the analytical model described in Section IV and the results are discussed in Section V.

It is also important to compare the engine c.g. acceleration response spectra of the various isolator configurations. By comparison of the data given in Figures 8, 10, and 11 it can be seen that overall there is very little difference in acceleration response spectra among the different isolator configurations; however, there is a trend for the band of low level elevated Y-axis acceleration response, i.e., response above the estimated levels, to shift to lower frequencies with decreased isolator stiffness. This response basically follows the engine rigid body support frequencies. Nevertheless, the reasonably constant engine acceleration response indicates that the use of transfer function data based on a constant force to obtain a relative comparison of isolator performance would be, for the most part, duplicated using a constant acceleration source. Indeed, inflight engine excitation should appear as a force or acceleration source and therefore the above observation adds validity to the present test and evaluation procedures.

Direct comparison of the narrow band SPL transfer function data is difficult due to the rich narrow band response. To improve the comparison, hand smooth peak response transfer functions were developed and typical data are given in Figures 12 and 13. The data given in Figures 12 and 13 clarify the previous observation for the Load Case #2 excitation and shows that the original equipment isolators were much less effective for

longitudinal (Load Case #3) excitations. This should be expected based on the high radial stiffness of the OA isolators, ref. Table 2.

B. Peak One-Third Octave Data

The test aircraft in flight operates at an engine speed ranging from 2100 rpm to 2700 rpm. The resulting engine excitation spectra consist of engine 1/2 rpm harmonics of multiples ranging from 17.5 Hz to 22.5 Hz. The resulting combined operational excitation spectra is therefore dense beyond 70 Hz. The probability of coincidence of an engine harmonic with peaks in the measured structure-borne noise transfer function spectra would be high for normal flight conditions. With this in mind, the sound pressure level transfer function data were analyzed with a FFT analyzer set on the peak capture mode for one-third octave resolution. A plot of the resulting SPL transfer function data at P1 for Load Case #2; isolator configurations R1, OA, and AA are given in Figure 14. Similar data for Load Case #3 are given in Figure 15. These data are also presented in tabular form in Tables 5 and 6 along with other run configuration data. As can be seen by examination of Figures 14 and 15, presentation of the data in terms of peak one-third octave transfer functions greatly improves the interpretation of the relative performance of the various isolators.

C. Isolator Relative Performance

A measure of the expected performance of the various isolators for engine running excitations was developed by utilizing data taken from previous engine running ground tests of the aircraft. The measured engine alone-interior removed one-third octave SPL given in Table 7 were taken from Reference 23. The location of the reference microphone MIR used in the engine running ground tests was close to the P1 microphone position used in the present study. To be consistent with the measured transfer function data, the overall sound pressure levels (OASPL) given in Table 7 are based on the listed responses through the 1000 Hz band. The engine running test data were obtained with the original equipment, OA, isolators installed. Thus, with the engine running performance of the OA isolators known, a force level correction factor, relative to 89 N rms, can be

obtained from

$$FL = SPL_{ER} - SPL_{OA}$$

where SPL_{ER} are the engine running one-third octave sound pressure levels given in Table 7 and SPL_{OA} are the peak transfer function levels given in Table 5. The force level correction factors are then added to the peak transfer function levels for the other isolator configurations to determine their engine running levels.

Typical results from the above analysis are plotted in Figures 16 and 17 for transfer functions taken from Load Case #2 and Load Case #3 excitations, respectively. The data denoted as OA are the measured interior levels. The rigid isolator predictions show a considerable increase in low frequency noise over the original equipment. This is especially noticeable for Load Case #3 excitation. Summary results of the analyses are given in Table 8 in the form of linear and A-weighted OASPL. OASPL were computed based on analyses of data in one-third octave band from 20 Hz through 800 Hz and from 20 Hz through 1000 Hz. It was initially felt that including the 1000 Hz band transfer function data would contaminate the overall levels. However, as can be seen by comparison of the OASPL for the two cases, the force level correction reasonably well accounts for the high response in the 1000 Hz band. The EA isolators provide somewhat less isolation than the original isolators. While the AA isolators show anywhere from 2.7 dBA to near 10 dBA noise reduction over that of the original equipment isolators. The largest gains in structure-borne noise reductions are obtained from extrapolation of the Load Case #2 transfer function data.

D. System Linearity

A check on the system linearity was provided by the data obtained in Runs 3, 4, and 14, (reference Table 4). In these runs transfer function sweeps were carried out with 178 N rms excitation. Narrow band data for isolator, configuration AA, Load Case #3 are given in Figure 18 for the two excitation levels. Due to large engine motions at the lowest frequencies the sweeps were initiated around 15 Hz for the higher level excitation. A 6 dB increase in response levels should result due to the doubling of

the input harmonic excitation. The input 6 dB increase is verified by the acceleration spectra given in Figure 18, however, there appears to be various levels of nonlinear response in the resulting interior sound pressure level spectra. The one-third octave peak SPL data given in Table 5, under configuration AA, gives a quantitative measure of the degree of nonlinearity in the response. These data are plotted in Figure 19 for Load Case #3 type excitation. The highest degree of nonlinearity occurs below 40 Hz; an area of much less interest than the remainder of the spectra. The importance of the nonlinear response to the overall isolator design, analysis and evaluation process is at this time unknown. However, as isolation imprives, one should expect a decreasing influence of the nonlinear response. Since the nonlinear response appears mainly as a leveling off of interior responses, design analyses should yield conservative estimates of cabin noise levels for a given isolator design.

E. Engine Mount Damping Effectiveness

The engine mount structure is an assemblage of 1.91 and 1.59 cm 4130 steel tubes which form a very strong and lightweight carrythrough structure. The engine mount structure weighs only 5.22 kilograms, while the engine it supports weighs 170 kg. During one of the sweep tests with the rigid isolators installed, all four lower tube support members were held handtight. Comparison to hands-off data revealed that the added damping and whatever induced mass and stiffness had no noticeable effect on the transmitted structural-borne interior noise levels. A more systematic study of the importance of the engine mount structure in the noise transmission phenomena was carried out analytically and the results are presented in Section V.

F. Fuselage Tail Cone Isolation

The original interior trim bulkhead at Body Station 108 was a thin plastic panel with molded stiffners. As previously mentioned, this bulkhead was replaced by a 1.27 cm plywood bulkhead to provide some acoustic isolation from the tail cone. During the sweep tests it was of interest then to see what effect the bulkhead had on the interior pressures over that of the completely bare fuselage. Narrow band SPL spectrum at P1 for the

bulkhead removed configuration is given in Figure 20. The dashed line spectra given in Figure 20 is for the bulkhead installed configuration. As can be seen the spectrum for the bulkhead installed case is overall higher than for the bare fuselage case. In particular, the response in the 200 Hz to 400 Hz area is significantly increased by insertion of the bulkhead.

IV. ANALYTICAL MODEL

A. Model Concept

Coupled structural acoustic modeling procedures for light aircraft type structures have been given some attention over the past few years (ref. 30-33), however the purposed procedures have not been validated for the higher frequency region of interest to this study (ref. 34) (up through 1000 Hz). The scope of the present study was for the most part limited to investigating the engine mount structure and vibration isolator design and therefore changes to the fuselage/cabin area were not anticipated. For these reasons it was decided that the fuselage/cabin response would be characterized empirically. On the other hand all components forward of the fuselage firewall were to be modeled analytically so that design variations could be easily incorporated into the system model. A model of this nature is basically a retrofit design tool. However, the procedures used for coupling the system subcomponents are valid whether the component characterization is experimental or analytical.

The model was developed using the conventional global axis system, where X is aft along the centerline of the fuselage, Y is to the pilot's right and Z is upward for a right-handed system.

B. Component Representation

In this section each of the four model components; the engine, the vibration isolators, the engine mount structure, and fuselage cabin response, will be described.

1. Engine as a Rigid Body

The engine was modeled as a rigid body; the mass properties used are those given in Table 1. In Figure 21 the engine is schematically shown with its associated centroidal coordinate set $(X_R) = [X, Y, Z, \theta_X, \theta_Y, \theta_Z]$. Also shown are the assumed rigid extension arms to each of the four isolator attach points. At the isolator attach points it is assumed that the three translational degrees of freedom are sufficient to model the

transmitted engine loads to the vibration isolators. The rotational degrees of freedom were not represented and therefore no moment carrythrough exists at these points. It is felt that moment continuity at these points will be of second order importance. The degree of freedom set at the isolator attach points is denoted as $\{X_{S1}\} = \lfloor X_1, Y_1, Z_1, X_2, Y_2, Z_2, X_3, Y_3, Z_3, X_4, Y_4, Z_4 \rfloor$.

The motion at isolator attach point i due to a prescribed engine motion is given by the rigid body transformation

$$\begin{Bmatrix} X_i \\ Y_i \\ Z_i \end{Bmatrix} = \left[\begin{array}{c|c|c|c|c} 1 & & & Z_i - Z_{cg} & Y_{cg} - Y_i \\ \hline & 1 & & Z_{cg} - Z_i & X_i - X_{cg} \\ \hline & & 1 & Y_i - Y_{cg} & X_{cg} - X_i \end{array}\right] \begin{Bmatrix} X \\ Y \\ Z \\ \theta_X \\ \theta_Y \\ \theta_Z \end{Bmatrix}, \tag{1}$$

$$= T_{cg}^{\,i} \{X_R\}, \tag{2}$$

where $\lfloor X_i, Y_i, Z_i \rfloor$ is the position of the ith attach point and $\lfloor X_{cg}, Y_{cg}, Z_{cg} \rfloor$ the position of the engine c.g. in the global reference system. For the complete attach point coordinate set we may write

$$\{X_{S1}\} = \begin{bmatrix} T_{cg}^1 \\ T_{cg}^2 \\ T_{cg}^3 \\ T_{cg}^4 \end{bmatrix} \{X_R\} \equiv \left[T_{cg}\right] \{X_R\}. \tag{3}$$

The dynamic equations of motion for the rigid body may be written as

$$\left[M_R\right] \{\ddot{X}_R\} = \{F_R\} + \left[T_{cg}\right]^T \{F_{S1}\}_R \tag{4}$$

where M_R is the dummy engine diagonal mass matrix comprised of (M, M, M, I_{XX}, I_{YY}, I_{ZZ}) see Table 1. $\{\ddot{X}_R\}$ are the c.g. accelerations, $\{F_{S1}\}_R$ are the attach point nodal forces associated with the displacement set $\{X_{S1}\}$. Throughout this report differentiation with respect to time will be denoted by dot superscript, thus, for accelerations the double dot superscripts are employed.

2. Vibration Isolators

The vibration isolators were modeled in their local axis as being independent radial, k_r, and axial k_a, frequency dependent springs,

$$k_r = k_r^* (\omega) \left[1 + i\, \eta(\omega)\right] \tag{5}$$

and

$$k_a = k_a^* (\omega) \left[1 + i\, \eta(\omega)\right] \tag{6}$$

where i is the complex number $\sqrt{-1}$, $k_r^*(\omega)$ and $k_a^*(\omega)$ are the radial and axial spring modulus amplitudes and $\eta(\omega)$ is the isolator material loss factor, both being a function of the frequency of excitation. At this point we have for the most part specified harmonic excitation. However, the equations of motion hereafter will still retain their time domain formulations for a consistent representation among all components of the model. The isolators are considered to have an effective dynamic mass equal to their physical mass. If the mass of the isolators is very small as compared to the engine mass, their dynamic effects may be neglected. We have herein included the isolator mass for the sake of completeness.

The vibration isolator is schematically shown in Figure 22 in its local and global axis representation. Transformation of the isolator mechanical properties from the local axis to the global axes results in

the following unassembled isolator element mass and stiffness matrices:

Mass Matrix for the ith isolator element

$$[M_i] = \begin{bmatrix} M & | & 0 \\ - & + & - \\ 0 & | & M \end{bmatrix} \tag{7}$$

where

$$[M] = \text{dia}\left[M_i/2,\ M_i/2,\ M_i/2\right].$$

Stiffness Matrix for the ith isolator element

$$[K^i] = \begin{bmatrix} K^i_{11} & | & K^i_{12} \\ - & + & - \\ K^i_{21} & | & K^i_{22} \end{bmatrix} \tag{8}$$

where

$$[K^i_{22}] = [K^i_{11}] = \begin{bmatrix} k_r & | & \\ - & + & - \\ & | & 1/2(k_r + k_a) \end{bmatrix} \quad \begin{bmatrix} & | & \\ - & + & - \\ \frac{\delta^i}{2}(k_r - k_a) & | & \end{bmatrix} \quad \begin{bmatrix} & | & \\ - & + & - \\ & | & \frac{\delta^i}{2}(k_r - k_a) \end{bmatrix} \quad \begin{bmatrix} & | & \\ - & + & - \\ & | & 1/2(k_r + k_a) \end{bmatrix} \tag{9}$$

and

$$[K^i_{12}] = [K^i_{21}] = \begin{bmatrix} -k_r & | & \\ - & + & - \\ & | & -1/2(k_r + k_a) \end{bmatrix} \quad \begin{bmatrix} & | & \\ - & + & - \\ \frac{\delta^i}{2}(k_a - k_r) & | & \end{bmatrix} \quad \begin{bmatrix} & | & \\ - & + & - \\ & | & \frac{\delta^i}{2}(k_a - k_r) \end{bmatrix} \quad \begin{bmatrix} & | & \\ - & + & - \\ & | & -1/2(k_r + k_a) \end{bmatrix} \tag{10}$$

where δ^i is positive for i = 1 and 2, and is negative for i = 3 and 4. These transformed element matrices reflect the isolator axial alignment being 45 degrees to the global Z axis, see Figure 3. The coordinate sets (d.o.f.) associated with the isolators are those on the engine side of the isolator, previously defined as $\{X_{S1}\}$ and a corresponding set on the engine mount side of the isolator, $\{X'_{S1}\}$.

The dynamic equations of motion for the isolators may be written as

$$\begin{bmatrix} M_{VI}^{11} & 0 \\ 0 & M_{VI}^{22} \end{bmatrix} \begin{Bmatrix} \ddot{X}_{S1} \\ \ddot{X}'_{S1} \end{Bmatrix} + \begin{bmatrix} K_{VI}^{11} & K_{VI}^{12} \\ K_{VI}^{21} & K_{VI}^{22} \end{bmatrix} \begin{Bmatrix} X_{S1} \\ X'_{S1} \end{Bmatrix} = \begin{Bmatrix} F_{S1} \\ F'_{S1} \end{Bmatrix}_{VI} \tag{11}$$

where

$$M_{VI} = \text{dia}\left[M, M, M, \ldots, M\right], \tag{12}$$

$$\left[K_{VI}\right] = \begin{bmatrix} K_{11}^1 & & & & K_{12}^1 & & & \\ & K_{11}^2 & & & & K_{12}^2 & & \\ & & K_{11}^3 & & & & K_{12}^3 & \\ & & & K_{11}^4 & & & & K_{12}^4 \\ & & & & K_{11}^1 & & & \\ & & & & & K_{11}^2 & & \\ & & & & & & K_{11}^3 & \\ & & & & & & & K_{11}^4 \end{bmatrix} \quad \text{sym} \tag{13}$$

and $\{F_{S1}\}$ and $\{F'_{S1}\}$ are the nodal forces associated with the $\{X_{S1}\}$ and $\{X'_{S1}\}$ coordinate sets, respectively.

3. Engine Mount Structure

The engine mount structure is an assemblage of 1.91 and 1.59 cm 4130 steel tubes which form a very strong and lightweight (5.22 kilograms) carrythrough structure. The engine mount is schematically shown in Figure 23 with its corresponding coupling degrees of freedom. The coordinate set $\{X'_{S1}\}$ is the coupling degrees of freedom associated with the isolator attach points and the set $\{X'_{S2}\}$ are associated with the engine mount to fuselage attach points. A finite element model of the engine mount was developed to represent its dynamic characteristics out through 1000 Hz. The model consisted of 72 structural nodes interconnected with 70 elastic beam elements resulting in a dynamic model with 201 degrees of freedom. The isolator attachment lugs, see Figure 3, were not modeled in the finite element model. These lugs are modeled as a spring in series with the isolator. The lowest stiffness is in the axial direction with a minimum value of 3389 N/m. Thus the local stiffness of the lugs are of interest only in the "rigid" isolator configuration.

Modal synthesis techniques (ref. 35-40) were used to reduce the number of degrees of freedom in the model. The model was expanded in terms of its free-free normal mode responses. A total of fifty-one (51) normal modes of the free structure exist in the frequency range out to 1000 Hz. A plot of mode number versus frequency for the engine mount structure is given in Figure 24 and a list of the frequencies along with the engine strut number(s) with the largest contribution to the eigenvector is given in Table 9. In addition to the 51 elastic modes, an additional six (6) rigid body degrees of freedom are necessary to completely describe the engine mount response to arbitrary motion. Due to the high number of elastic mode responses, the modes were band selected in groups of 30 each during the model predictions. The mode numbers used for a given prediction range are listed in Table 10. The six rigid body modes were then used in conjunction with the thirty elastic modes to represent the engine mount dynamics in any of the desired prediction ranges.

The resulting dynamic equations of motion for the engine mount structure are, in matrix form,

$$\begin{bmatrix} M_M & | & 0 \\ - & - & - \\ 0 & | & I \end{bmatrix} \begin{Bmatrix} \ddot{q}_r \\ - \\ \ddot{q}_e \end{Bmatrix} + \begin{bmatrix} 0 & | & 0 \\ - & - & - \\ 0 & | & 2\beta\omega_e \end{bmatrix} \begin{Bmatrix} \dot{q}_r \\ - \\ \dot{q}_e \end{Bmatrix} + \begin{bmatrix} 0 & | & 0 \\ - & - & - \\ 0 & | & \omega_e^2 \end{bmatrix} \begin{Bmatrix} q_r \\ - \\ q_e \end{Bmatrix}$$

$$= \begin{bmatrix} Q_{R1}^T \\ - \\ Q_{e1}^T \end{bmatrix} \{F'_{S1}\}_M + \begin{bmatrix} Q_{R2}^T \\ - \\ Q_{e2}^T \end{bmatrix} \{F'_{S2}\}_M \tag{14}$$

where M_M is the engine mount rigid body mass matrix, I a unit diagonal matrix, β an imposed critical damping ratio for each mode, ω_e the normal mode frequency, Q_{R1} and Q_{e1}, respectively, are the rigid body and elastic mode components associated with the $\{X'_{S1}\}$ degree of freedom set, Q_{R2} and Q_{e2} are, respectively, the rigid body and elastic mode components associated with the $\{X_{S2}\}$ degree of freedom set, $\{F'_{S1}\}_M$ are the nodal forces at the isolator attach points, $\{F_{S2}\}_M$ are the nodal forces at the fuselage attach points, $\{q_r\}$ are the six rigid body degrees of freedom, and $\{q_e\}$ are the elastic mode degrees of freedom. The nodal degrees of freedom of the engine mount are rleated to the rigid body and elastic mode degrees of freedome via the normal mode eigenvectors:

$$\begin{Bmatrix} X'_{S1} \\ - \\ X'_{S2} \\ - \\ X_I \end{Bmatrix} = \begin{bmatrix} Q_{R1} & | & Q_{e1} \\ - & - & - \\ Q_{R2} & | & Q_{e2} \\ - & - & - \\ Q_{RI} & | & Q_{eI} \end{bmatrix} \begin{Bmatrix} q_r \\ - \\ q_e \end{Bmatrix} \tag{15}$$

For completeness in the above expression all interior nodal degrees of freedom of the engine mount structure, $\{X_I\}$ have been included. However, it should be noted that the interior set $\{X_I\}$ are not needed in the description of the engine mount component and therefore were not retained.

4. Aircraft Fuselage and Interior Response

The dynamic characteristics of the fuselage at the engine mount attachment points and the response of selected cabin interior locations were determined by what is generally referred to as point and/or transfer impedance testing. The choice of the displacement, velocity or acceleration based response measurement is a matter of convenience with respect to instrumentation response and the desired representation. For the problem at hand it would be most convenient to represent the fuselage as a series of coupled spring-like elements wherein mathematically we may write

$$\left[K^*_{S2}\right] \{X_{S2}\} = \{F_{S2}\}_F \tag{16}$$

K^*_{S2} is the frequency dependent dynamic stiffness matrix, $\{X_{S2}\}$ the nodal displacements on the fuselage at the engine mount attach points, and $\{F_{S2}\}_F$ are the corresponding nodal forces. The degrees of freedom associated with the firewall are shown in Figure 25. Consistent with the engine mount representation only the translational degrees of freedom at the firewall are characterized.

Direct measurement of displacement was not considered to be convenient or reliable for the determination of K^*_{S2}. However, the use of acceleration as a base would allow direct and accurate recording of the inertance at the points of interest for a number of possible forms of excitation. In terms of inertance

$$\{\ddot{X}_{S2}\} = \left[C^*_{S2}\right] \{F_{S2}\}_F \tag{17}$$

where $\{\ddot{X}_{S2}\}$ are the nodal accelerations and C^*_{S2} is the frequency dependent inertance matrix. Upon inversion of the inertance matrix we obtain the system apparent mass

$$\left[M^*_{S2}\right] = \left[C^*_{S2}\right]^{-1} \tag{18}$$

where

$$\left[M^{*}_{S2}\right]\{\ddot{X}_{S2}\} = \{F_{S2}\}_{F}. \tag{19}$$

For harmonic motion $\{\ddot{X}_{S2}\} = -\omega^{2}\{X_{S2}\}$ which allows formulation of the desired dynamic stiffness matrix in terms of the measurable inertance matrix;

$$\left[K^{*}_{S2}\right] = -\omega^{2}\left[C^{*}_{S2}\right]^{-1}. \tag{20}$$

Sound pressure level responses at selected points within the cabin interior, namely at those points previously denoted as P1, P2, and P3 in the transfer function sweep tests, are also characterized with respect to the nodal forces $\{F_{S2}\}_{F}$ as

$$\{P_{I}\} = \left[P^{*}_{S2}\right]\{F_{S2}\}_{F} \tag{21}$$

where $\{P_{I}\}$ are the responses at P1, P2, and P3, and P^{*}_{S2} is a matrix of firewall force excitation to cabin SPL transfer functions.

Application of a single nodal force, with all other nodes force free, will allow determination of a column of the inertance matrix, C^{*}_{S2}, by recording all nodal accelerations and a column of the pressure matrix, P^{*}_{S2}, by recording all interior pressure responses. The choice of the force excitation is also one of convenience, consistent with the required accuracy, available equipment, and available analysis software. Traditionally, continuous waveform electrodynamic or hydraulic shaker excitation in the form of random, slow sweep or rapid sweep is used. Impulse techniques have also been successfully applied in a number of related investigations (ref. 41).

A continuous random source was chosen for the present investigation. Data analysis procedures for the random data are straightforward (ref. 42), however, rather lengthy. All data were recorded on magnetic tape, the instrumentation and data acquisition procedures were straightforward. The data specifications used during the tests are given in Table 11. A triaxial accelerometer arrangement was used to simultaneously record orthogonal acceleration responses at a single engine mount attach point along with the input

force signal and the three interior pressure responses. Using a single triaxial accelerometer arrangement required 48 runs to capture the required data.

Data digitization and reduction were carried out using a 12-bit analog to digital converter via a CAMAC interface to a Digital Equipment Corporation PDP 11/70 computer. Prior to the digitization process, the data was low passed at 1250 Hz and high passed at 10 Hz. Parameters used during the digitization process are:

Per Channel Sampling Rate	4096 samples/second
Per Channel Record Length	2048 points
Number of Correlated Records	100

This results in an analysis bandwidth of $B_e = 2.0$ Hz. A trace length of $T_r = 50$ seconds and therefore the number of degrees of freedom for the spectral calculations is $N = 2B_eT_r = 200$. The normalized standard error in the process is then $\epsilon_r = \left[1/B_eT_r\right]^{1/2} = 0.10 (<1dB)$.

A 100-spectra average of the force spectrum input at attach point 1, driving in the X direction is given in Figure 26. The higher frequency roll off in the force spectrum was due to limitations of the 220 N shaker. The 30 dB differential across the spectrum is well within the peak 43 dB magnetic tape and 60 dB A to D process dynamic range. A typical driving point inertance spectrum is given in Figure 27. The magnitude is given in gravity units per Newton input force, both magnitude and phase spectrum are shown. From the magnitude spectrum we note that the overall response is very much to stiffness like throughout the major region of interest.

The measured spectra also show the fuselage to be dynamically a very symmetric structure; this can be seen by comparing the magnitude of the driving point spectrum at X1, in Figure 27, to the driving point spectrum at X4, given in Figure 28. Similar data for the lower engine mount attach points are shown in Figure 29.

It is also of interest to compare transfer inertance spectra and verify that reciprocity was reasonably well satisfied during the data

acquisition process. This is shown to be the case by examination of the typical transfer spectra shown in Figure 30. For use in the analytical model, these quasi-symmetric off-diagonal terms were averaged to insure reciprocity.

Sound pressure level transfer function spectra for the responses at P1 and P3 due to excitation at F_{X1} are given in Figure 31. Recall that microphone P1 is located approximately at the pilot's right ear and P3 at the mid-cabin rear passenger position. The arrow around 64 Hz in these spectra indicate the response at the cabin fundamental acoustic resonance. The fundamental mode response at P3 is much more distinct than at the forward position, P1. This is attributed to the mode node line being very close to the P1 microphone position (see reference 23).

The dynamic stiffness matrices, $\left[K^*_{S2}\right]$, and the pressure transfer function matrices, $\left[P^*_{S2}\right]$, were developed at 2.0 Hz intervals from 10 Hz through 1000 Hz for characterization of the fuselage. Linear interpolation of the complex matrices allowed continuous representation of these quantities throughout the frequency range of interest.

C. Component Coupling Procedures

In development of the model components a number of relationships were developed between the system physical quantities and their associated degrees of freedom. These relationships and auziliary expressions are repeated herein for reference:

1) Engine As a Rigid Body

$$\{X_{S1}\} = \left[T_{cg}\right]\{X_R\} \tag{3}$$

$$\left[M_R\right]\{\ddot{X}_R\} = \{F_R\} + \left[T_{cg}\right]^T\{F_{S1}\}_R \tag{4}$$

2) Vibration Isolators

$$[M_{VI}^{11}]\{\ddot{X}_{S1}\} + [K_{VI}^{11}]\{X_{S1}\} + [K_{VI}^{12}]\{X'_{S1}\} = \{F_{S1}\}_{VI} \tag{11a}$$

$$[M_{VI}^{22}]\{\ddot{X}'_{S1}\} + [K_{VI}^{21}]\{X_{S1}\} + [K_{VI}^{22}]\{X'_{S1}\} = \{F'_{S1}\}_{VI} \tag{11b}$$

3) Engine Mount Structure

$$\begin{bmatrix} M_M & 0 \\ 0 & I \end{bmatrix} \begin{Bmatrix} \ddot{q}_r \\ \ddot{q}_e \end{Bmatrix} + \begin{bmatrix} 0 & 0 \\ 0 & 2\beta\omega_e \end{bmatrix} \begin{Bmatrix} \dot{q}_r \\ \dot{q}_e \end{Bmatrix} + \begin{bmatrix} o & o \\ o & \omega_e^2 \end{bmatrix} \begin{Bmatrix} q_r \\ q_e \end{Bmatrix}$$

$$= \begin{bmatrix} Q_{R1}^T \\ Q_{e1}^T \end{bmatrix} \{F'_{S1}\}_M + \begin{bmatrix} Q_{R2}^T \\ Q_{e2}^T \end{bmatrix} \{F_{S2}\}_M \tag{14}$$

$$\{X'_{S1}\} = [Q_{R1} \; Q_{e1}] \begin{Bmatrix} q_r \\ q_e \end{Bmatrix} \tag{15a}$$

$$\{X_{S2}\} = [Q_{R2} \; Q_{e2}] \begin{Bmatrix} q_r \\ q_e \end{Bmatrix} \tag{15b}$$

4) Aircraft Fuselage and Interior Response

$$[K_{S2}^*]\{X_{S2}\} = \{F_{S2}\}_F \tag{16}$$

$$\{P_I\} = [P_{S2}^*]\{F_{S2}\}_F \tag{21}$$

The independent degrees of freedom chosen for the model are the six engine rigid body d.o.f., $\{X_R\}$, the six engine mount rigid body d.o.f., $\{q_r\}$, and the 30 band selected engine mount elastic d.o.f., $\{q_e\}$. At the

interface between the rigid engine and isolators a nodal force summation specifies that

$$\{F_{S1}\}_R + \{F_{S1}\}_{VI} = 0 \tag{22}$$

when no external loads are applied at the nodes. This being the case, Equation (3) may be substituted into Equation (11a) and the resultant substituted into Equation (22) to yield the following expression

$$[M_R + T_{cg}^T M_{VI}^{11} T_{cg}]\{\ddot{X}_R\} + [T_{cg}^T K_{VI}^{11} T_{cg}]\{X_R\}$$

$$+ [T_{cg}^T K_{VI}^{12}]\{X'_{S1}\} = \{F_R\}. \tag{23}$$

The $\{X'_{S1}\}$ d.o.f. set may be replaced by equivalent elastic motion of the engine mount via the use of Equation (15a), resulting in

$$[M_R + T_{cg}^T M_{VI}^{11} T_{cg}]\{\ddot{X}_R\} + [T_{cg}^T K_{VI}^{11} T_{cg}]\{X_R\}$$

$$+ [T_{cg}^T K_{VI}^{12} Q_{R1}]\{q_r\} + [T_{cg}^T K_{VI}^{12} Q_{e1}]\{q_e\} = \{F_R\}. \tag{24}$$

Likewise a summation of forces at the isolator to engine mount attach points specifies that

$$\{F'_{S1}\}_{VI} + \{F'_{S1}\}_M = 0. \tag{25}$$

Combining the expressions of Equations (11b), (14), (15a), and (25) yields

$$\left[\begin{array}{c|c} M_M + Q_{R1}^T M_{VI}^{22} Q_{R1} & Q_{R1}^T M_{VI}^{22} Q_{e1} \\ \hline Q_{e1}^T M_{VI}^{22} Q_{R1} & [I] + Q_{e1}^T M_{VI}^{22} Q_{e1} \end{array}\right] \left\{\begin{array}{c} \ddot{q}_r \\ \hline \ddot{q}_e \end{array}\right\} + \left[\begin{array}{c|c} 0 & 0 \\ \hline 0 & 2\beta\omega_e \end{array}\right] \left\{\begin{array}{c} \dot{q}_r \\ \hline \dot{q}_e \end{array}\right\}$$

$$+ \left[\begin{array}{c|c} Q_{R1}^T K_{VI}^{22} Q_{R1} & Q_{R1}^T M_{VI}^{22} Q_{e1} \\ \hline Q_{e1}^T K_{VI}^{22} Q_{R1} & [\omega_e^2] + Q_{e1}^T K_{VI}^{22} Q_{e1} \end{array}\right] \left\{\begin{array}{c} q_r \\ \hline q_e \end{array}\right\} + \left[\begin{array}{c} Q_{R1}^T \\ \hline Q_{e1}^T \end{array}\right] [K_{VI}^{21} T_{cg}]\{X_R\} = \left[\begin{array}{c} Q_{R2}^T \\ \hline Q_{e2}^T \end{array}\right] \{F_{S2}\}_M \tag{26}$$

which may be combined with Equation (24) resulting in

$$\begin{bmatrix} M_R + T_{cg}^T M_{VI}^{11} T_{cg} & 0 & 0 \\ 0 & M_m + Q_{R1}^T M_{VI}^{22} Q_{R1} & Q_{R1}^T M_{VI}^{22} Q_{e1} \\ 0 & Q_{e1}^T M_{VI}^{22} Q_{R1} & [I] + Q_{e1}^T M_{VI}^{22} Q_{e1} \end{bmatrix} \begin{Bmatrix} \ddot{X}_R \\ \ddot{q}_r \\ \ddot{q}_e \end{Bmatrix}$$

$$+ \begin{bmatrix} 0 & 0 & 0 \\ 0 & 0 & 0 \\ 0 & 0 & 2\beta\omega_e \end{bmatrix} \begin{Bmatrix} \dot{X}_e \\ \dot{q}_r \\ \dot{q}_e \end{Bmatrix}$$

$$+ \begin{bmatrix} T_{cg}^T K_{VI}^{11} T_{cg} & T_{cg}^T K_{VI}^{12} Q_{R1} & T_{cg}^T K_{VI}^{12} Q_{e1} \\ Q_{R1}^T K_{VI}^{21} T_{cg} & Q_{e1}^T K_{VI}^{22} Q_{R1} & Q_{R1}^T K_{VI}^{22} Q_{e1} \\ Q_{e1}^T K_{VI}^{21} T_{cg} & Q_{e1}^T K_{VI}^{22} Q_{R1} & \lceil \omega_e^2 \rfloor + Q_{e1}^T K_{VI}^{22} Q_{e1} \end{bmatrix} \begin{Bmatrix} X_R \\ q_r \\ q_e \end{Bmatrix}$$

$$= \begin{bmatrix} 0 \\ Q_{R2}^T \\ Q_{e2}^T \end{bmatrix} \{F_{S2}\}_M + \begin{Bmatrix} F_R \\ 0 \\ 0 \end{Bmatrix} \tag{27}$$

The last step is to couple in the fuselage dynamic stiffness by a force summation at the engine mount to fuselage attach points;

$$\{F_{S2}\}_M + \{F_{S2}\}_F = 0 \tag{28}$$

Making use of this expression along with expressions in Equations (15b) and (16) results in the fully coupled system equations:

$$\begin{bmatrix} M_R + T_{cg}^T M_{VI}^{11} T_{cg} & 0 & 0 \\ 0 & M_M + Q_{R1}^T M_{VI} Q_{R1} & Q_{R1}^T M_{VI}^{22} Q_{e1} \\ 0 & Q_{e1}^T M_{VI}^{22} Q_{R1} & [I] + Q_{e1}^T M_{VI}^{22} Q_{e1} \end{bmatrix} \begin{Bmatrix} \ddot{X}_e \\ \ddot{q}_r \\ \ddot{q}_e \end{Bmatrix}$$

$$+ \begin{bmatrix} 0 & 0 & 0 \\ 0 & 0 & 0 \\ 0 & 0 & 2\beta\omega_e \end{bmatrix} \begin{Bmatrix} \dot{X}_e \\ \dot{q}_r \\ \dot{q}_e \end{Bmatrix}$$

$$+ \begin{bmatrix} T_{cg}^T K_{VI}^{22} T_{cg} & T_{cg}^T K_{VI}^{12} Q_{R1} & T_{cg}^T K_{VI}^{12} Q_{e1} \\ Q_{R1}^T K_{VI}^{21} T_{cg} & Q_{R1}^T K_{VI}^{22} Q_{R1} + Q_{R2}^T K_{S2}^* Q_{R2} & Q_{R1}^T K_{VI}^{22} Q_{e1} + Q_{R2}^T K_{S2}^* Q_{e2} \\ Q_{e1}^T K_{VI}^{21} T_{cg} & Q_{e1}^T K_{VI}^{22} Q_{R1} + Q_{e2}^T K_{S2}^* Q_{R2} & [\omega_e^2] + Q_{e1}^T K_{VI}^{22} Q_{e1} + Q_{e2}^T K_{S2}^* Q_{e2} \end{bmatrix} \begin{Bmatrix} X_R \\ q_r \\ q_e \end{Bmatrix}$$

$$= \begin{Bmatrix} F_R \\ 0 \\ 0 \end{Bmatrix} \qquad (29)$$

Upon specification of a set of applied engine c.g. forces the resulting system motion is governed by the above expression. The resulting interior pressures are computed from the expression;

$$\{P_I\} = [P^*_{S2}][K^*_{S2}][Q_{R2}\ Q_{e2}] \left\{\begin{array}{c} q_r \\ \hline q_e \end{array}\right\} \tag{30}$$

which is obtained via Equations (15b), (16), and (21). These complex valued expressions were programmed for solution in FORTRAN VI-Plus on a D.E.C. PDP 11/70 computer.

D. Coupled Model Normal Mode Response

In the process of verifying the analytical representation of the system components, the coupling procedures, and numerical solution procedures, several preliminary models were developed. The first model, denoted as Model #1 consisted of the rigid engine with the vibration isolators attached to ground. The equations of motion for this system are obtained from the expression given in Equation (23) by setting $\{X'_S\}$ equal to zero, thus

$$[M_R + T^T_{cg} M^{11}_{VI} T_{cg}]\{\ddot{X}_R\} + [T^T_{cg} K^{11}_{VI} T_{cg}]\{X_R\} = \{F_R\}. \tag{31}$$

The dynamic degrees of freedom of Model #1 are the engine center of gravity motions, $\{X_R\} = \lfloor X, Y, Z, \theta_X, \theta_Y, \theta_Z \rfloor$, denoted as numbers one through six, respectively. Assuming that the isolators can be solely represented by their static stiffness the engine support frequencies for the various isolators used during the sweep tests were computed and are listed in Table 12. The radial and axial stiffness properties of the isolators are also listed in the table. One additional "rigid" isolator configuration, R5, is listed which represents the effective decrease in axial stiffness due to local lug compliance at the isolator attach points. As can be seen, the isolator configurations listed cover a reasonably broad range of support frequencies.

Isolator design based on single degree of freedom theory shows that isolation begins at the point where the ratio of the disturbing frequency (f_d) to system natural frequency (f_n) is greater than $\sqrt{2}$. The design support frequency will need to be lowered even further depending on the isolator damping and the desired transmissibility. Here we define the

transmissibility in the usual way as the ratio of dynamic output to dynamic input (ref. 43);

$$T = [1 + (2\gamma\beta)^2]^{1/2} / [(1 - \gamma^2)^2 + (2\beta\gamma)^2]^{1/2} \qquad (32)$$

where γ is the ratio f_d/f_n and β the critical damping ratio.

In Table 12 the support frequencies corresponding to the mode most easily driven by torsional excitation of the engine are noted for each of the isolator configurations. Previous studies (ref. 23) showed that the response at the propeller tone is the dominant low frequency structure-borne noise component. For a minimum inflight speed of 2100 rpm the propeller tone is at 70 Hz (two bladed propeller). With an assumed critical damping ratio of $\beta = 0.05$, Equation (32) predicts configuration AA will yield increased transmission losses of 5.0, 4.3, and 3.0 dB for excitations in the 63, 80, and 100 Hz bands, respectively. These values do not compare directly with the measured values of 7.8, 5.4, 4.6 dB as taken from Table 5a, but do have a similar decreasing trend.

In model #2, the flexibility of the engine mount structure was included. The engine mount was tied to ground with a series of uncoupled fuselage springs, k_F. A diagonal matrix of springs replaced the measured dynamic stiffness matrix, K^*_{S2}. The resultant free vibration equations were a modified set of Equation 29 wherein the damping terms are all set to zero and the system is force free. The model consisted of a full 42 degrees of freedom, the engine mount rigid body d.o.f. were numbered 7 through 12 and the elastic modes numbered 13 through 42. In Table 13 predicted frequencies for the coupled model are given for fuselage spring rates ranging from $k_F = 1.13 \times 10^4$ up to 1.13×10^{10} N/m. The lowest spring rate represents the upper range of expected local fuselage stiffnesses. The higher values give a measure of the effect of stiffening the firewall. By comparison of the frequencies given in Table 13 to the support frequencies given in Table 12, for configuration R1, it can be seen that when the fuselage becomes rigid, the primary engine support frequencies readily appear along

with higher engine mount modes. The data in Table 13 demonstrate the strong effect of fuselage stiffness on the overall system coupling.

Adjacent to the predicted frequencies in Tables 13 through 17, the degree of freedom with the largest contribution to the eigenvector for the given mode is also listed. From these entries one can readily determine which component mode or degree of freedom is most active in the coupled mode response.

When employing modal expansion techniques convergence always seems to be a question, in particular when using free-free modal functions. A sufficient number of modes must be used to insure convergence, which is most difficult when introducing fixed boundaries. While the fuselage is not a rigid structure, the rigid fuselage representation using k_F = 1.13×10^8 N/m will be used to demonstrate the level of convergence expected with the present model. Results from a convergence study are given in Table 14 for the case of rigid isolators and a rigid fuselage. This serves to be a most severe test. As can be seen convergence out to mode 10 (145 Hz) is obtained by including only 10 of the 30 elastic modes. Convergence improves when a more realistic fuselage stiffness is used, as can be seen by the data in Table 15 for $k_F = 1.13 \times 10^4$ N/m. Convergence out to mode 15 is obtained when including only 10 of the elastic modes.

Computed system normal mode frequencies for all isolator configurations are given in Table 16. Beyond 84 Hz, isolator stiffness, for configurations OA, EA, and AA, has little if any effect on the engine mount frequencies. The fuselage stiffness appears to be the stronger parameter effecting the resonant response of the coupled system.

In these studies data using elastic modes from the first prediction band or lowest set of engine mount elastic modes, were presented. Similar convergence and sensitivity studies were carried out using the elastic modes in each of the other three prediction bands, reference Table 10, and similar trends were found. In Table 17 resonant responses in all four prediction bands are given for the configuration AA isolators. When using component frequency band selection for coupled system response prediction

it is important that sufficient component modes, which may lie outside the prediction range, be used to insure adequate coupling to other system components. As can be seen by the data given in Table 17, there is sufficient margin for additional coupling due to increased fuselage or isolator stiffness in all of the prediction bands. Note that many of the listed responses are local engine mount resonances, independent of isolator or fuselage stiffness. The noted exceptions are the responses whose eigenvector normalized on one of the engine mount rigid body degrees of freedom, i.e., 7 through 12.

V. COMPARISON OF ANALYTICAL AND EXPERIMENTAL RESULTS

The dynamic equations of motion of the system as given by Equations (29) and (30) were programmed in FORTRAN IV Plus on a D.E.C. PDP 11/70 computer. Spectra of translational accelerations at the engine center of gravity, AX, AY, and AZ, and interior sound pressure levels at microphone locations P1, P2, and P3 were computed using a 1/35 octave computation bandwidth from 10 Hz to 1000 Hz. Results for the three load cases denoted in Figure 4 were solved simultaneously by expanding the input vector in Equation (29) to three vectors corresponding to the engine c.g. force and moment vectors given in Table 18. The fuselage dynamic stiffness data bank was linearly interpolated for continuous representation between the 2.0 Hz resolution data. Nominal material property values for the isolator configurations are those listed in Table 2. The nominal value of the engine mount component damping ratio, g , was set to 1% critical. These nominal values were used in all computations unless otherwise denoted.

A. Narrow Band Spectra

Typical predicted narrow band transfer function data are represented by the complete set of spectra shown in Figure 32. These spectra are for Load Case #2 excitation of the rigid isolators, configuration R1, and may be compared directly to their experimental counterparts given in Figure 8. These predictions show that the SPL spectra at the various interior locations exhibit only minor variations from position to position as did the measured spectra of Figure 8. As can be seen the predicted spectra are also rich in narrow band response. The predicted acceleration response closely resembles the measured spectra for the AY and AZ axes. However, the 23 Hz and 76 Hz engine rigid body modes clearly seen in the AX response spectra of Figure 8d are not as clear in the predicted spectra of Figure 32d. The most noticeable difference in all of the spectra is absence of the engine elastic mode resonance response at 970 Hz in the predicted results. The engine elastic mode was not included in the analysis. The relatively high level of acceleration response along the X axis is also present in the predicted results

with some shift to the higher frequencies. Similar predicted spectra are shown in Figure 33 for Load Case #3 type excitation and direct comparison may be made to the measured results given in Figure 9.

Predictions for the original equipment isolators, OA and the soft rubber isolators, AA, are given in Figures 34 and 35, respectively. These spectra may also be compared directly to the corresponding measured spectra given in Figures 10 and 11. By examination of these data it can be seen that the analytical model underpredicts the measured SPL responses in the higher frequencies. The predicted interior response falls off somewhat like transmissibility curves of a single degree of freedom isolator with a constant spring rate. The higher frequency roll off between predicted results and measured data is more clearly seen in the hand smooth data shown in Figures 36 and 37.

B. One-Third Octave Spectra

To further clarify the differences in predicted and measured SPL transfer function responses the predicted spectra were reduced to peak one-third octave data for direct comparison to the measured data given in Section III.B. In Figure 38 comparisons of measured and predicted spectra for isolator configurations, R1, OA, and AA are given for Load Case #2 type excitation. Similar data for Load Case #3 type excitation are given in Figure 39. These data clearly show that the analytical model underpredicts the measured interior sound pressure levels in the higher frequencies. As the isolator becomes softer, i.e., a lower frequency support, the tendency for the model to underpredict the high frequency response greatly increases. This trend tends to point to the characterization of the isolators as being responsible for the lack of correlation in the higher frequencies. A series of analyses were carried out to obtain a measure of the sensitivity of the interior sound pressure levels to the various model parameters. These studies are discussed in the following section.

VI. MODEL PARAMETER SENSITIVITY STUDY

In Section V nominal values of the systems parameters were used for comparison of model predictions to the measured data. In the sections to follow the sensitivity of predicted interior sound pressure level spectra to changes from the nominal system parameters will be discussed.

A. Engine Mount Parameters

As previously mentioned in Section IV.B.3 the engine mount structural model did not include the local stiffness of the isolator attachment lugs, reference Figure 3. The lowest stiffness of the attachment lugs was estimated to be 3389 N/m in the isolator axial direction. The lug stiffness in the radial direction was considered rigid. Spectra were generated for the rigid isolator configuration using an axial isolator stiffness equal to the lug stiffness k_a = 3389 N/m and a radial isolator stiffness of k_r = 11,300 N/m. The configuration was denoted as R5 and a comparison of results to the R1 predicted and measured results are given in Figure 40 for Load Case #2 and #3 type excitation. As should be expected, the spectra generated with Load Case #2 type excitation (torsion) was most sensitive to the change in attachment lug stiffness. However, the local attachment lug stiffness is only important for the rigid isolator case since it's stiffness is in series with that of the isolator. For example, an isolator with an axial stiffness of 226 N/m with a local lug stiffness of 3389 N/m results in an effective isolator stiffness of 212 N/m. The sensitivity of the interior SPL spectra to changes in isolator stiffness on the order of ten percent are discussed in Section VI.B.

Early in the model prediction studies it was found that varying the engine mount critical damping parameter, β, from the nominal value of 0.01 in the range [0,0.10] for the rigid isolator configuration had no measurable effect on the predicted interior sound pressure level spectra. These results were somewhat verified by the test data discussed in Section III.E. The engine mount structural response is mainly governed by the

components to which it is attached. Any damping energy generated within the mount structure is small compared to the energy dissipated at its boundaries. In Figure 41 spectra are given for the case where the weight and stiffness of the engine mount structure was increased by a factor of ten (10) and β was varied in the range [0.01,0.10]. This configuration is denoted as R3 in Figure 41 and results are compared to configuration R1 data. As can be seen, no increase in engine mount damping sensitivity was realized, however a measurable increase in interior SPL response occured just above 500 Hz.

B. Isolator Properties

A variation of plus or minus ten percent in isolator stiffness was found to have little effect on the predicted interior sound pressure level spectra. Typical supporting data are given by the spectra shown in Figure 42 for the configuration AA isolators subjected to Load Case #2 type excitation. In Figure 43 the effects of varying the isolator material loss factor η from the nominal value of 0.10 up to 1.0 are given. As expected, changes in isolator damping mainly effected the response at the engine fundamental support frequency. However it should be noted that doubling the isolator material loss factor did not decrease the interior response by 6 dB at the engine support frequency, but more on the order of 2.5 to 3.0 dB were realized. This is due to other system damping being present, such as interior absorption or cabin radiation losses which are reflected in the fuselage dynamic stiffness.

The rapid fall off of predicted interior SPL transfer function response in the higher frequency region for the OA and AA isolators as compared to the measured data is attributed to the frequency dependence of the isolator material properties. The exact material properties of the isolators were not known; only their static deflection characteristics were known with a reasonable degree of certainty. The above studies showed that reasonable changes to the static isolator properties will in no way account for the discrepancy between predicted and measured data. Results of a study to determine the degree of frequency dependence of the isolator material properties necessary to bring the model predictions up to the measured results

are shown in Figures 44 and 45. In Figures 44 and 45 one-third octave peak SPL transfer function measured data are compared to predictions for: (1) Configuration AA wherein the nominal static isolator properties are used, (2) Configuration AC wherein the isolator stiffness increaded linearly to five (5) times its static value in the frequency range from 10 Hz to 1000 Hz, and (3) Configuration AD wherein a linear increase to twenty-five (25) times the static stiffness occurs over the predicted frequency range. The results given in Figures 44 and 45 show that the variation in isolator stiffness with frequency is a strong parameter for correlation to the measured data. Similar studies were made with changes in the isolator material loss factor which showed the material loss factor to be a weak parameter.

VII. CONCLUSIONS AND RECOMMENDATIONS

A laboratory based test procedure was developed to simulate engine induced structure-borne noise transmission in a test aircraft. Analysis of interior sound pressure level transfer function data for a series of isolators with varying mechanical properties support the following conclusions.

(1) As expected, decreasing engine support frequencies results in reduced structure-borne noise transmissions beyond the engine support frequency out to approximately 150 Hz.

(2) The elastomeric isolators do not appear to operate as constant property single degree-of-freedom systems with respect to noise isolation. Noise isolation beyond approximately 150 Hz levels off and appears to decrease somewhat above 600 Hz.

Analytical models of the simulated engine, vibration isolators and engine mount structure were coupled to an empirical model of the fuselage for the purpose of developing a structure-borne transmission model of the test aircraft. By comparison of predicted structure-borne noise transmission to laboratory based measurements the following observations were made.

(3) The frequency dependence of the isolator material properties appear to play an important role in the transmission of structure-borne noise in the mid to high frequency region of the spectrum. Isolator stiffness is a strong parameter while isolator damping is a much weaker parameter.

(4) For the test aircraft, moderate changes to the lightweight high strength engine mount structure did not effect the transmission phenomena.

(5) The modeling procedures used appear to be adequate to judge the relative performance of candidate isolators for the purpose of retro-fit isolator design if the mechanical properties of the isolators are known.

To insure the adequacy of the modeling method and to extend the procedures to a fully developed retrofit design tool the following additional work is recommended.

(1) Experimentally determine isolator mechanical properties as a function of frequency and load and re-correlate predictions to measured results for model verification. Tune model as necessary to achieve good correlation for a baseline configuration.

(2) Implement an optimization procedure into the model for determining optimum mechanical properties of the isolators for a given engine excitation.

(3) Determine the feasibility of manufacturing the optimum isolator and the impact on noise transmission for an off-optimum design.

(4) Build and test the optimum isolator for proof of concept demonstration.

REFERENCES

1. Tobias, Jerry V.: "Cockpit Noise Intensity: Fifteen Single-Engine Light Aircraft," Aerospace Medicine, September, 1969, pp. 963-966.

2. Stone, R.B.: "Cockpit Noise Environment of Airline Aircraft," Aerospace Medicine, September 1969, pp. 989-993.

3. Catherines, John J.; and Mayes, William H.: "Interior Noise Levels of Two Propeller-Driven Light Aircraft," NASA TM X-72716, NASA Langley Research Center, Hampton, VA, July 1975.

4. Smith, E.W.; Burks, D.G.; and Graf, E.R.: "Cabin Noise in Light Aircraft," Proceedings of the 1975 IEEE Southeast-Con., Region 3 Conference Volume 1, The Institute of Electrical and Electronics Engineers, Inc., 1975.

5. Howlett, J.T.; Williams, L.H.; and Catherines, J.J.: "Measurement, Analysis and Prediction of Aircraft Interior Noise," AIAA Paper No. 76-551, American Institute of Aeronautics and Astronautics, New York, N.Y., 1976.

6. Catherines, John J.; and Jha, Sunil, K.: "Sources and Characteristics of Interior Noise in General Aviation Aircraft," NASA TM X-72839, NASA Langley Research Center, Hampton, VA, April 1976.

7. Rupf, John A.; "Noise Effects on Passenger Communication in Light Aircraft,' SAE Paper No. 770446, Society of Automotive Engineers, Warrendale, PA, April, 1977.

8. Mixson, John S.; and Barton, C. Kearney: "Interior Noise Analysis and Control for Light Aircraft, SAE Paper 770445, Society of Automotive Engineers, Warrendale, PA, April 1977.

9. Mixson, J.S.; Barton, C.K.; and Vaicaitis, R.: "Investigation of Interior Noise in a Twin-Engine Light Aircraft," Journal of Aircraft, Vol. 15, No. 4, April 1978, pp. 227-233.

10. Jha, S.K.; and Catherines, J.J.: "Interior Noise Studies for General Aviation Types of Aircraft, Part I: Field Studies," Journal of Sound and Vibration, Vol. 58, No. 3, 1978, pp. 378-390.

11. Jha, S.K.; and Catherines, J.J.: "Interior Noise Studies for General Aviation Types of Aircraft, Part II: Laboratory Studies," Journal of Sound and Vibration, Vol. 58, No. 3, 1978, pp. 391-406.

12. Mixson, J.S.; Barton, C.K.; Piersol, A.G.; and Wilby, J.F.: "Characteristics of Propeller Noise on an Aircraft Fuselage Related to Interior Noise Transmission," AIAA Paper No. 79-0644, American Institute of Aeronautics and Astronautics, New York, N.Y., March 1979.

13. Keefe, L.: "Interior Noise Path Identification in Light Aircraft Using Multivariate Spectral Analysis," AIAA Paper No. 79-0644, American Institute of Aeronautics and Astronautics, New York, N.Y. March 1979.

14. Stephens, David G.; and Leatherwood, Jack D.: "Physical and Subjective Studies of Aircraft Interior Noise and Vibration" NASA TM-80084, National Aeronautics and Space Administration, Langley Research Center, Hampton, VA, April 1979.

15. Henderson, Terry D.: "A Research Program to Reduce Interior Noise in General Aviation Airplanes - Design of an Acoustic Panel Test Facility," NASA-CR-155152, on NASA Grant NSG 1301, The University of Kansas Center for Research, Inc., Lawrence, Kansas, August 1977.

16. SenGupta, G.: "Reduction of Cabin Noise and Vibration by Intrinsic Structural Tuning," AIAA Journal, Vol. 15, No. 6, June 1978, pp. 545-546.

17. Roskan, J.; Grosveld, F.; and van Aken, J.: "Summary of Noise Reduction Characteristics of Typical General Aviation Materials," SAE Paper No. 790627, Society of Automotive Engineers, Inc., Warrendale, PA, 1979.

18. Koval, L.R.: "On Sound Transmission Into an Orthotropic Shell," Journal of Sound and Vibration, Vol. 63, No. 1, 1979, pp. 51-59.

19. Dym, C.L.; Ventres, C.S.; and Lang, M.A.: "Transmission of Sound Through Sandwich Panels: A Reconsideration," Journal of the Acoustic Society of America, Vol. 59, No. 2, February 1976, pp. 364-367.

20. Barton, C.K.; and Mixson, J.S.: "Noise Transmission and Control for a Light Twin-Engine Aircraft," Paper No. 80-1036, AIAA 6th Aeroacoustics Conference, Hartford, CT, June 4-6, 1980.

21. Cockburn, J.A.; and Jolly, A.C.: "Structural-Acoustic Response, Noise Transmission Losses and Interior Noise Levels of an Aircraft Fuselage Excited by Random Pressure Fields," Tech. Rept. AFFDL-TR-68-2, U.S. Air Force, Aug. 1968.

22. Howlett, James T.; and Morales, David A.: "Prediction of Light Aircraft Interior Noise," NASA TM X-62838, NASA Langley Research Center, Hampton, Virginia, April 1976.

23. Unruh, J.F.; Schedit, D.C.; and Pomerening, D.J.: "Engine Induced Structural-Borne Noise in a General Aviation Aircraft," NASA CR-159099, SwRI Project 02-4860, August, 1979.

24. Lord Kinematics, "Vibration/Shock/Noise Control Products," Product Literature, 1635 W. 12th St., P.O. Box 2051, Erie, PA, 16512.

25. Barry Controls, "Application Selection Guide--Vibration, Shock, Noise," Product Literature, Division of Barry Wright Corp., 700 Pleasant Street, Watertown, Maine 02172.

26. Cole, John E., III: "The Effects of Frequency, Amplitude and Load on the Dynamic Properties of Elastomers," Paper No. A772134, 93rd Meeting Acoustical Soc. Am., University Park, Penn. June 1977.

27. Rogers, L., Editor "Conference on Aerospace Polymeric Visioelastic Damping Technology for the 1980's," AFFDL-TM-78-78-FBA, Dayton, Ohio, Feb. 1978.

28. Hobaica, E.C., and Sweet, G.: "Behavior of Elastomeric Materials Under Dynamic Loads," Shock Vib. Dig., 8(3), March 1976.

29. Snowdon, J.C.: "Handbook of Vibration and Noise Control," Report No. AD/A-071 485, Applied Research Laboratory, Penn. State Univ., April 1979.

30. Dowell, E.H.; Gorman, G.F., III; and Smith, D.A." Acoustoelasticity: General Theory, Acoustic Natural Modes and Forced Response to Sinusoidal Excitation, Including Comparisons with Experiment," Journal of Sound and Vibration, Vol. 52, No. 4, 1977, pp. 519-542.

31. Dowell, Earl H.: "Master Plan for Prediction of Vehicle Interior Noise," AIAA 5th Aeroacoustic Conference, Seattle, Washington, 1979.

32. Unruh, J.F." "Finite Element Subvolume Technique for Structural-Borne Interior Noise Prediction," AIAA Journal of Aircraft, Vol. 17, No. 6, June 1980.

33. Vaicaitis, R.: "Noise Transmission Into a Light Aircraft," AIAA Journal of Aircraft, Vol. 17, No. 3, Feb. 1980.

34. Unruh, J.F.: "Structural-Borne Noise Prediction for a Single Engine General Aviation Aircraft," Paper No. 80-1037, AIAA 6th Aeroacoustics Conference, Hartford, CT, June 1980.

35. Hou, S.N.: "Review of Modal Synthesis Techniques and A New Approach - Case 320," TM-69-2031-5, Bellcomm, Inc., Washington, D.C., 1969. (Available as NASA CR-110769.)

36. Jones, C.E.: "Advanced Substructuring Techniques." NASA CR-119927, June 1971.

37. Whetstone, W.D.; and Jones, C.E.: "Substructuring Techniques," NASA CR-121051, Oct. 1971.

38. Craig, Roy R., Jr.; and Chang, C-J: "Substructure Coupling for Dynamic Analysis and Testing," NASA CR-2781, Feb. 1977.

39. Craig, Roy R., Jr.; and Chang, Ching-Jone: "A Review of Substructure Coupling Methods for Dynamic Analysis," Advances in Engineering Science, Volume 2, NASA CP-2001, [1976], pp. 393-406.

40. Noor, A.K.; Kamel, H.A.; and Fulton, R.E.: "Substructuring Techniques - Status and Projections," Computers and Structures, Vol. 8, Pergamon Press, Ltd., London, 1978, pp. 621-632.

41. House, M.E.; and Pinder, J.N.: "Impact Excited Mobility Measurements in the Audio Frequency Range," Symposium on Internal Noise in Helicopters, University of Southhampton, July 1979.

42. Bendat, J.S.; and Piersol, A.G.: Random Data: Analysis and Measurement Procedures, Wiley-Interscience, 1971.

43. Harris, C.M.; and Crede, C.E., Ed.: Shock and Vibration Handbook, McGraw-Hill, 1976.

TABLE 1. RIGID ENGINE MASS PROPERTIES

ITEM		DESIRED* PARAMETERS	DESIGNED † PARAMETERS
M	(kg)	170	170
I_{XX}	(kg-m^2)	1.756	1..7
I_{YY}	(kg-m^2)	7.901	8.369
I_{ZZ}	(kg-m^2)	14.338	8.837
X_{cg}	(m)	-0.522	-0.522
Y_{cg}	(m)	0	0
Z_{cg}	(m)	0.070	0.070

* measured
† calculated

TABLE 2. ISOLATOR STATIC MECHANICAL PROPERTIES

ISOLATOR CONFIGURATION	RADIAL STIFFNESS k_r* (N/m)	AXIAL STIFFNESS k_a* (N/m)	LOSS FACTOR η	MASS (ea) (kg)
R1 - Rigid	11300	11300	0	0.642
OA - Original Equip.	3888	299	0.10	0.436
EA - Hard Rubber	1203	741	0.10	0.262
AA - Soft Rubber	183	141	0.10	0.249

TABLE 3. NOISE AND VIBRATION DATA ACQUISITION SPECIFICATION FOR ISOLATOR PERFORMANCE TESTS

CHANNEL	TRANSDUCER	TRANSDUCER FUNCTION
1	B&K 4166-2619 1/2" Microphone & Preamplifier	SPL, Position P1
2	Spectral Dynamics 104A-5 Sweep Oscillator	D.C. Signal Proportional to Frequency
3	B&K 4166-2619 1/2" Microphone & Preamplifier	SPL, Position P2
4	Spectral Dynamics 104A-5 Sweep Oscillator	A.C. Drive Signal
5	B&K 4166-2619 1/2" Microphone & Preamplifier	SPL, Position P3
7	KIAG Swiss Type 9322 Load Cell Kistler 504 Charge Amplifier	Drive Force
9	Endevco #2220 Accelerometer Endevco 2721A Charge Amplifier	Engine c.g. Acceleration, AX
11	Endevco #2220 Accelerometer Endevco 2721A Charge Amplifier	Engine c.g. Acceleration, AY
13	Endevco #2220 Accelerometer Endevco 2721A Charge Amplifier	Engine c.g. Acceleration, AZ

TABLE 4. TEST SCHEDULE

RUN NO.	LOAD CASE	ISOLATOR CONFIGURATION	DRIVE FORCE	EXCEPTIONS/ADDITIONS
1	2	R1	89 N	None
2	2	AA	89 N	
3	2	AA	178 N	
4	1	AA	178 N	
5	1	OA	89 N	
6	2	OA	89 N	
7	2	EA	89 N	
8	1	EA	89 N	
9	1	AA	89 N	
10	1	R1	89 N	
11	3	R1	89 N	
12	3	OA	89 N	
13	3	AA	89 N	
14	3	AA	178 N	
15	3	EA	89 N	None
16	3	R1	89 N	Bulkhead @ B.S. 108 Removed, P1 and P3 Recorded, No Tape Record
17	3	R1	89 N	Same as 16 With Lower 4 Engine Mount Struts Held Hand Tight
18	2	R1	89 N	Same as 16.

TABLE 5. MEASURED ONE-THIRD OCTAVE PEAK SPL TRANSFER FUNCTIONS AT MICROPHONE POSITION P1; REF. 89 N RMS

(a) Load Case #2

CENTER FREQUENCY	ISOLATOR CONFIGURATION				
	R1	OA	EA	AA	AA*
20.0	82.9	89.4	79.8	87.0	92.7
25.0	90.9	93.9	99.4	84.6	92.4
31.5	89.8	96.1	94.4	98.8	97.3
40.0	95.4	95.3	98.8	88.4	95.0
50.0	97.5	95.1	96.3	89.3	93.6
63.0	98.3	89.2	92.1	81.4	89.2
80.0	93.2	77.6	92.7	72.2	80.4
100.0	89.7	75.4	88.4	70.8	79.6
125.0	91.5	83.6	90.2	77.4	84.4
160.0	88.2	77.1	87.2	73.2	77.1
200.0	76.6	74.5	79.5	67.1	74.8
250.0	76.9	72.4	75.2	63.4	73.1
315.0	76.9	69.8	82.8	61.9	70.4
400.0	77.9	69.6	77.5	63.4	66.3
500.0	84.3	72.8	84.5	62.1	71.3
630.0	80.4	78.0	79.1	67.9	74.1
800.0	76.3	83.1	83.3	65.5	73.5

(b) Load Case #3

CENTER FREQUENCY	ISOLATOR CONFIGURATION				
	R1	OA	EA	AA	AA*
20.0	73.0	68.7	75.4	77.0	84.5
25.0	86.3	80.0	77.9	86.5	88.0
31.5	76.7	89.7	85.1	82.3	80.3
40.0	81.0	94.2	87.4	72.2	78.0
50.0	85.0	89.7	95.2	77.6	82.3
63.0	90.5	81.4	87.7	65.6	71.2
80.0	100.4	78.8	86.6	65.0	73.1
100.0	81.5	72.1	76.5	60.8	64.1
125.0	80.9	80.4	78.4	72.0	77.8
160.0	78.5	69.3	73.8	68.0	72.5
200.0	75.2	64.7	70.1	66.5	72.8
250.0	77.0	71.5	64.5	64.1	69.4
315.0	65.7	67.8	68.1	58.7	63.3
400.0	73.0	63.5	64.6	66.7	70.7
500.0	68.6	71.6	63.8	62.4	67.8
630.0	82.5	78.9	77.7	62.5	71.0
800.0	92.7	88.8	85.4	66.2	76.1

* Ref. 178 N rms

TABLE 6. MEASURED ONE-THIRD OCTAVE PEAK SPL TRANSFER FUNCTIONS AT MICROPHONE POSITION P3; REF. 89 N RMS

(a) Load Case #2

CENTER FREQUENCY	ISOLATOR CONFIGURATION				
	R1	OA	EA	AA	AA*
20.0	84.5	88.2	85.7	88.1	91.7
25.0	93.2	98.6	94.4	89.5	94.8
31.5	91.5	95.6	94.2	98.8	96.0
40.0	95.9	99.1	96.8	87.9	93.3
50.0	93.3	95.2	88.3	86.2	90.3
63.0	94.0	85.7	92.2	77.1	87.6
80.0	95.7	82.6	90.1	75.9	82.2
100.0	91.0	75.7	90.6	73.8	79.7
125.0	89.4	80.3	87.9	76.3	81.2
160.0	80.9	68.7	77.6	71.2	77.5
200.0	80.1	68.5	78.2	65.0	70.4
250.0	72.2	68.1	67.8	59.5	65.3
315.0	80.6	69.6	71.2	65.6	71.5
400.0	76.9	73.8	74.4	66.8	72.6
500.0	81.4	67.9	77.0	62.0	67.4
630.0	83.9	82.2	82.5	72.4	79.1
800.0	81.1	79.2	80.3	68.1	75.1

(b) Load Case #3

CENTER FREQUENCY	ISOLATOR CONFIGURATION				
	R1	OA	EA	AA	AA*
20.0	80.7	73.6	89.4	83.5	90.1
25.0	81.2	80.6	75.7	82.8	81.1
31.5	79.1	89.7	79.3	76.6	81.1
40.0	80.1	89.0	79.5	67.4	75.3
50.0	78.4	81.3	89.8	69.7	76.4
63.0	88.4	74.9	85.2	68.0	78.7
80.0	101.7	77.7	87.3	65.3	74.4
100.0	80.9	70.7	80.7	57.3	64.8
125.0	72.5	77.1	71.3	73.1	78.1
160.0	67.7	64.2	63.2	69.1	75.2
200.0	70.3	63.8	68.2	65.4	70.0
250.0	66.9	64.1	62.7	60.1	66.4
315.0	69.4	66.7	71.7	57.7	64.9
400.0	81.0	69.1	70.0	67.7	74.3
500.0	67.9	66.2	65.5	64.0	69.3
630.0	82.1	82.5	80.4	74.5	74.6
800.0	92.0	85.7	83.3	67.0	75.3

*Ref. 178 N rms

TABLE 7. MEASURED ENGINE ALONE-INTERIOR REMOVED ONE-THIRD OCTAVE SPL AT MIR

(a) Unweighted Levels

CENTER FREQUENCY	RPM 1680	1920	2160
20.0	0.0	0.0	0.0
25.0	93.6	0.0	0.0
31.5	96.2	102.5	0.0
40.0	87.0	86.8	92.4
50.0	96.0	88.0	83.8
63.0	98.0	108.2	100.8
80.0	77.2	83.0	106.6
100.0	89.5	85.7	92.5
125.0	93.2	0.0	91.7
160.0	87.2	88.0	95.5
200.0	86.8	89.3	99.2
250.0	86.0	80.0	94.2
315.0	82.9	83.1	87.0
400.0	80.0	85.0	88.3
500.0	81.5	84.2	87.8
630.0	81.2	84.5	86.0
800.0	80.3	87.6	88.0
1000.0	83.7	86.0	88.3
OASPL	103.5	109.5	109.1

(b) A-Weighted Levels

CENTER FREQUENCY	RPM 1680	1920	2160
20.0	0.0	0.0	0.0
25.0	48.9	0.0	0.0
31.5	56.8	63.1	0.0
40.0	52.4	52.2	57.8
50.0	65.8	57.8	53.6
63.0	71.8	82.0	74.6
80.0	54.7	60.5	84.1
100.0	70.4	66.6	73.4
125.0	77.1	0.0	75.6
160.0	73.8	74.6	82.1
200.0	75.9	78.4	88.3
250.0	77.4	71.4	85.6
315.0	76.3	76.5	80.4
400.0	75.2	80.2	83.5
500.0	78.3	81.0	84.6
630.0	79.3	82.6	84.1
800.0	79.5	86.8	87.2
1000.0	83.7	86.0	88.3
OASPL	88.8	92.1	95.6

TABLE 8. ISOLATOR PERFORMANCE COMPARISONS, OASPL AT P1 BASED ON ENGINE RUNNING DATA

(a) Load Case #2

RPM	OASPL - dB				OASPL - dBA			
	R1	OA*	EA	AA	R1	OA*	EA	AA
1680	110.5 (110.5)**	103.5 (103.5)	108.6 (108.7)	100.6 (100.6)	94.7 (94.7)	87.1 (88.8)	95.1 (95.4)	78.7 (80.0)
1920	117.6 (117.6)	109.5 (109.5)	112.5 (112.5)	106.5 (106.5)	97.1 (97.2)	90.8 (92.1)	97.1 (97.4)	81.1 (82.3)
2160	122.8 (122.8)	109.0 (109.1)	122.2 (122.2)	103.1 (103.1)	103.3 (103.1)	94.7 (103.1)	103.5 (95.6)	86.6 (87.3)

(b) Load Case #3

RPM	OASPL - dB				OASPL - dBA			
	R1	OA*	EA	AA	R1	OA*	EA	AA
1680	109.7 (109.7)	103.5 (103.5)	107.2 (107.2)	101.2 (101.2)	92.8 (94.7)	87.1 (88.8)	88.2 (91.3)	82.6 (83.9)
1920	117.7 (117.7)	109.5 (109.5)	114.8 (114.8)	98.8 (98.8)	97.1 (98.4)	90.8 (92.1)	92.5 (94.7)	85.8 (86.9)
2160	128.4 (182.4)	109.0 (109.1)	115.8 (115.8)	103.0 (103.0)	107.2 (107.4)	94.7 (95.6)	97.7 (99.0)	92.4 (92.9)

* Measured engine alone levels.
** ( ) 1000 Hz band included in analysis.

TABLE 9. ENGINE MOUNT FREE-FREE NORMAL MODE FREQUENCIES

MODE NO.	FREQUENCY Hz	STRUT* NO.(S)	MODE NO.	FREQUENCY Hz	STRUT NO.(S)
1	33.36	1	27	415.59	8
2	34.90	7	28	428.38	8,6
3	37.67	1	29	438.55	9
4	44.98	7	30	452.77	9
5	48.49	7	31	460.45	8
6	84.65	11,12	32	481.98	4
7	103.39	11,6,12	33	489.29	8
8	119.02	6	34	537.44	11,12
9	137.31	6	35	614.15	11,12
10	151.87	4,6	36	645.82	7
11	163.07	4,6	37	683.54	1
12	167.78	4	38	697.73	1,3
13	199.58	7	39	710.24	1
14	210.43	11,1,12	40	725.64	7
15	217.22	1	41	748.32	7
16	240.53	1	42	772.14	6
17	248.63	7	43	785.76	3
18	283.50	11,12	44	810.99	6
19	320.99	5	45	863.21	4
20	345.68	11,6,12	46	915.11	4
21	348.57	5	47	929.49	11,12
22	369.08	1	48	954.15	9
23	382.94	2	49	979.45	8
24	392.37	3	50	989.80	5
25	398.63	9	51	1018.86	5
26	409.27	8			

*Strut(s) with maximum contribution to eigenvector; see Figure 23.

TABLE 10. ENGINE MOUNT NORMAL MODE SELECTION BANDS

PREDICTION RANGE Hz	MODE NUMBER	MODE FREQUENCY RANGE Hz
10 - 256	1 - 30	33.36 - 452.8
256+ - 504	7 - 36	103.4 - 645.8
504+ - 752	15 - 44	217.2 - 811.0
752+ - 1000	22 - 51	369.1 - 1019.

TABLE 11. DATA SPECIFICATION - FUSELAGE INERTANCE AND NOISE TRANSMISSION TESTS

CHANNEL	TRANSDUCER	TRANSDUCER FUNCTION
1	Wilcoxon S-36 Load Cell Endevco 2721A Charge Amplifier	Input Force, F_j
3	Endevco #2221D Accelerometer Endevco 2721A Charge Amplifier	Acceleration, a_{xi}
4	Endevco #2221D Accelerometer Endevco 2721A Charge Amplifier	Acceleration, a_{yi}
5	Endevco #2221D Accelerometer Endevco 2721A Charge Amplifier	Acceleration, a_{zi}
7	B & K 4166 - 2619 1/2" Microphone & Preamplifier	SPL, P1
9	B & K 4166 - 2619 1/2" Microphone & Preamplifier	SPL, P2
11	B & K 4166 - 2619 1/2" Microphone & Preamplifier	SPL, P3

Note: Index i = 1, 2, 3, 4 for every j, j = 1, to 12
Total of 48 data sets.

TABLE 12. MODEL #1 - PREDICTED ENGINE SUPPORT FREQUENCIES FOR VARIOUS ISOLATORS

	CONFIGURATION				
	R1	R5	OA	EA	AA
RADIAL STIFFNESS k_r, (N/m)	11,300	11,300	3,888	1,203	183
AXIAL STIFFNESS k_a, (N/m)	11,300	3,389	299	741	141
MODE	Hz (d.o.f.)*				
1	68.49(2)	57.96(1)	31.38(1)	20.65(1)	8.34(1)
2	68.56(1)	67.53(2)	34.30(2)†	22.26(2)	8.69(2)
3	102.26(3)	82.95(3)	44.37(3)	30.09(3)	12.27(3)
4	120.38(6)	106.26(6)	46.38(2)	36.86(6)	14.76(6)
5	145.56(1)	136.69(2)†	60.14(2)	46.09(1)	18.18(1)
6	245.76(2)†	137.97(1)	79.65(1)	63.14(2)†	27.52(2)†
TORSIONAL ISOLATION FREQUENCY	347.6	193.3	48.5	89.3	38.9

* Degree of freedom with largest contribution to eigenvector
† Mode most excited by torsional excitation - Load Case #2

TABLE 13. MODEL #2 FUSELAGE STIFFNESS VARIATION, ISOLATOR CONFIGURATION R1, 30 ELASTIC MODES, PREDICTED FREQUENCIES, HZ

MODE NUMBER	k_F ~ SIMULATED FUSELAGE STIFFNESS - (N/m)			
	1.13×10^4	1.13×10^6	1.13×10^8	1.13×10^{10}
1	33.46 (13)*	43.52 (13)	68.25 (2)	68.47 (2)
2	35.28 (14)	48.54 (15)	68.54 (1)	68.55 (1)
3	37.58 (15)	60.98 (16)	85.02 (18)	88.39 (18)
4	41.78 (3)	63.82 (16)	94.79 (19)	102.26 (3)
5	44.15 (16)	68.49 (1)	102.22 (3)	112.38 (20)
6	47.62 (2)	69.53 (2)	111.41 (20)	120.38 (6)
7	48.94 (17)	73.45 (14)	120.39 (6)	125.49 (21)
8	60.72 (1)	86.82 (18)	125.64 (21)	132.35 (22)
9	84.70 (18)	100.27 (3)	142.21 (22)	145.54 (1)
10	103.65 (19)	109.50 (19)	145.54 (1)	151.98 (23)
11	105.46 (8)	119.47 (20)	156.29 (24)	162.25 (24)
12	113.61 (7)	120.26 (6)	161.03 (23)	174.90 (25)
13	119.06 (20)	138.80 (21)	172.01 (24)	190.09 (27)
14	137.33 (21)	144.90 (1)	183.66 (27)	202.8[illegible] (26)
15	151.90 (22)	153.11 (22)	203.19 (26)	220.44 (30)
16	163.08 (23)	163.25 (23)	233.05 (28)	235.83 (28)
17	167.78 (24)	167.92 (24)	244.46 (30)	245.76 (2)
18	185.55 (8)	200.41 (25)	245.74 (2)	248.20 (29)
19	199.61 (25)	211.10 (26)	247.83 (29)	266.53 (30)
20	210.48 (26)	217.86 (27)	281.64 (27)	321.80 (31)
21	217.23 (27)	241.00 (28)	316.06 (31)	345.00 (32)
22	240.54 (28)	244.02 (2)	343.87 (32)	345.94 (33)
23	248.63 (29)	248.68 (29)	344.62 (33)	380.20 (36)

*(X) Degree of freedom with largest contribution to eigenvector.

TABLE 14. MODEL #2 MODE CONVERGENCE, ISOLATOR CONFIGURATION R1, FUSELAGE STIFFNESS - 1.13×10^8 N/m
PREDICTED FREQUENCIES, HZ

MODE NUMBER	NUMBER OF ELASTIC MODES			
	30	20	15	10
1	68.25 (2)*	68.25 (2)	68.25 (2)	68.25 (2)
2	68.54 (1)	68.54 (1)	68.55 (1)	68.55 (1)
3	85.02 (18)	85.07 (18)	85.09 (18)	85.18 (18)
4	94.79 (19)	94.89 (19)	95.00 (19)	95.07 (19)
5	102.22 (3)	102.22 (3)	102.22 (3)	102.22 (3)
6	111.41 (20)	111.43 (20)	112.30 (20)	113.39 (20)
7	120.39 (6)	120.39 (6)	120.39 (6)	120.40 (6)
8	125.64 (21)	126.26 (21)	126.35 (21)	126.74 (21)
9	142.21 (22)	142.28 (22)	143.34 (22)	145.52 (22)
10	145.54 (1)	145.54 (1)	145.56 (1)	145.65 (22)
11	156.29 (24)	157.37 (24)	159.26 (24)	245.73 (2)
12	161.03 (23)	161.09 (23)	161.72 (23)	260.04 (15)
13	172.01 (24)	172.26 (24)	174.38 (24)	366.05 (13)
14	183.66 (27)	185.33 (27)	187.74 (27)	491.13 (17)
15	203.19 (26)	203.59 (26)	205.33 (26)	592.52 (16)
16	233.05 (28)	233.33 (28)	245.74 (2)	657.32 (14)
17	244.46 (30)	244.91 (30)	320.99 (15)	
18	245.74 (2)	245.75 (2)	422.76 (13)	
19	247.83 (29)	247.93 (29)	505.19 (17)	
20	281.65 (27)	303.80 (31)	594.52 (16)	

*(X) Degree of Freedom with largest contribution to eigenvector

TABLE 15. MODEL #2 MODE CONVERGENCE, ISOLATOR CONFIGURATION R1, FUSELAGE STIFFNESS 1.13 x 10^4 N/m, PREDICTED FREQUENCIES, HZ

MODE NUMBER	NUMBER OF ELASTIC MODES			
	30	20	10	5
1	33.46 (13)*	33.46 (13)	33.46 (13)	33.46 (13)
2	35.28 (14)	35.28 (14)	35.28 (14)	35.28 (14)
3	37.58 (15)	37.58 (15)	37.58 (15)	37.58 (15)
4	41.78 (3)	41.78 (3)	41.78 (3)	41.78 (3)
5	44.15 (16)	44.15 (16)	44.15 (16)	44.15 (16)
6	47.62 (2)	47.62 (2)	47.63 (2)	47.63 (2)
7	48.94 (17)	48.94 (17)	48.94 (17)	48.94 (17)
8	60.72 (1)	60.72 (1)	60.72 (1)	60.72 (1)
9	84.70 (18)	84.70 (18)	84.70 (18)	105.46 (8)
10	103.65 (19)	103.65 (19)	103.65 (19)	113.64 (7)
11	105.46 (8)	105.46 (8)	105.47 (8)	185.54 (8)
12	113.61 (7)	113.61 (7)	113.62 (7)	743.31 (9)
13	119.06 (20)	119.06 (20)	119.06 (20)	775.84 (8)
14	137.33 (21)	137.33 (21)	137.33 (21)	830.36 (7)
15	151.90 (22)	151.90 (22)	151.90 (22)	
16	163.08 (23)	163.08 (23)	185.56 (8)	
17	167.78 (24)	167.78 (24)	743.31 (9)	
18	185.55 (8)	185.55 (8)	775.85 (8)	
19	199.61 (25)	199.61 (25)	830.36 (7)	
20	210.48 (26)	210.48 (26)		

*(X) Degree of freedom with largest contribution to eigenvector

TABLE 16. MODEL #2, PREDICTED RESONANT FREQUENCIES, HZ
FUSELAGE STIFFNESS 1.13 x 10^4 N/m, 30 ELASTIC MODES

MODE NUMBER	ISOLATOR CONFIGURATION				
	R1	R5	OA	EA	AA
1	33.46 (13)*	33.45 (13)	29.17 (1)	20.10 (1)	8.31 (1)
2	35.28 (14)	35.27 (14)	31.97 (2)	21.09 (2)	8.62 (2)
3	37.58 (15)	37.47 (15)	33.31 (13)	25.78 (3)	11.91 (3)
4	41.78 (3)	40.13 (3)	33.95 (3)	33.52 (13)	14.71 (6)
5	44.15 (16)	44.13 (16)	35.52 (14)	35.28 (14)	18.05 (1)
6	47.62 (2)	47.58 (2)	37.85 (15)	36.28 (14)	27.24 (2)
7	48.94 (17)	48.92 (17)	40.88 (2)	37.79 (15)	33.50 (13)
8	60.72 (1)	53.94 (1)	45.46 (16)	44.15 (1)	35.43 (14)
9	84.70 (18)	84.66 (18)	48.69 (17)	45.31 (16)	37.78 (15)
10	103.65 (19)	95.20 (8)	56.99 (8)	48.77 (17)	45.25 (16)
11	105.46 (8)	103.65 (19)	70.22 (1)	60.17 (2)	48.73 (17)
12	113.61 (7)	104.73 (7)	84.68 (18)	84.67 (18)	84.66 (18)
13	119.06 (20)	119.04 (20)	103.52 (19)	103.46 (19)	103.44 (19)
14	137.33 (21)	120.12 (8)	119.03 (20)	119.03 (20)	119.03 (20)
15	151.90 (22)	137.33 (21)	137.32 (21)	137.32 (21)	137.32 (21)
16	163.08 (23)	151.91 (22)	151.89 (22)	151.88 (22)	151.88 (22)
17	167.78 (24)	163.08 (23)	163.08 (23)	163.07 (23)	163.07 (23)
18	185.55 (8)	167.78 (24)	167.78 (24)	167.78 (24)	167.78 (24)
19	199.61 (25)	199.60 (25)	199.59 (25)	199.59 (25)	199.59 (25)
20	210.48 (26)	210.47 (26)	210.45 (26)	210.44 (26)	210.44 (26)
21	217.23 (27)	217.23 (27)	217.23 (27)	217.22 (27)	217.22 (27)
22	240.54 (28)	240.54 (28)	240.54 (28)	240.54 (28)	240.53 (28)
23	248.63 (29)	248.63 (29)	248.63 (29)	248.63 (29)	248.63 (29)

*(X) Degree of freedom with largest contribution to eigenvector

TABLE 17. MODEL #2 RESONANT FREQUENCIES FOR ALL PREDICTION BANDS, CONFIGURATION AA ISOLATORS, FUSELAGE STIFFNESS 1.13 x 10^4 N/m

MODE NUMBER	PREDICTION BAND 1	2	3	4
1	8.31 (1)*	8.31 (1)	8.31 (1)	8.31 (1)
2	8.62 (2)	8.62 (2)	8.62 (2)	8.62 (2)
3	11.91 (3)	11.91 (3)	11.91 (3)	11.91 (3)
4	14.71 (6)	14.71 (6)	14.71 (6)	14.71 (6)
5	18.05 (1)	18.05 (1)	18.05 (1)	18.05 (1)
6	27.24 (2)	27.24 (2)	27.25 (2)	27.25 (2)
7	33.50 (13)	103.44 (19)	217.22 (27)	332.59 (9)
8	35.43 (14)	119.03 (20)	240.53 (28)	369.09 (34)
9	37.78 (15)	137.32 (21)	248.63 (29)	382.94 (35)
10	45.25 (16)	151.88 (22)	283.51 (30)	392.37 (36)
11	48.73 (17)	163.07 (23)	321.00 (31)	398.63 (37)
12	84.66 (18)	167.78 (24)	332.59 (9)	409.17 (8)
13	103.44 (19)	199.59 (25)	345.68 (32)	410.29 (8)
14	119.03 (20)	210.44 (26)	348.57 (33)	415.59 (39)
15	137.32 (21)	217.22 (27)	369.09 (34)	428.38 (40)
16	151.88 (22)	240.53 (28)	382.94 (35)	438.55 (41)
17	163.07 (23)	248.63 (29)	392.37 (36)	452.77 (42)
18	167.78 (24)	283.51 (30)	398.63 (37)	460.45 (43)
19	199.59 (25)	321.00 (31)	409.17 (8)	481.98 (44)
20	210.44 (26)	332.59 (9)	410.29 (8)	489.29 (45)
21	217.22 (27)	345.68 (32)	415.59 (39)	537.44 (46)
22	240.53 (28)**	348.57 (33)	428.38 (40)	588.88 (7)
23	248.63 (29)	369.09 (34)	438.55 (41)	614.16 (47)
24	283.51 (30)	382.94 (35)	452.77 (42)	645.83 (48)
25	321.00 (31)	392.37 (36)	460.45 (43)	683.54 (49)
26	332.59 (9)	398.63 (37)	481.98 (44)	697.73 (50)
27	345.68 (32)	409.17 (8)	489.29 (45)	710.25 (51)
28	348.57 (33)	410.29 (8)	537.44 (46)	725.65 (52)
29	369.09 (34)	415.59 (39)	588.89 (7)	748.32 (53)
30	382.94 (35)	428.38 (40)	614.16 (47)	772.14 (54)
31	392.37 (36)	438.55 (41)	645.83 (48)	785.76 (55)
32	398.63 (37)	452.77 (42)	683.54 (49)	810.99 (56)
33	409.17 (8)	460.45 (43)	697.73 (50)	863.21 (57)
34	410.31 (8)	481.98 (44)	710.25 (51)	915.11 (58)
35	415.59 (39)	489.29 (45)	725.65 (52)	929.49 (59)
36	428.38 (40)	537.44 (46)	748.32 (53)	954.15 (60)
37	438.55 (41)	588.89 (7)	772.14 (54)	979.45 (61)
38	452.77 (42)	614.17 (47)	785.76 (55)	989.80 (62)
39	588.89 (7)	645.83 (48)	810.99 (56)	1018.86 (63)
40	1058.06 (8)	1058.05 (8)	1058.05 (8)	1058.05 (8)
41	1135.67 (9)	1135.67 (90	1135.67 (9)	1135.66 (9)
42	1230.79 (8)	1230.78 (8)	1230.78 (8)	1230.78 (8)

* Degree of freedom with largest contribution to eigenvector

** Modes between bands lie within prediction frequency range

TABLE 18. LOAD CASE FORCE VECTORS

LOAD CASE #	ENGINE C.G. FORCE AND MOMENTS			
	F_X (N)	F_Y (N)	F_Z (N)	M_X (m-N)
1	0	$-0.919\ F_S$	$0.395\ F_S$	0
2	0	$-0.875\ F_S$	$0.485\ F_S$	$0.121\ F_S$
3	$0.940\ F_S$	0	$0.342\ F_S$	0

F_S - Shaker Input Force - Nominally 89 N rms

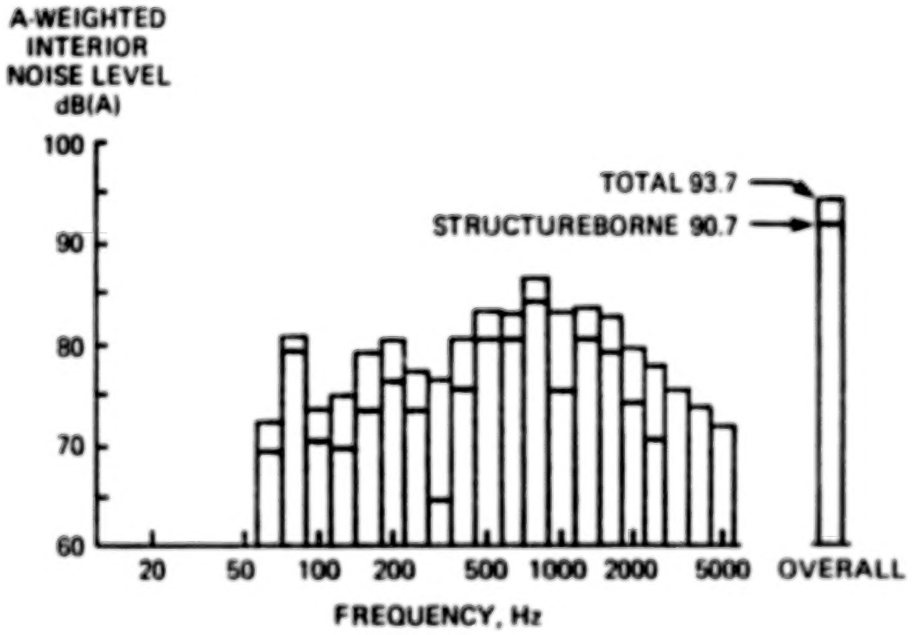

FIGURE 1. STRUCTURE-BORNE NOISE EQUALS AIRBORNE NOISE.

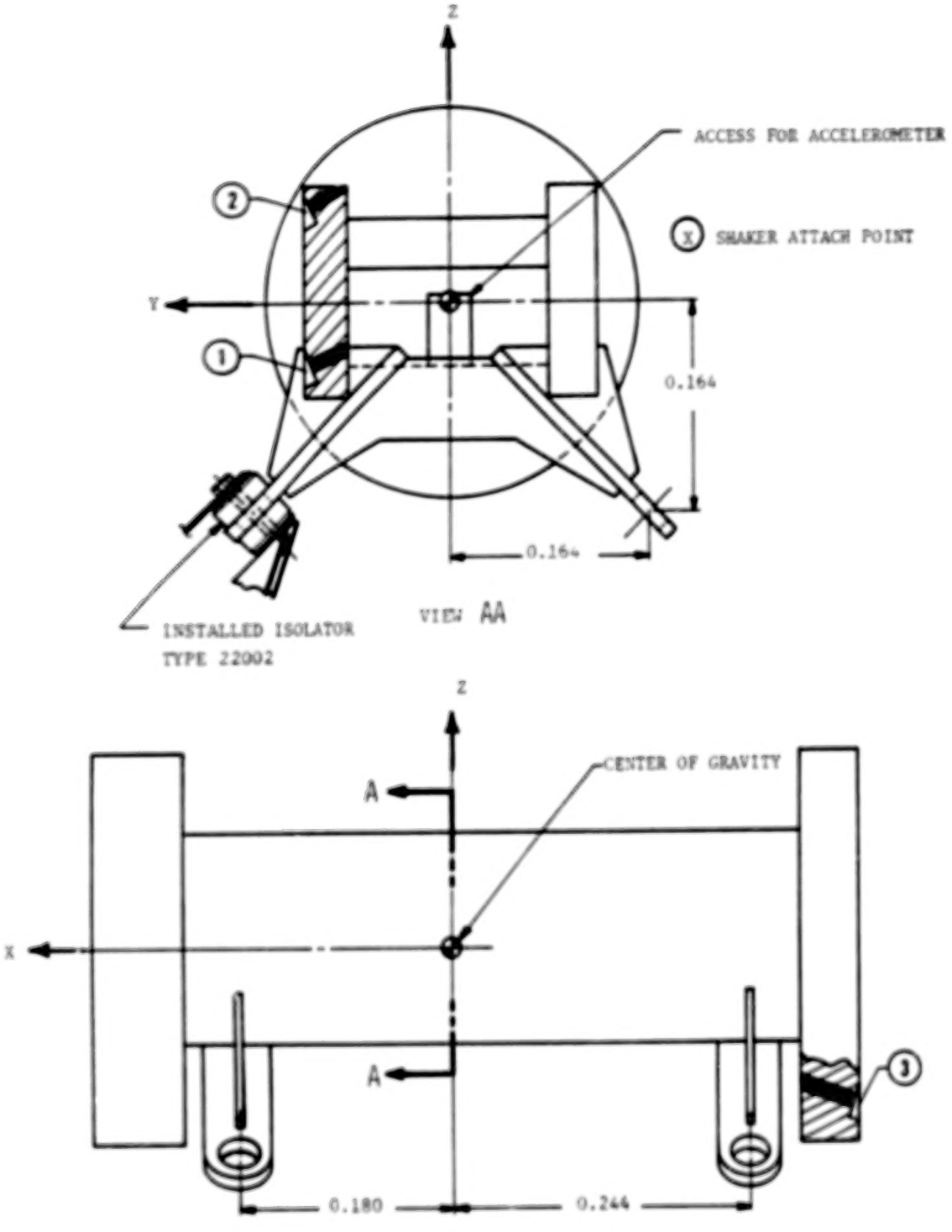

* All Dimensions Given In Meters

FIGURE 2. SKETCH OF THE RIGID ENGINE DESIGN.

BLANK

PAGE

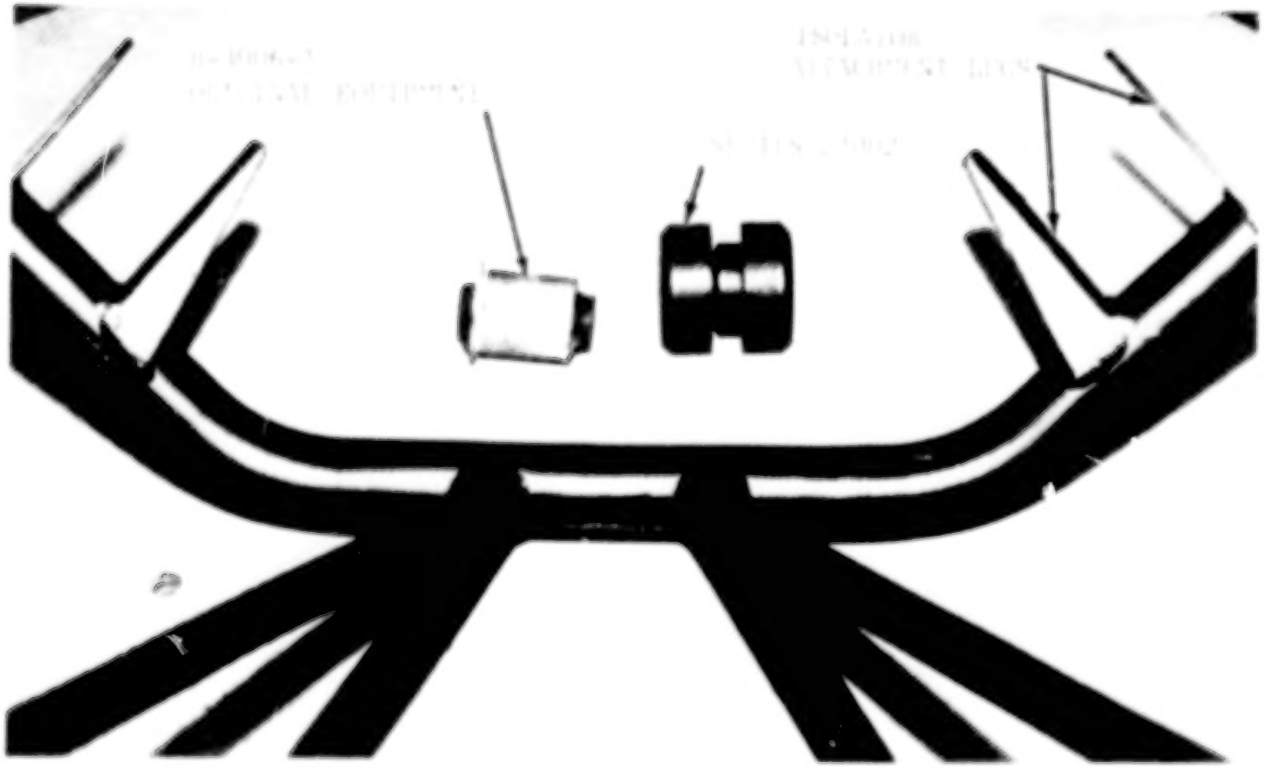

FIGURE 3. VIBRATION ISOLATORS AND MOUNTING LUGS.

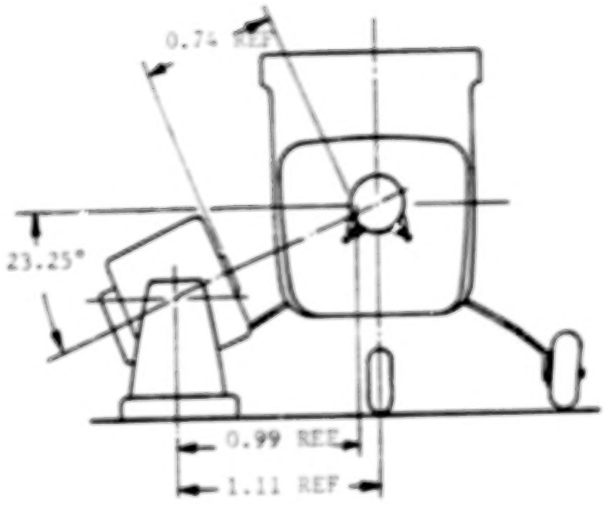

LOAD CASE 1

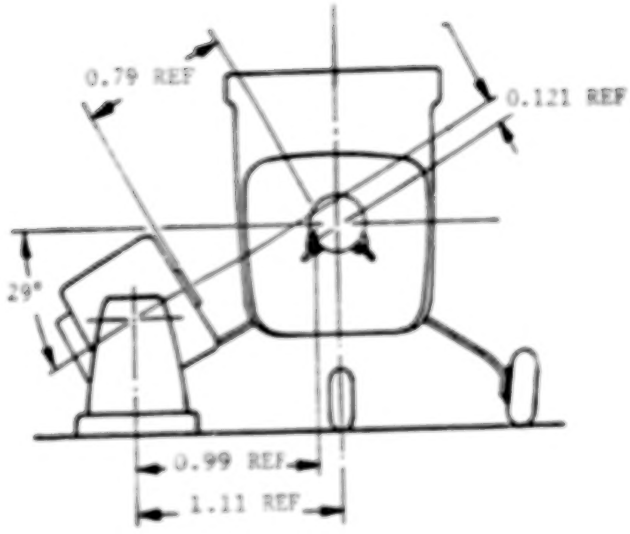

LOAD CASE 2

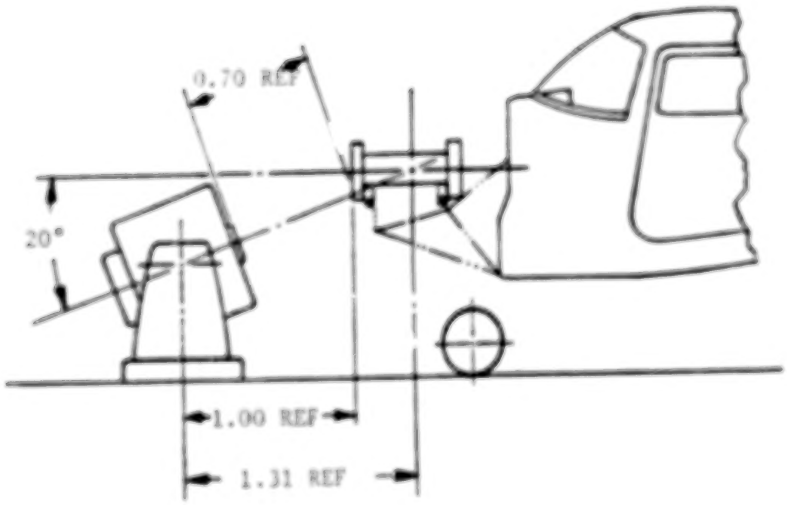

LOAD CASE 3

Dimension given in meters.

FIGURE 4. EXCITATION CONFIGURATIONS FOR TRANSFER FUNCTION TESTS.

BLANK

PAGE

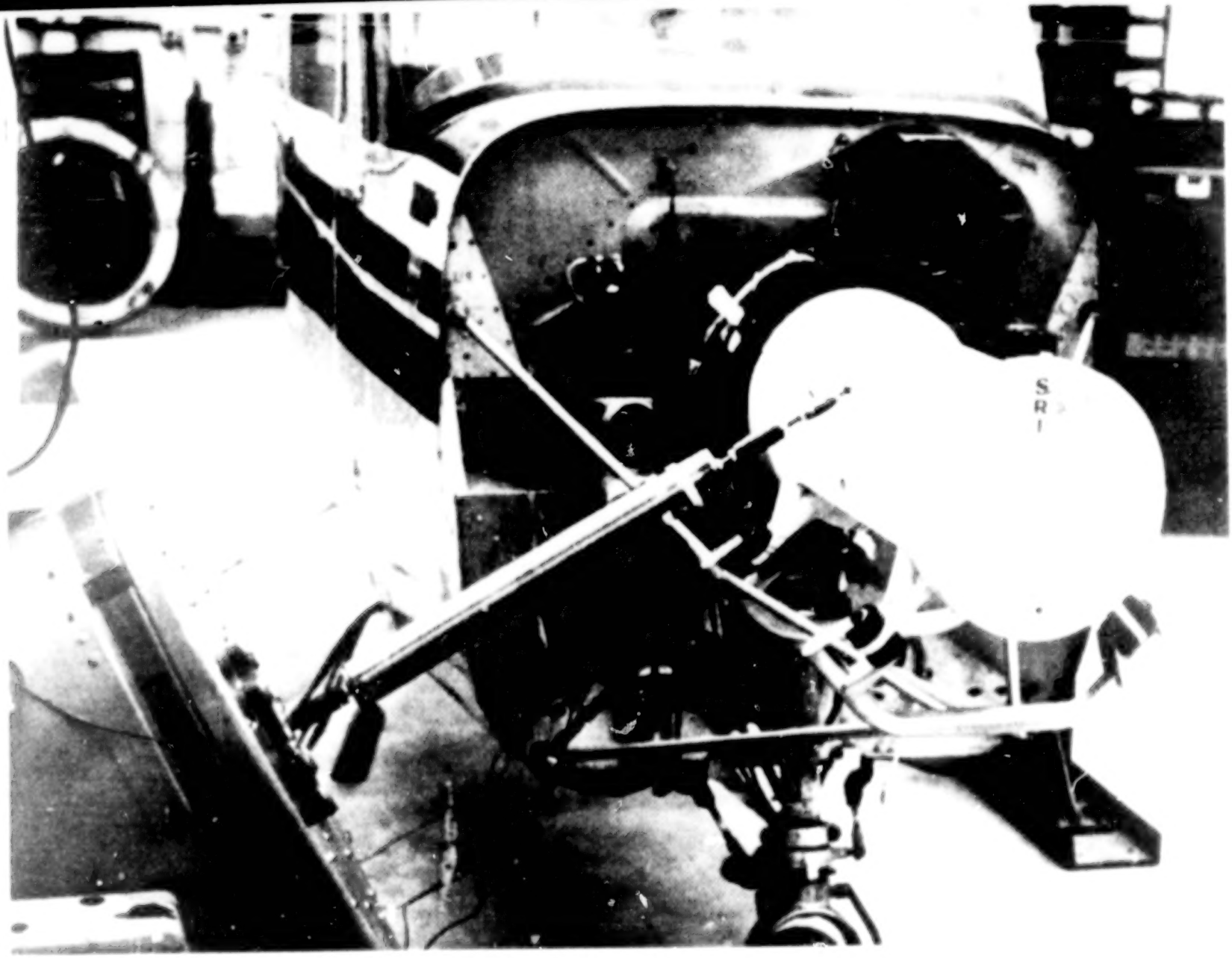

FIGURE 5. RIGID ENGINE AND TEST SETUP.

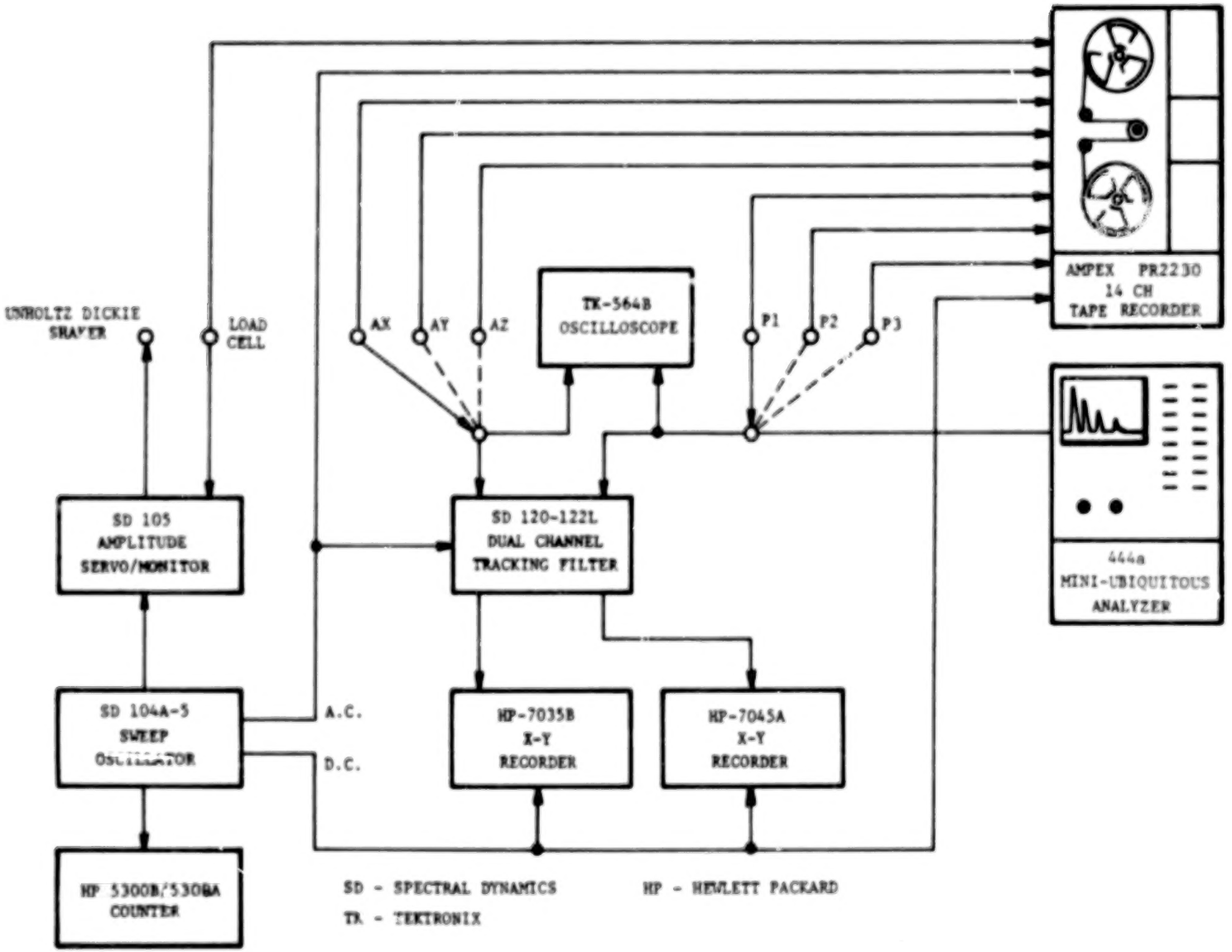

FIGURE 6. INSTRUMENTATION AND DATA ACQUISITION SYSTEM FOR ISOLATOR TRANSFER FUNCTION TESTS.

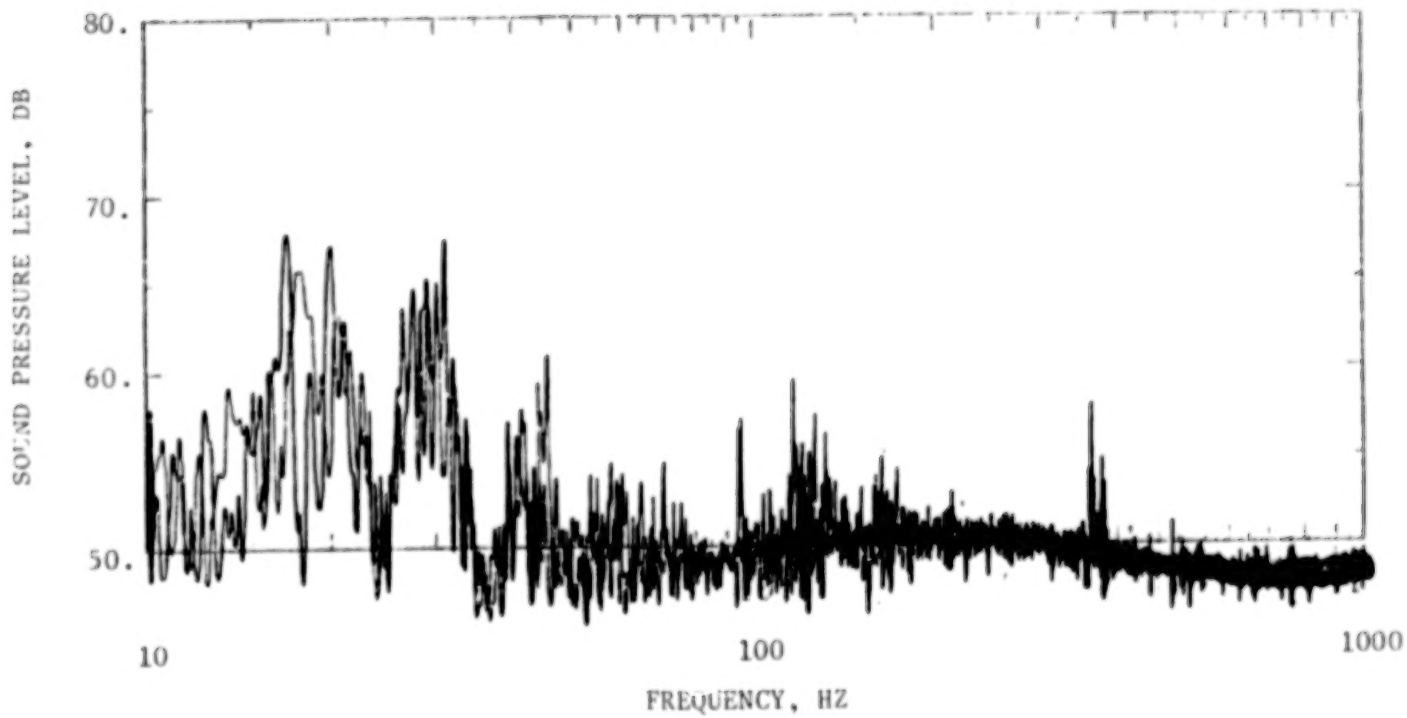

FIGURE 7. FACILITY NOISE FLOOR, SPL AT P1 SHAKER DETACHED WITH 0.05 G EXCITATION.

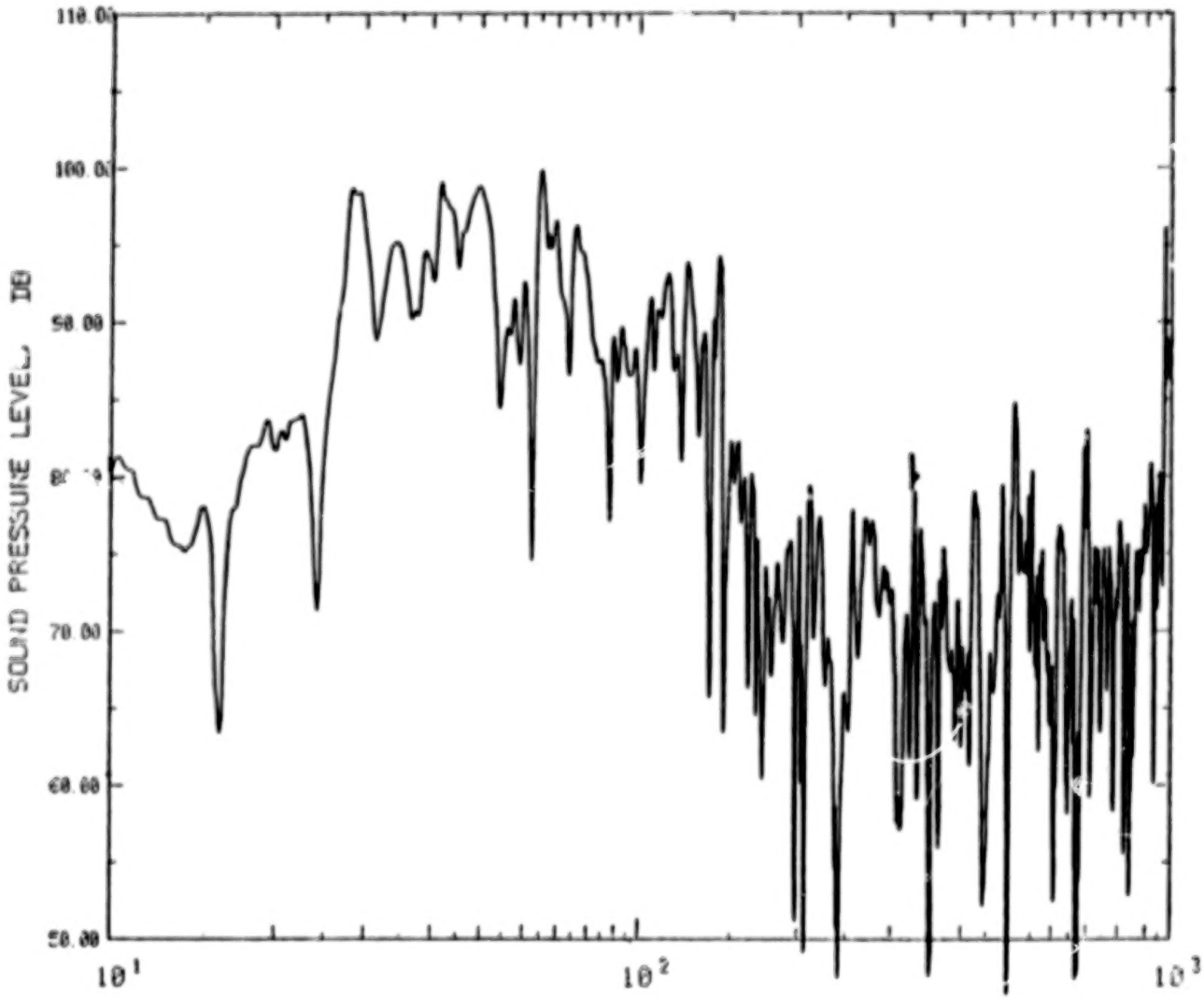

(a) Response P1.

FIGURE 8. MEASURED TRANSFER FUNCTION SPECTRA, LOAD CASE #2, ISOLATOR CONFIGURATION R1, REF. 89 N RMS.

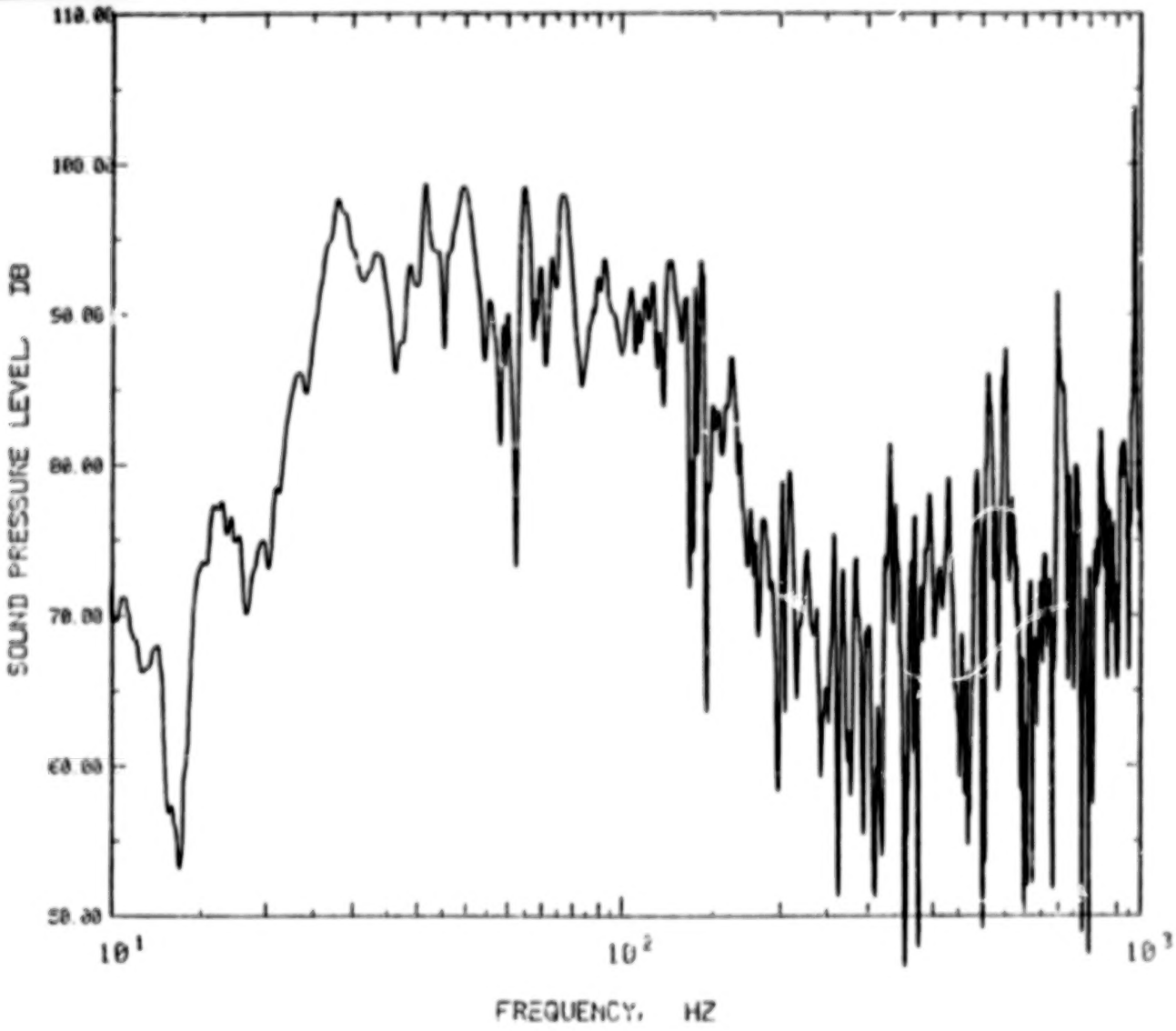

(b) Response P2.

FIGURE 8 (Continued). MEASURED TRANSFER FUNCTION SPECTRA, LOAD CASE #2, ISOLATOR CONFIGURATION R1, REF. 89 N RMS.

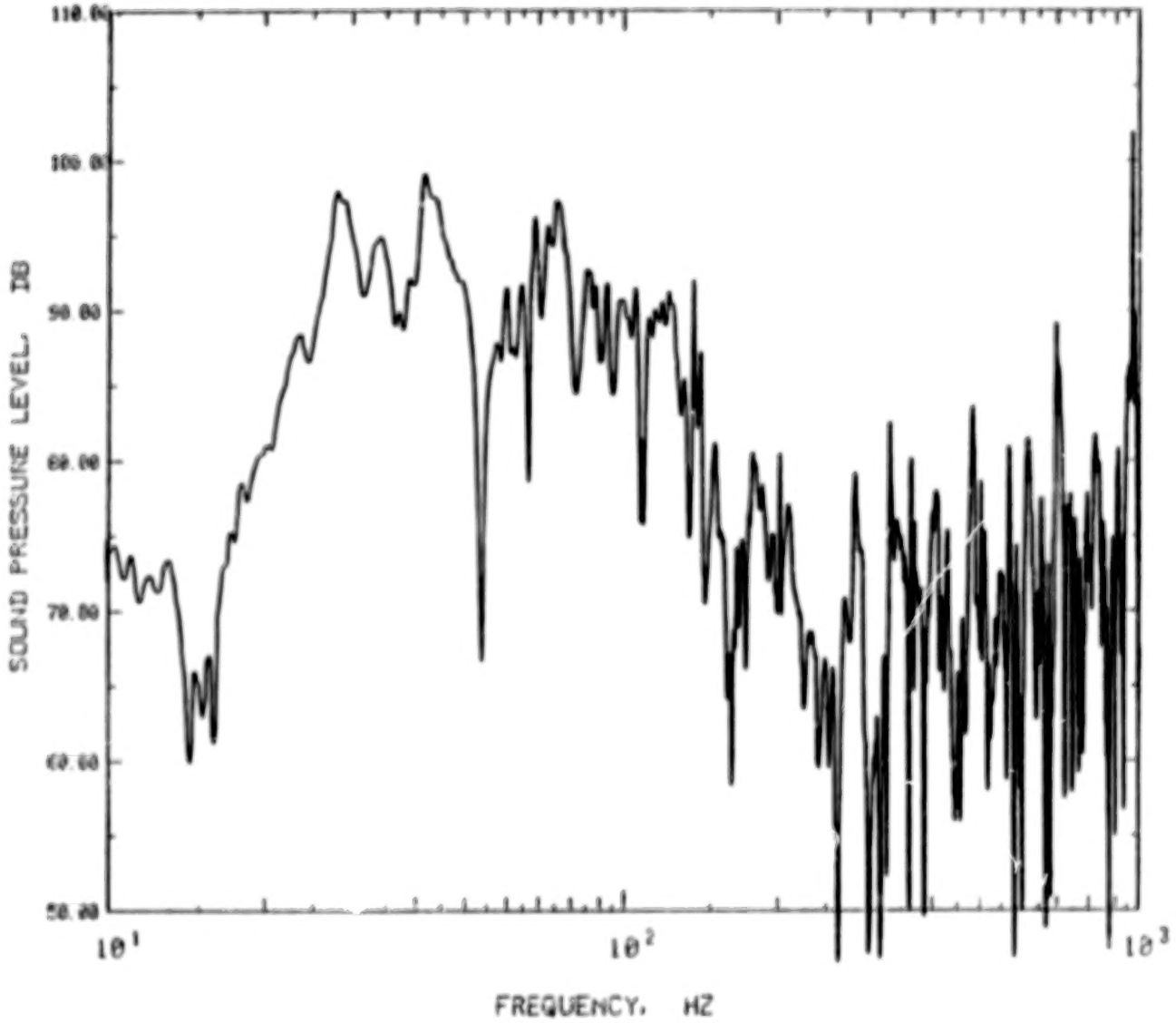

(c) Response P3.

FIGURE 8 (Continued). MEASURED TRANSFER FUNCTION SPECTRA, LOAD CASE #2, ISOLATOR CONFIGURATION R1, REF. 89 N RMS.

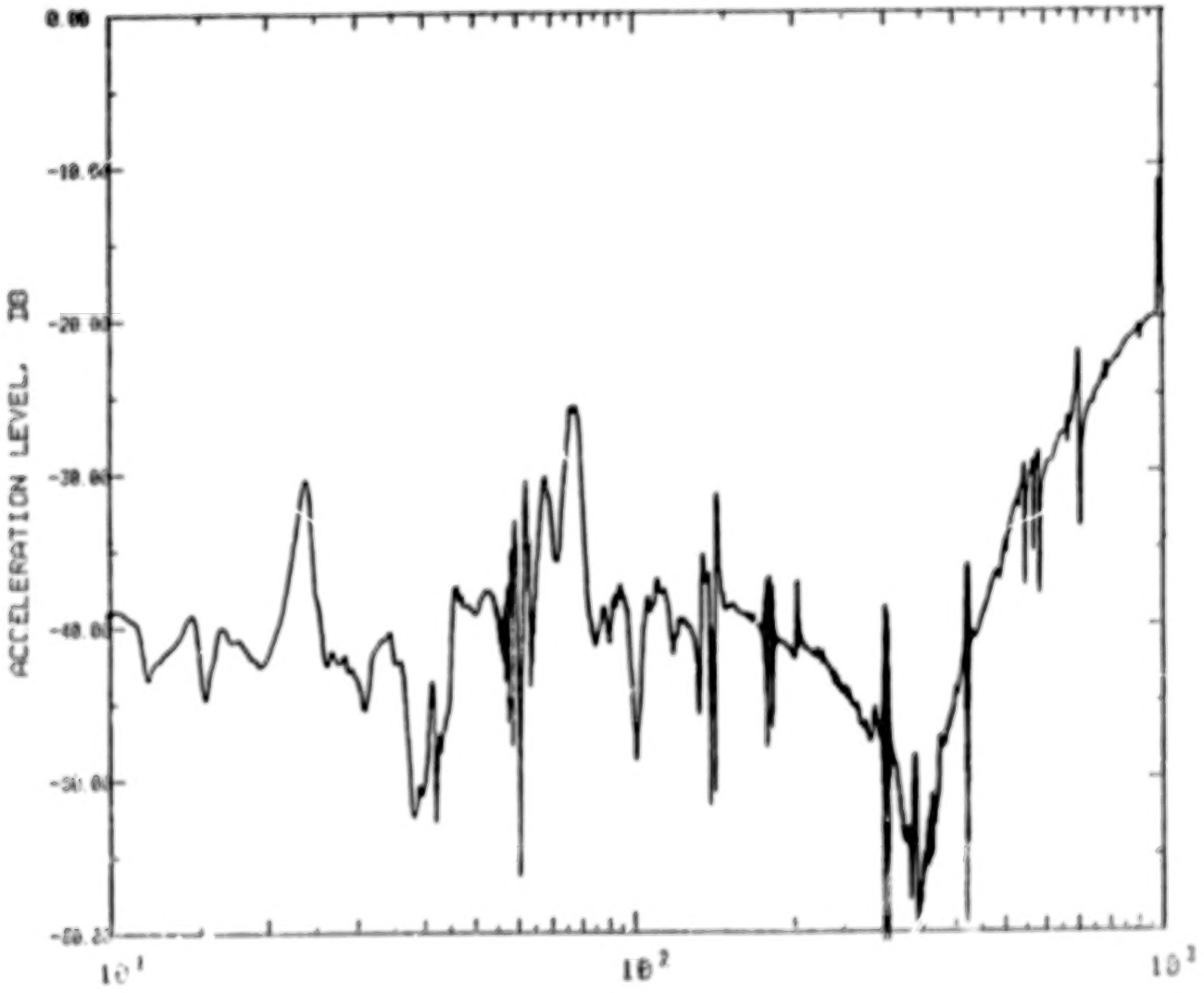

(d) Response AX.

FIGURE 8 (Continued). MEASURED TRANSFER FUNCTION SPECTRA, LOAD CASE #2, ISOLATOR CONFIGURATION R1, REF. 89 N RMS.

TABLE OF CONTENTS

List of Figures		vii	1/A11
List of Tables		x	1/A14
Nomenclature		xi	1/B1
I.	INTRODUCTION	1	1/B4
II.	TEST FACILITY, INSTRUMENTATION, AND PROCEDURES	3	1/B6
	A. Test Facility Description	3	1/B7
	B. Test Configurations	4	
	C. Instrumentation	5	1/B8
	D. Data Acquisition and Reduction	5	1/B9
	E. Facility Calibration	6	
III.	STRUCTURE-BORNE NOISE TRANSFER FUNCTIONS TESTS	8	1/B11
	A. Narrow Band Data	8	
	B. Peak One-Third Octave Data	11	1/B14
	C. Isolator Relative Performance	11	1/C1
	D. System Linearity	12	
	E. Engine Mount Damping Effectiveness	13	1/C2
	F. Fuselage Tail Cone Isolation	13	
IV.	ANALYTICAL MODEL	15	1/C4
	A. Model Concept	15	
	B. Component Representation	15	
	1. Engine As a Rigid Body	15	
	2. Vibration Isolators	17	1/C6
	3. Engine Mount Structure	20	1/C9
	4. Aircraft Fuselage and Interior Response	22	1/C11
	C. Component Coupling Procedures	25	1/C14
	D. Coupled Model Normal Mode Response	30	1/D5

TABLE OF CONTENTS (CONTINUED)

V.	COMPARISON OF ANALYTICAL AND EXPERIMENTAL RESULTS	34	1/D9
	A. Narrow Band Spectra	34	1/D10
	B. One-Third Octave Spectra	35	
VI.	MODEL PARAMETER SENSITIVITY STUDY	36	1/D11
	A. Engine Mount Parameters	36	1/D12
	B. Isolator Properties	37	
VII.	CONCLUSIONS AND RECOMMENDATIONS	39	1/D14
REFERENCES	. . . . .	41	1/E2

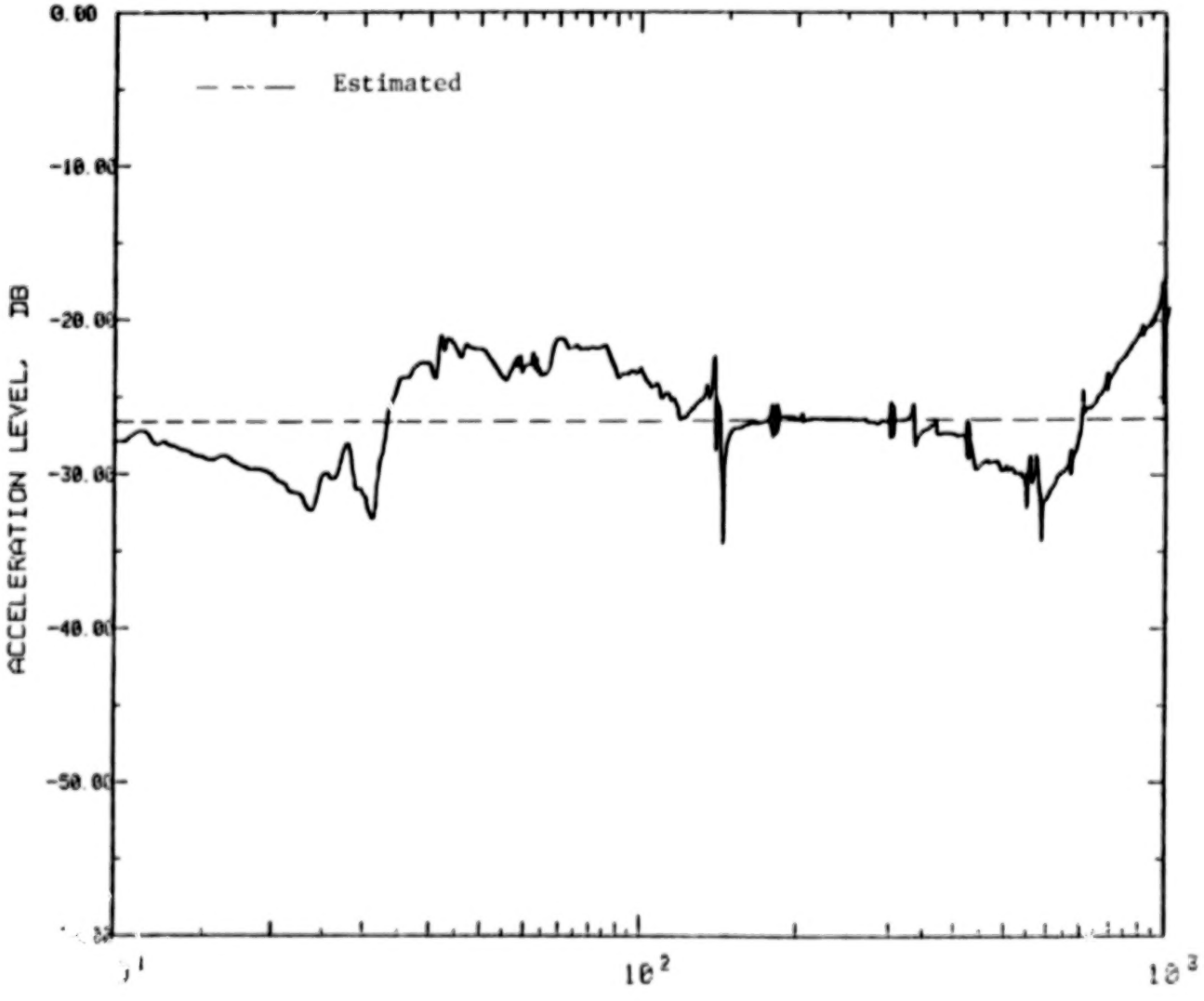

(e) Response AY.

FIGURE 8 (Continued). MEASURED TRANSFER FUNCTION SPECTRA, LOAD CASE #2, ISOLATOR CONFIGURATION R1, REF. 89 N RMS.

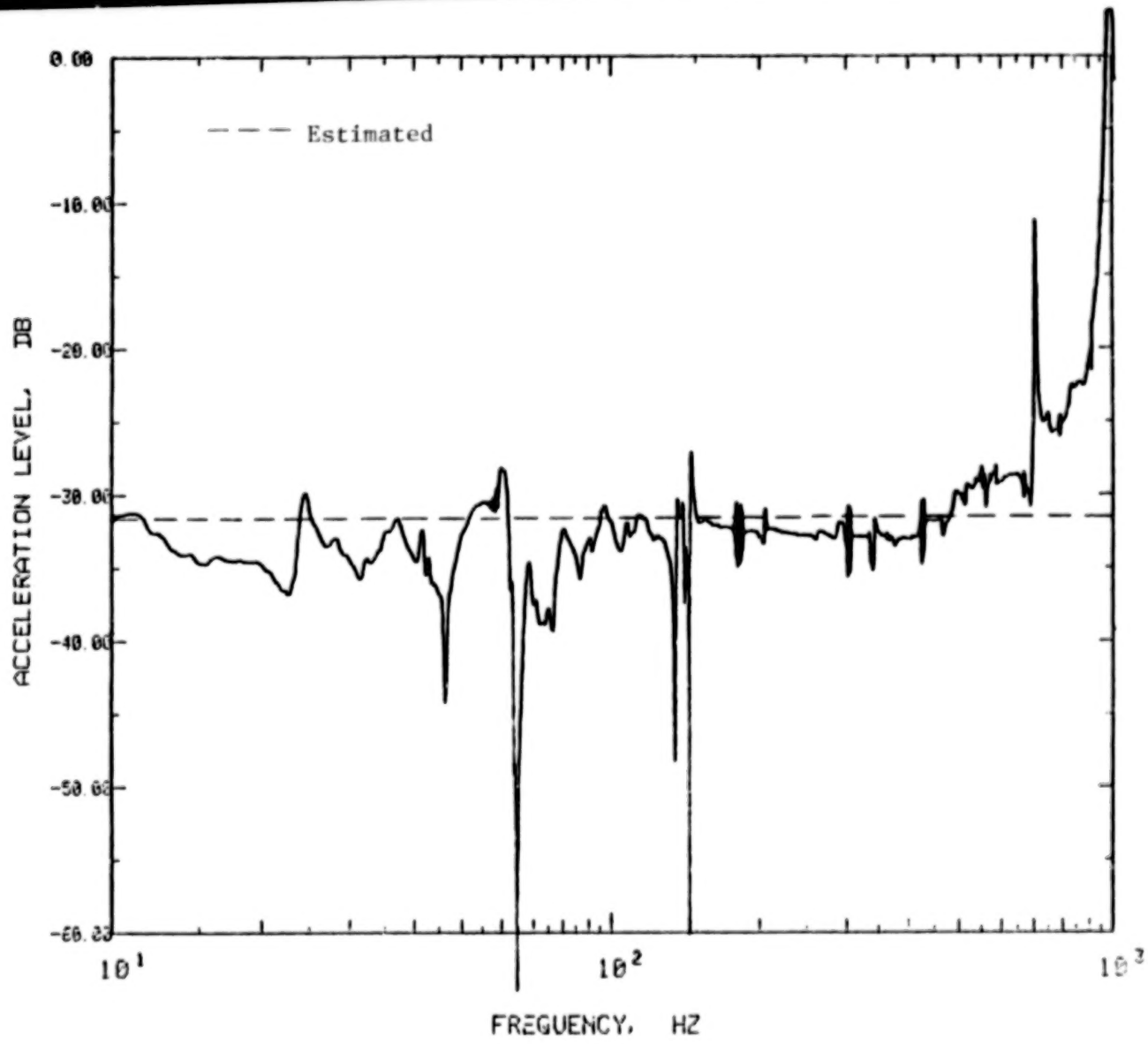

(f) Response AZ.

FIGURE 8 (Concluded). MEASURED TRANSFER FUNCTION SPECTRA, LOAD CASE #2, ISOLATOR CONFIGURATION R1, REF. 89 N RMS.

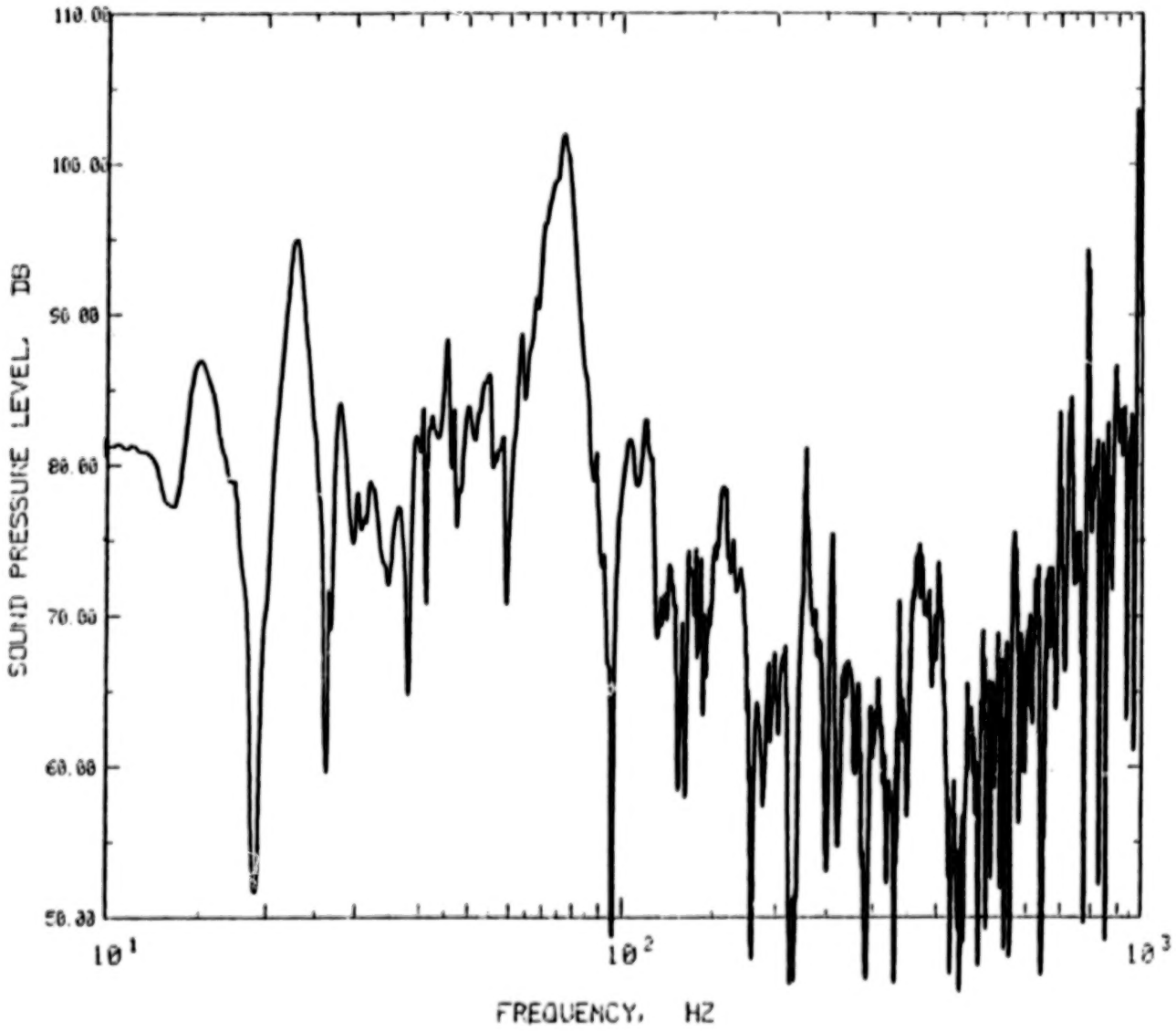

(a) Response P1.

FIGURE 9. MEASURED TRANSFER FUNCTION SPECTRA, LOAD CASE #3, ISOLATOR CONFIGURATION R1, REF. 89 N RMS.

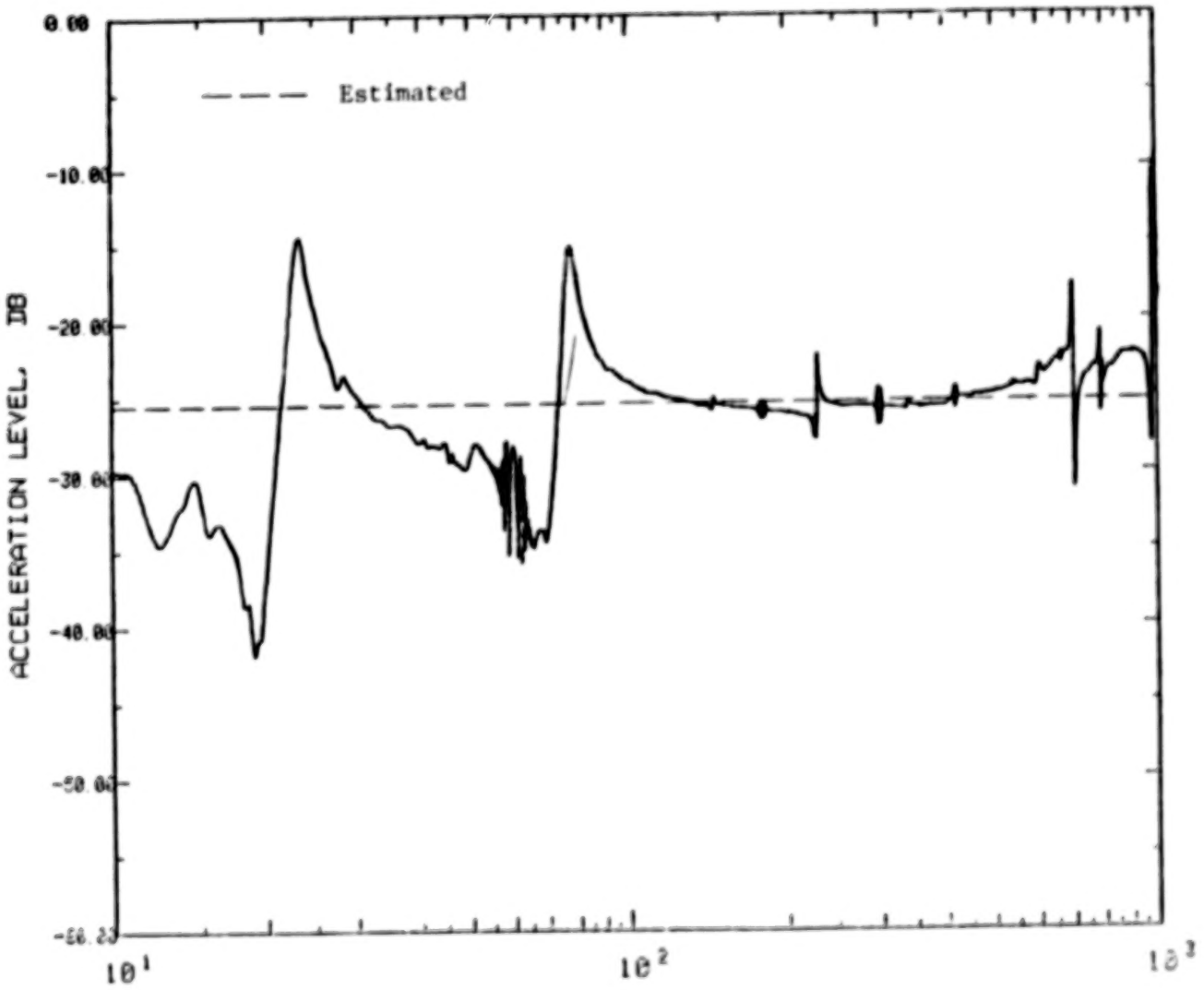

(b) Response AX.

FIGURE 9 (Continued). MEASURED TRANSFER FUNCTION SPECTRA, LOAD CASE #3, ISOLATOR CONFIGURATION R1, REF. 89 N RMS.

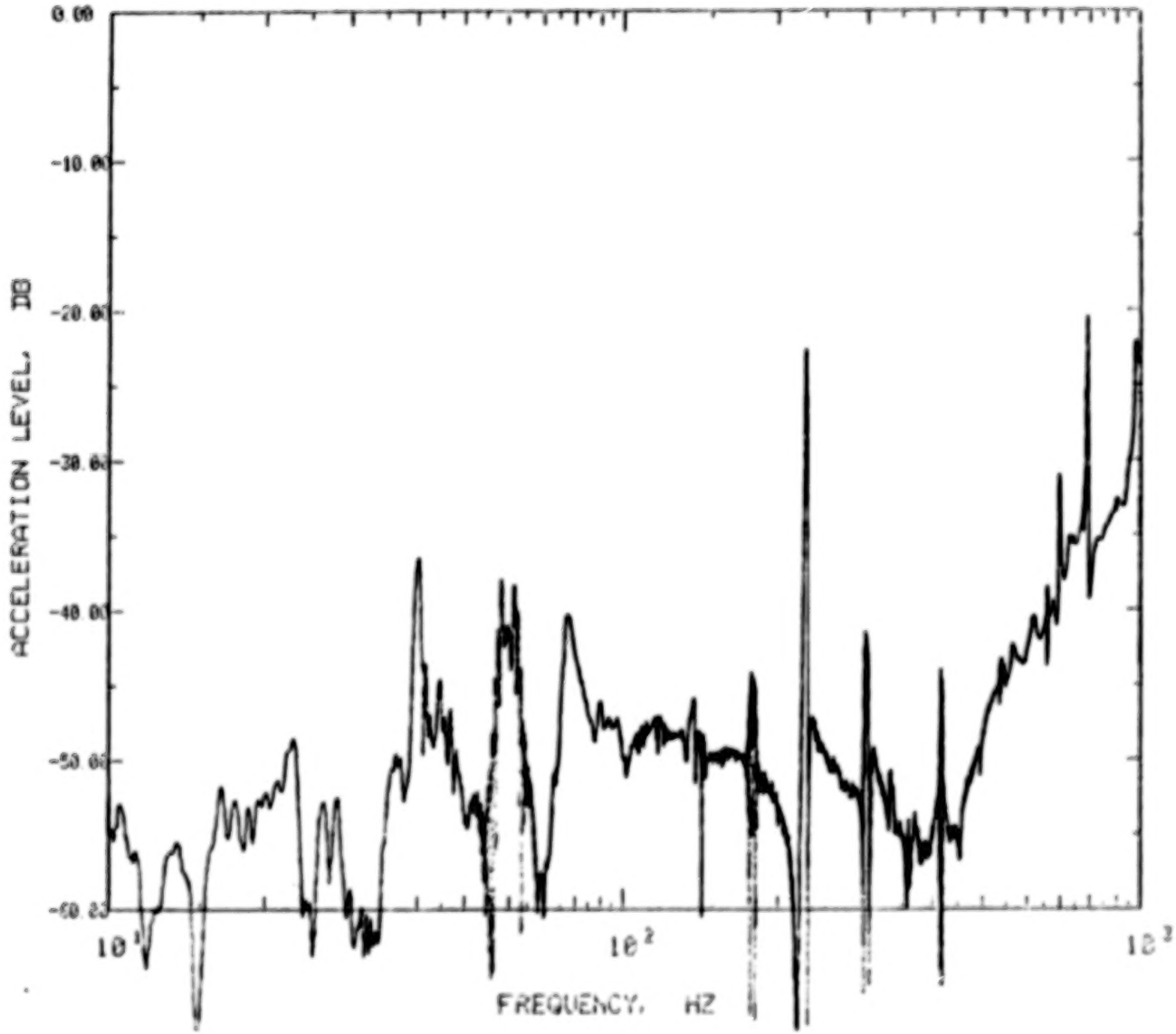

(c) Response AY.

FIGURE 9 (Continued). MEASURED TRANSFER FUNCTION SPECTRA, LOAD CASE #3, ISOLATOR CONFIGURATION R1, REF. 89 N RMS.

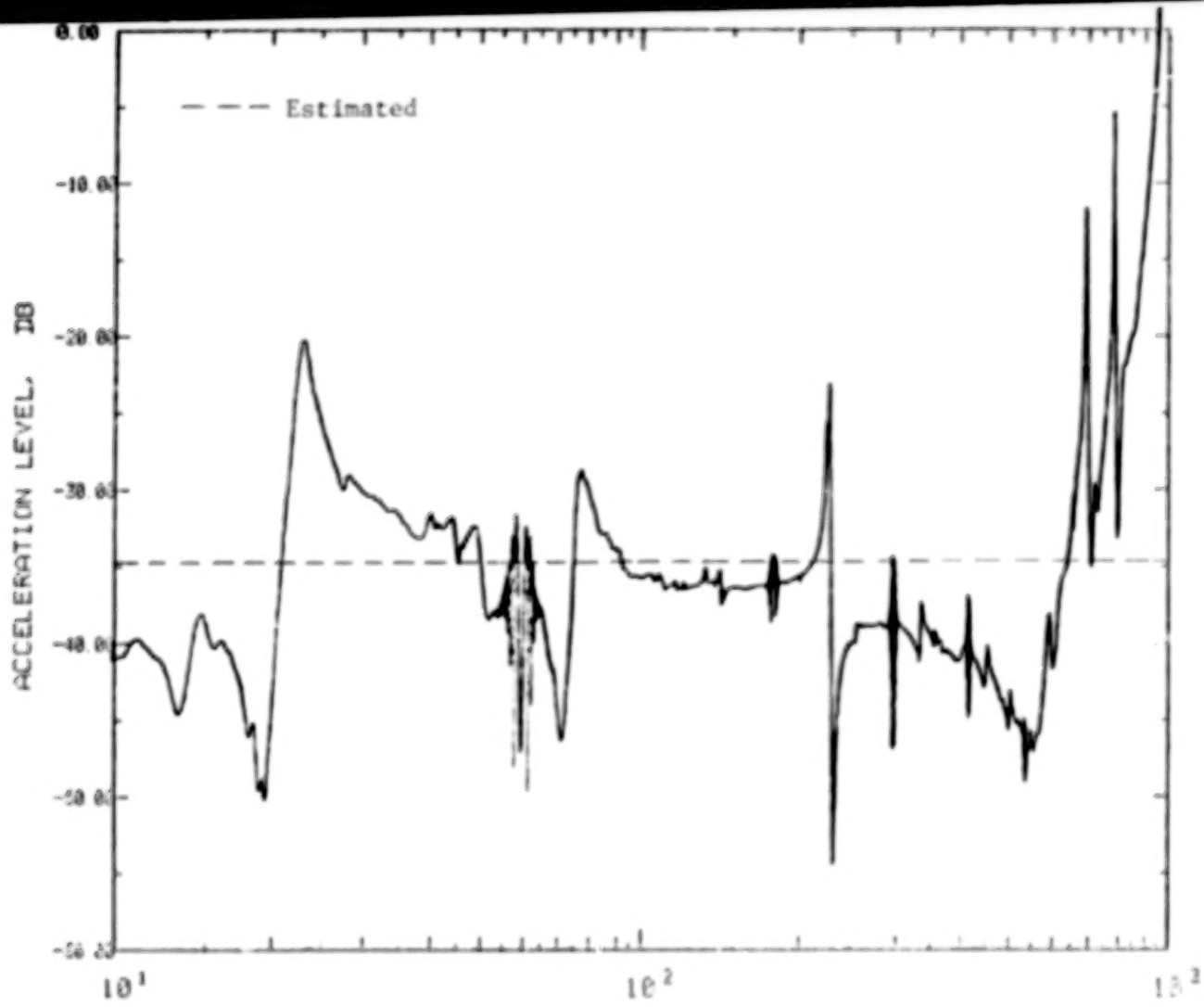

(d) Response AZ.

FIGURE 9 (Concluded). MEASURED TRANSFER FUNCTION SPECTRA, LOAD CASE #3, ISOLATOR CONFIGURATION R1, REF. 89 N RMS.

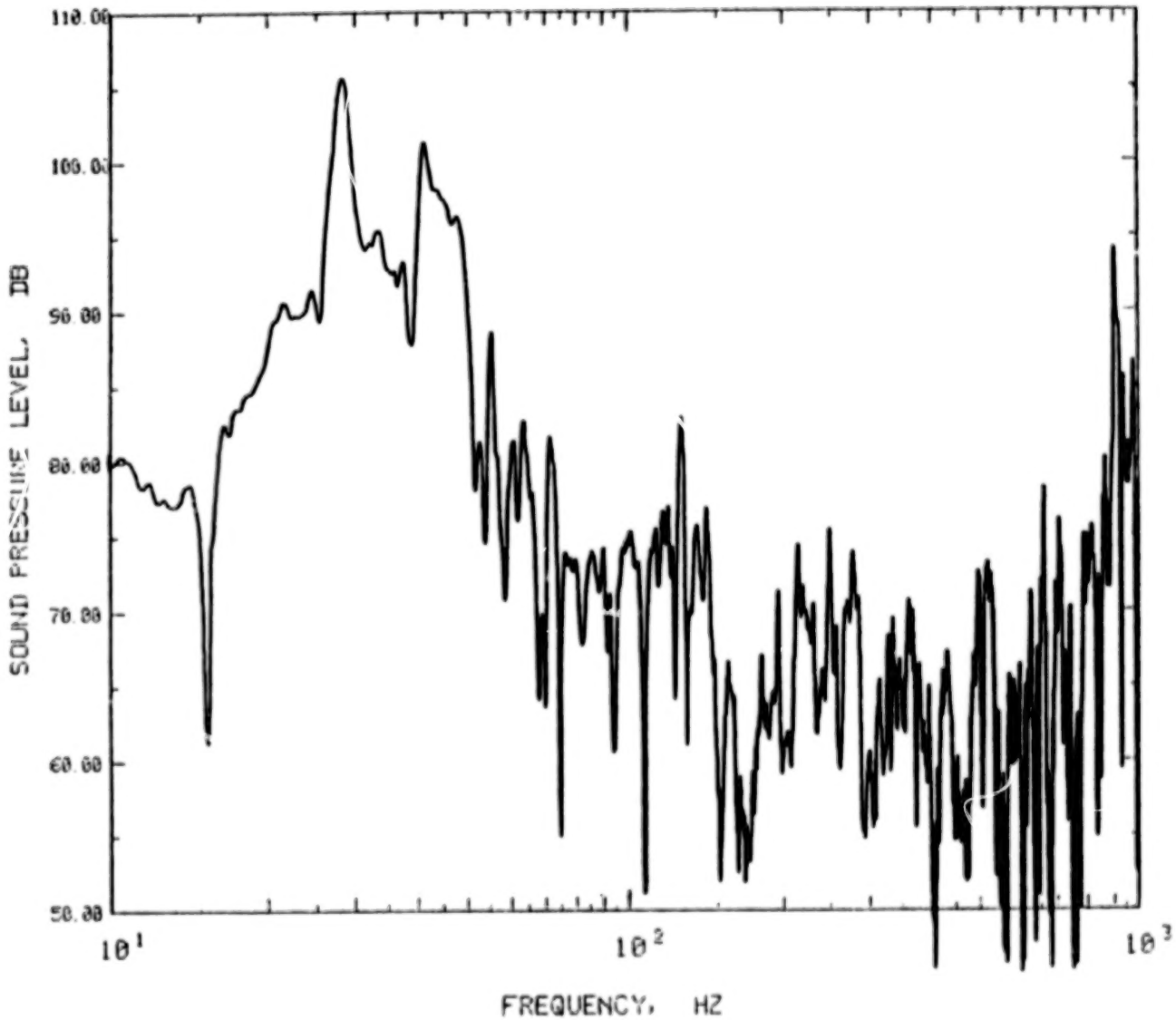

(a) Response P1.

FIGURE 10. MEASURED TRANSFER FUNCTION SPECTRA, LOAD CASE #2, ISOLATOR CONFIGURATION OA, REF. 89 N RMS.

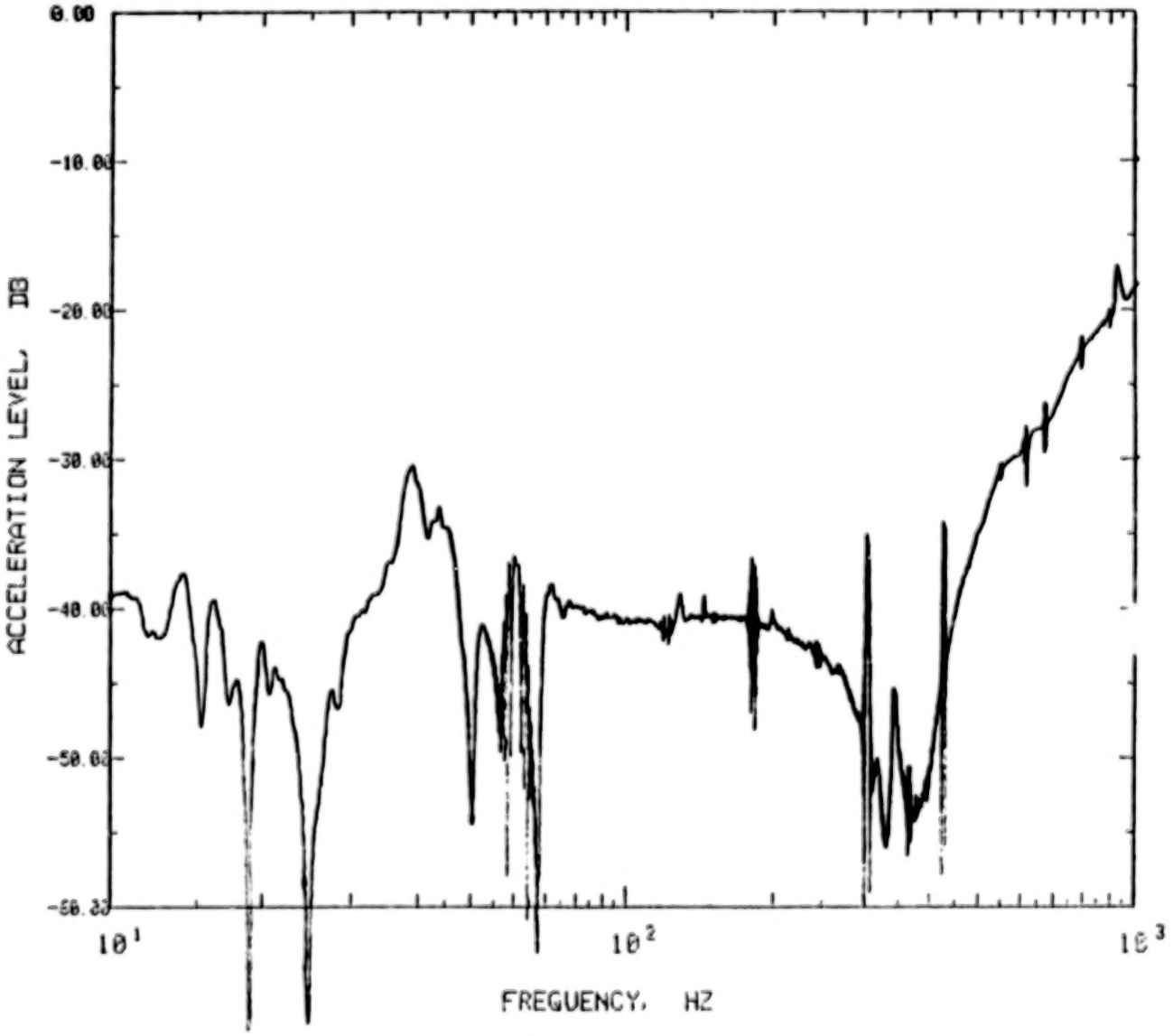

(b) Response AX.

FIGURE 10 (Continued). MEASURED TRANSFER FUNCTION SPECTRA, LOAD CASE #2, ISOLATOR CONFIGURATION OA, REF. 89 N RMS.

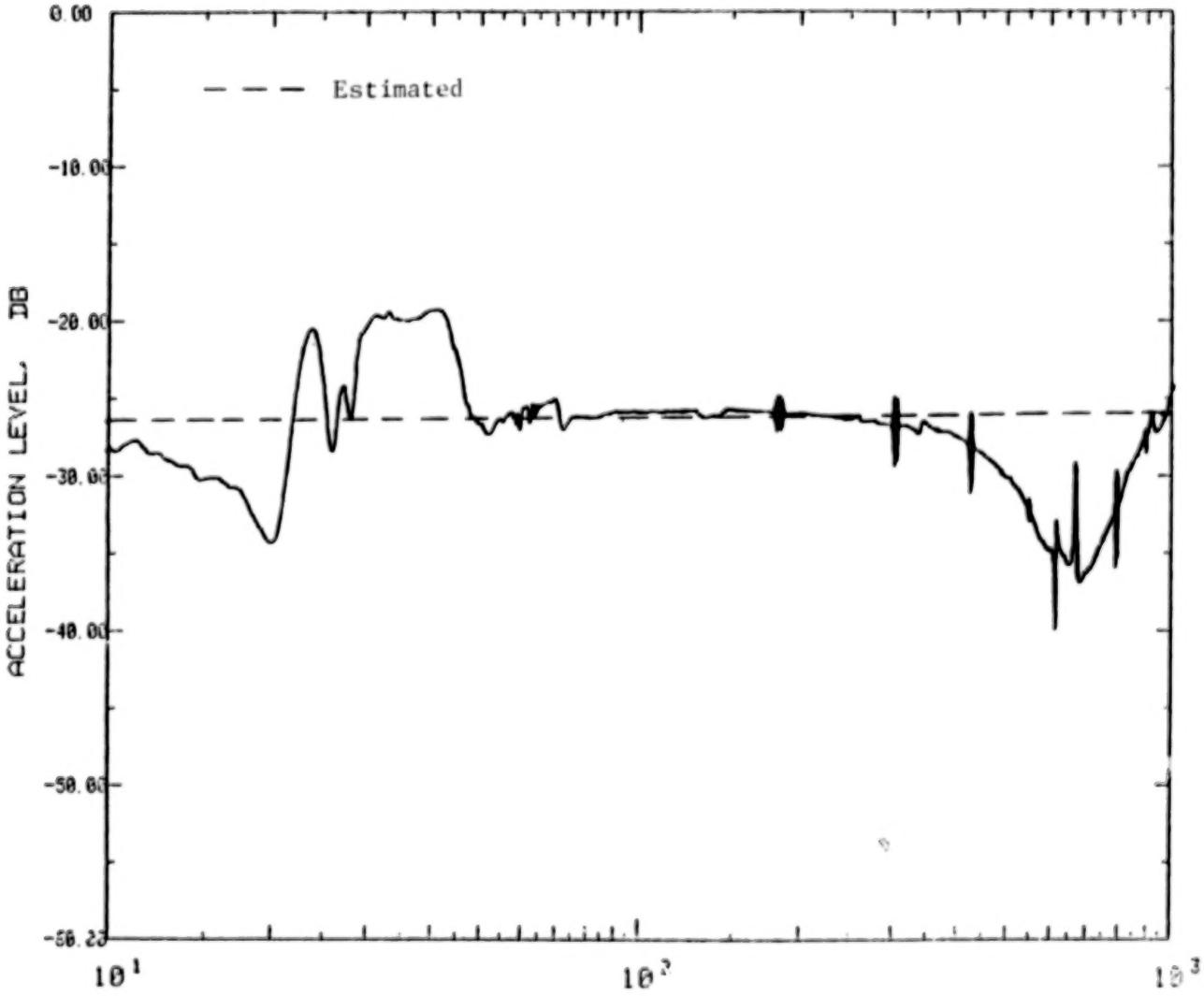

(c) Response AY.

FIGURE 10 (Continued). MEASURED TRANSFER FUNCTION SPECTRA, LOAD CASE #2, ISOLATOR CONFIGURATION OA, REF. 89 N RMS.

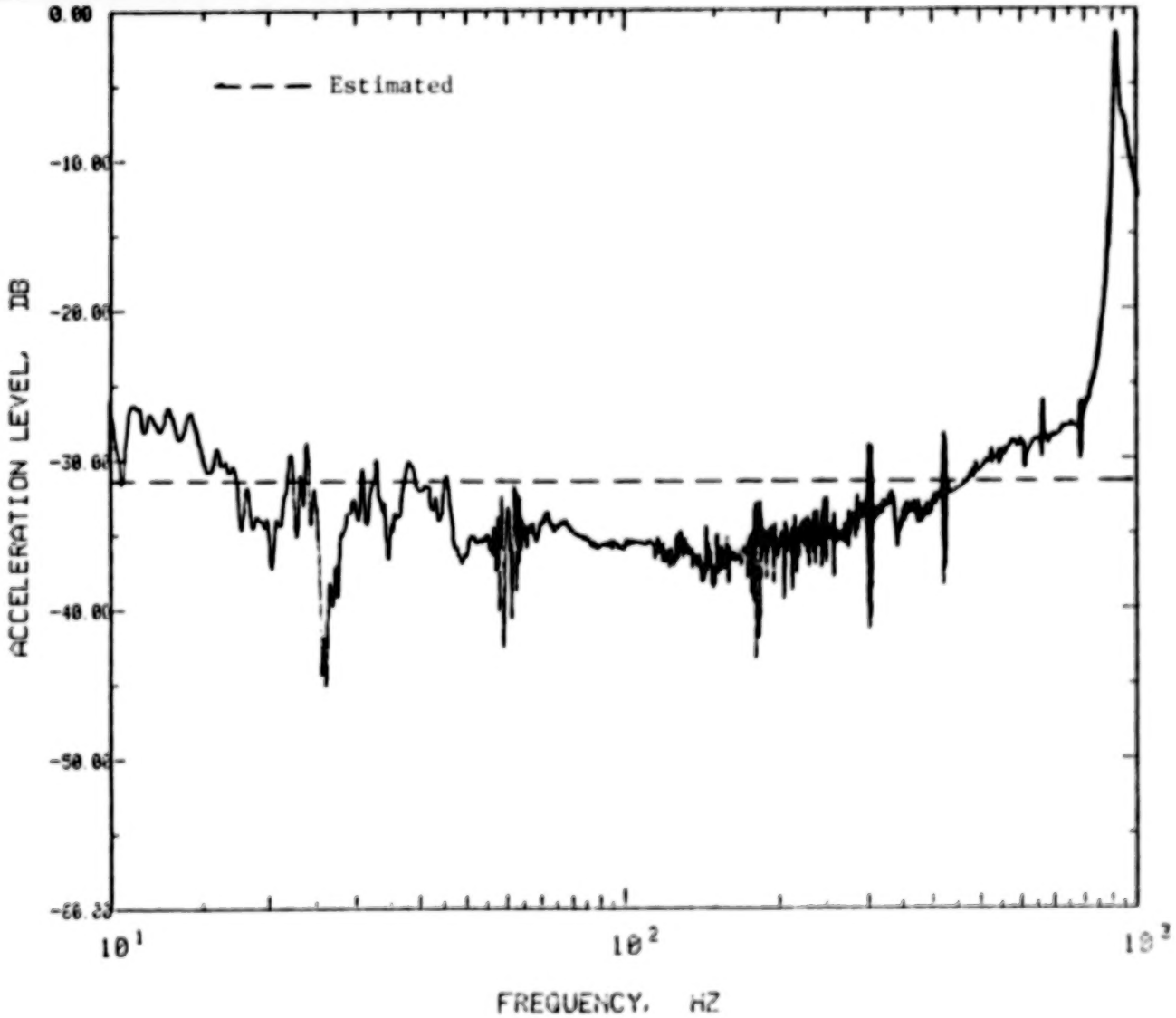

(d) Response AZ.

FIGURE 10 (Concluded). MEASURED TRANSFER FUNCTION SPECTRA, LOAD CASE #2, ISOLATOR CONFIGURATION OA, REF. 89 N RMS.

(a) Response P1.

FIGURE 11. MEASURED TRANSFER FUNCTION SPECTRA, LOAD CASE #2, ISOLATOR

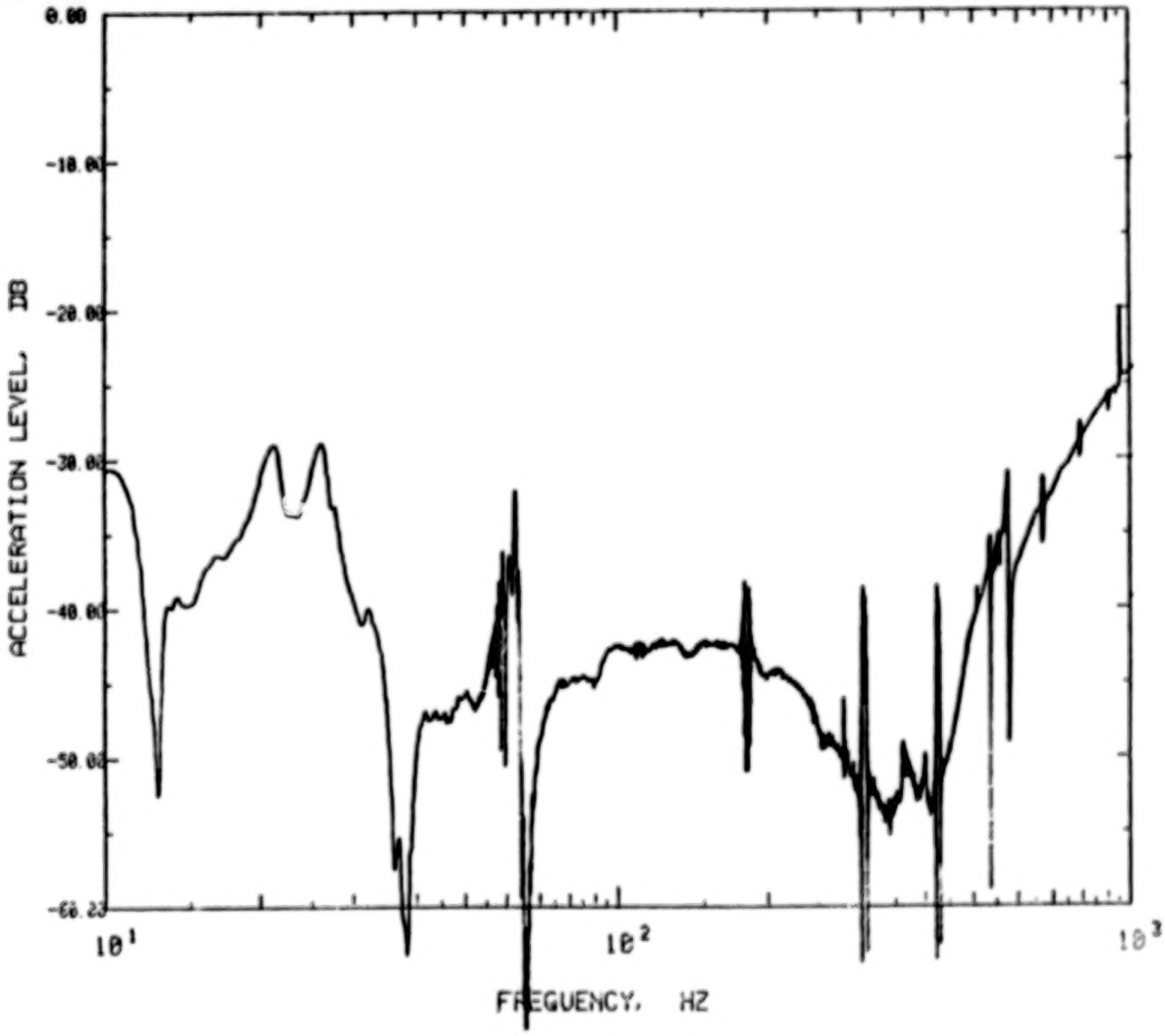

(b) Response AX.

FIGURE 11 (Continued). MEASURED TRANSFER FUNCTION SPECTRA, LOAD CASE #2, ISOLATOR CONFIGURATION AA, REF. 89 N RMS.

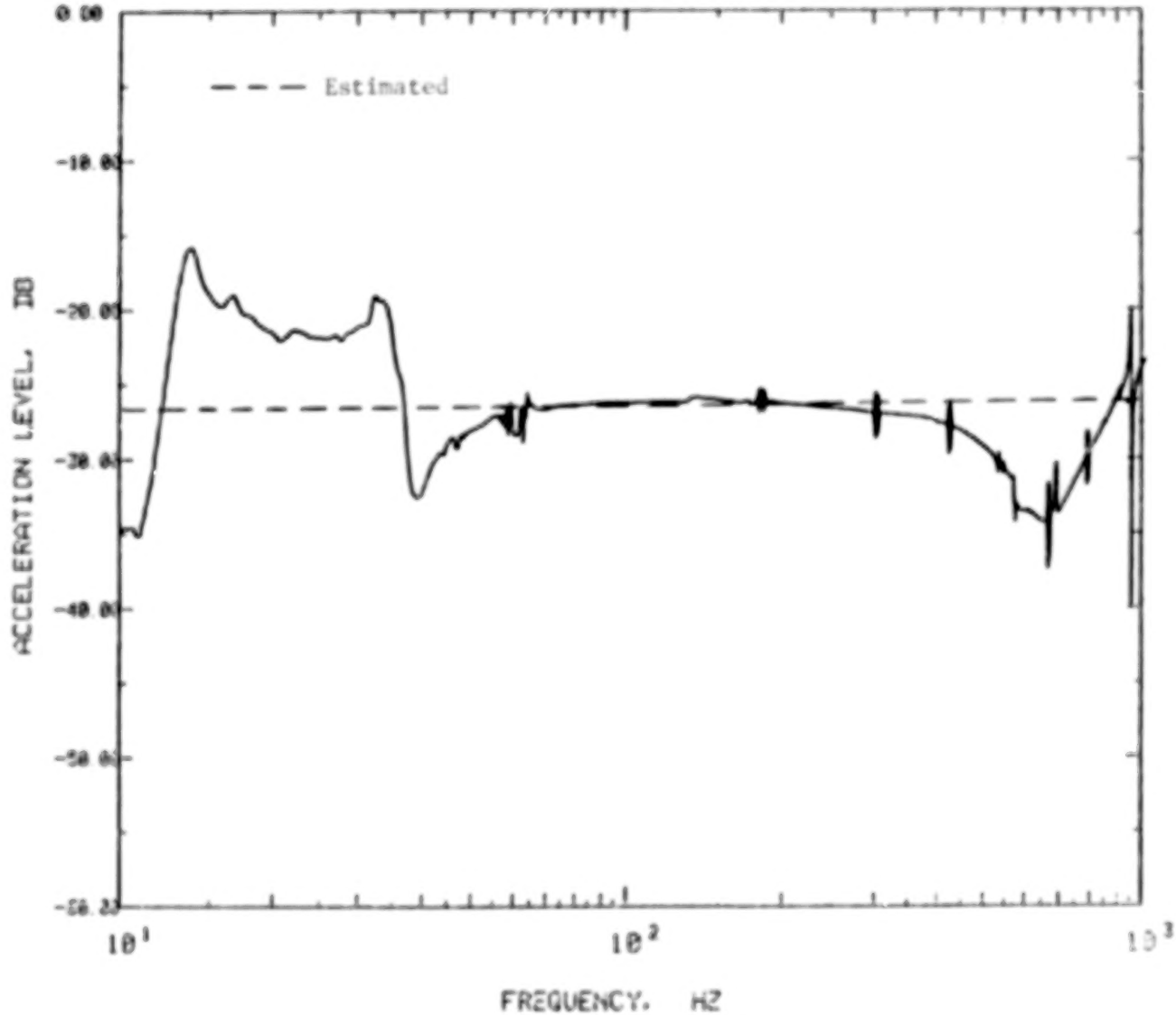

(c) Response AY.

FIGURE 11 (Continued). MEASURED TRANSFER FUNCTION SPECTRA, LOAD CASE #2, ISOLATOR CONFIGURATION AA, REF. 89 N RMS.

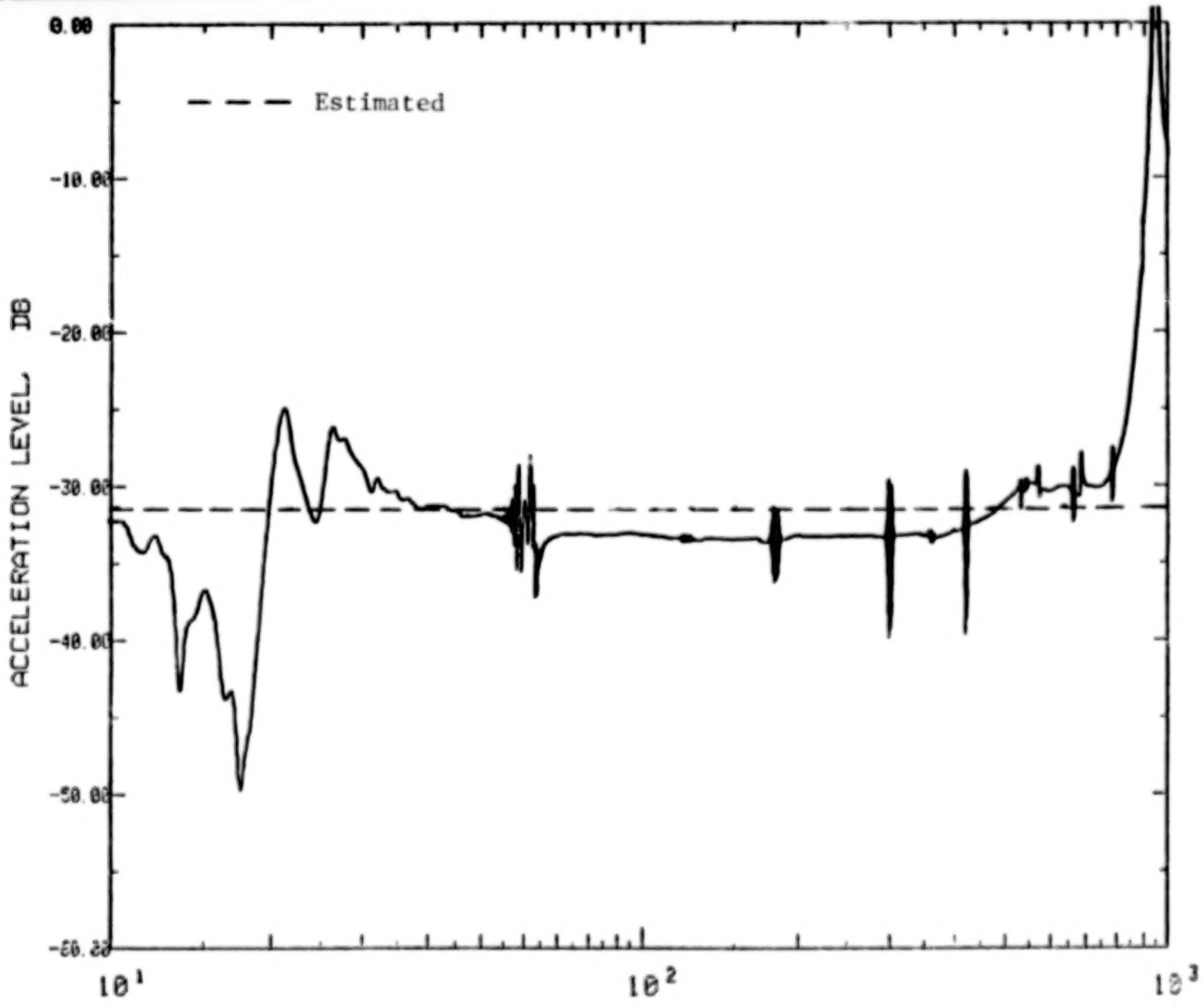

(d) Response AZ.

FIGURE 11 (Concluded). MEASURED TRANSFER FUNCTION SPECTRA, LOAD CASE #2, ISOLATOR CONFIGURATION AA, REF. 89 N RMS.

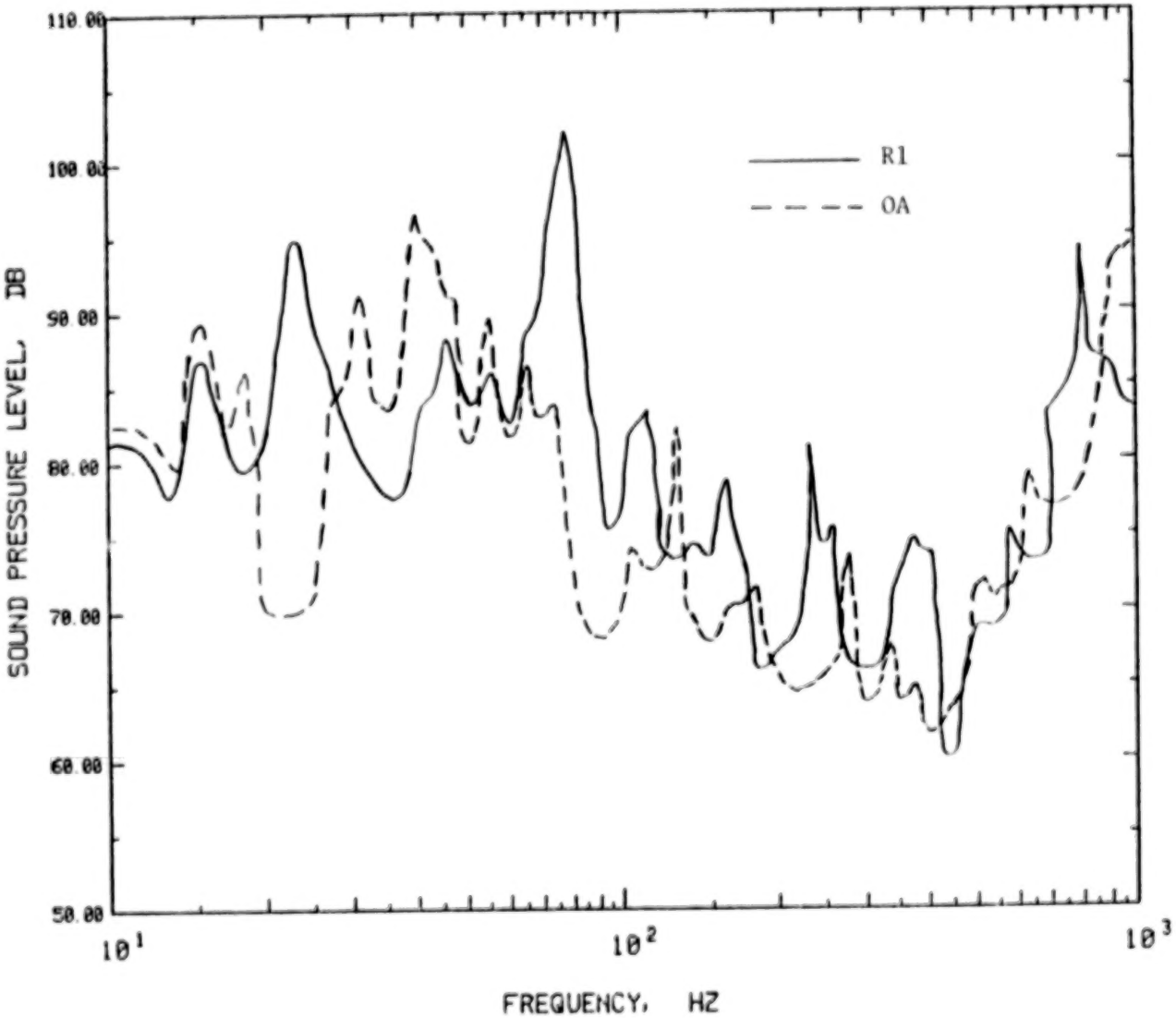

(a) Response P1, Load Case #3.

FIGURE 12. MEASURED INTERIOR NOISE TRANSMISSION, REF. 89 N RMS.

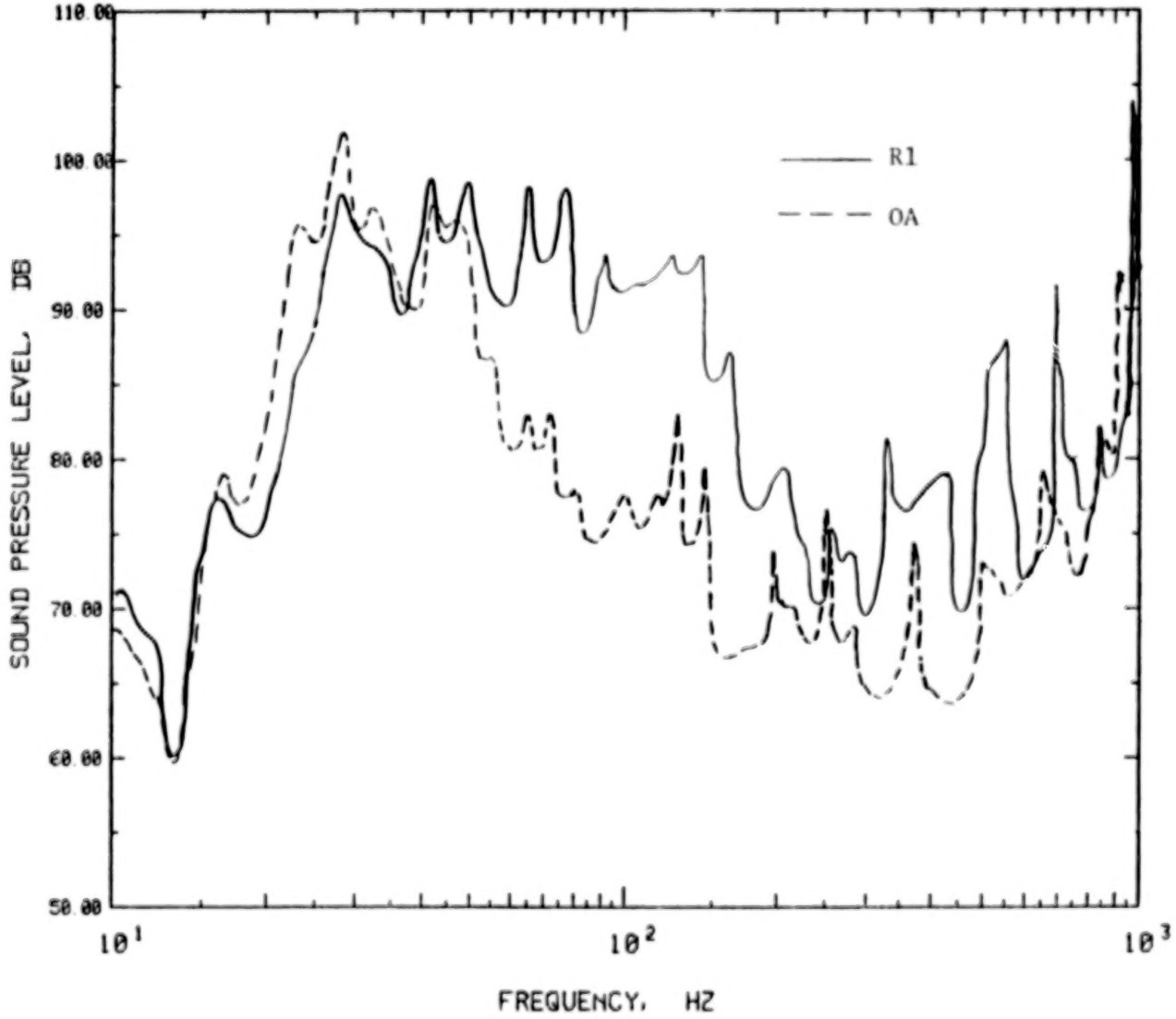

(b) Response P2, Load Case #2.

FIGURE 12 (Concluded). MEASURED INTERIOR NOISE TRANSMISSION, REF. 89 N RMS.

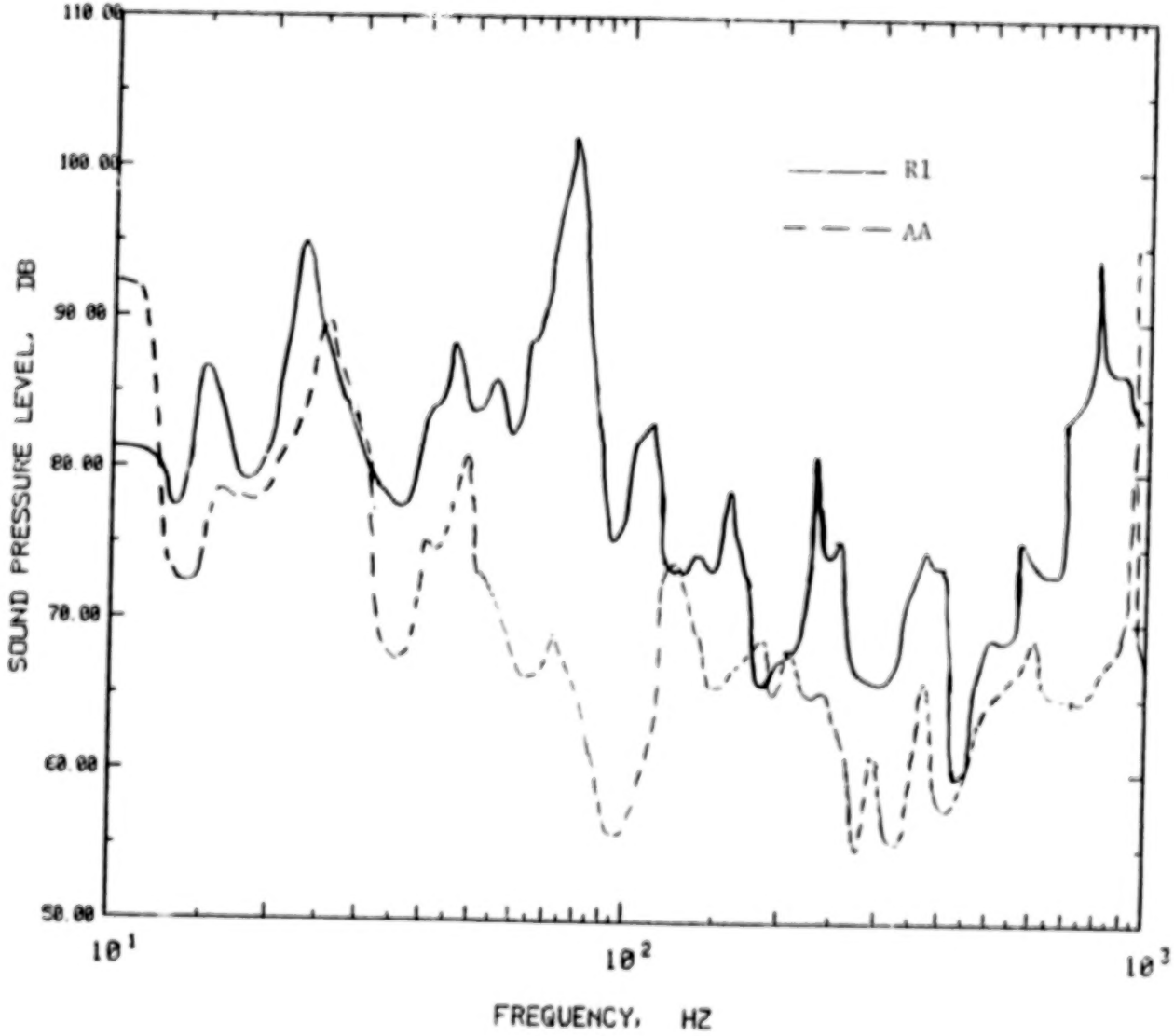

(a) Response P1, Load Case #3.

FIGURE 13. MEASURED INTERIOR NOISE TRANSMISSION, REF. 89 N RMS.

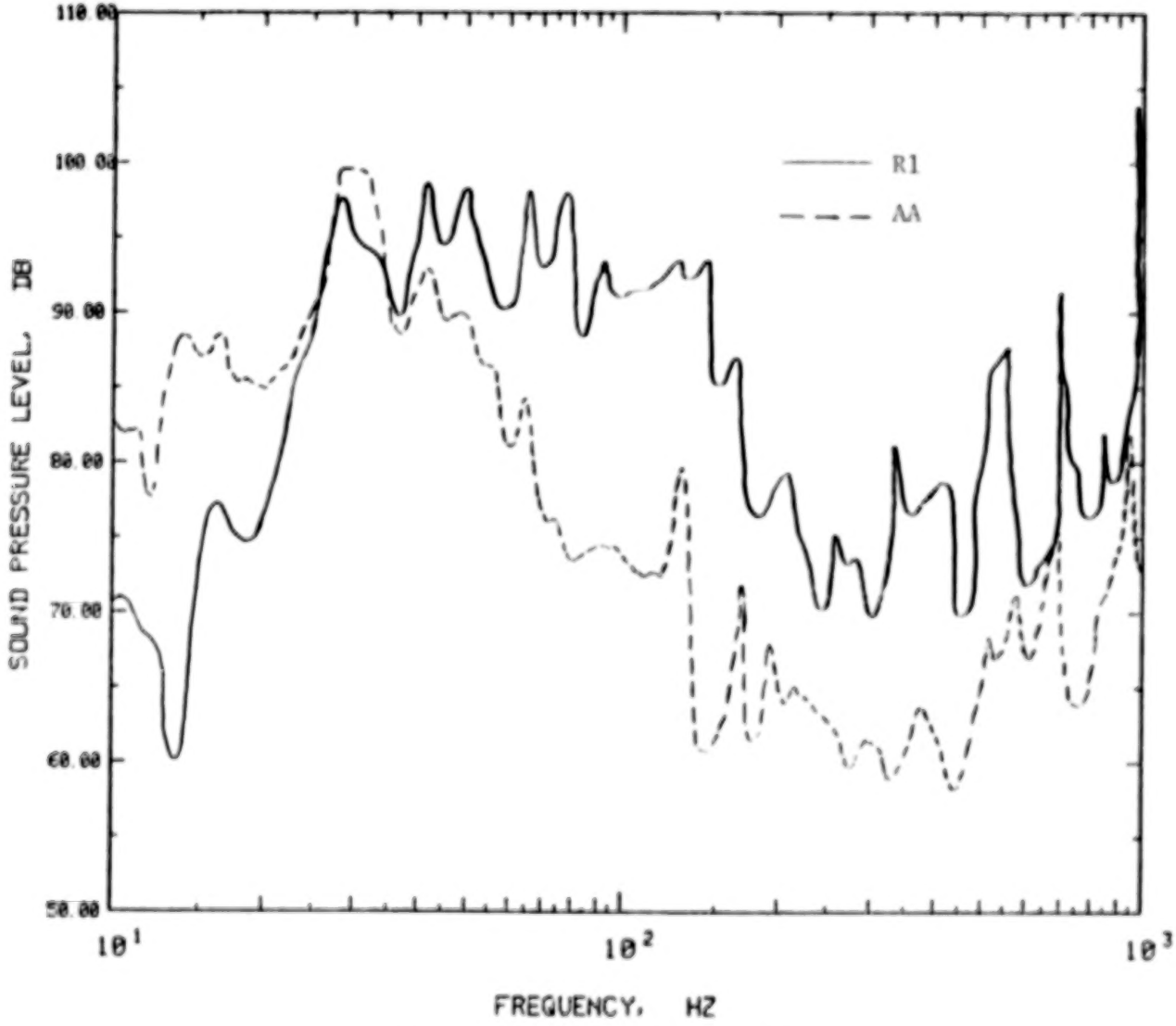

(b) Response P2, Load Case #2.

FIGURE 13 (Concluded). MEASURED INTERIOR NOISE TRANSMISSION, REF. 89 N RMS.

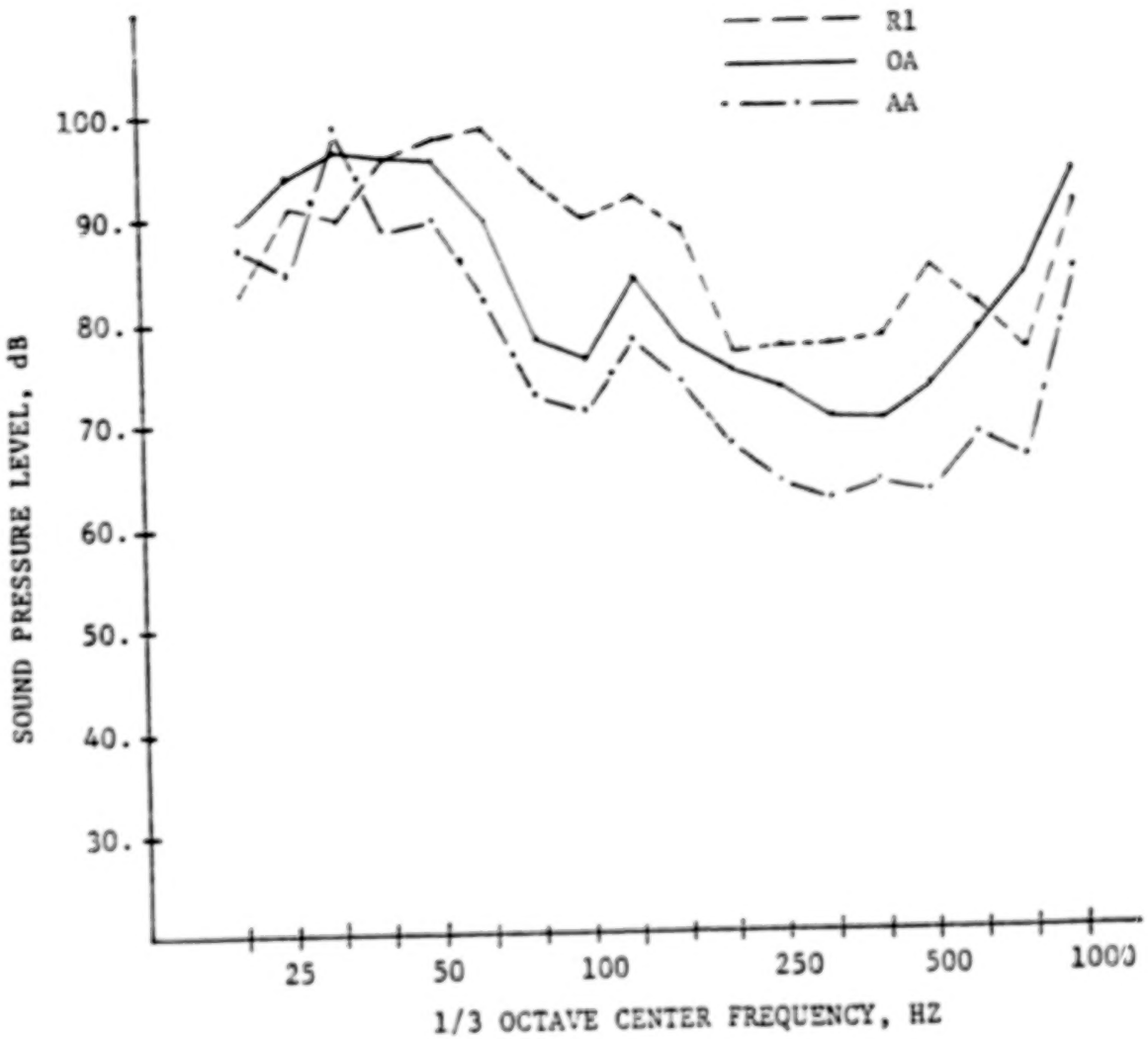

FIGURE 14. MEASURED ONE-THIRD OCTAVE PEAK SPL TRANSFER FUNCTION RESPONSE AT P1; LOAD CASE #2; REF 89 N RMS.

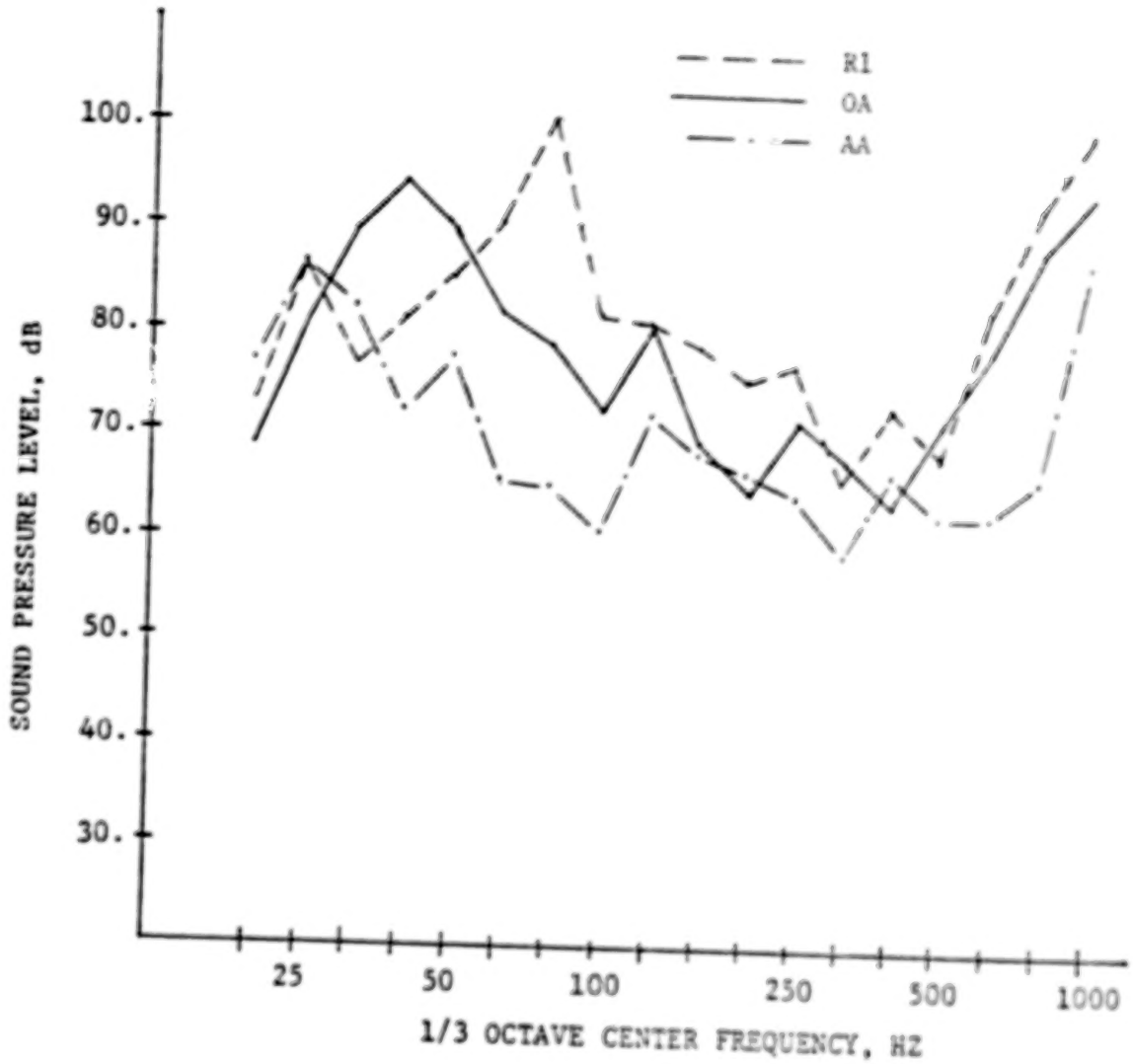

FIGURE 15. MEASURED ONE-THIRD OCTAVE PEAK SPL TRANSFER FUNCTION RESPONSE AT P1; LOAD CASE #3; REF. 89 N RMS.

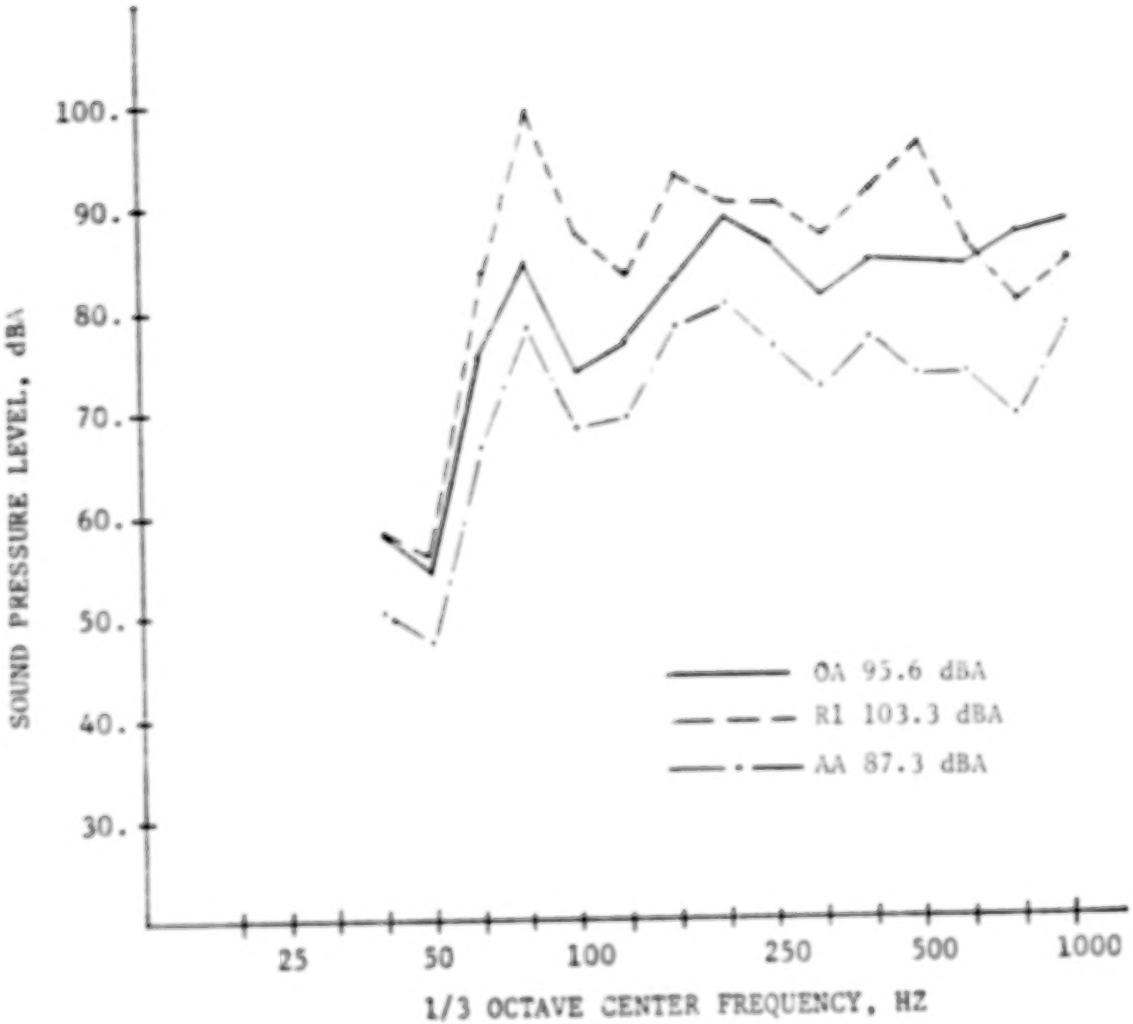

FIGURE 16. SPL AT P1 BASED ON ENGINE RUNNING DATA: 2160 RPM AND TRANSFER FUNCTIONS FROM LOAD CASE #2 EXCITATION.

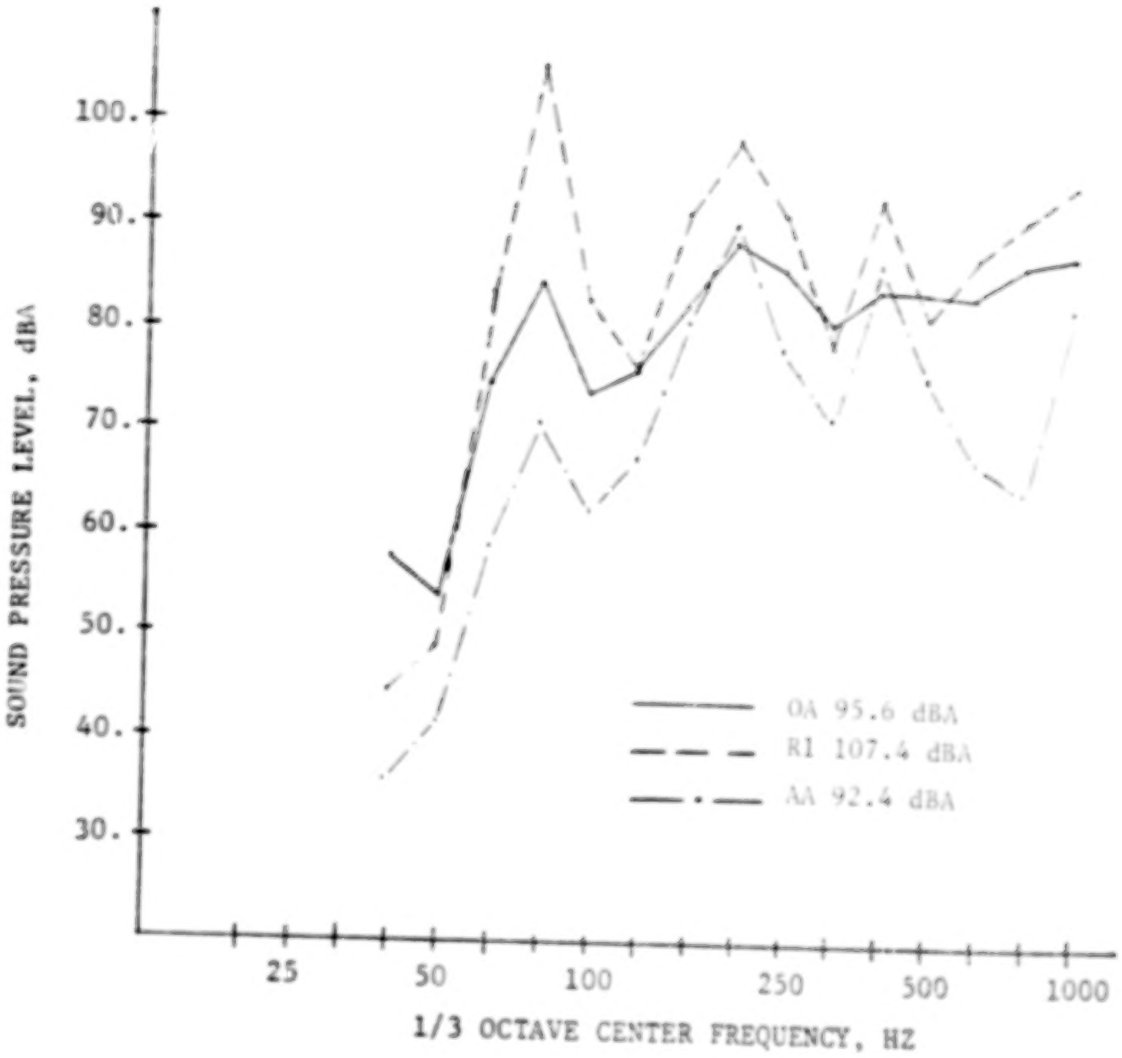

FIGURE 17. SPL AT P1 BASED ON ENGINE RUNNING DATA; 2160 RPM AND TRANSFER FUNCTIONS FROM LOAD CASE #3 EXCITATION.

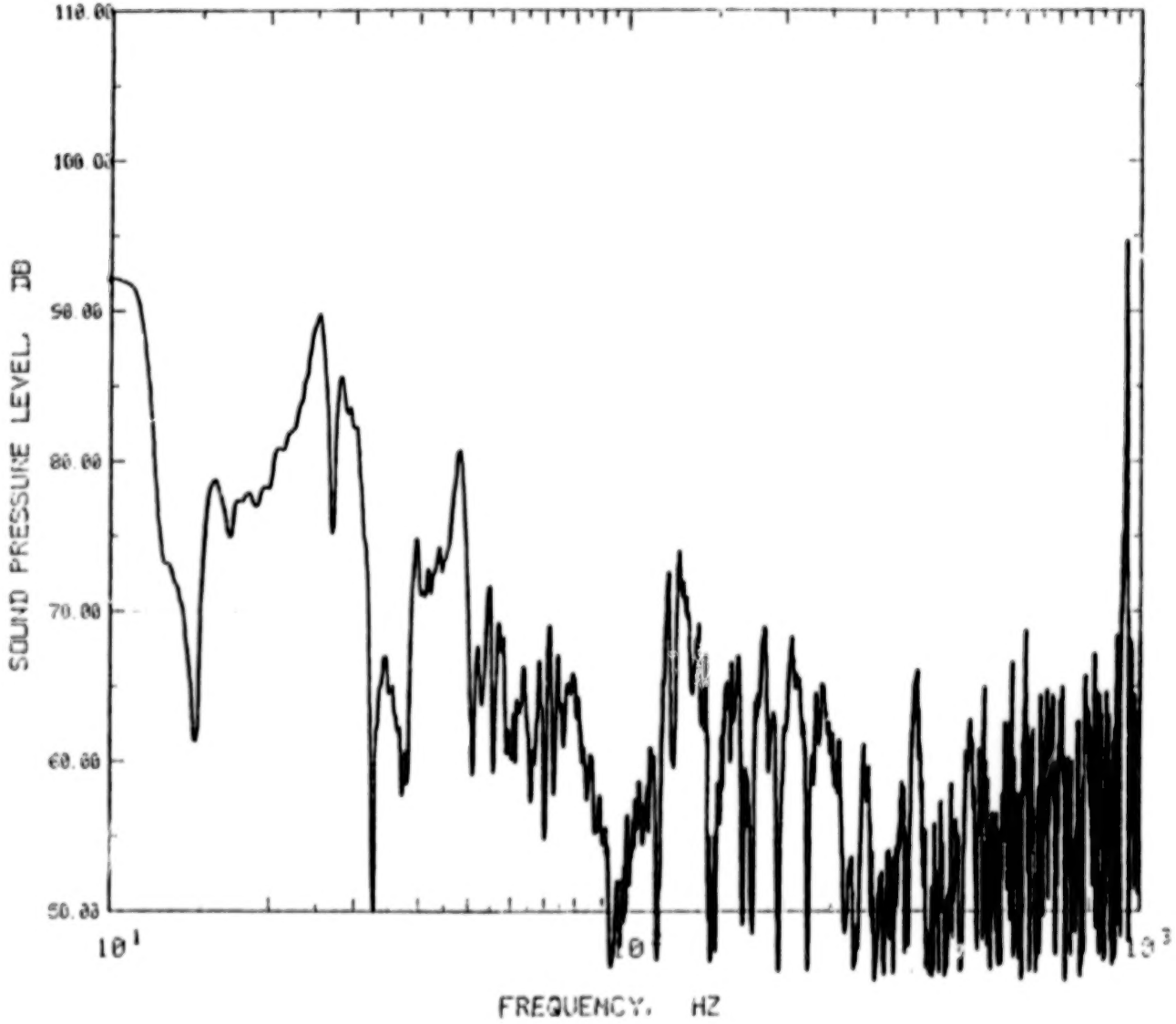

(a) Response P1, 89 N rms.

FIGURE 18. CHECK ON LINEARITY TRANSFER FUNCTION SPECTRA, LOAD CASE #3, ISOLATOR CONFIGURATION AA.

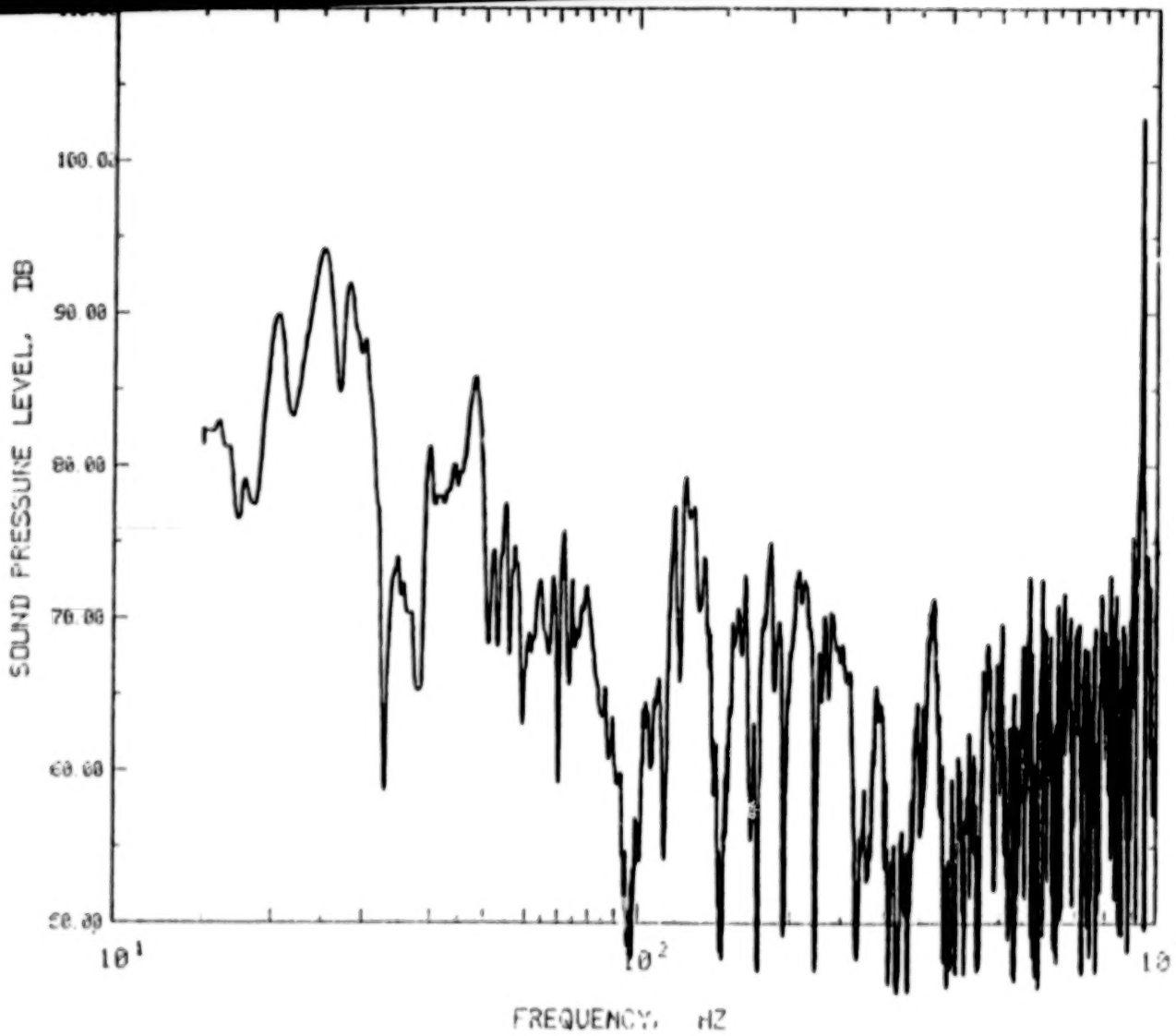

(b) Response P1, 178 N rms.

FIGURE 18 (Continued). CHECK ON LINEARITY TRANSFER FUNCTION SPECTRA, LOAD CASE #3, ISOLATOR CONFIGURATION AA.

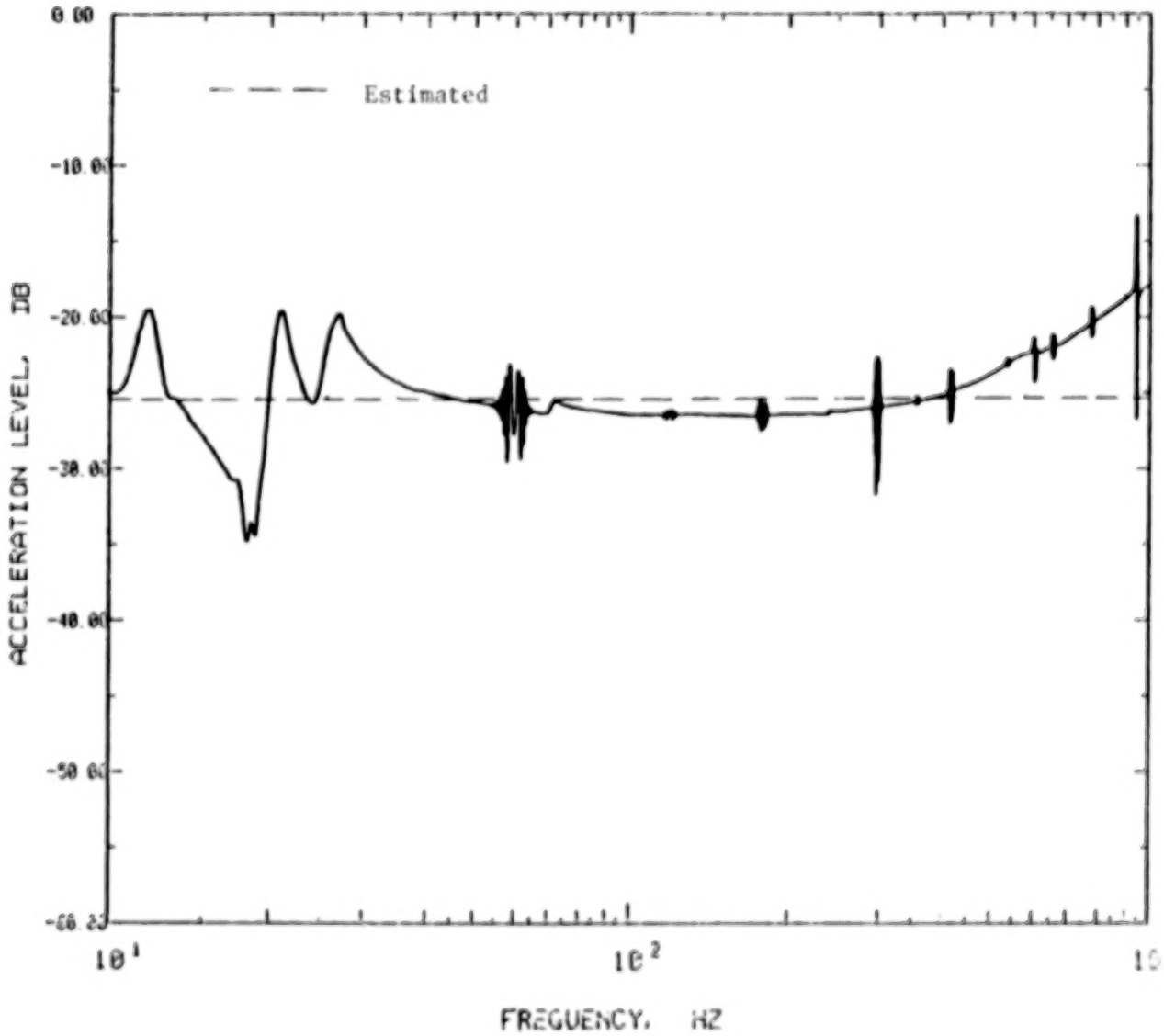

(c) Response AX, 89 N rms.

FIGURE 18 (Continued). CHECK ON LINEARITY TRANSFER FUNCTION SPECTRA, LOAD CASE #3, ISOLATOR CONFIGURATION AA.

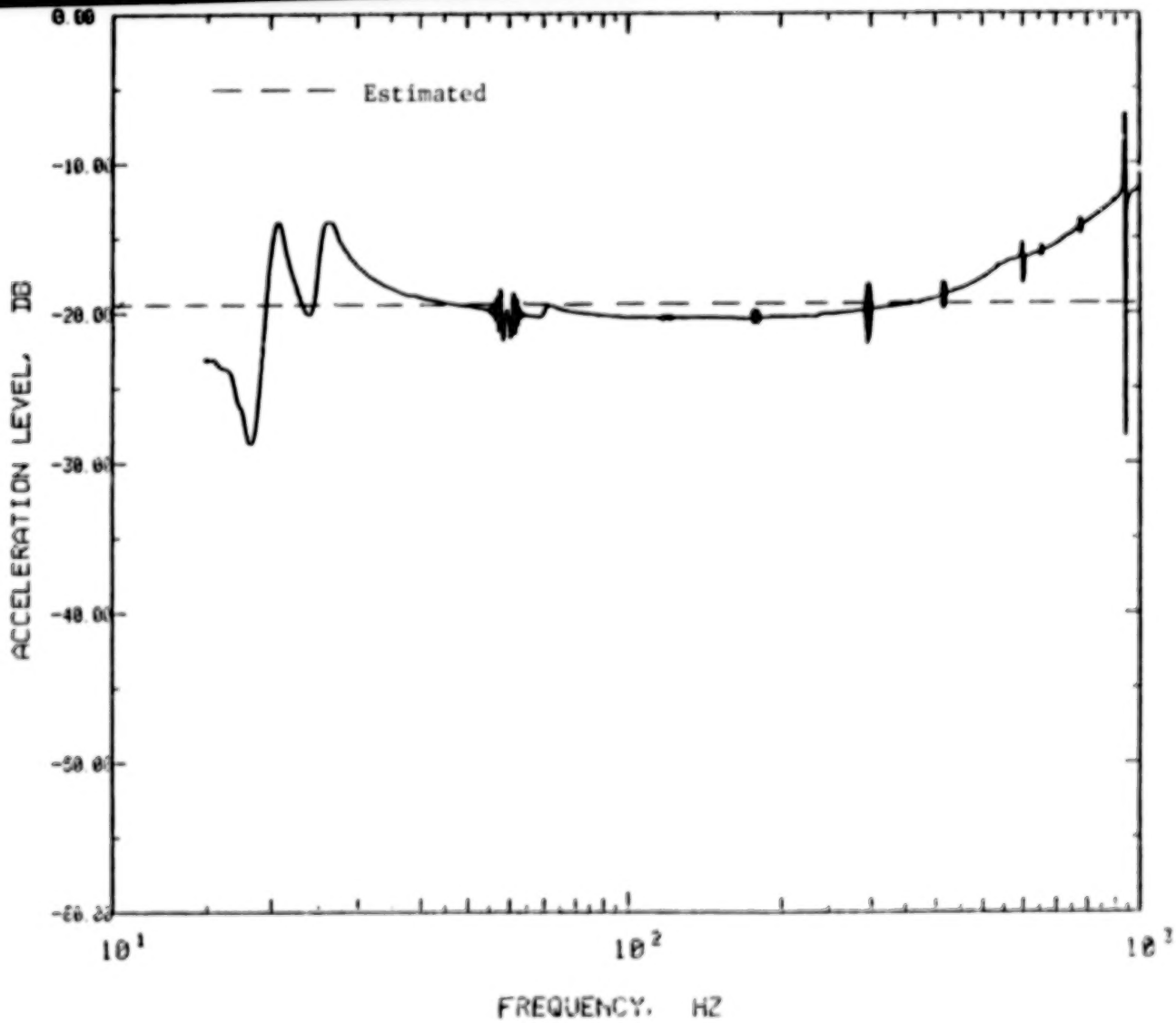

(d) Response AX, 178 N rms.

FIGURE 18 (Concluded). CHECK ON LINEARITY TRANSFER FUNCTION SPECTRA, LOAD CASE #3, ISOLATOR CONFIGURATION AA.

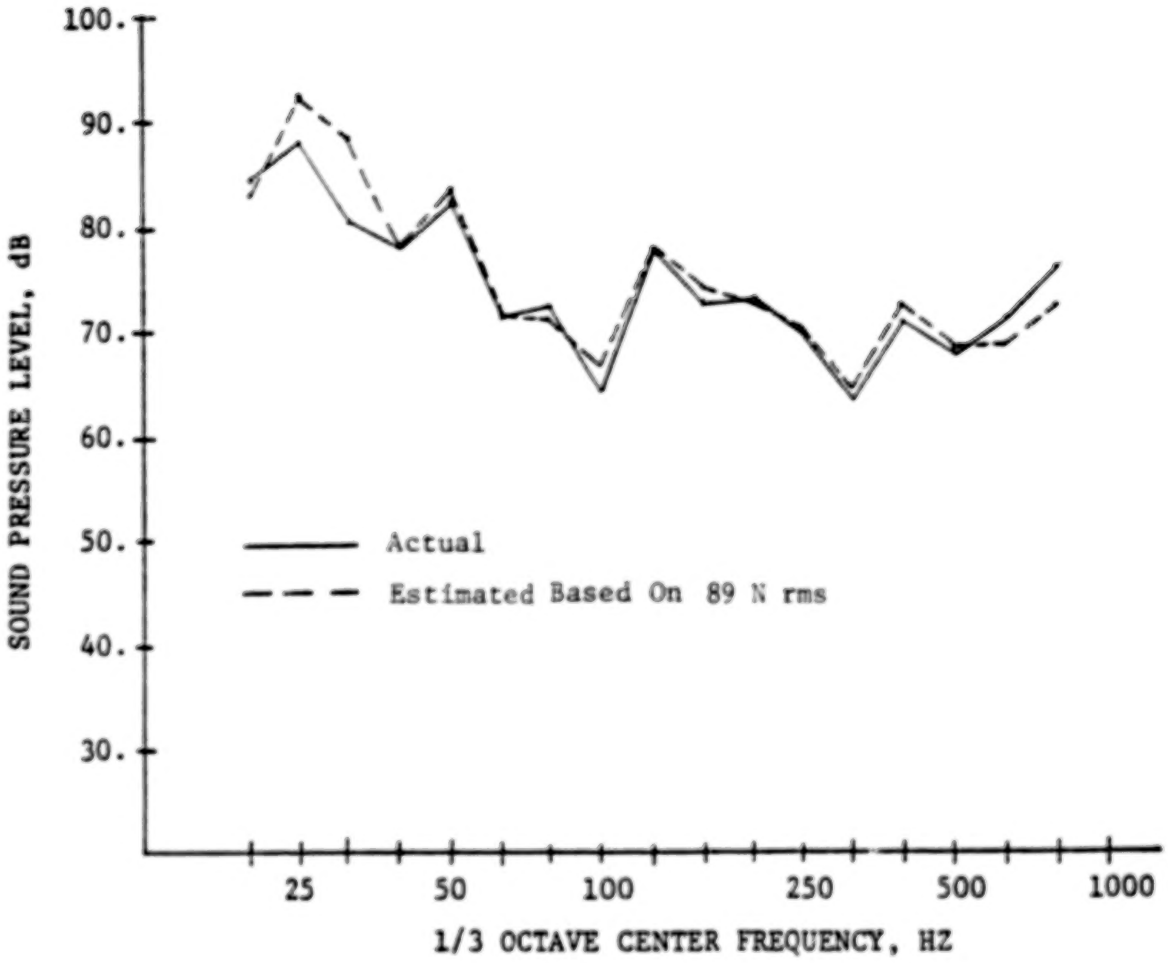

FIGURE 19. MEASURED PEAK SPL TRANSFER FUNCTION RESPONSE AT P1; LOAD CASE #3; ISOLATOR CONFIGURATION AA, REF. 178 N RMS.

BLANK

PAGE

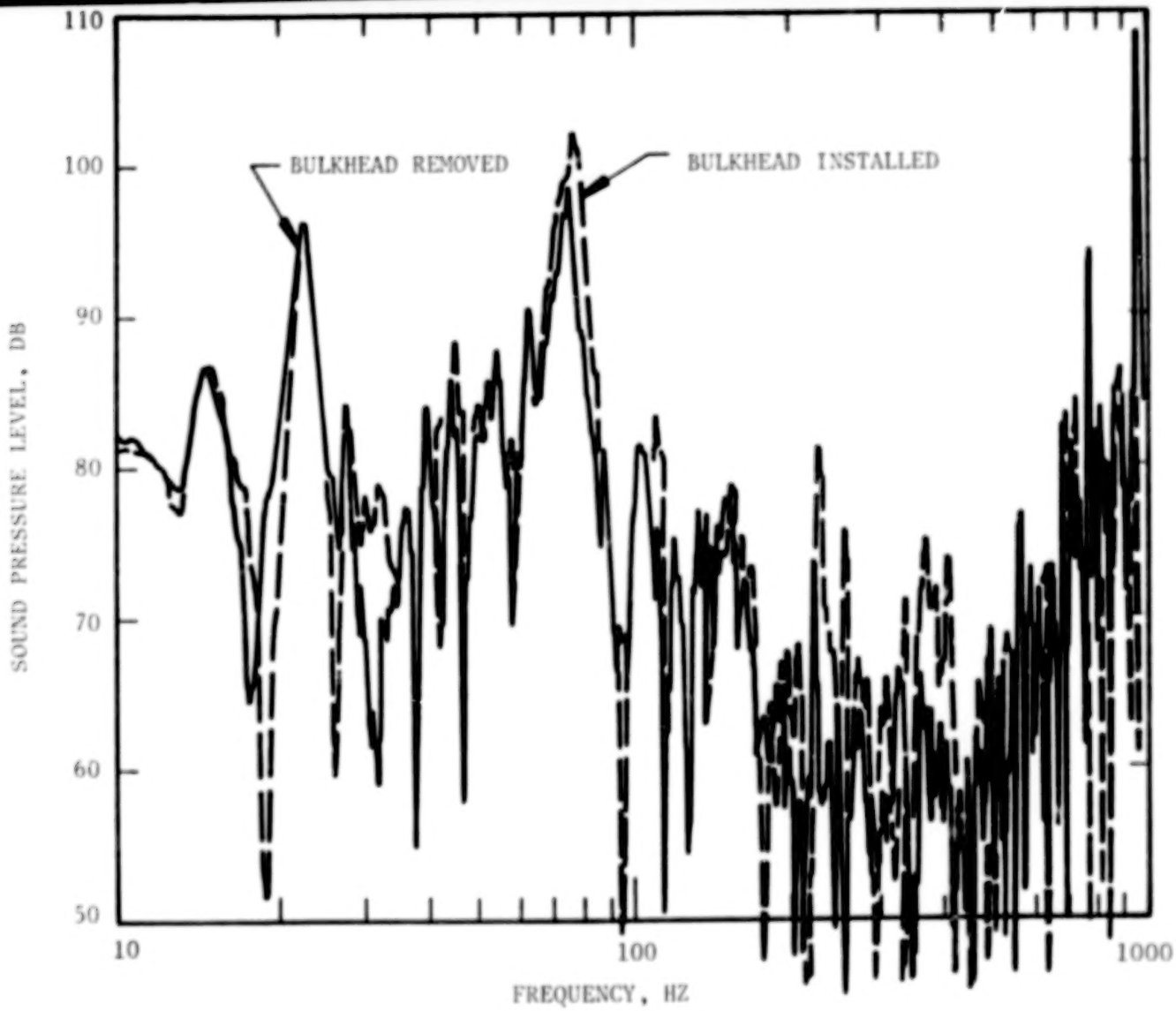

FIGURE 20. MEASURED SPL TRANSFER FUNCTION SPECTRA; LOAD CASE #3; RESPONSE P1, REF. 89 N RMS.

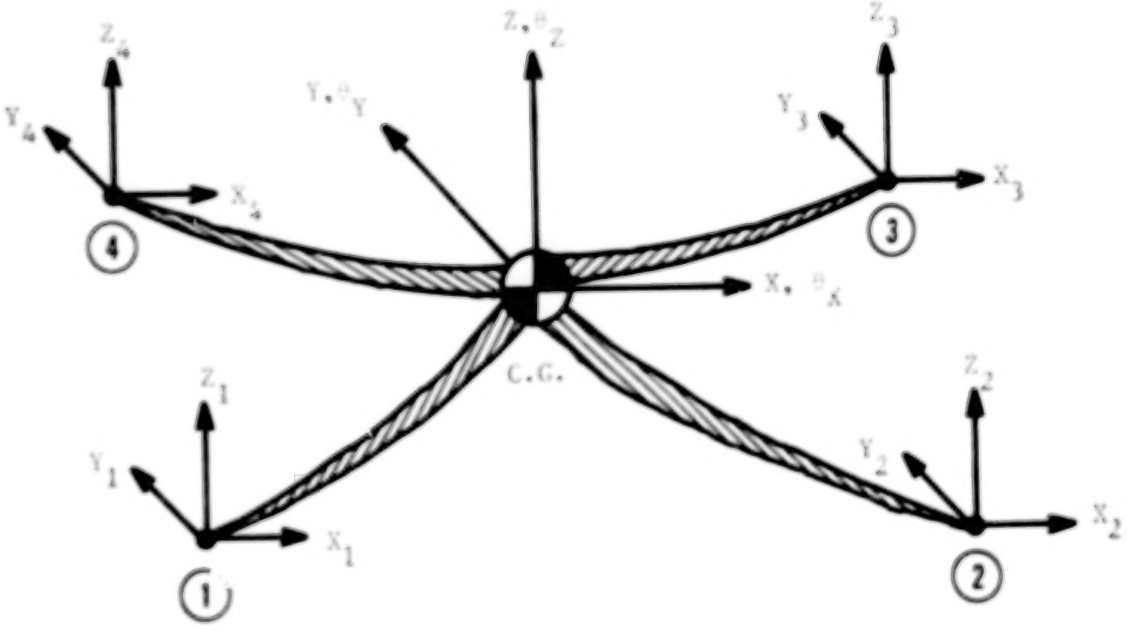

FIGURE 21. ENGINE RIGID BODY AND COUPLING DEGREES OF FREEDOM.

BLANK

PAGE

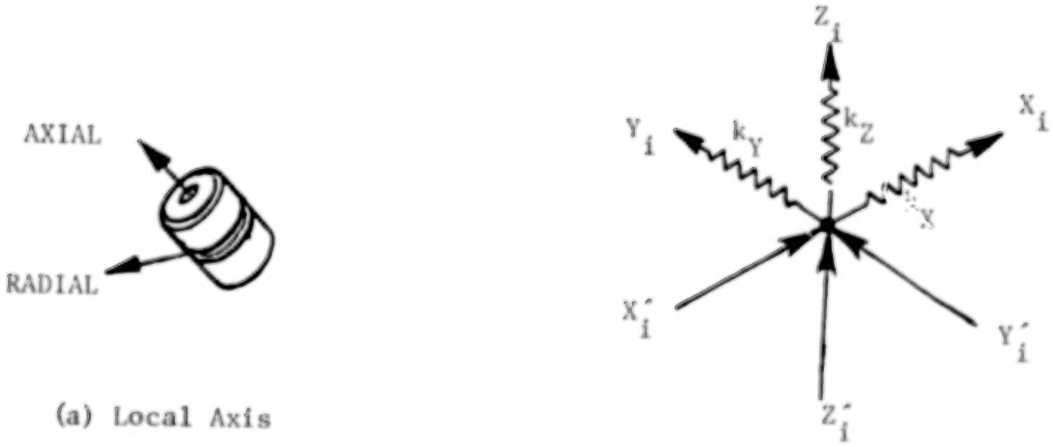

(a) Local Axis

(b) Global Axis

FIGURE 22. VIBRATION ISOLATOR DEGREES OF FREEDOM.

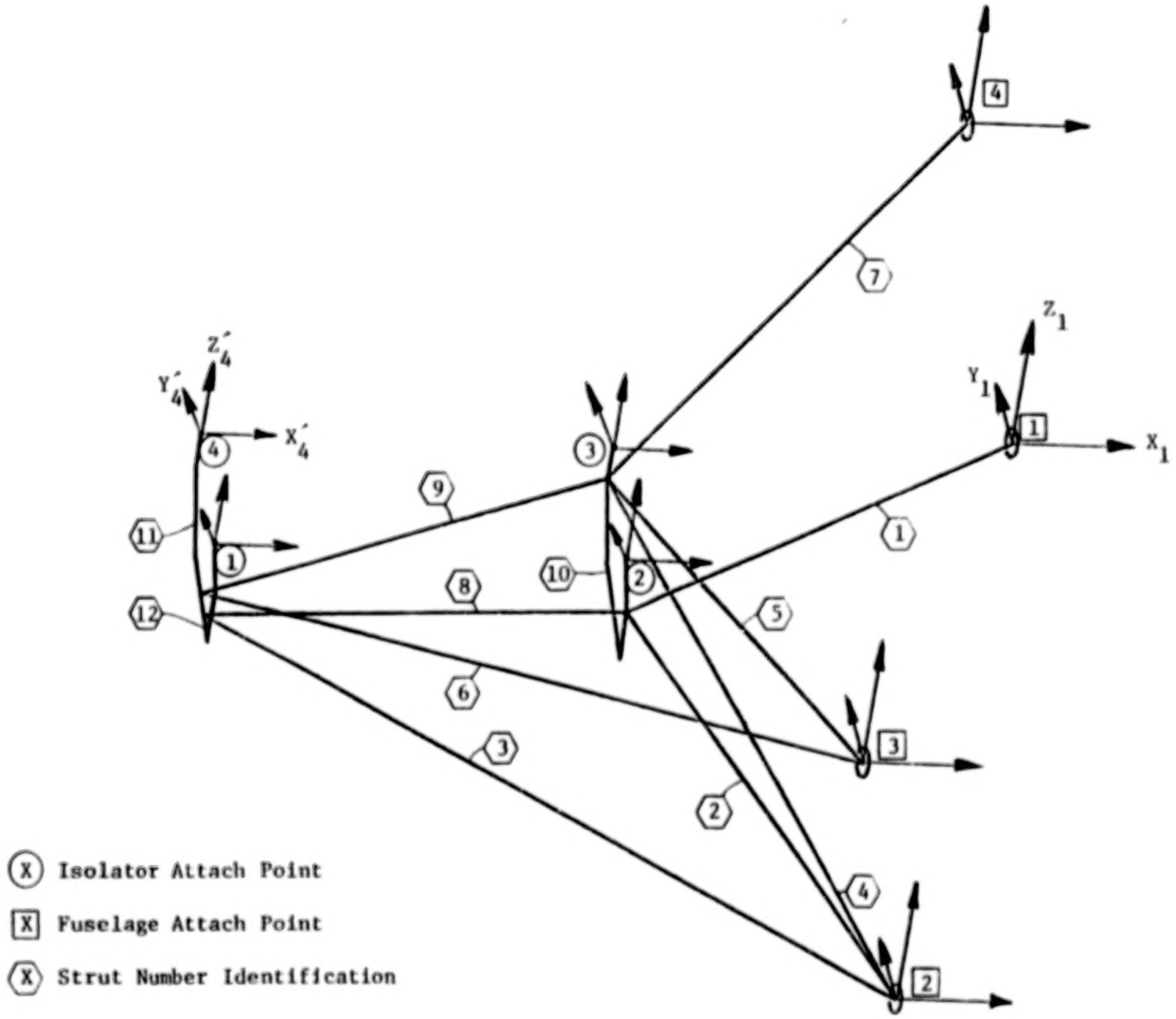

FIGURE 23. ENGINE MOUNT STRUCTURE WITH COUPLING DEGREES OF FREEDOM AND STRUT IDENTIFICATION.

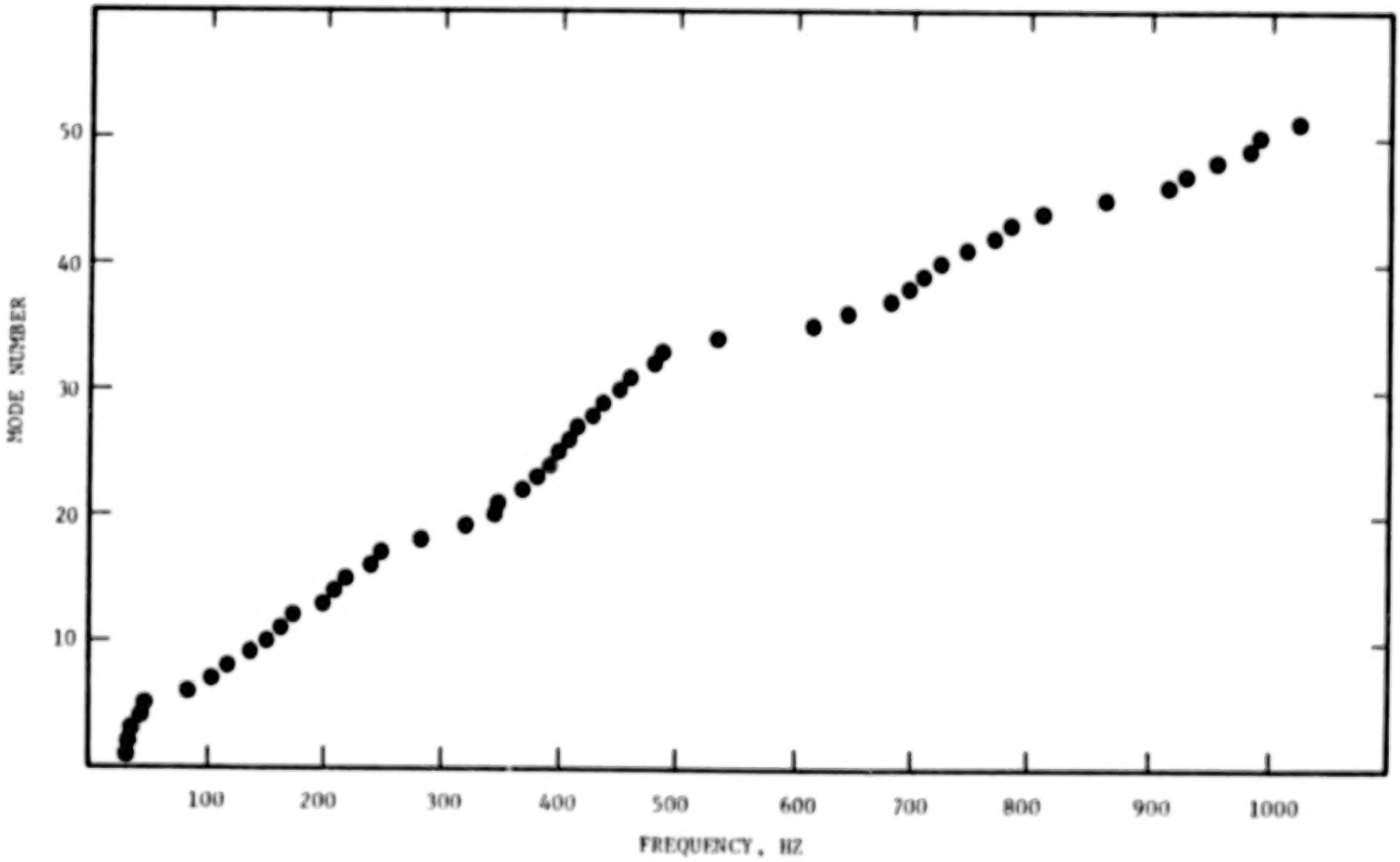

FIGURE 24. CESSNA MODEL 172 ENGINE MOUNT FREE-FREE NORMAL MODE FREQUENCIES.

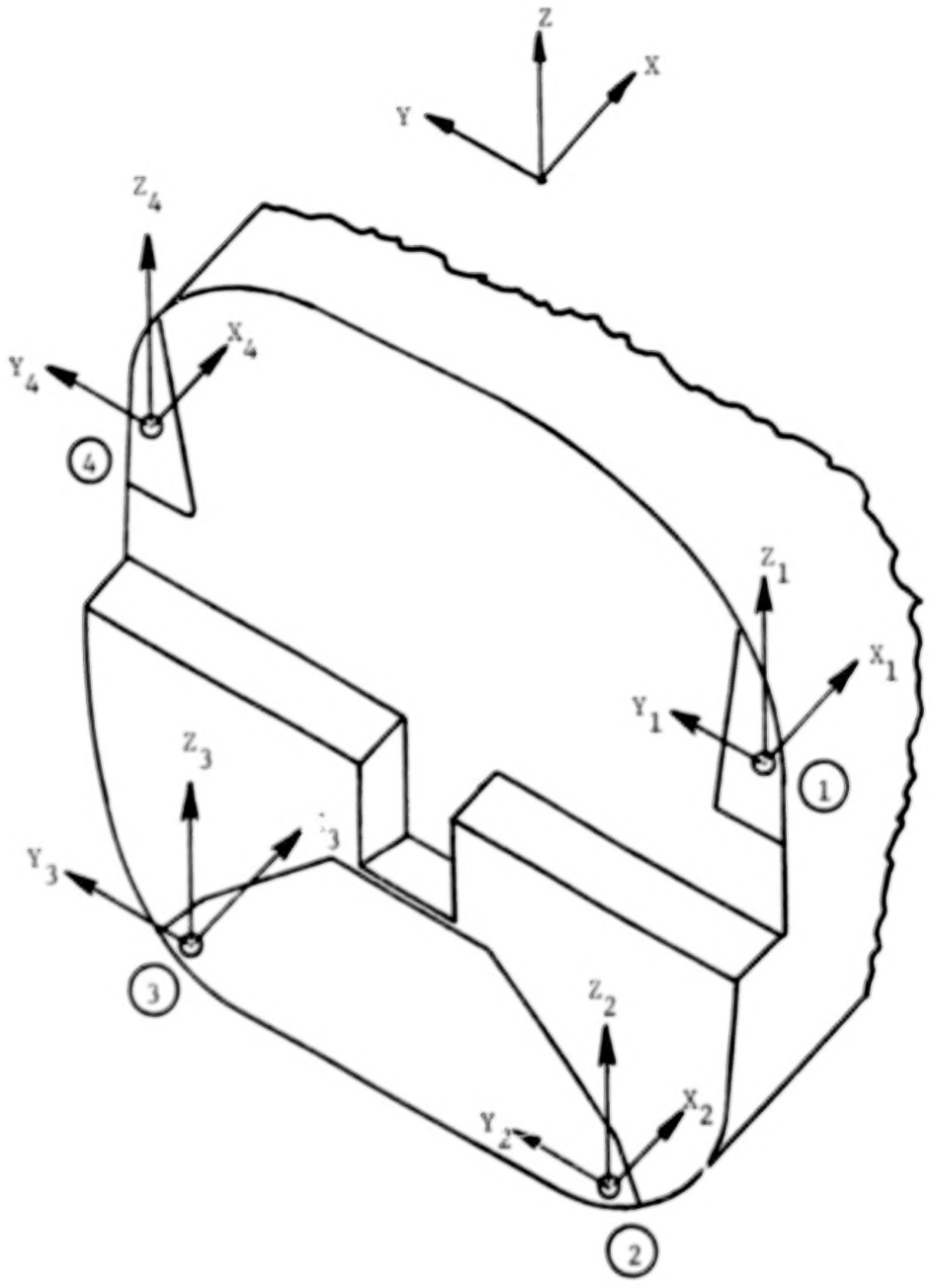

FIGURE 25. FIREWALL DEGREES OF FREEDOM NOTATION AT THE ENGINE ATTACH POINTS.

BLANK

PAGE

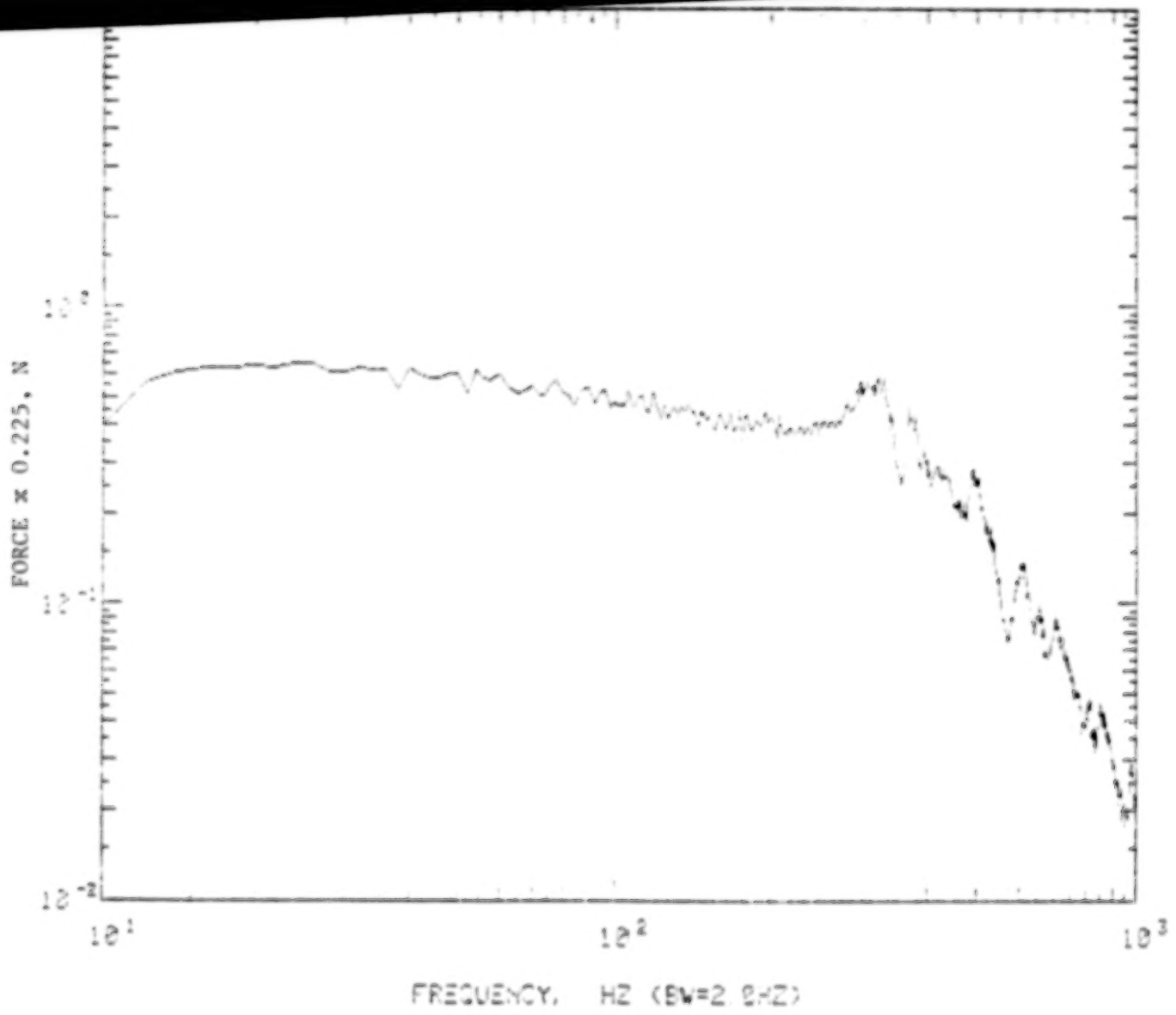

FIGURE 26. RANDOM NOISE INPUT FORCE SPECTRUM F_{X1}.

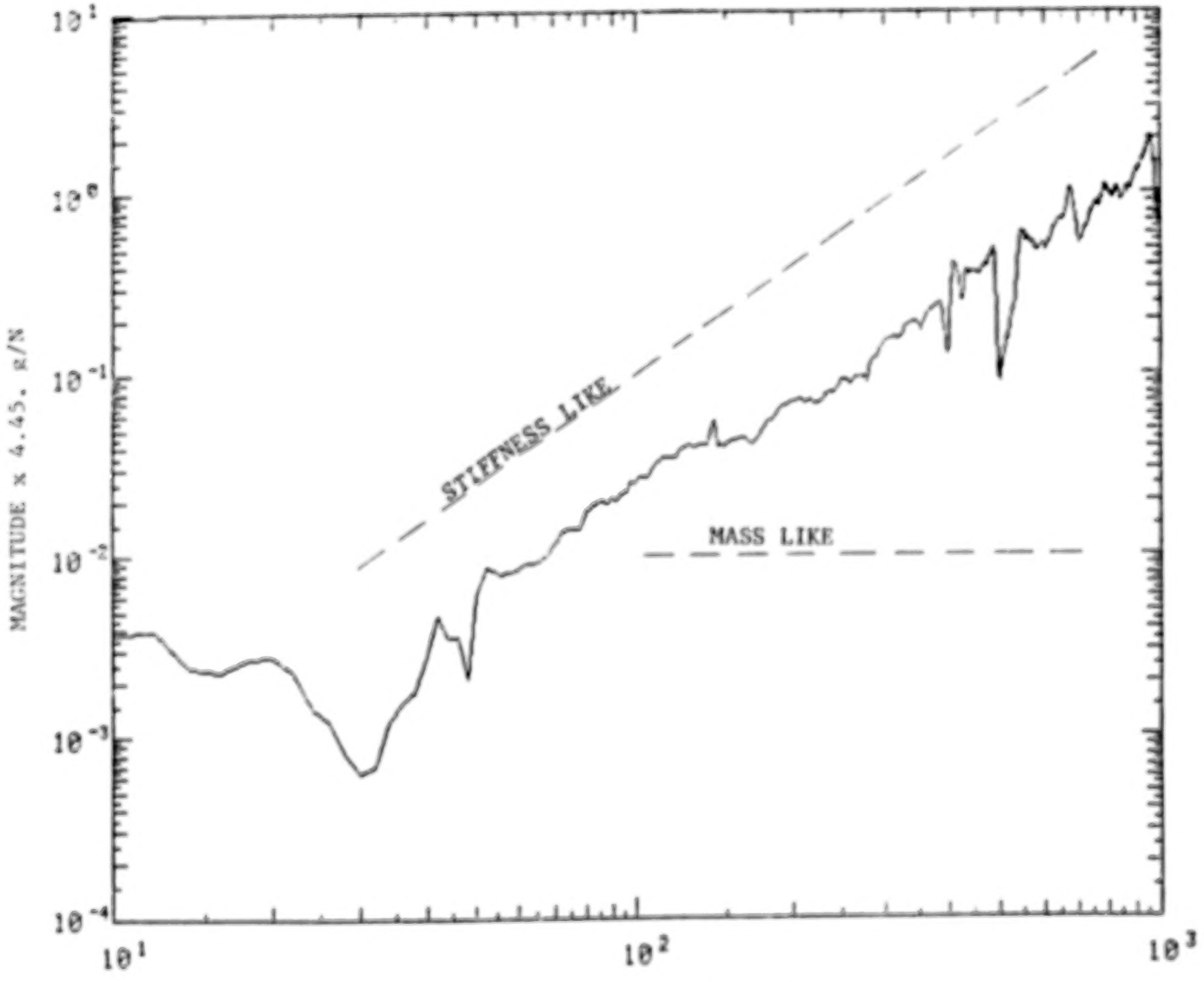

(a) Magnitude.

FIGURE 27. FUSELAGE DRIVING POINT INERTANCE AT X1.

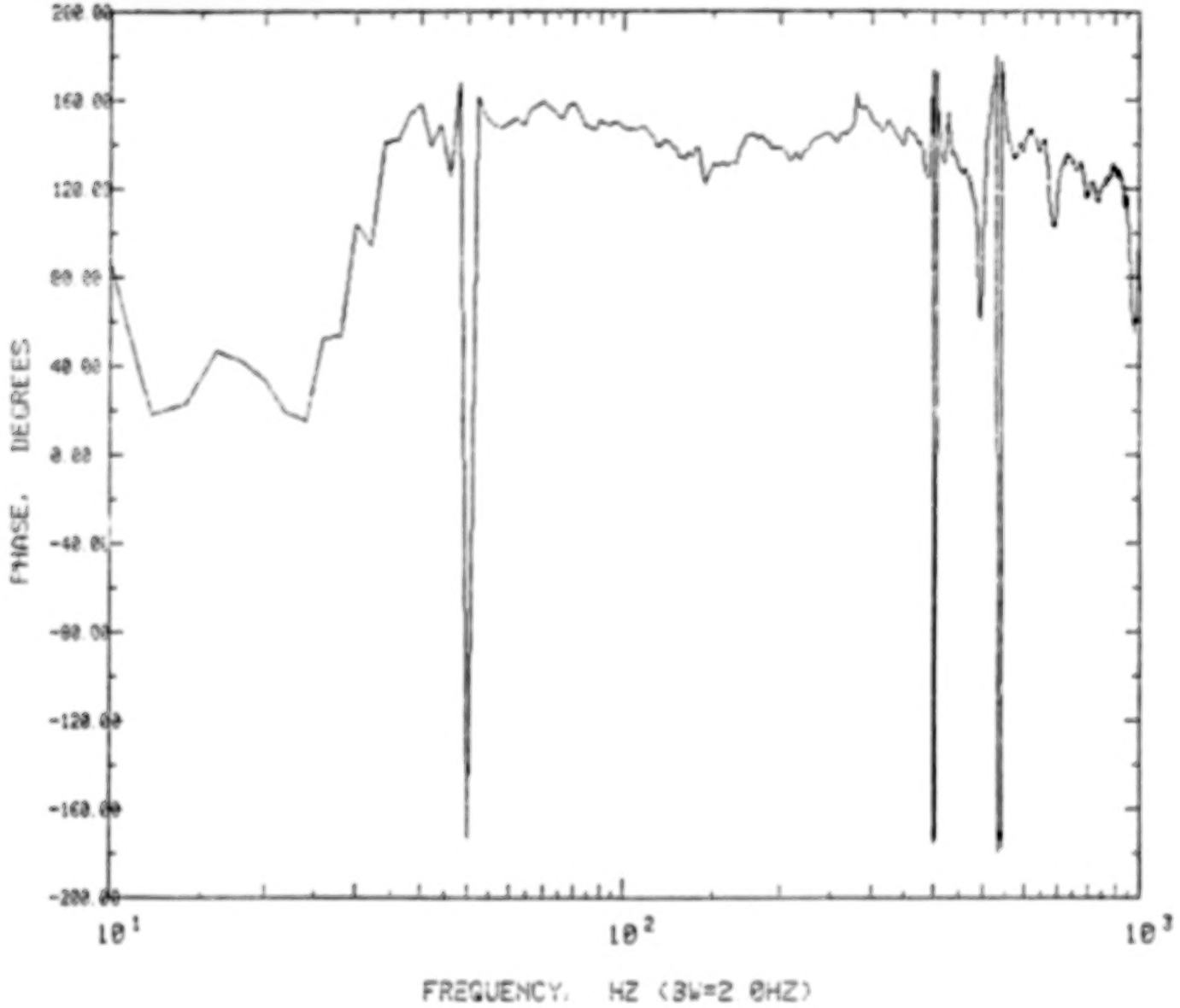

(b) Phase

FIGURE 27 (Concluded). FUSELAGE DRIVING POINT INERTANCE AT X1.

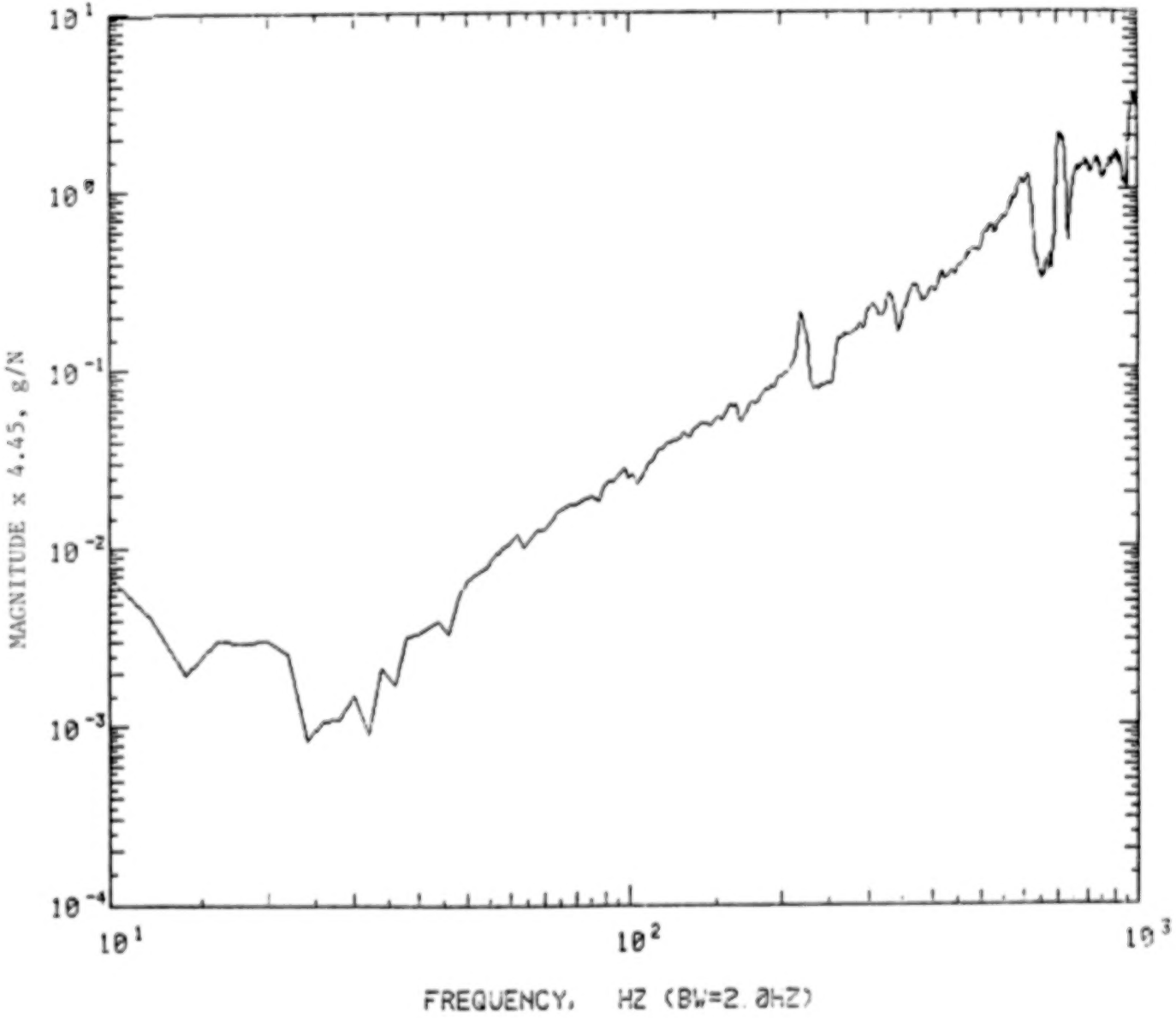

FIGURE 28. FUSELAGE DRIVING POINT INERTANCE AT X4.

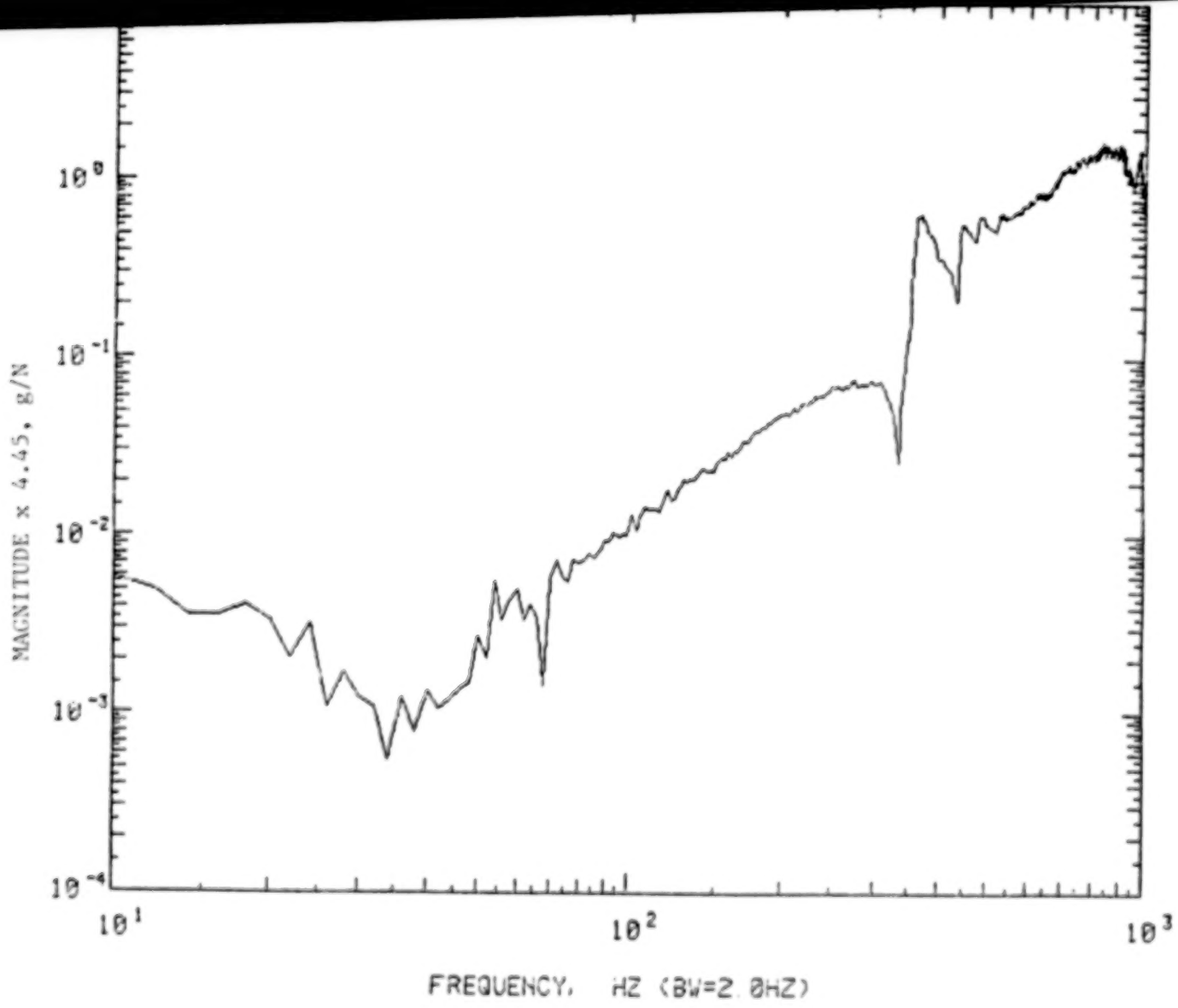

(a) Response X2.

FIGURE 29. DRIVING POINT INERTANCE - ENGINE MOUNT LOWER ATTACH POINTS.

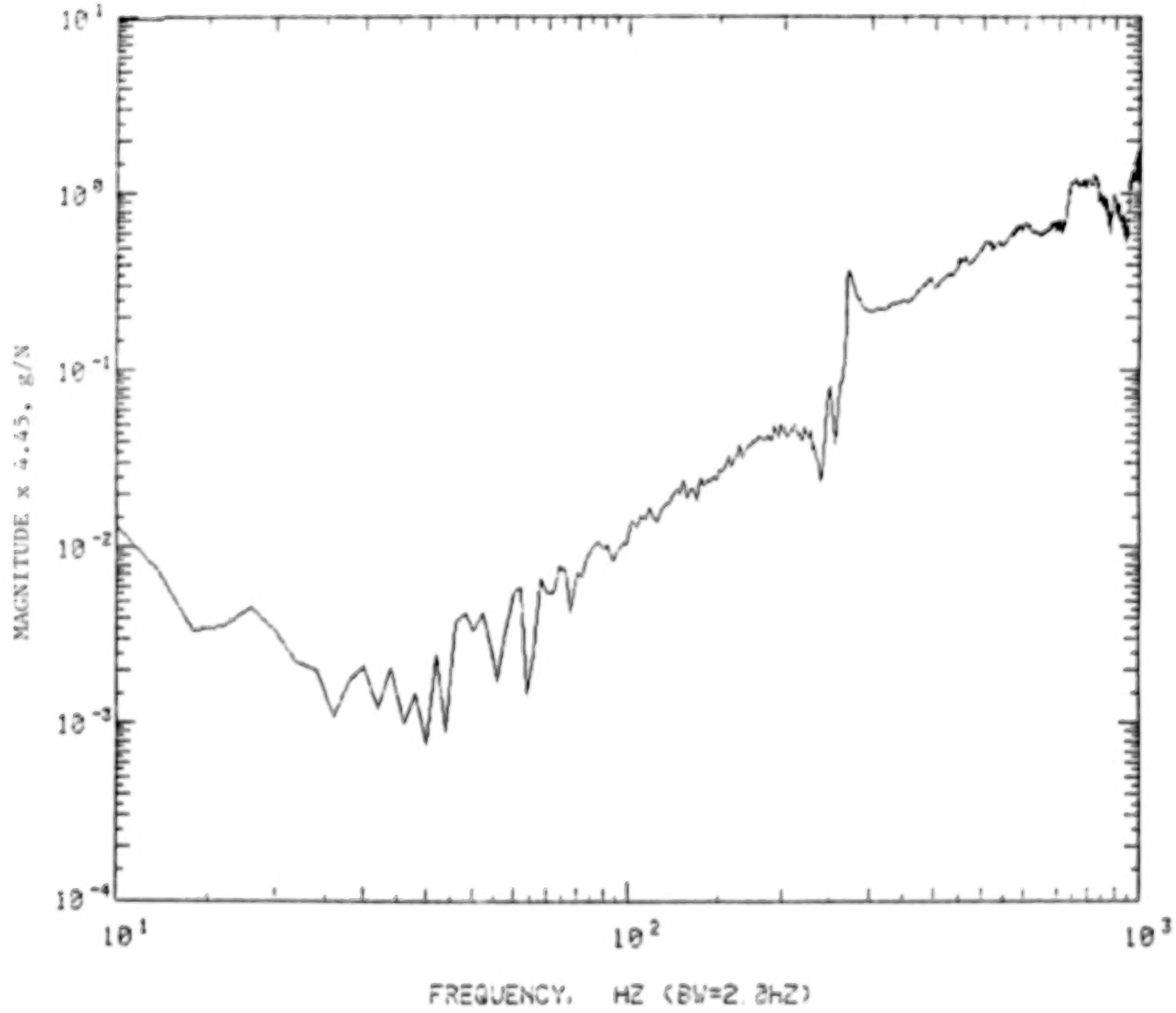

(b) Response X3.

FIGURE 29 (Concluded). DRIVING POINT INERTANCE - ENGINE MOUNT LOWER ATTACH POINTS.

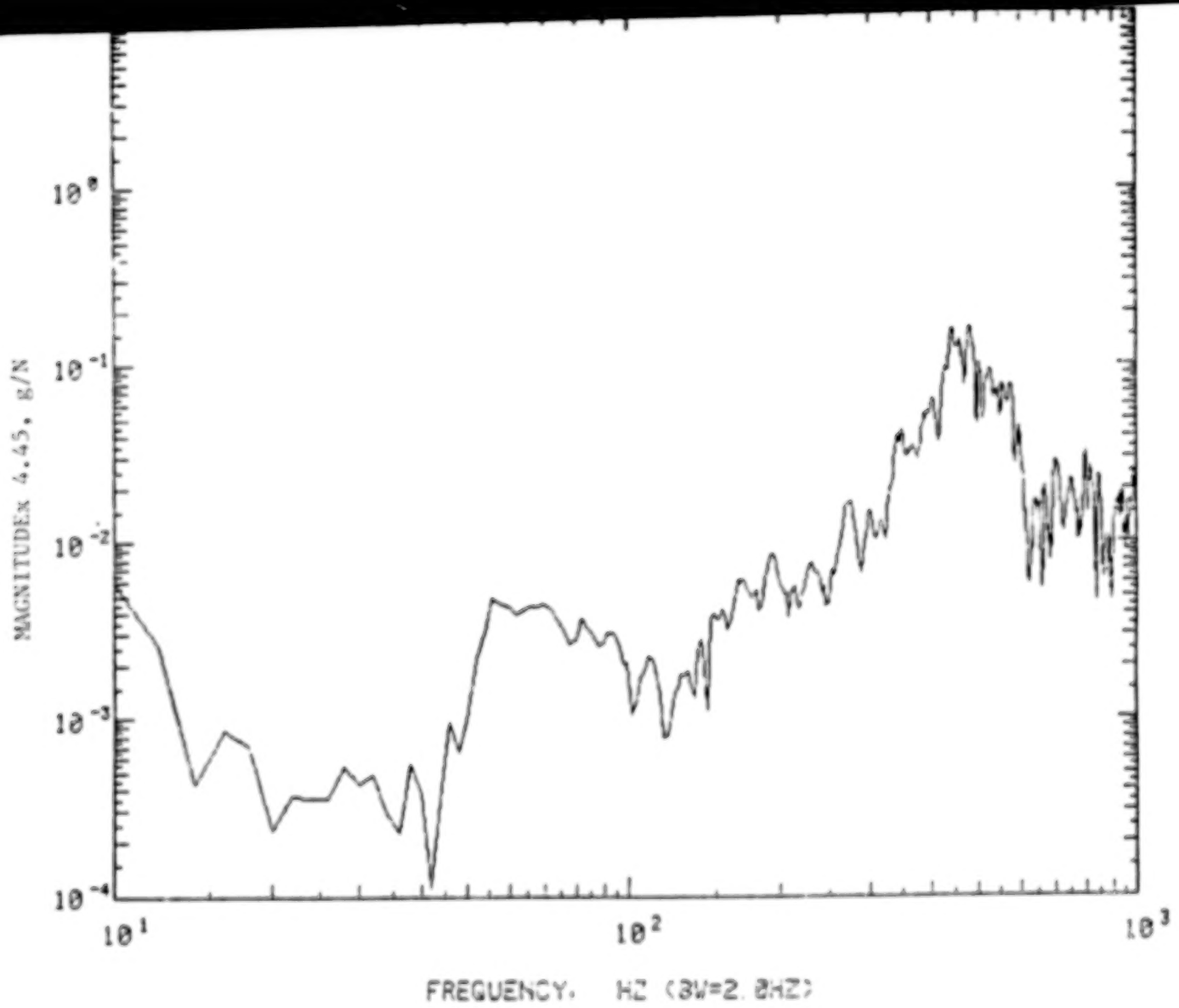

(a) Response Z4, Input X1.

FIGURE 30. FUSELAGE TRANSFER INERTANCE - COMPARISON FOR RECIPROCITY.

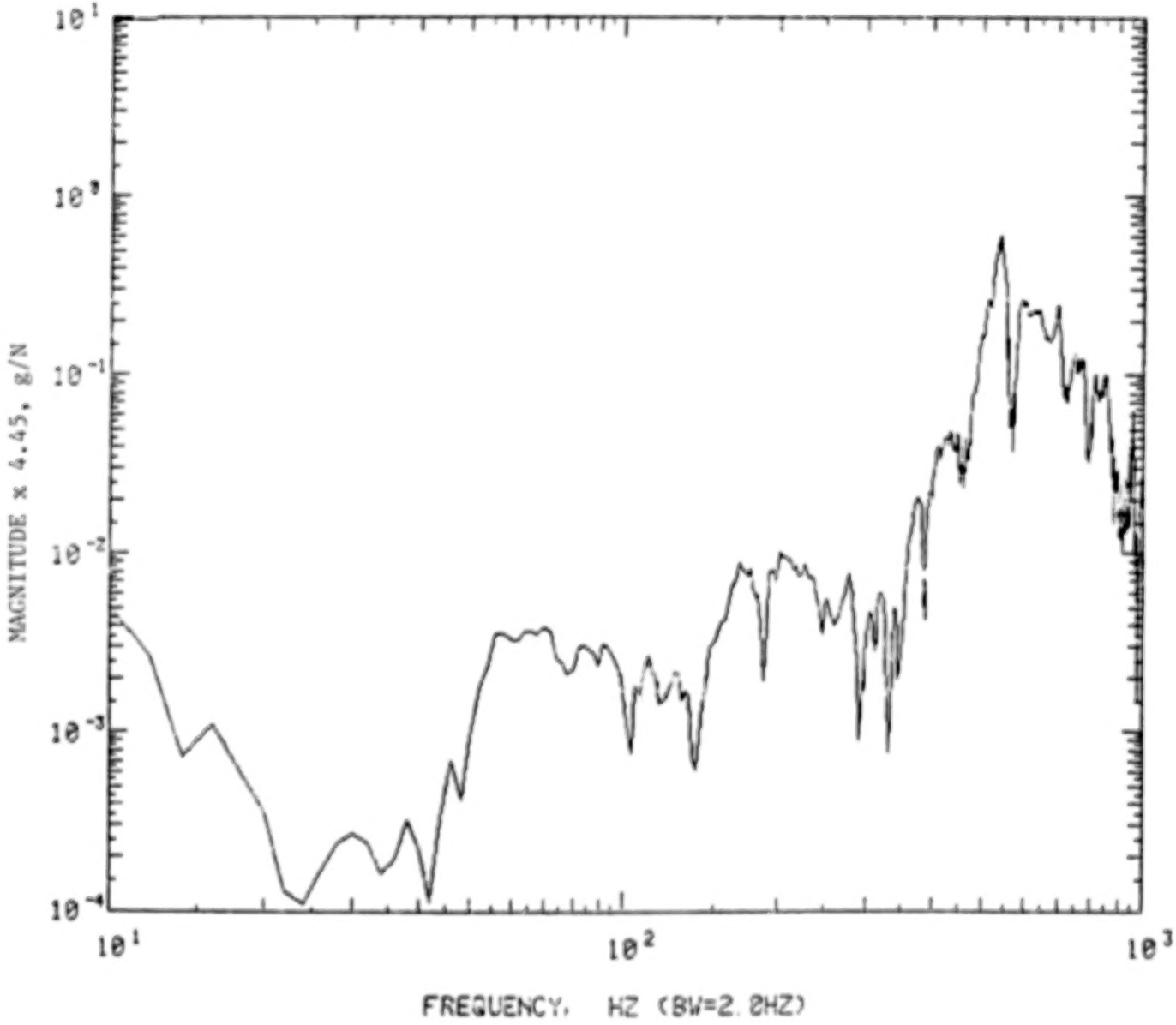

(b) Response X1, Input Z4.

FIGURE 30 (Concluded). FUSELAGE TRANSFER INERTANCE - COMPARISON FOR RECIPROCITY.

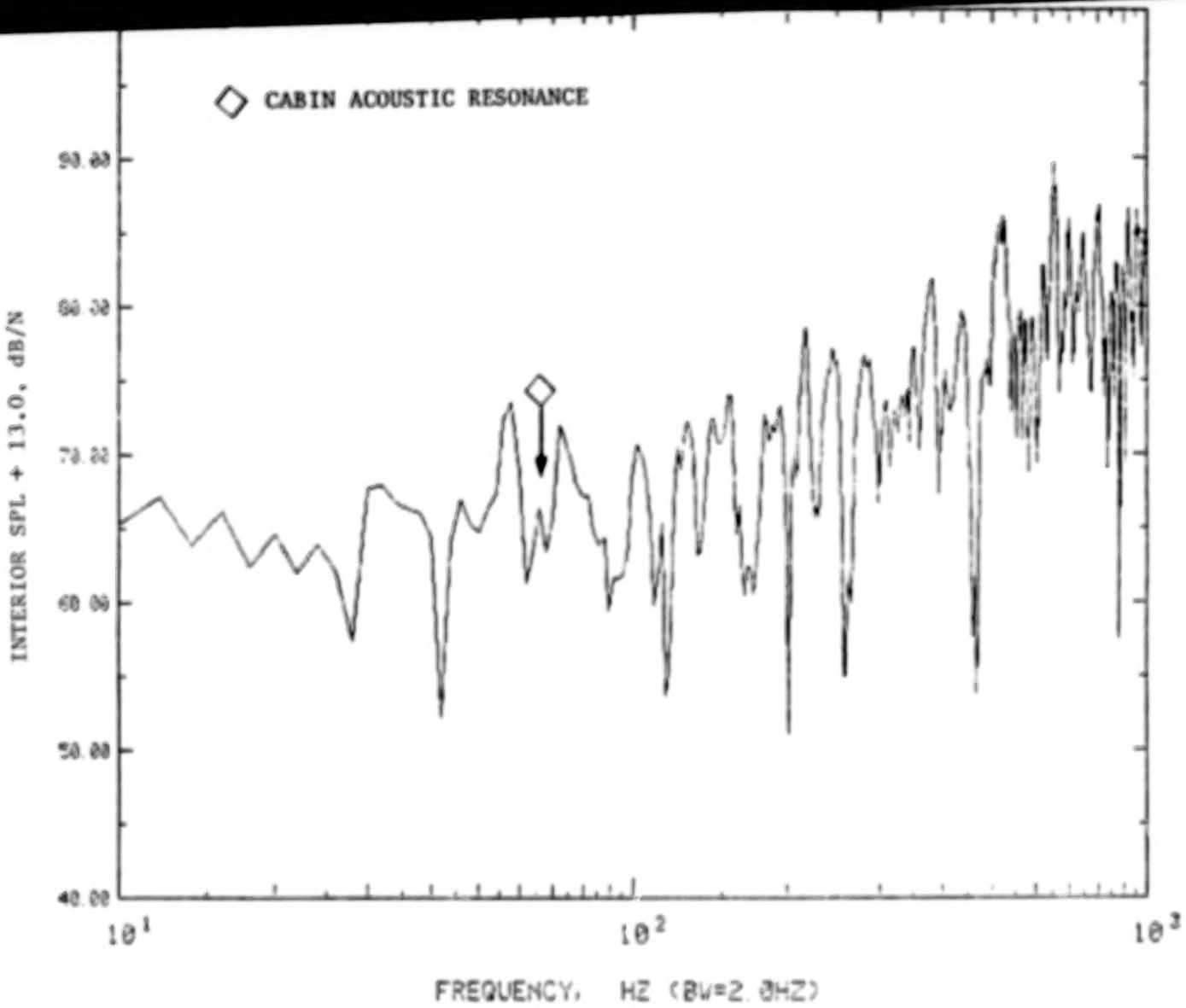

(a) Response P1

FIGURE 31. FUSELAGE SOUND PRESSURE LEVEL TRANSFER FUNCTION, INPUT AT X1.

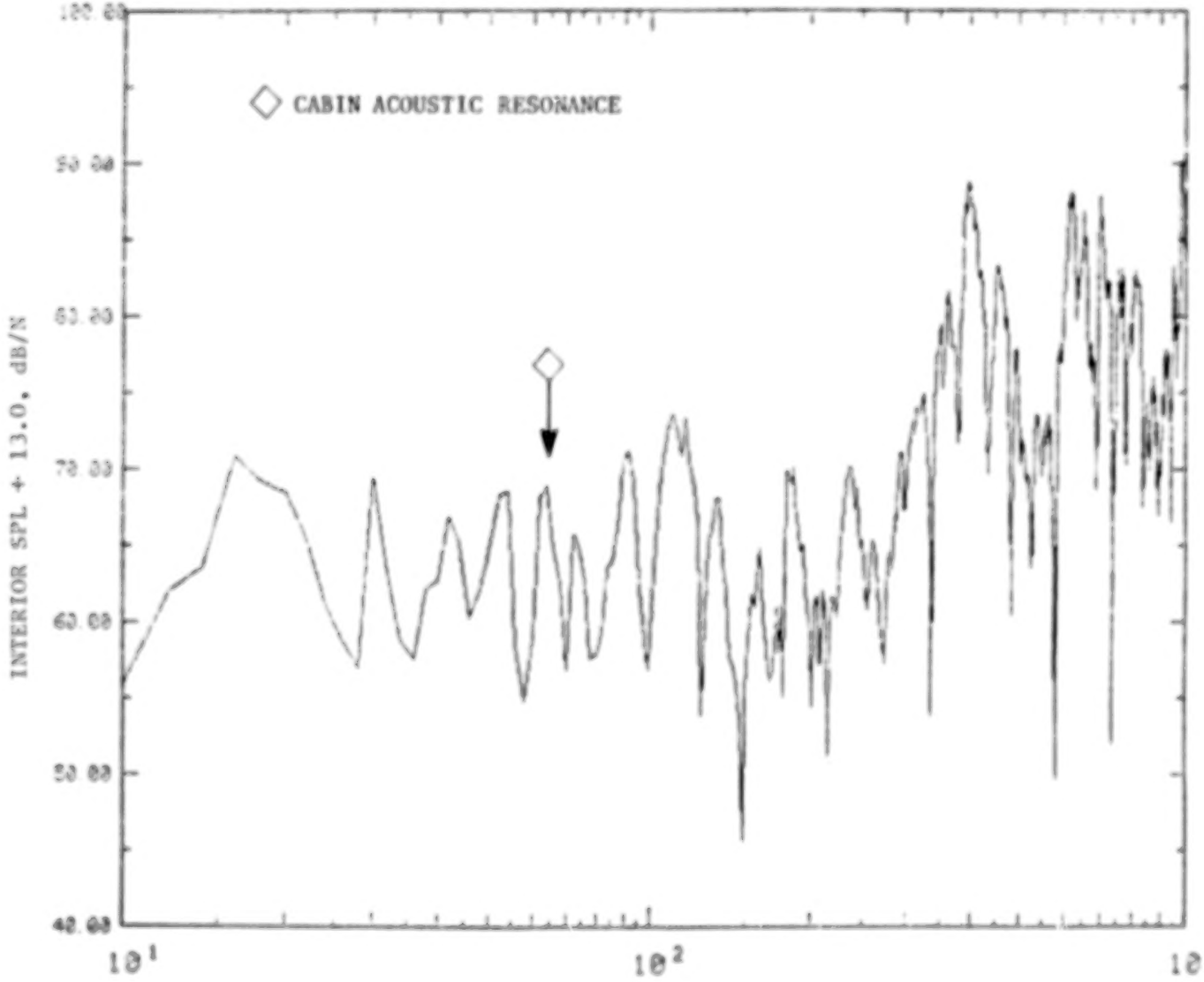

(b) Response P3.

FIGURE 31 (Concluded). FUSELAGE SOUND PRESSURE LEVEL TRANSFER FUNCTION, INPUT AT X1.

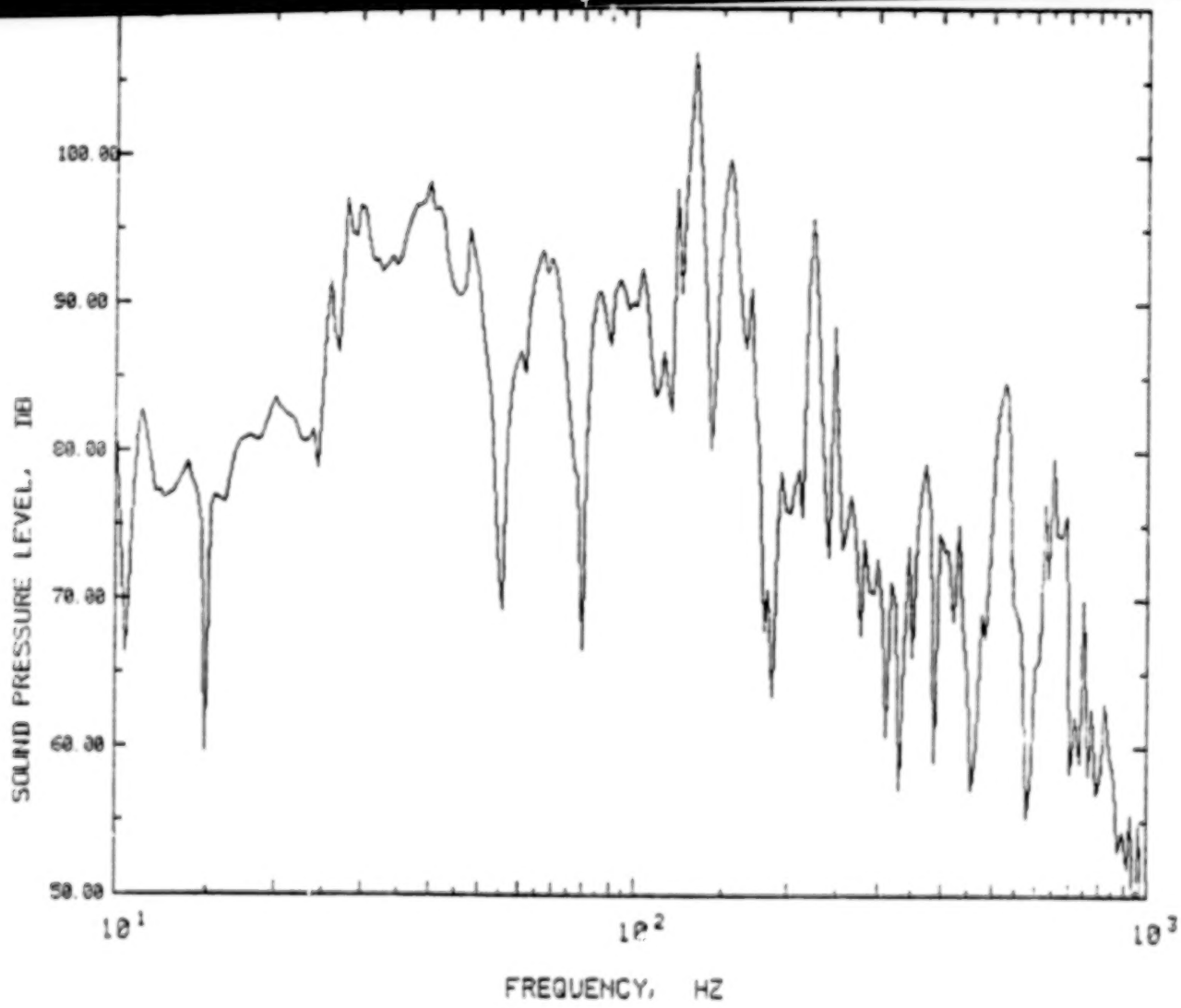

(a) Response P1.

FIGURE 32. PREDICTED TRANSFER FUNCTION SPECTRA, LOAD CASE #2, ISOLATOR CONFIGURATION R1, REF. 89 N RMS.

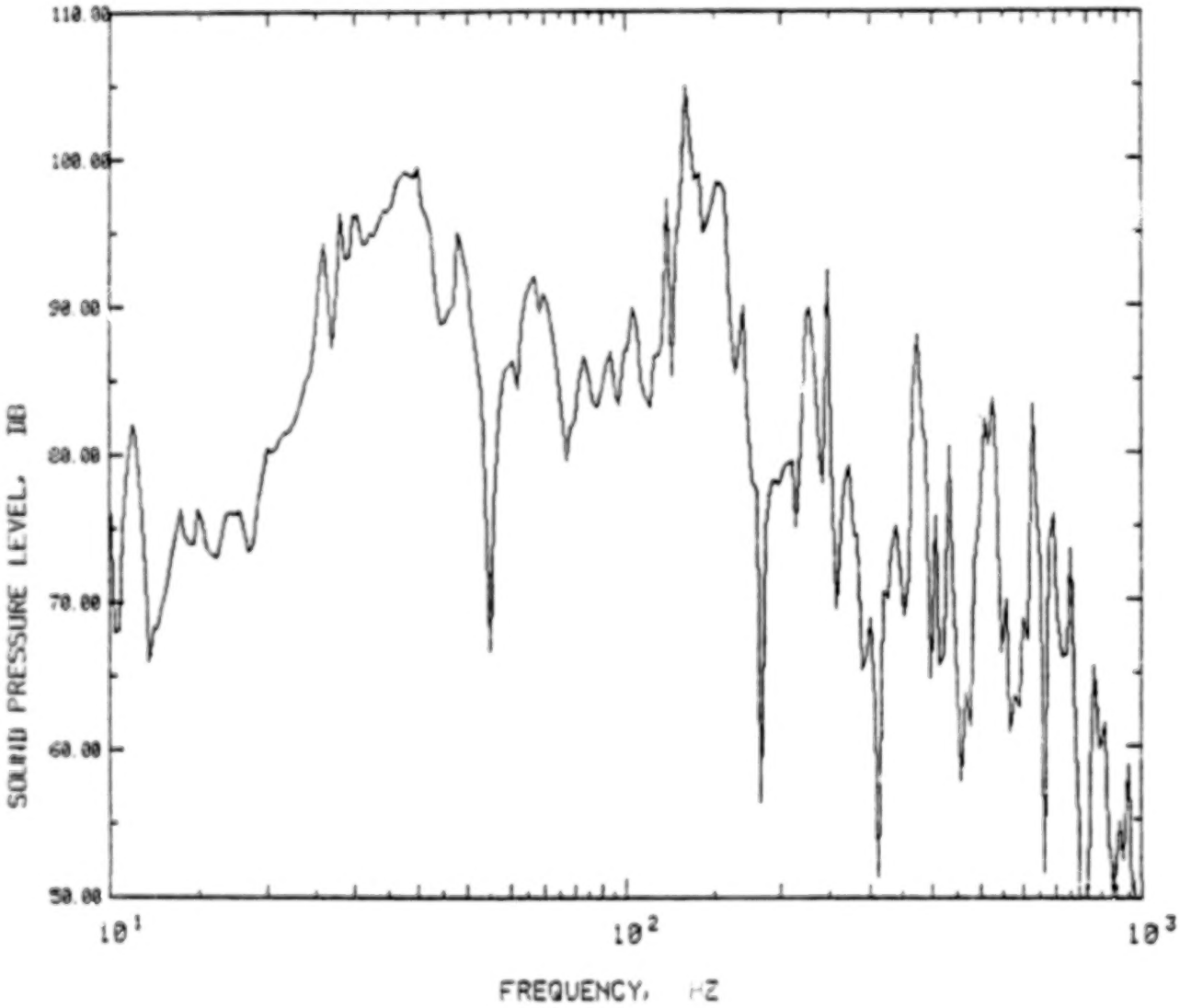

(b) Response P2.

FIGURE 32 (Continued). PREDICTED TRANSFER FUNCTION SPECTRA, LOAD CASE #2, ISOLATOR CONFIGURATION R1, REF. 89 N RMS.

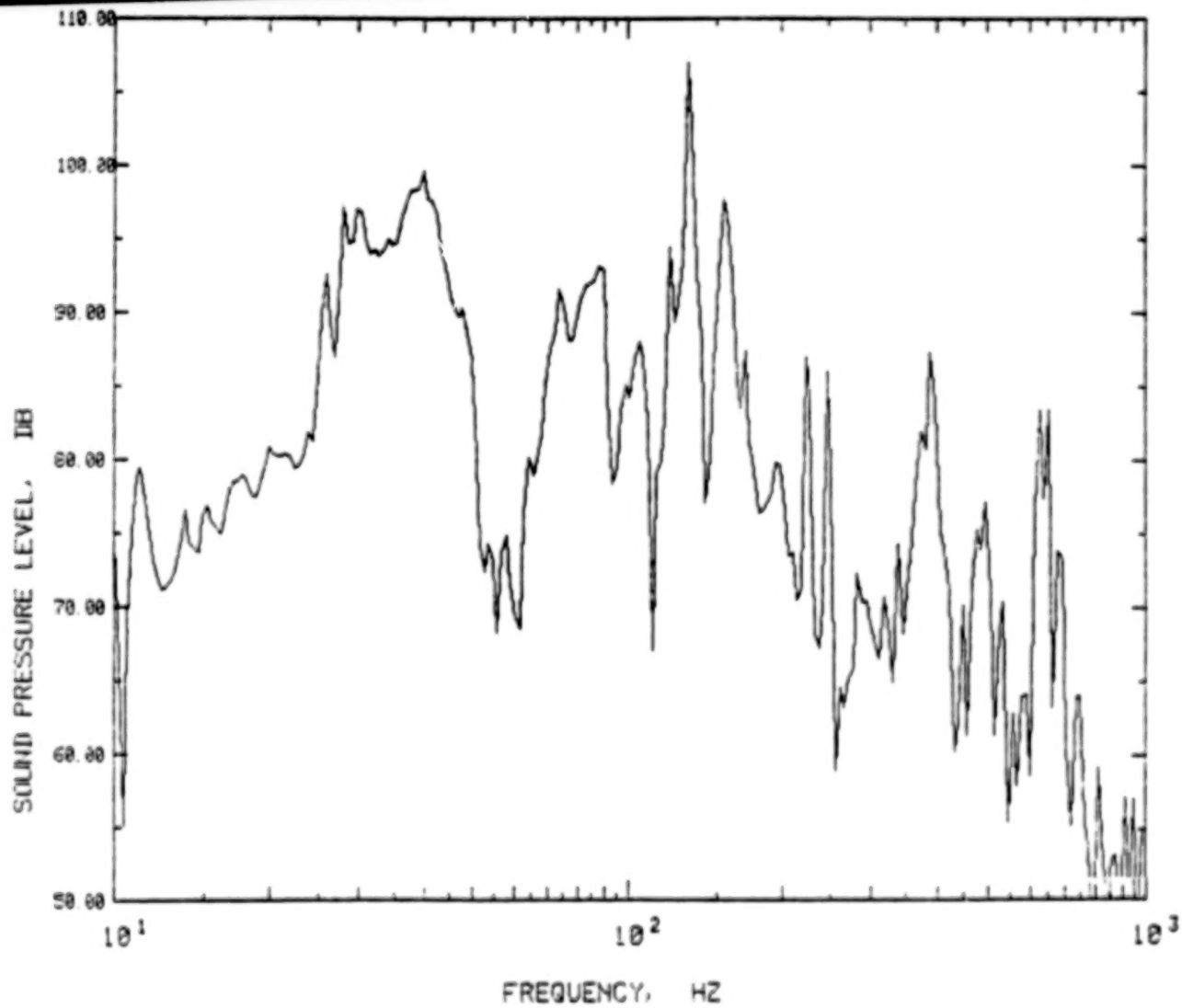

(c) Response P3.

FIGURE 32 (Continued). PREDICTED TRANSFER FUNCTION SPECTRA, LOAD CASE #2, ISOLATOR CONFIGURATION R1, REF. 89 N RMS.

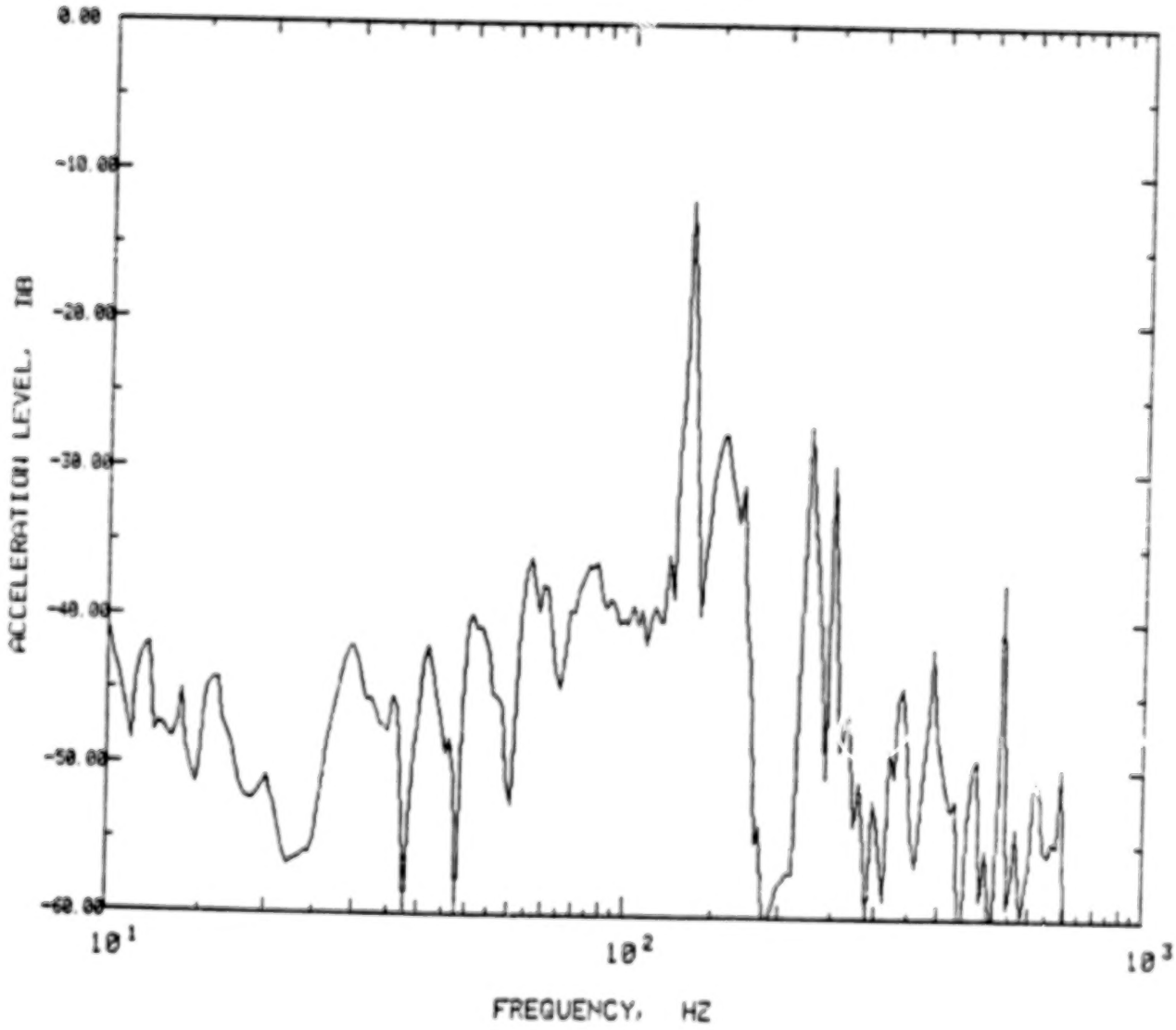

(d) Response AX.

FIGURE 32 (Continued). PREDICTED TRANSFER FUNCTION SPECTRA, LOAD CASE #2, ISOLATOR CONFIGURATION R1, REF. 89 N RMS.

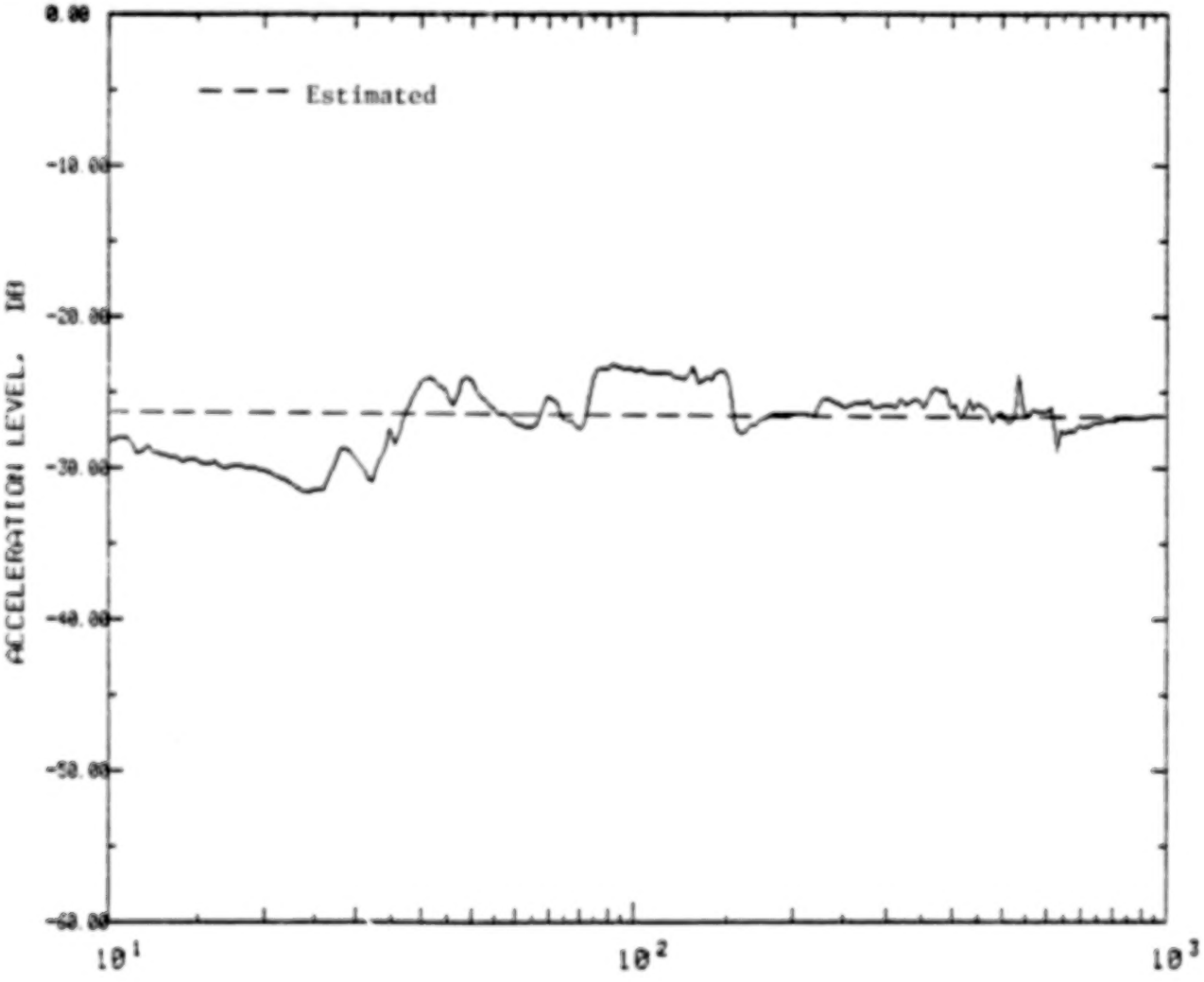

(c) Response AY.

FIGURE 32 (Continued). PREDICTED TRANSFER FUNCTION SPECTRA, LOAD CASE #2, ISOLATOR CONFIGURATION R1, REF. 89 N RMS.

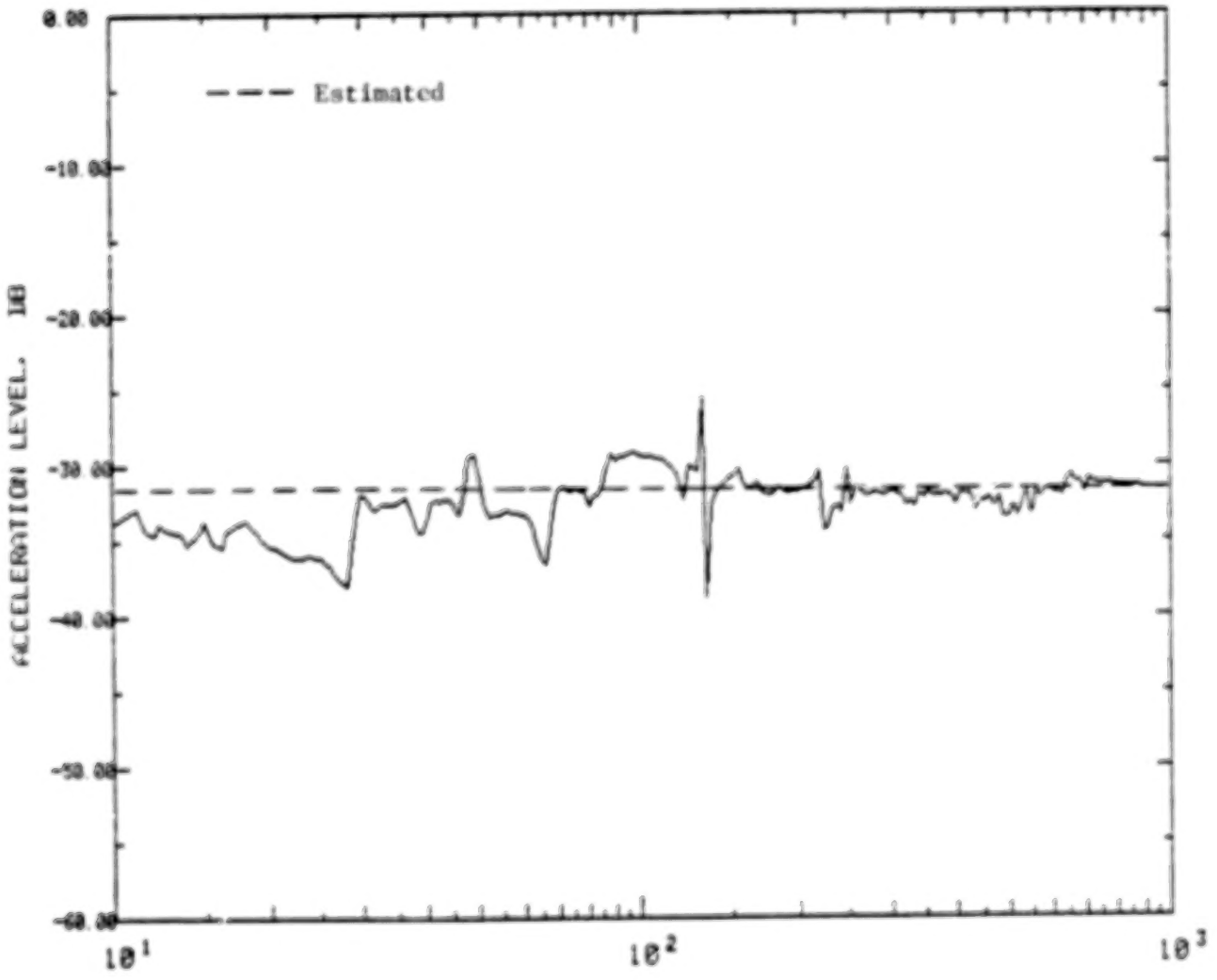

(f) Response AZ.

FIGURE 32 (Concluded). PREDICTED TRANSFER FUNCTION SPECTRA, LOAD CASE #2, ISOLATOR CONFIGURATION R1, REF. 89 N RMS.

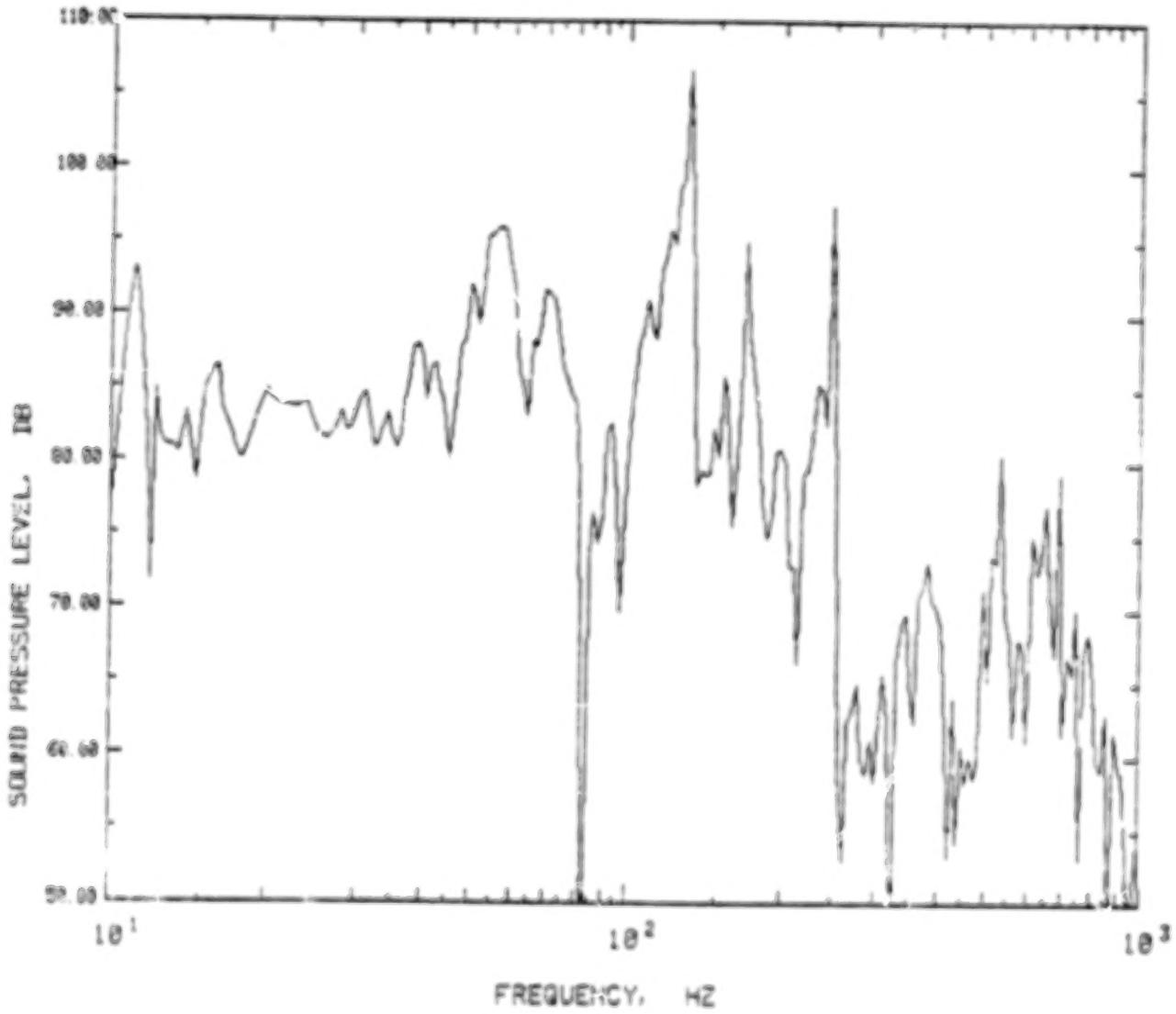

(a) Response P1.

FIGURE 33. PREDICTED TRANSFER FUNCTION SPECTRA, LOAD CASE #3, ISOLATOR CONFIGURATION R1, REF. 89 N RMS.

TABLE OF CONTENTS

List of Figures		vii	1/A11
List of Tables		x	1/A14
Nomenclature		xi	1/B1
I.	INTRODUCTION	1	1/B4
II.	TEST FACILITY, INSTRUMENTATION, AND PROCEDURES	3	1/B6
A.	Test Facility Description	3	1/B7
B.	Test Configurations	4	
C.	Instrumentation	5	1/B8
D.	Data Acquisition and Reduction	5	1/B9
E.	Facility Calibration	6	
III.	STRUCTURE-BORNE NOISE TRANSFER FUNCTIONS TESTS	8	1/B11
A.	Narrow Band Data	8	
B.	Peak One-Third Octave Data	11	1/B14
C.	Isolator Relative Performance	11	1/C1
D.	System Linearity	12	
E.	Engine Mount Damping Effectiveness	13	1/C2
F.	Fuselage Tail Cone Isolation	13	
IV.	ANALYTICAL MODEL	15	1/C4
A.	Model Concept	15	
B.	Component Representation	15	
1.	Engine As a Rigid Body	15	
2.	Vibration Isolators	17	1/C6
3.	Engine Mount Structure	20	1/C9
4.	Aircraft Fuselage and Interior Response	22	1/C11
C.	Component Coupling Procedures	25	1/C14
D.	Coupled Model Normal Mode Response	30	1/D5

TABLE OF CONTENTS (CONTINUED)

V.	COMPARISON OF ANALYTICAL AND EXPERIMENTAL RESULTS	34	1/D9
	A. Narrow Band Spectra	34	
	B. One-Third Octave Spectra	35	1/D10
VI.	MODEL PARAMETER SENSITIVITY STUDY	36	1/D11
	A. Engine Mount Parameters	36	
	B. Isolator Properties	37	1/D12
VII.	CONCLUSIONS AND RECOMMENDATIONS	39	1/D14
REFERENCES	. . . . .	41	1/E2

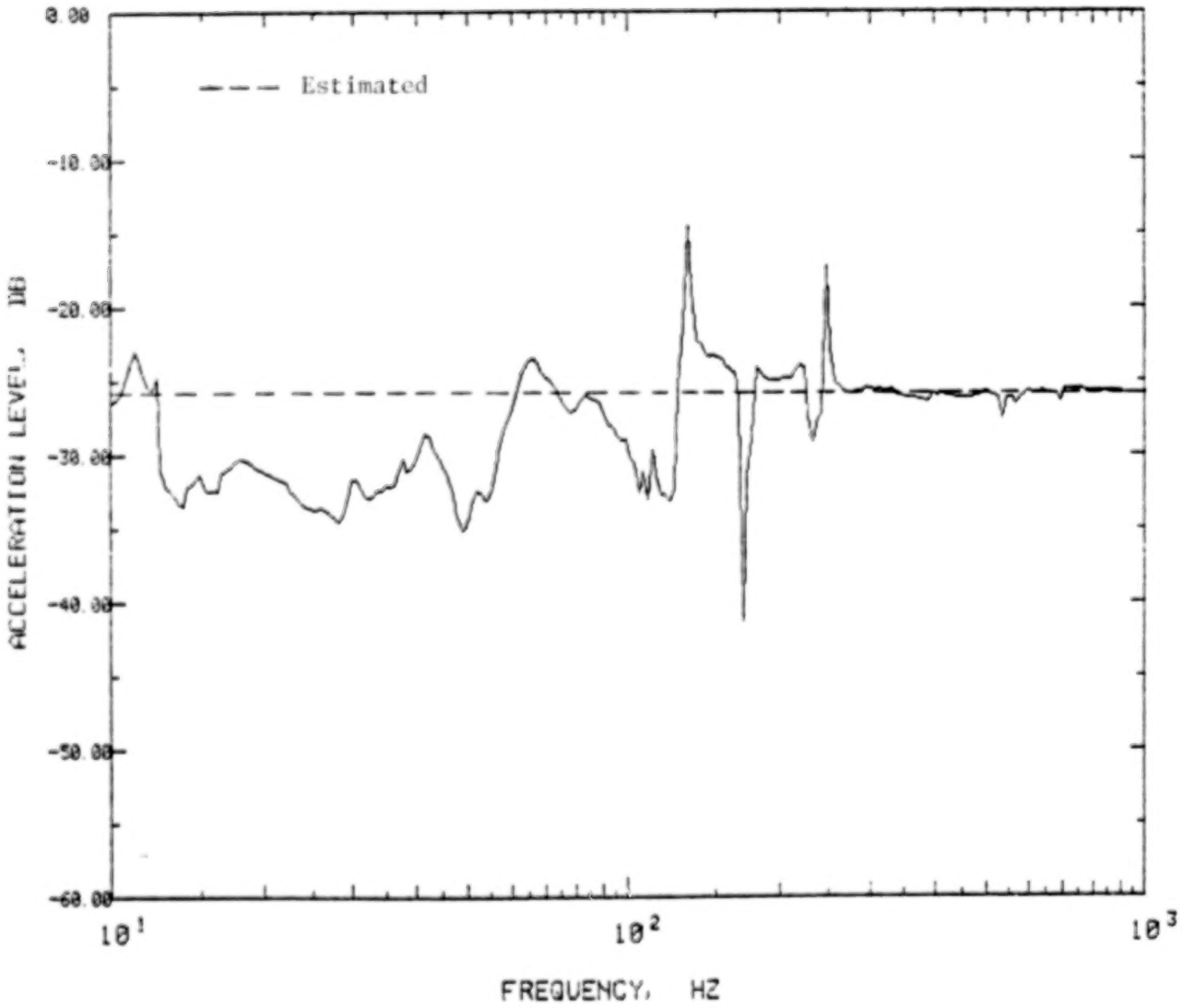

(b) Response AX.

FIGURE 33 (Continued). PREDICTED TRANSFER FUNCTION SPECTRA, LOAD CASE #3, ISOLATOR CONFIGURATION R1, REF. 89 N RMS.

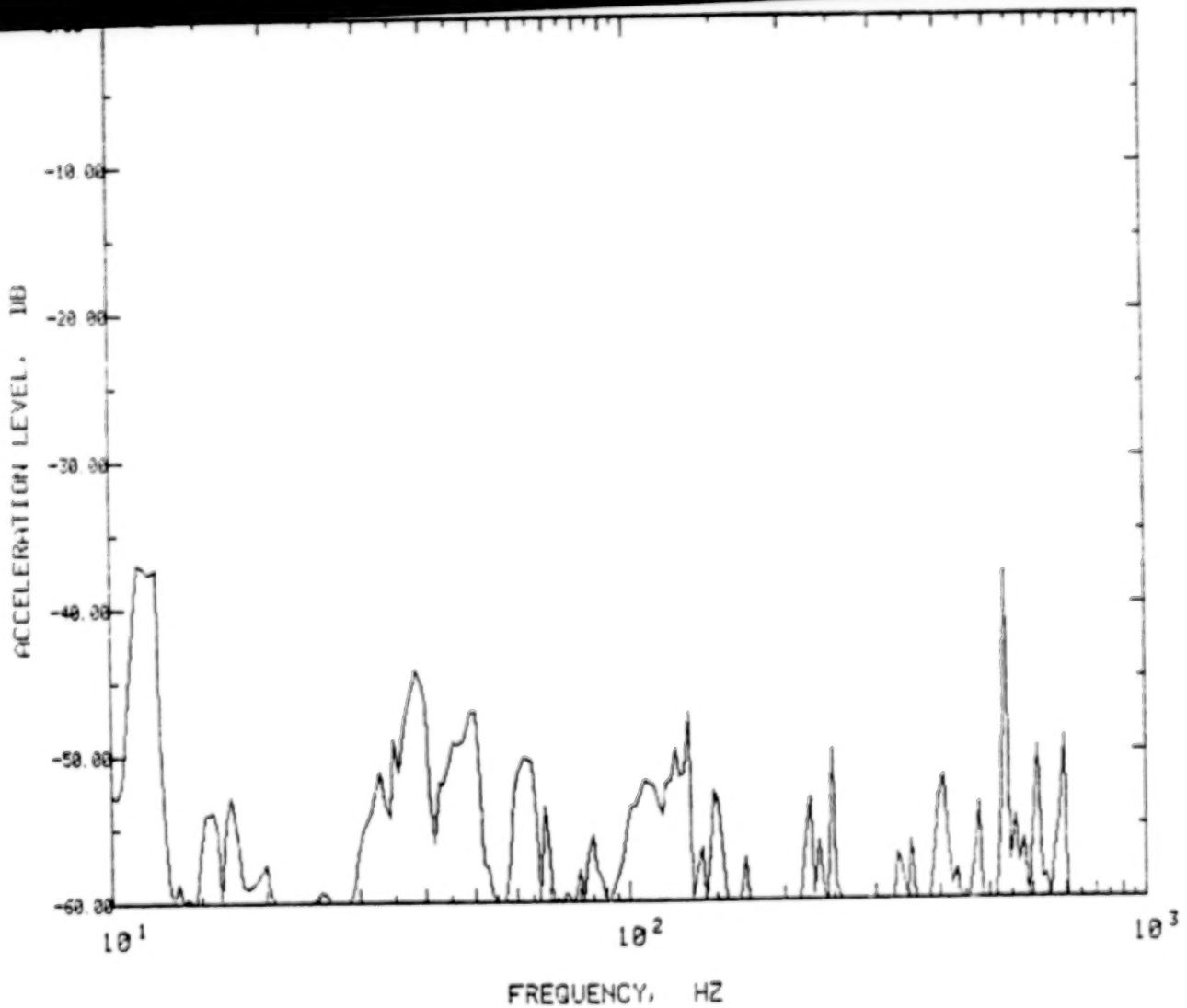

(c) Response AY.

FIGURE 33 (Continued). PREDICTED TRANSFER FUNCTION SPECTRA, LOAD CASE #3, ISOLATOR CONFIGURATION R1, REF. 89 N RMS.

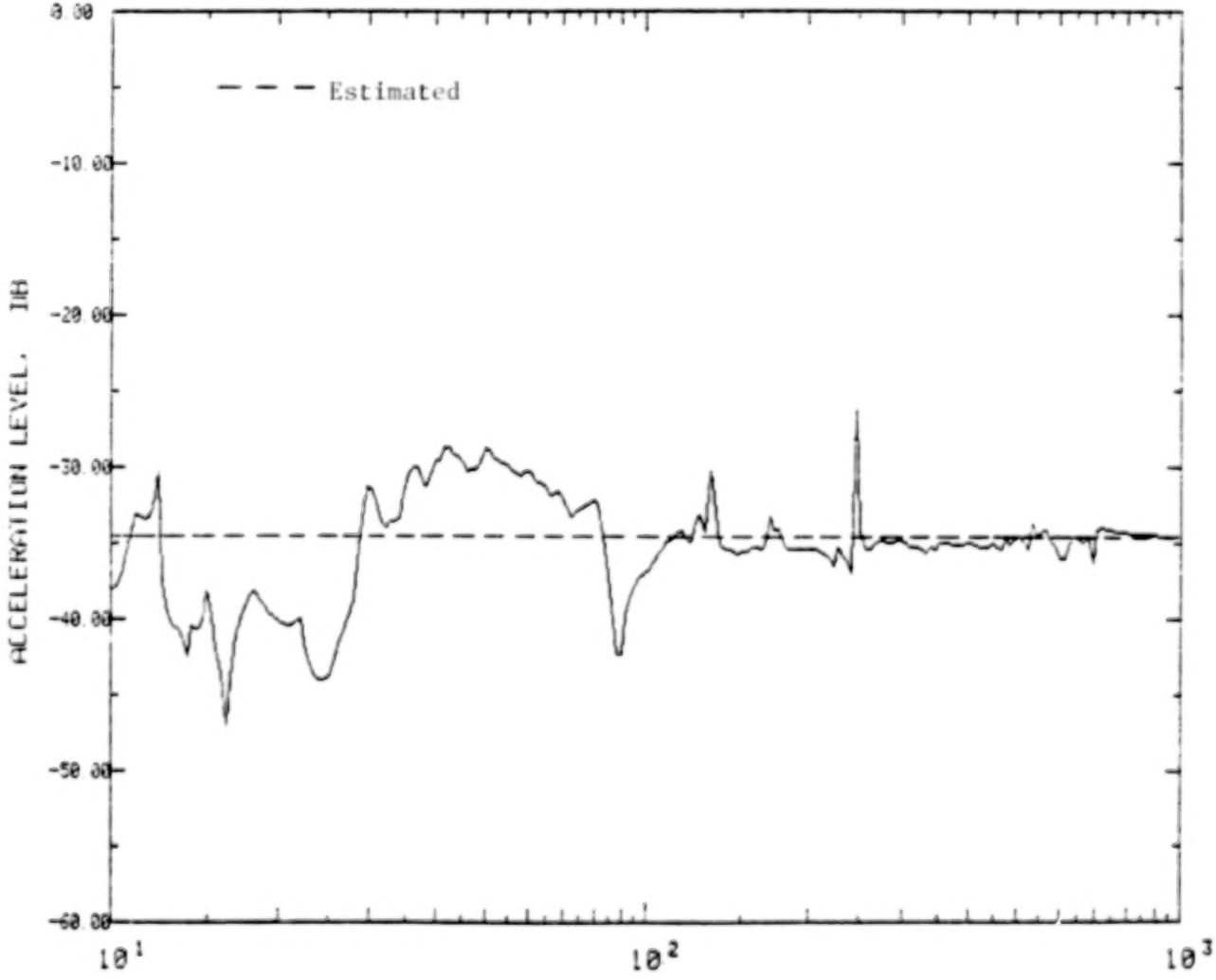

(d) Response AZ.

FIGURE 33 (Concluded). PREDICTED TRANSFER FUNCTION SPECTRA, LOAD CASE #3, ISOLATOR CONFIGURATION R1, REF. 89 N RMS.

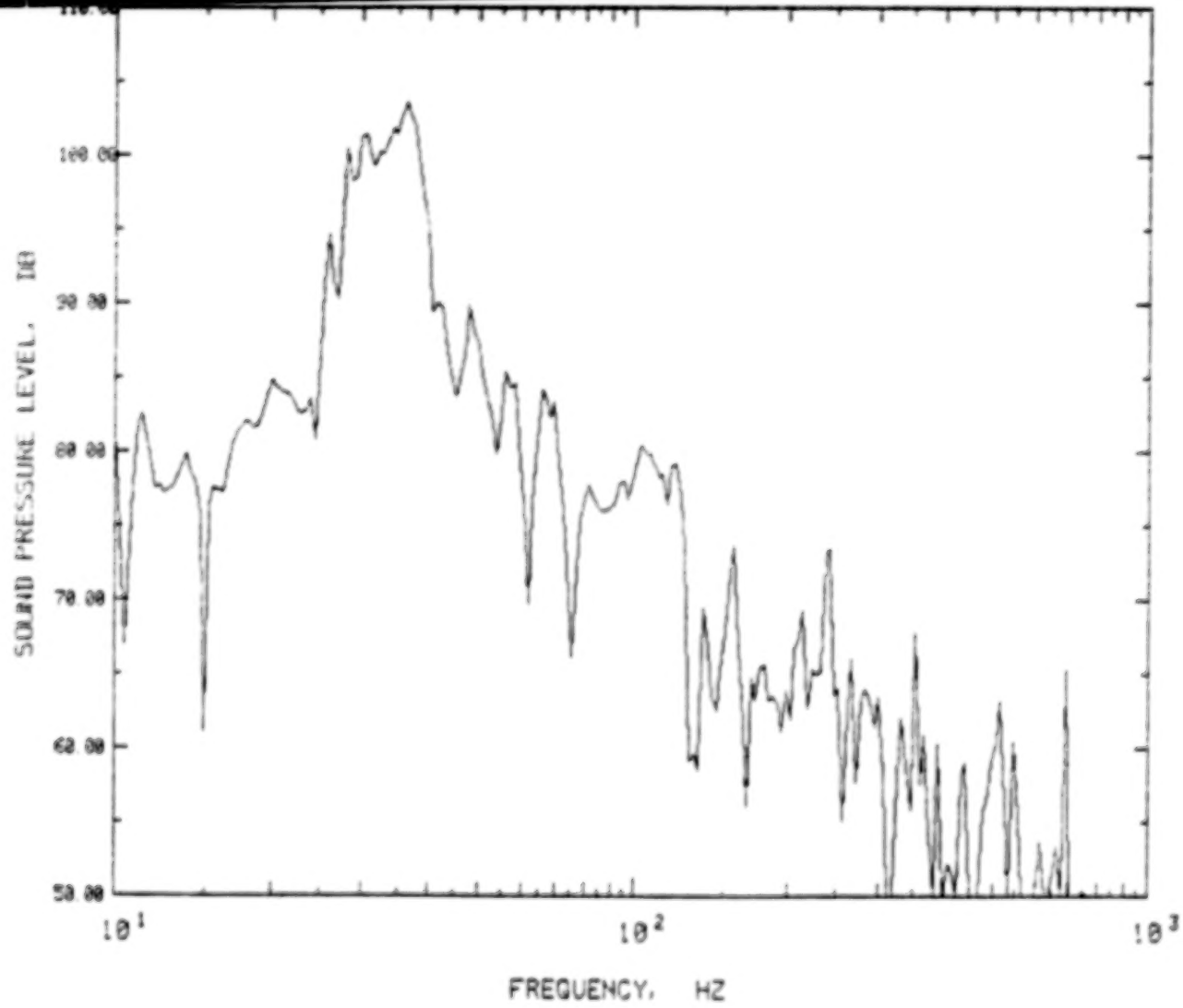

(a) Response P1.

FIGURE 34. PREDICTED TRANSFER FUNCTION SPECTRA, LOAD CASE #2, ISOLATOR CONFIGURATION OA, REF. 89 N RMS.

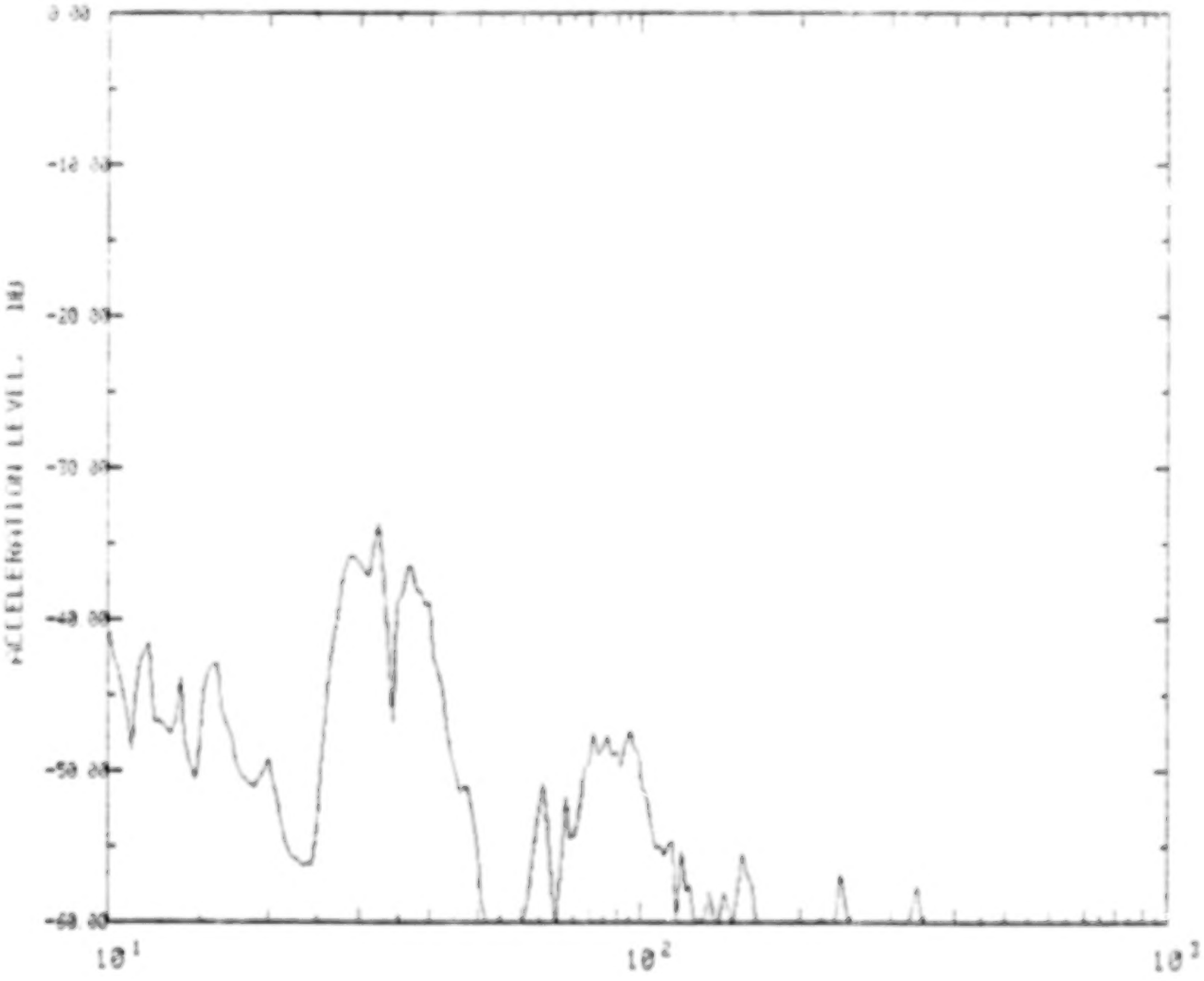

(b) Response AX.

FIGURE 34 (Continued). PREDICTED TRANSFER FUNCTION SPECTRA, LOAD CASE #2, ISOLATOR CONFIGURATION 0A, REF. 89 N RMS.

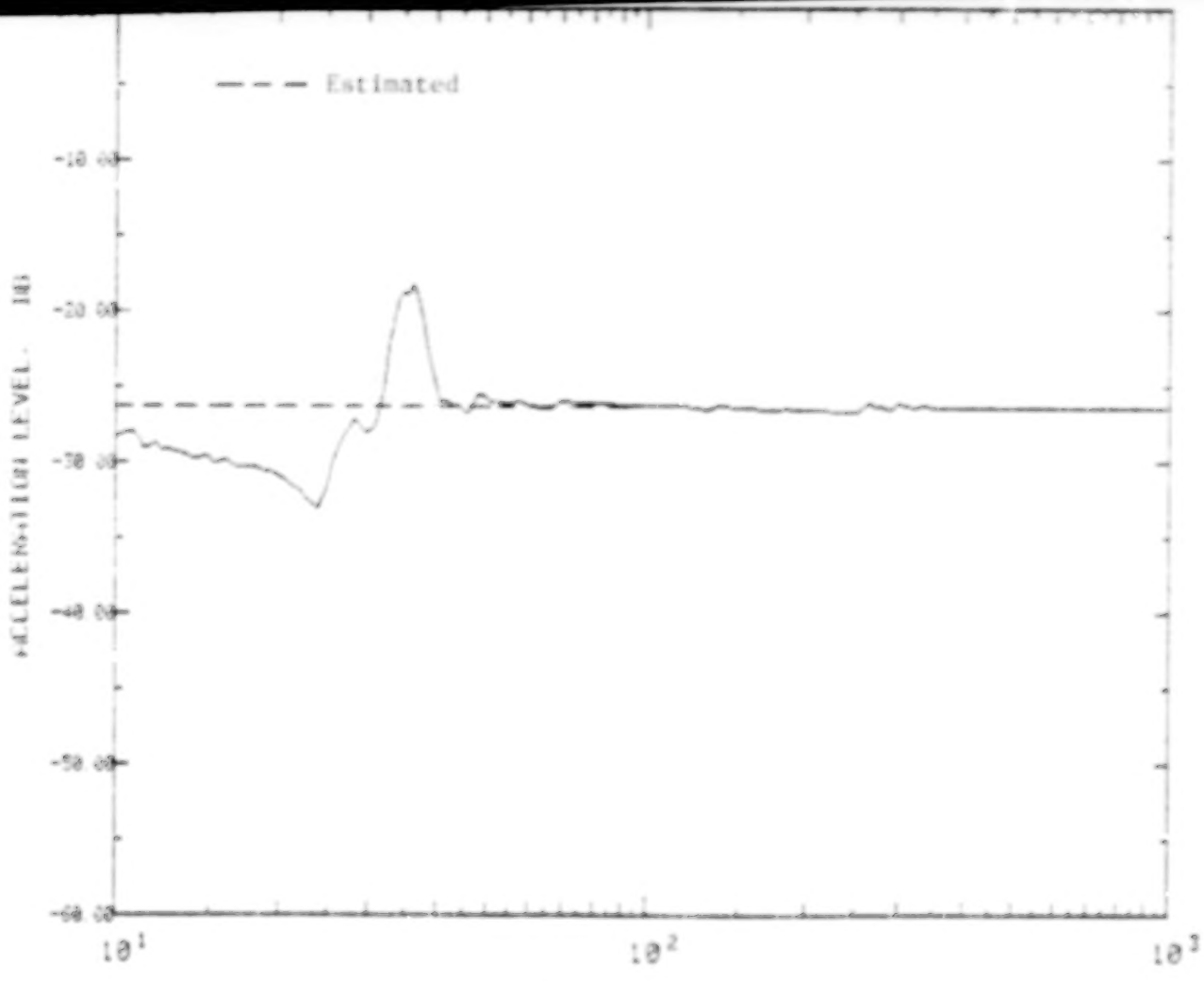

(c) Response AY.

FIGURE 34 (Continued). PREDICTED TRANSFER FUNCTION SPECTRA, LOAD CASE #2, ISOLATOR CONFIGURATION 0A, REF. 89 N RMS.

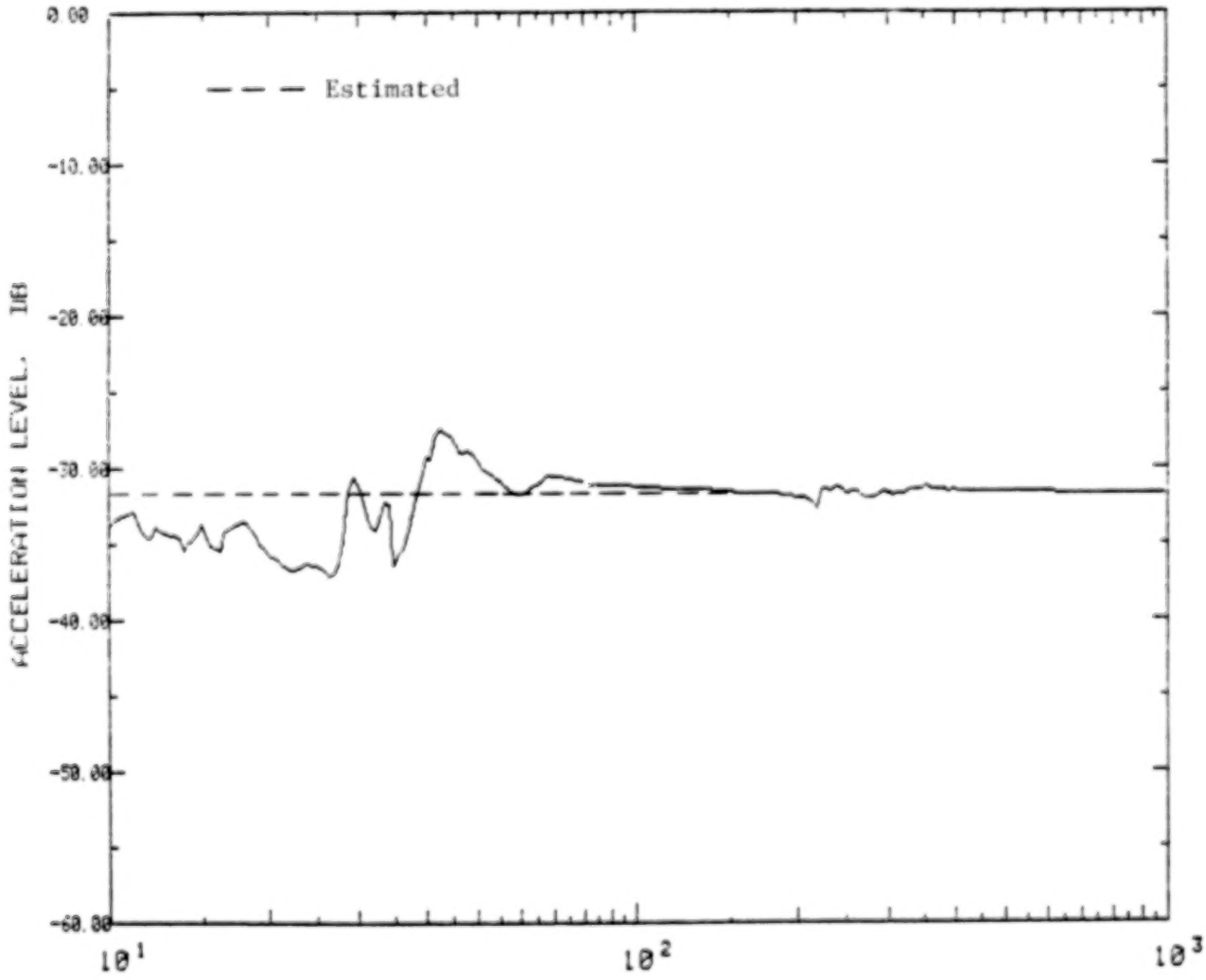

(d) Response AZ.

FIGURE 34 (Concluded). PREDICTED TRANSFER FUNCTION SPECTRA, LOAD CASE #2, ISOLATOR CONFIGURATION OA, REF. 89 N RMS.

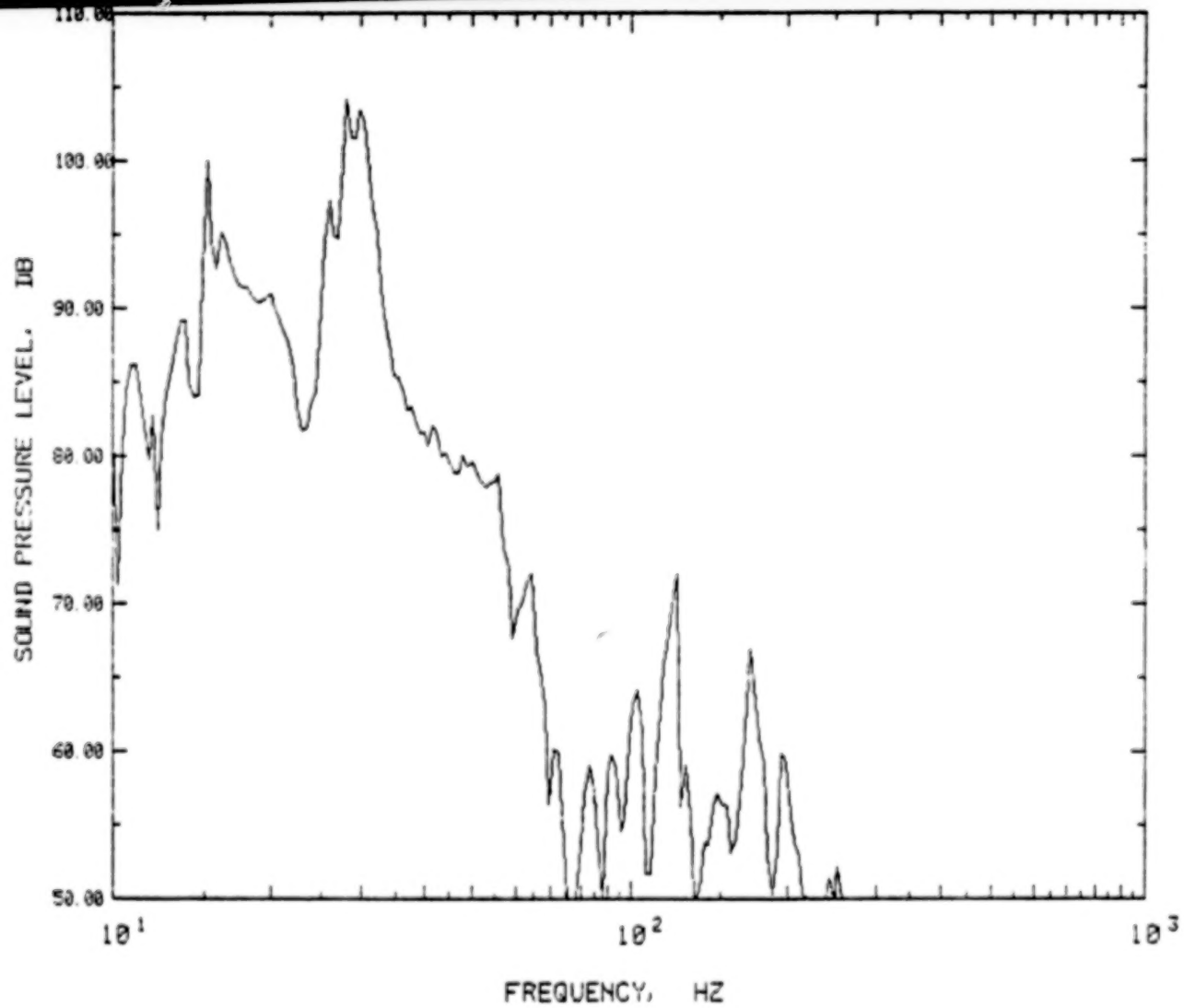

(a) Response P1.

FIGURE 35. PREDICTED TRANSFER FUNCTION SPECTRA, LOAD CASE #2, ISOLATOR CONFIGURATION AA, REF. 89 N RMS.

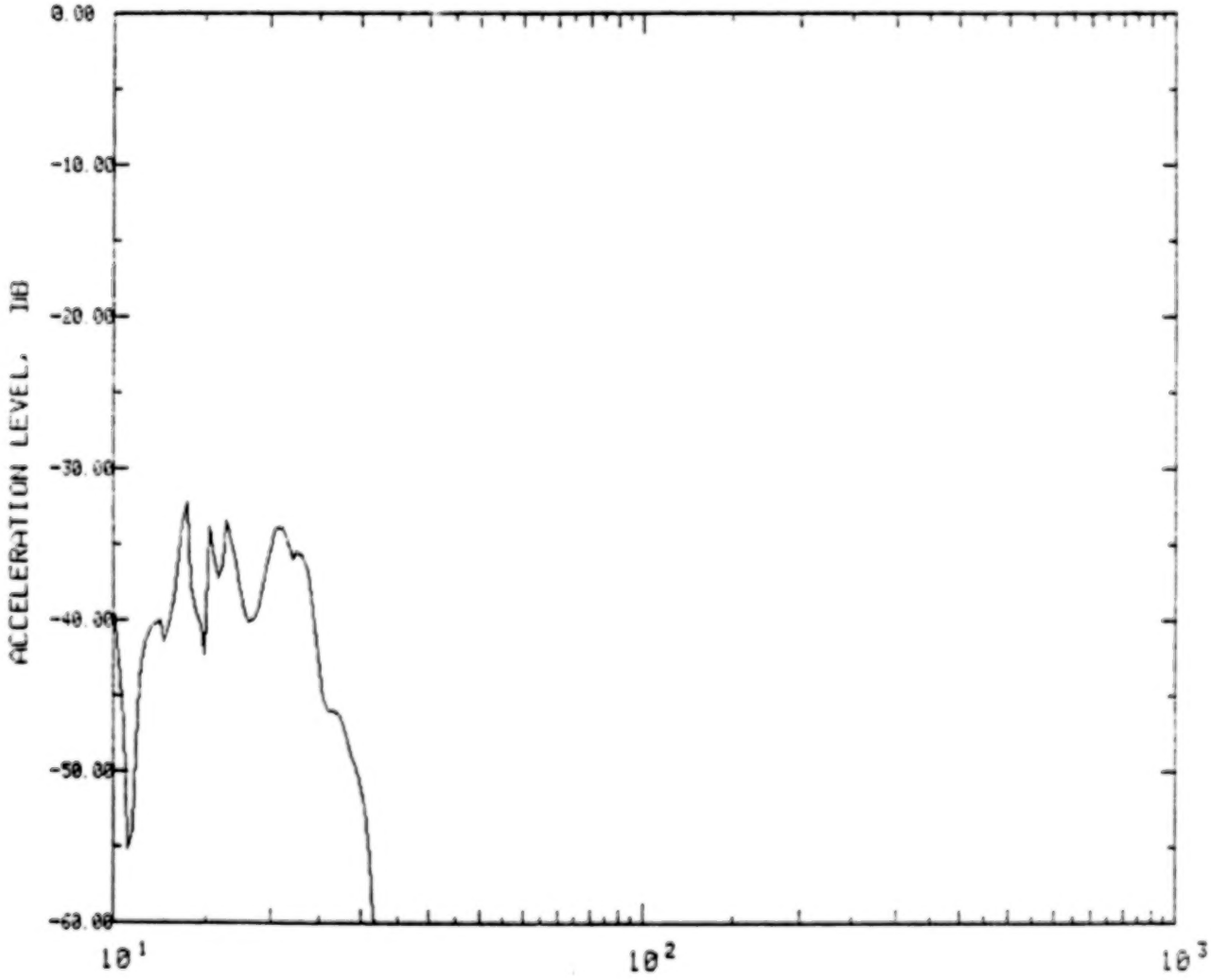

(b) Response AX.

FIGURE 35 (Continued). PREDICTED TRANSFER FUNCTION SPECTRA, LOAD CASE #2, ISOLATOR CONFIGURATION AA, REF. 89 N RMS.

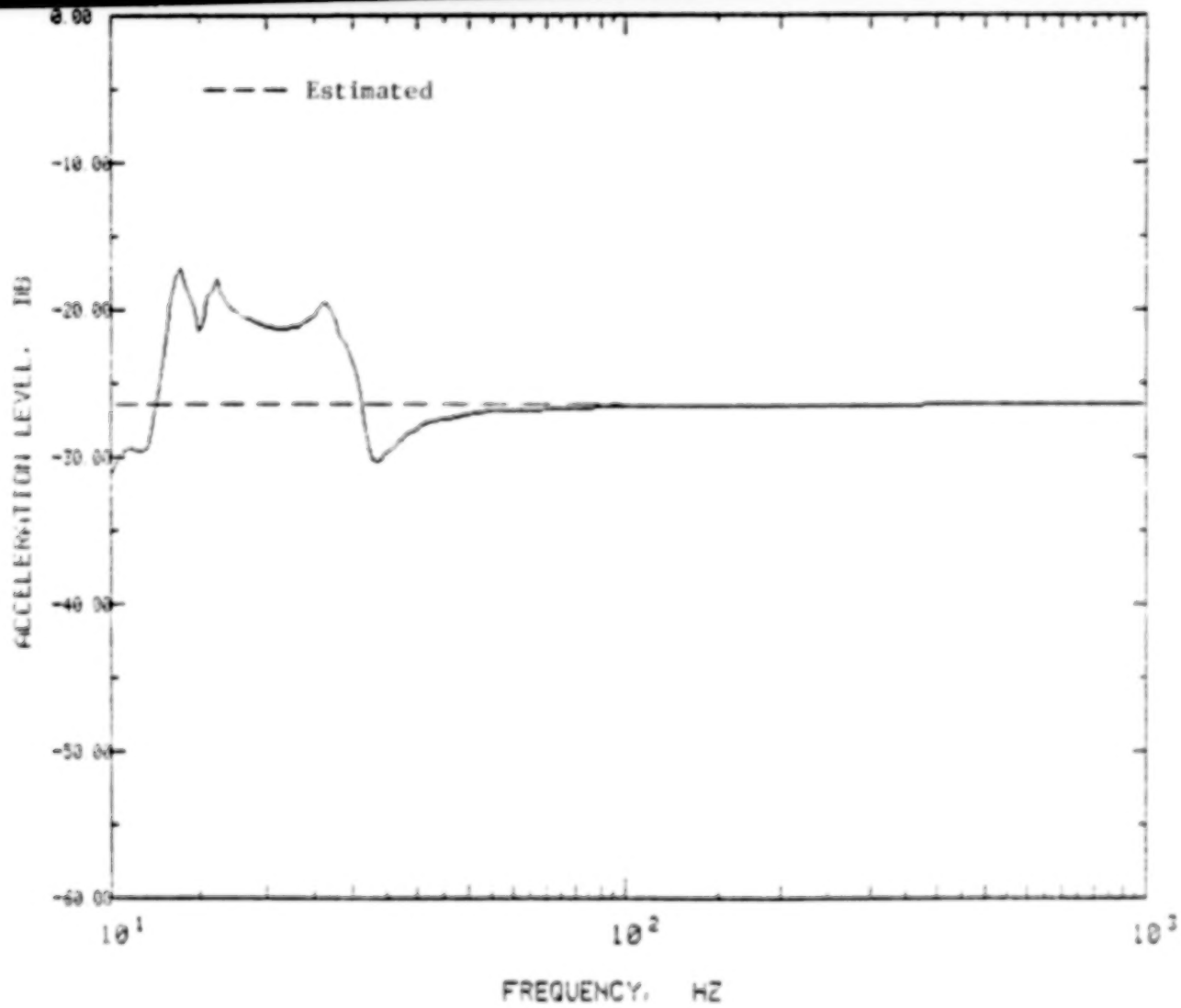

(c) Response AY.

FIGURE 35 (Continued). PREDICTED TRANSFER FUNCTION SPECTRA, LOAD CASE #2, ISOLATOR CONFIGURATION AA, REF. 89 N RMS.

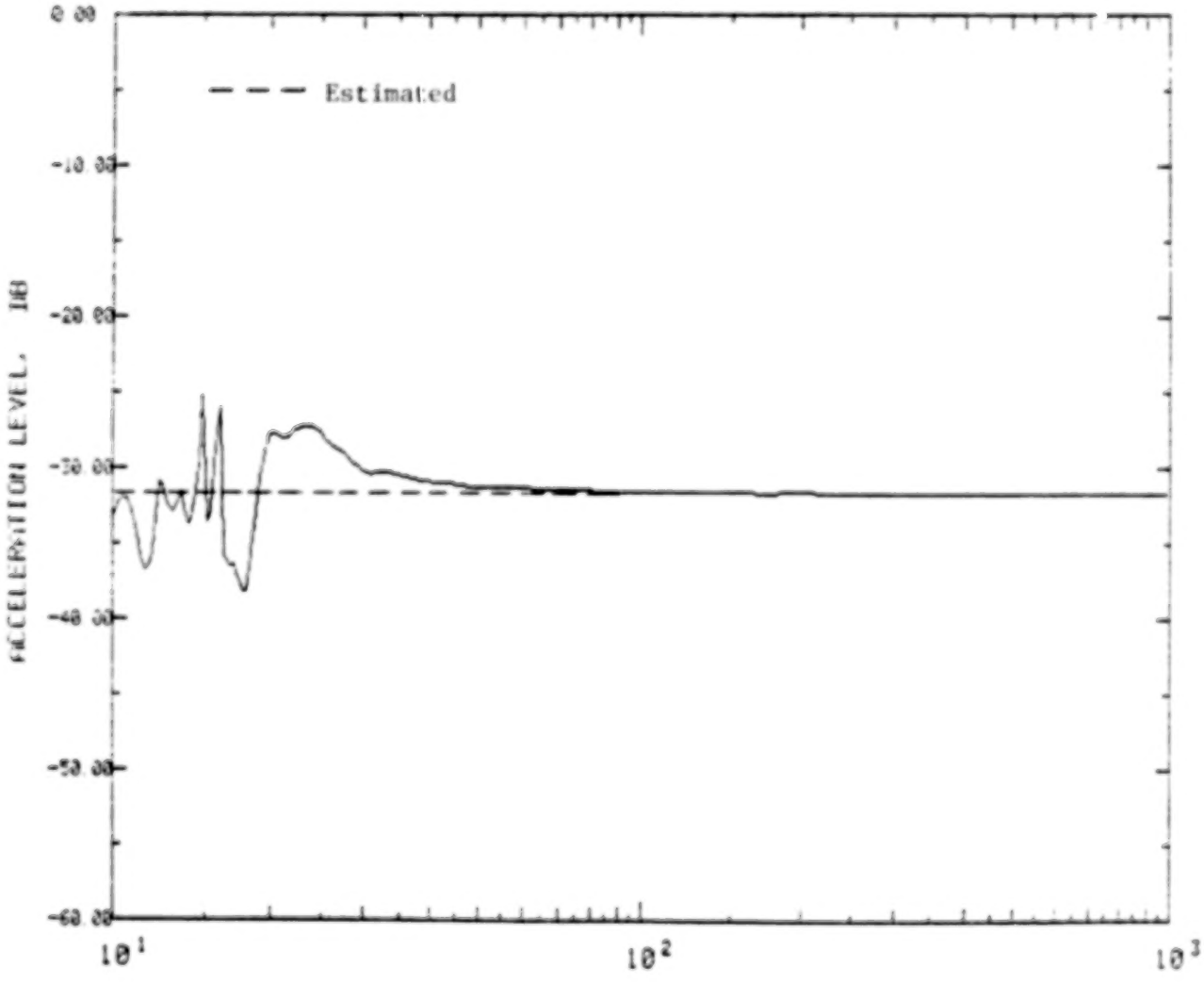

(d) Response AZ.

FIGURE 35 (Concluded). PREDICTED TRANSFER FUNCTION SPECTRA, LOAD CASE #2, ISOLATOR CONFIGURATION AA, REF. 89 N RMS.

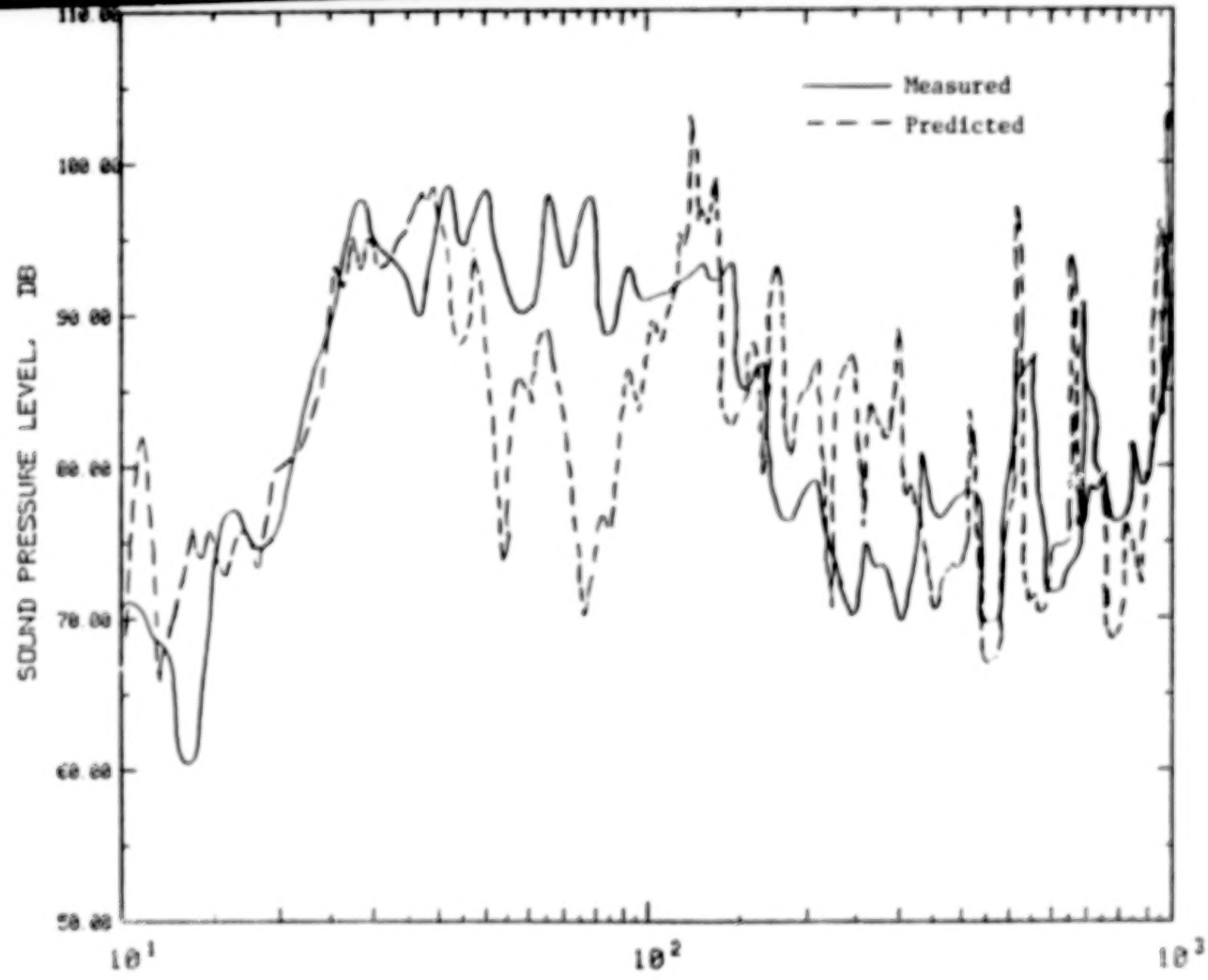

(a) Configuration R1.

FIGURE 36. COMPARISON OF NARROW BAND SPL TRANSFER FUNCTION SPECTRA, LOAD CASE #2, RESPONSE P2, REF. 89 N RMS.

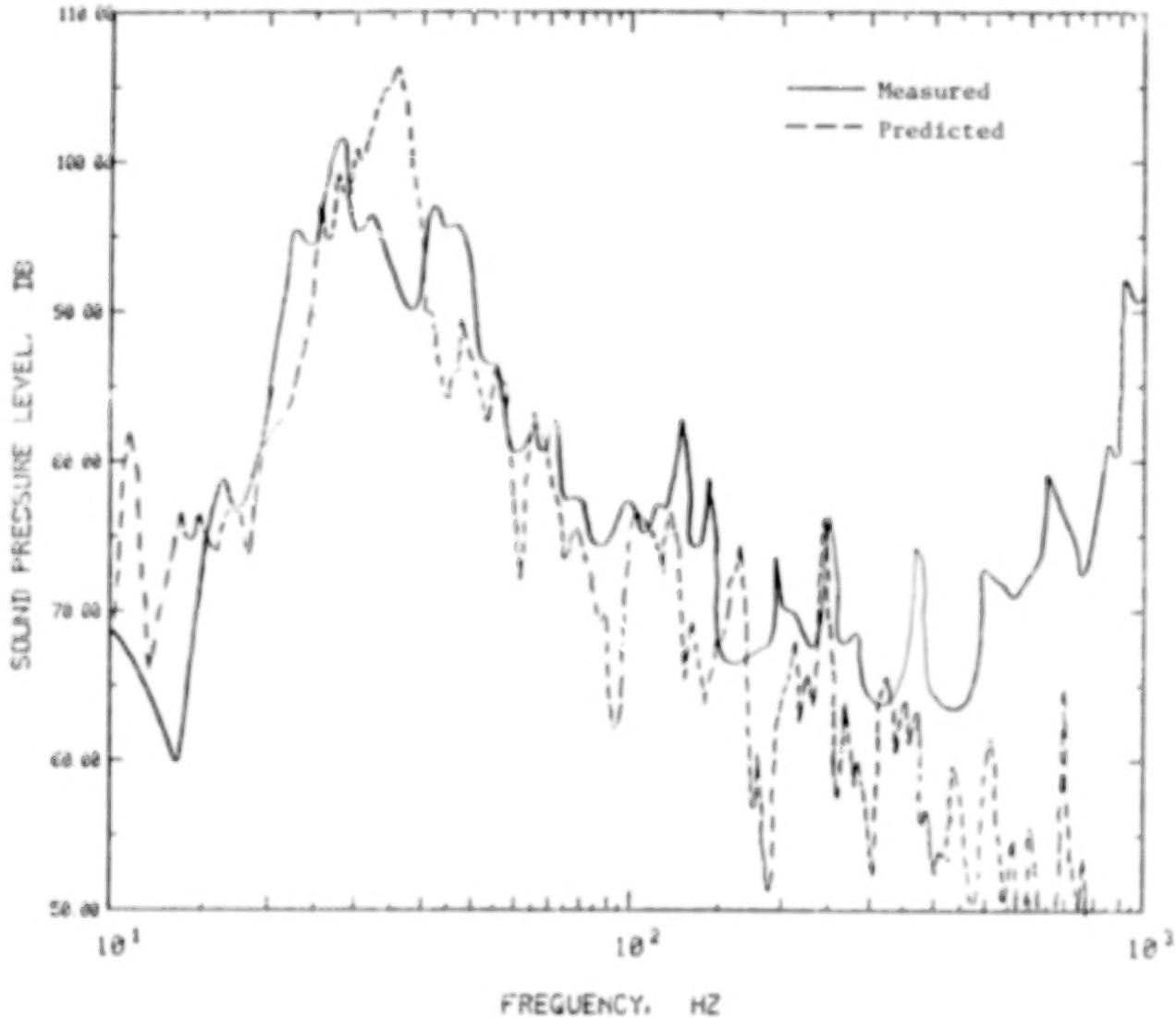

(b) Configuration 0A.

FIGURE 36 (Continued). COMPARISON OF NARROW BAND SPL TRANSFER FUNCTION SPECTRA, LOAD CASE #2, RESPONSE P2, REF. 89 N RMS.

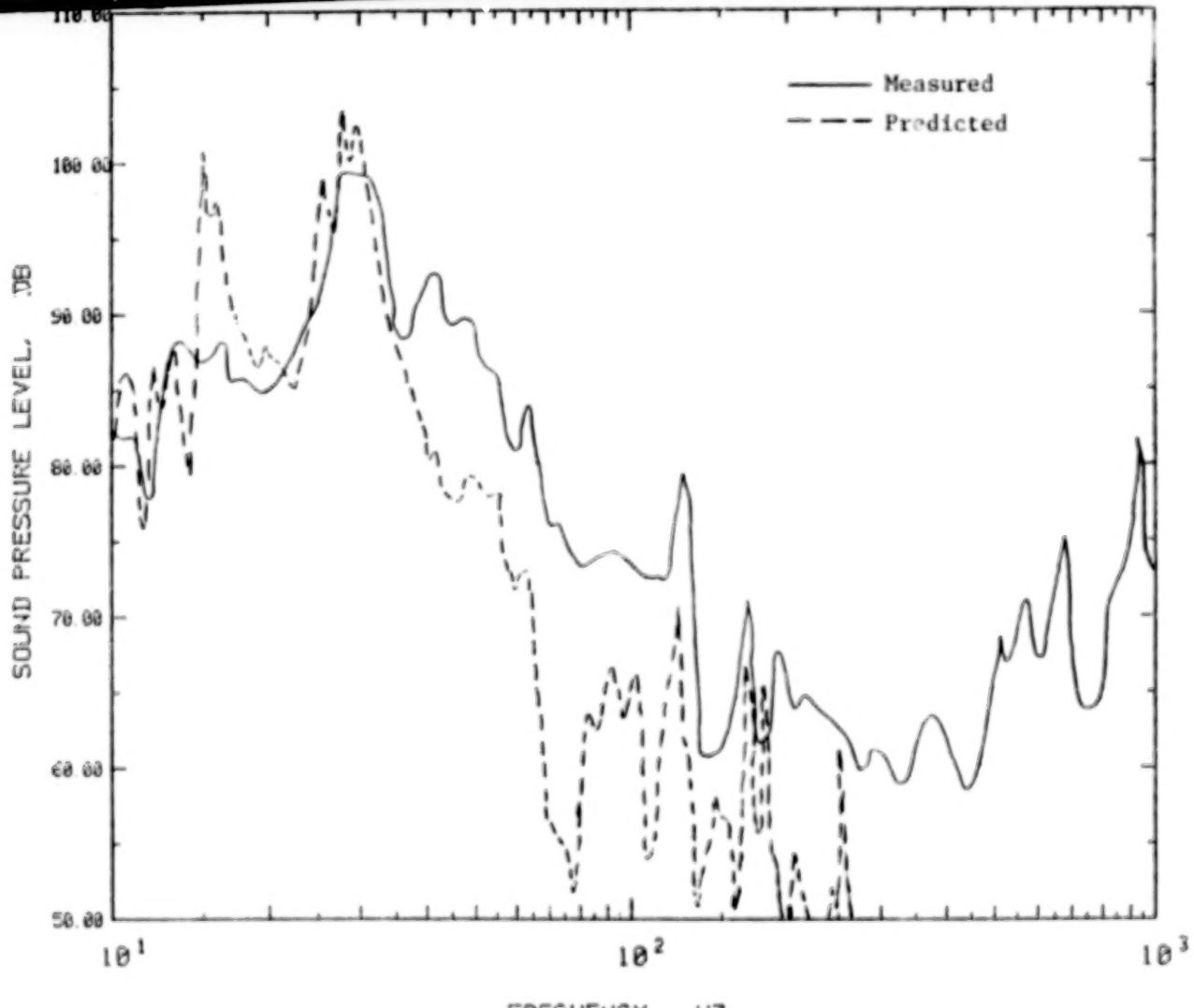

(c) Configuration AA.

FIGURE 36 (Concluded). COMPARISON OF NARROW BAND SPL TRANSFER FUNCTION SPECTRA, LOAD CASE #2, RESPONSE P2, REF. 89 N RMS.

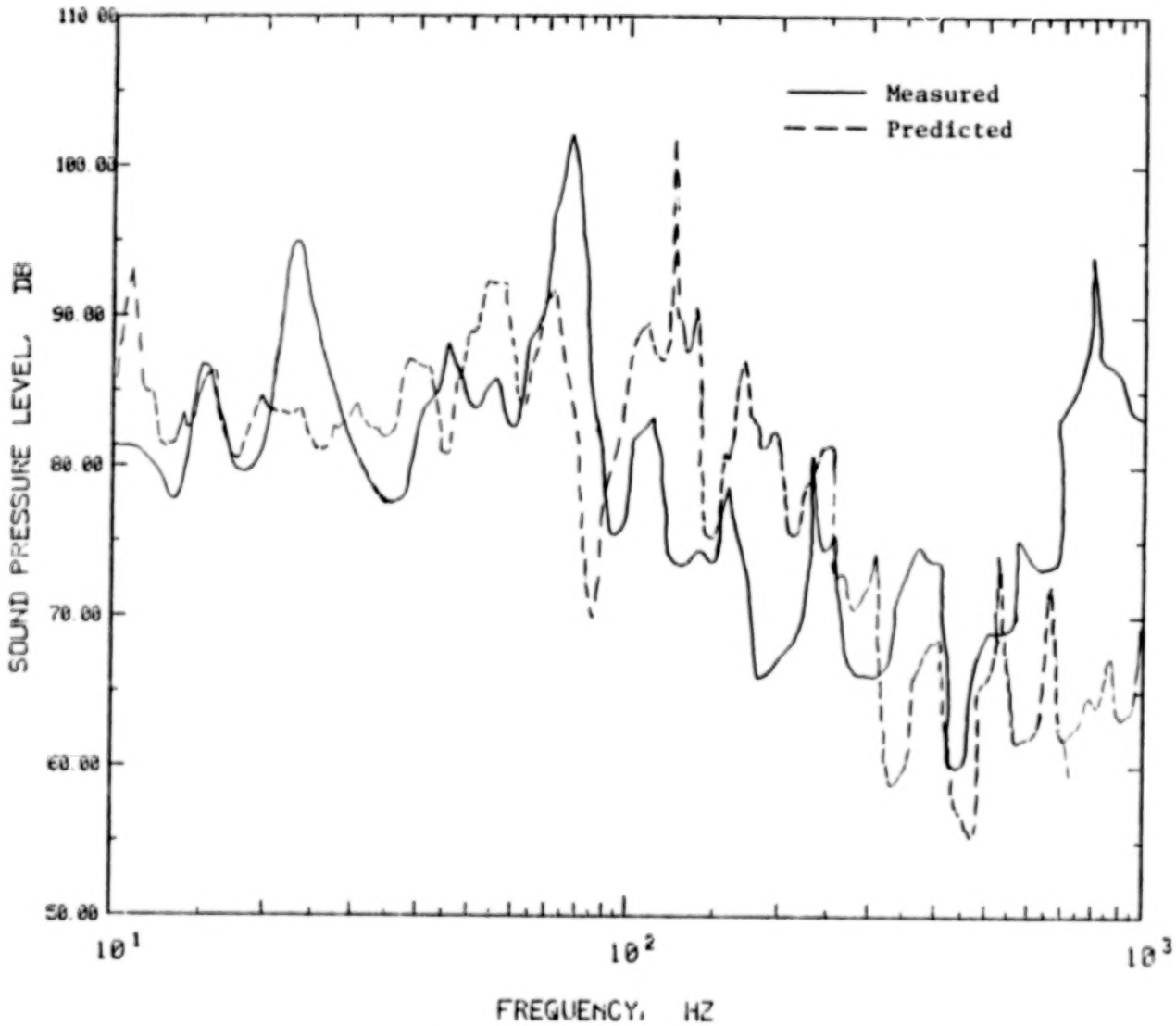

(a) Configuration R1.

FIGURE 37. COMPARISON OF NARROW BAND SPL TRANSFER FUNCTION SPECTRA, LOAD CASE #3, RESPONSE P1, REF. 89 N RMS.

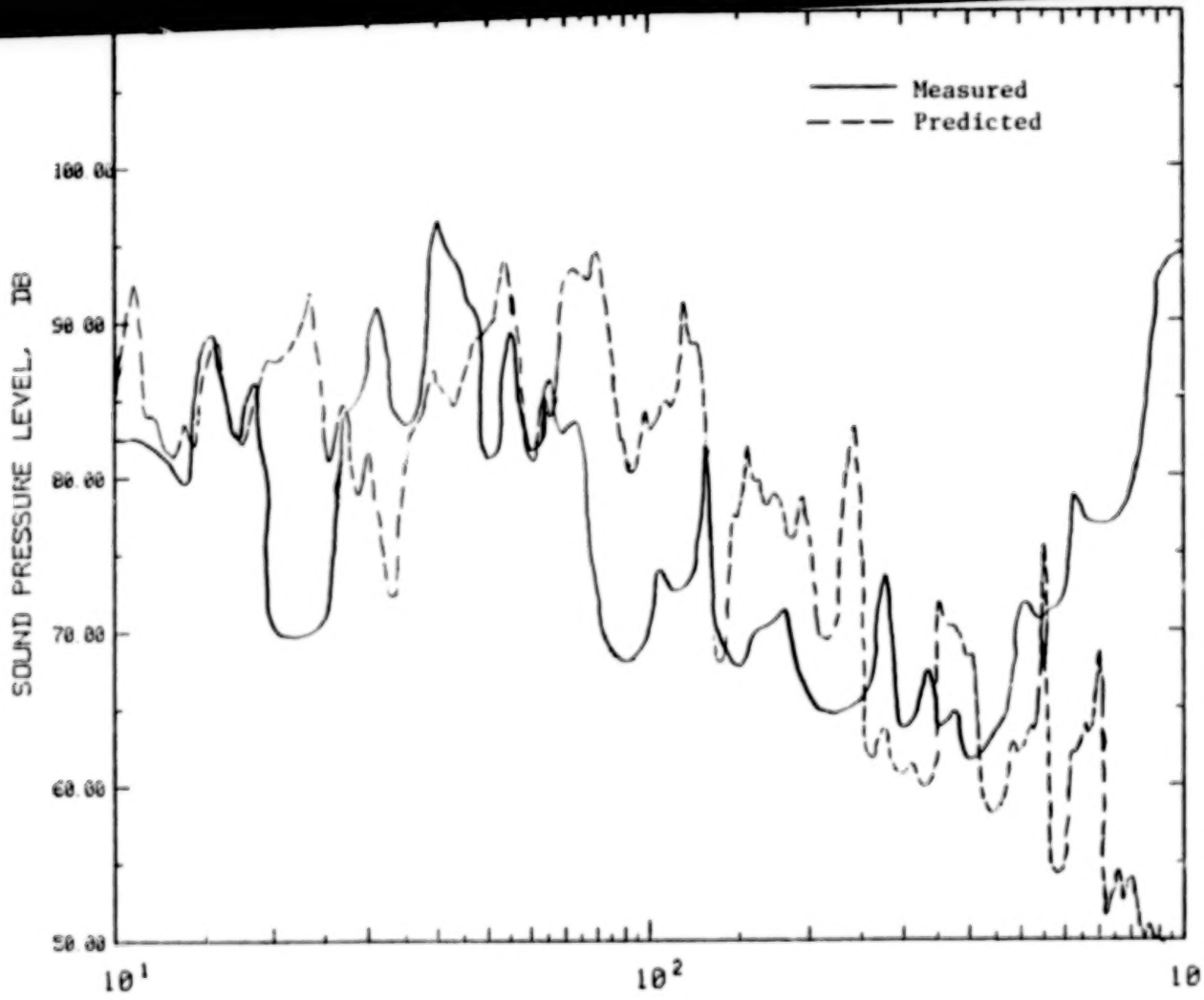

(b) Configuration OA.

FIGURE 37 (Continued). COMPARISON OF NARROW BAND SPL TRANSFER FUNCTION SPECTRA, LOAD CASE #3, RESPONSE P1, REF. 89 N RMS.

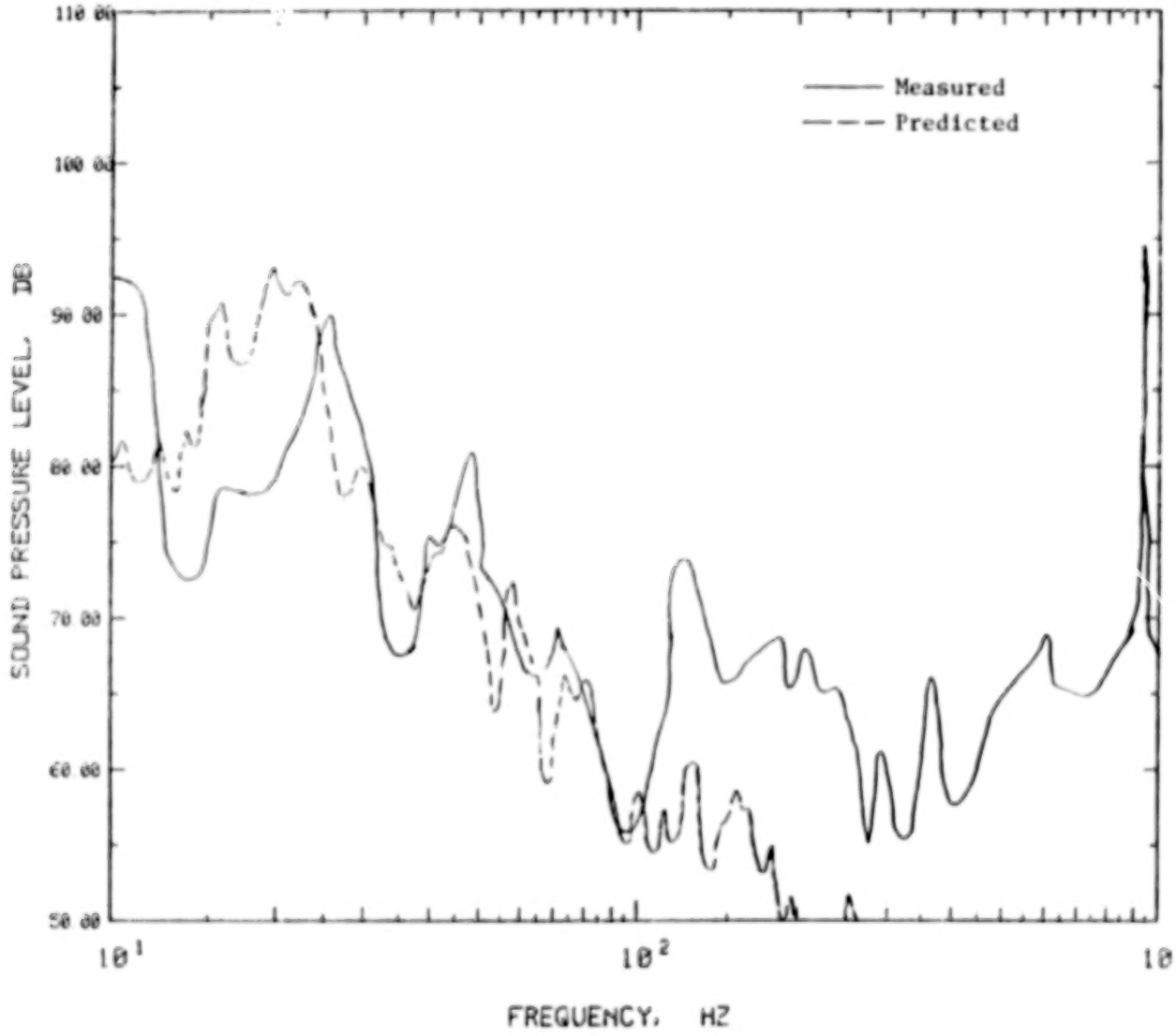

(c) Configuration AA.

FIGURE 37 (Concluded). COMPARISON OF NARROW BAND SPL TRANSFER FUNCTION SPECTRA, LOAD CASE #3, RESPONSE P1, REF. 89 N RMS.

BLANK

PAGE

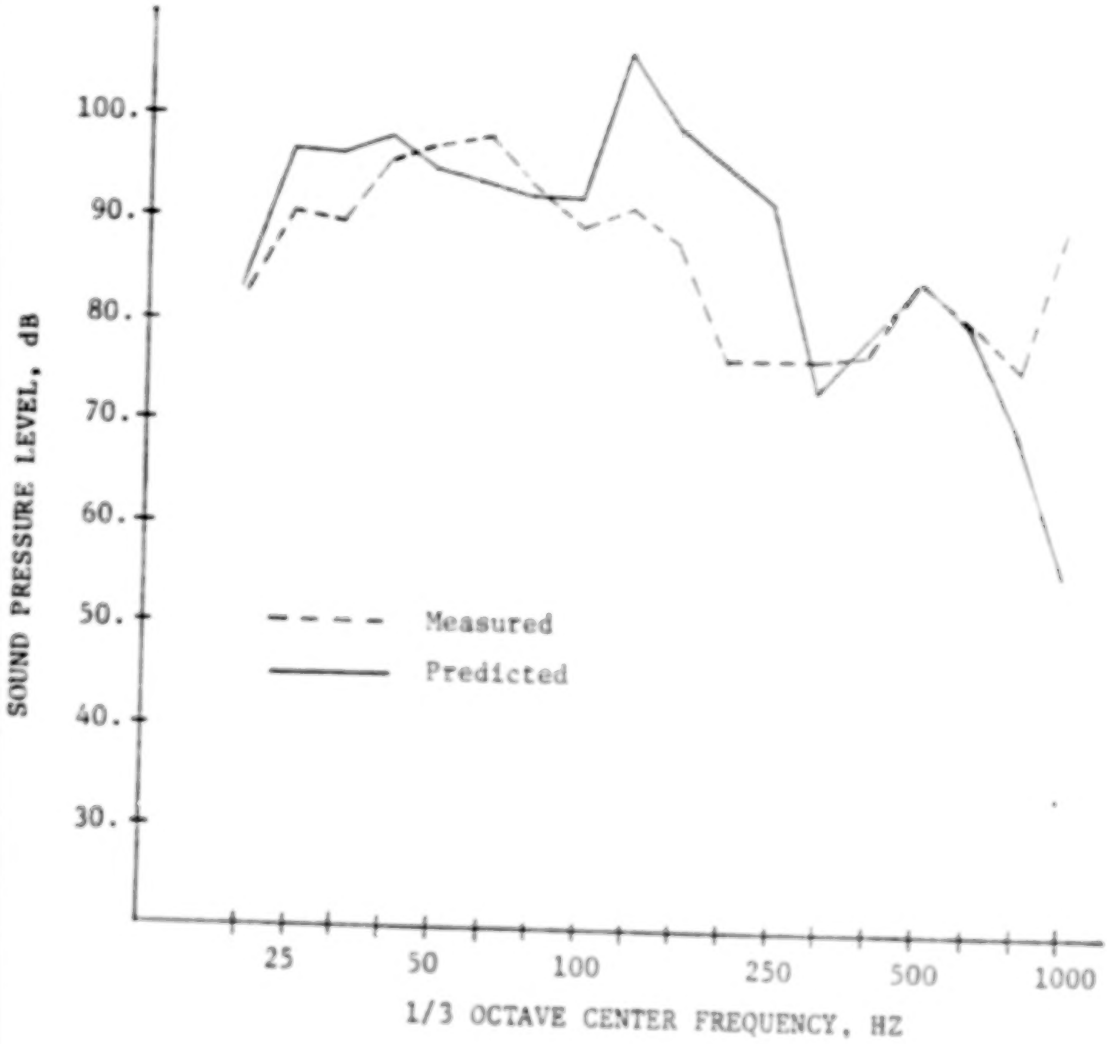

(a) Configuration R1.

FIGURE 38. COMPARISON OF ONE-THIRD OCTAVE PEAK SPL TRANSFER FUNCTION SPECTRA AT P1, LOAD CASE #2, REF. 89 N RMS.

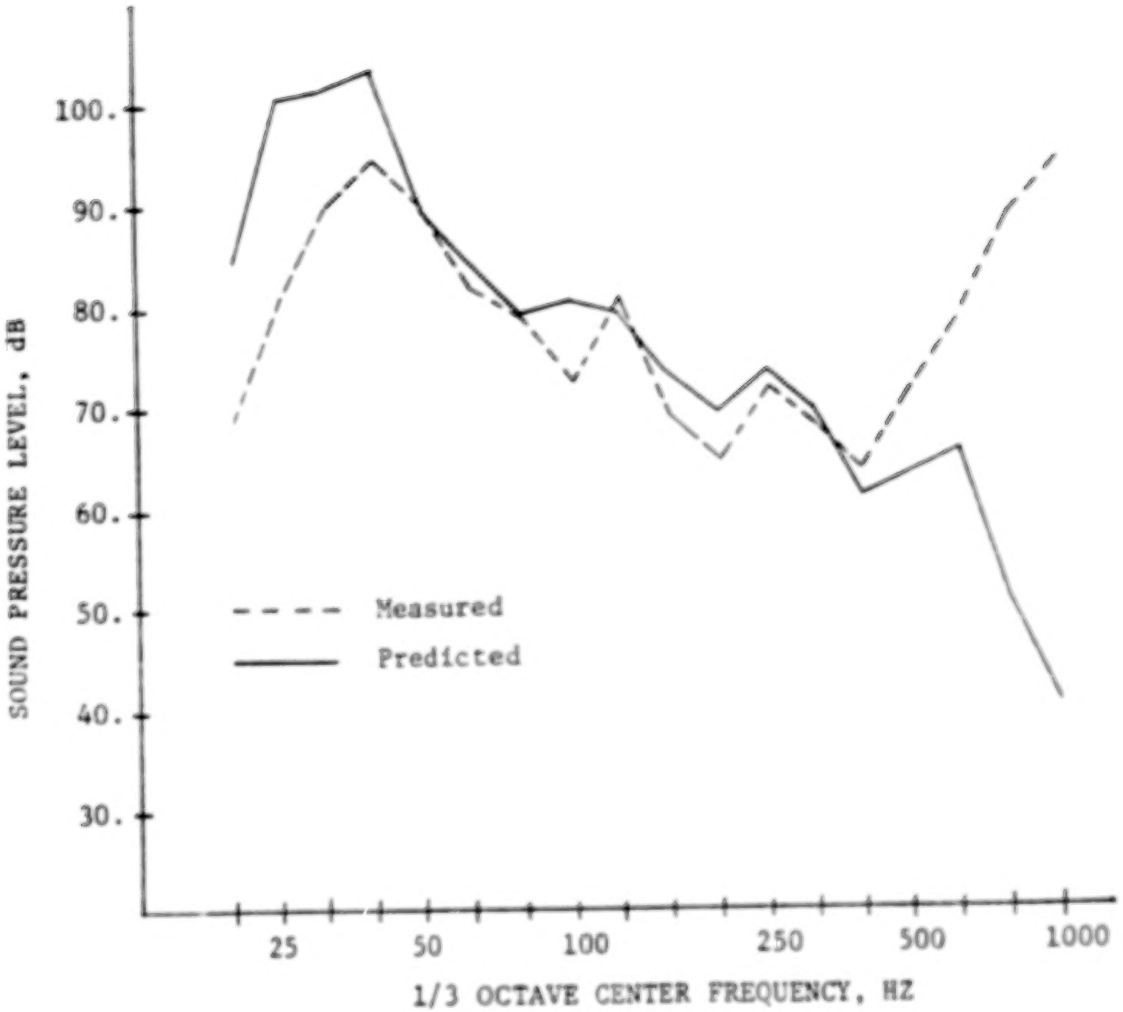

(b) Configuration OA.

FIGURE 38 (Continued). COMPARISON OF ONE-THIRD OCTAVE PEAK SPL TRANSFER FUNCTION SPECTRA AT P1, LOAD CASE #2, REF. 89 N RMS.

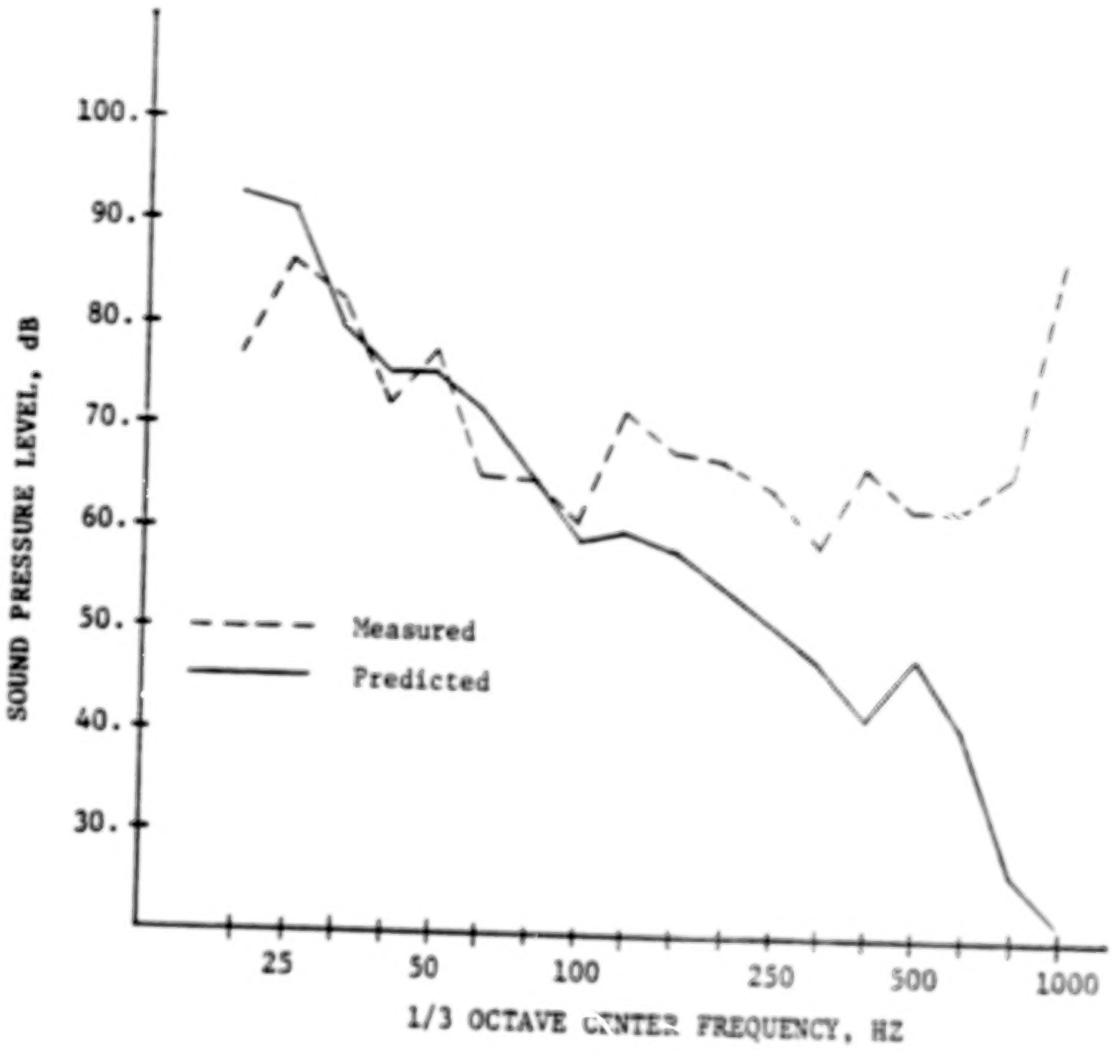

(c) Configuration AA.

FIGURE 38 (Concluded). COMPARISON OF ONE-THIRD OCTAVE PEAK SPL TRANSFER FUNCTION SPECTRA TA P1, LOAD CASE #2, REF. 89 N RMS.

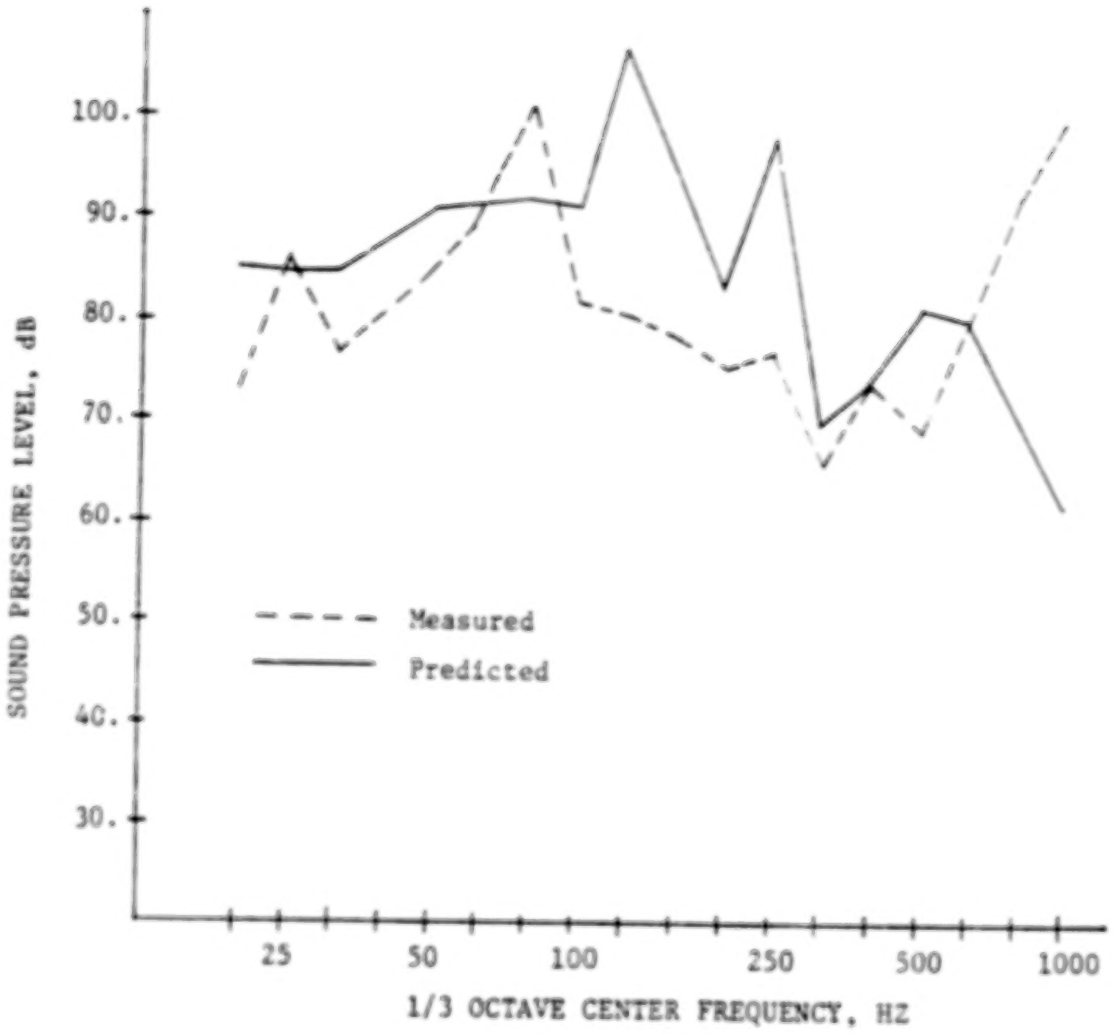

(a) Configuration R1.

FIGURE 39. COMPARISON OF ONE-THIRD OCTAVE PEAK SPL TRANSFER FUNCTION SPECTRA AT P1, LOAD CASE #3, REF. 89 N RMS.

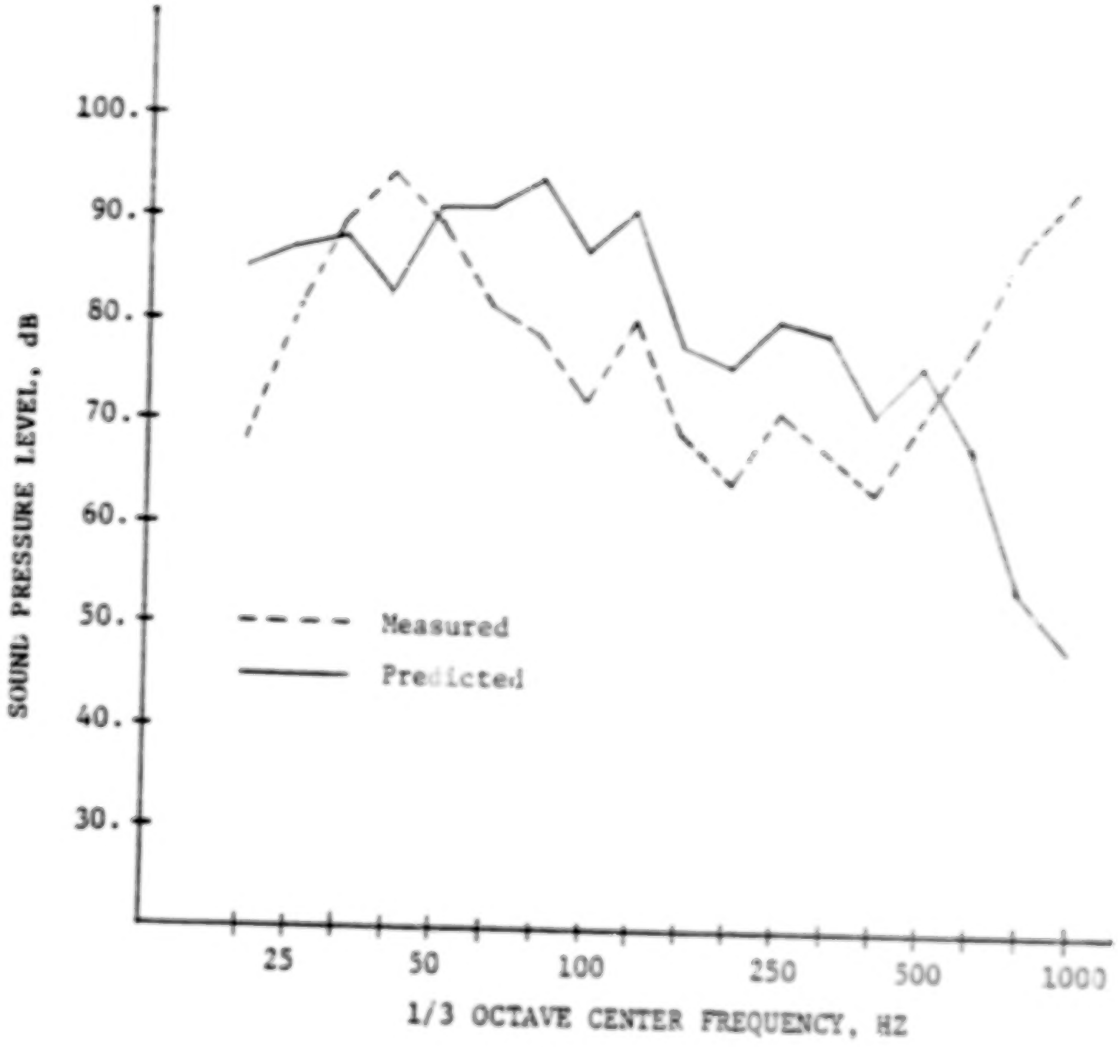

(b) Configuration 0A.

FIGURE 39 (Continued). COMPARISON OF ONE-THIRD OCTAVE PEAK SPL TRANSFER FUNCTION SPECTRA AT P1, LOAD CASE #3, REF. 89 N RMS.

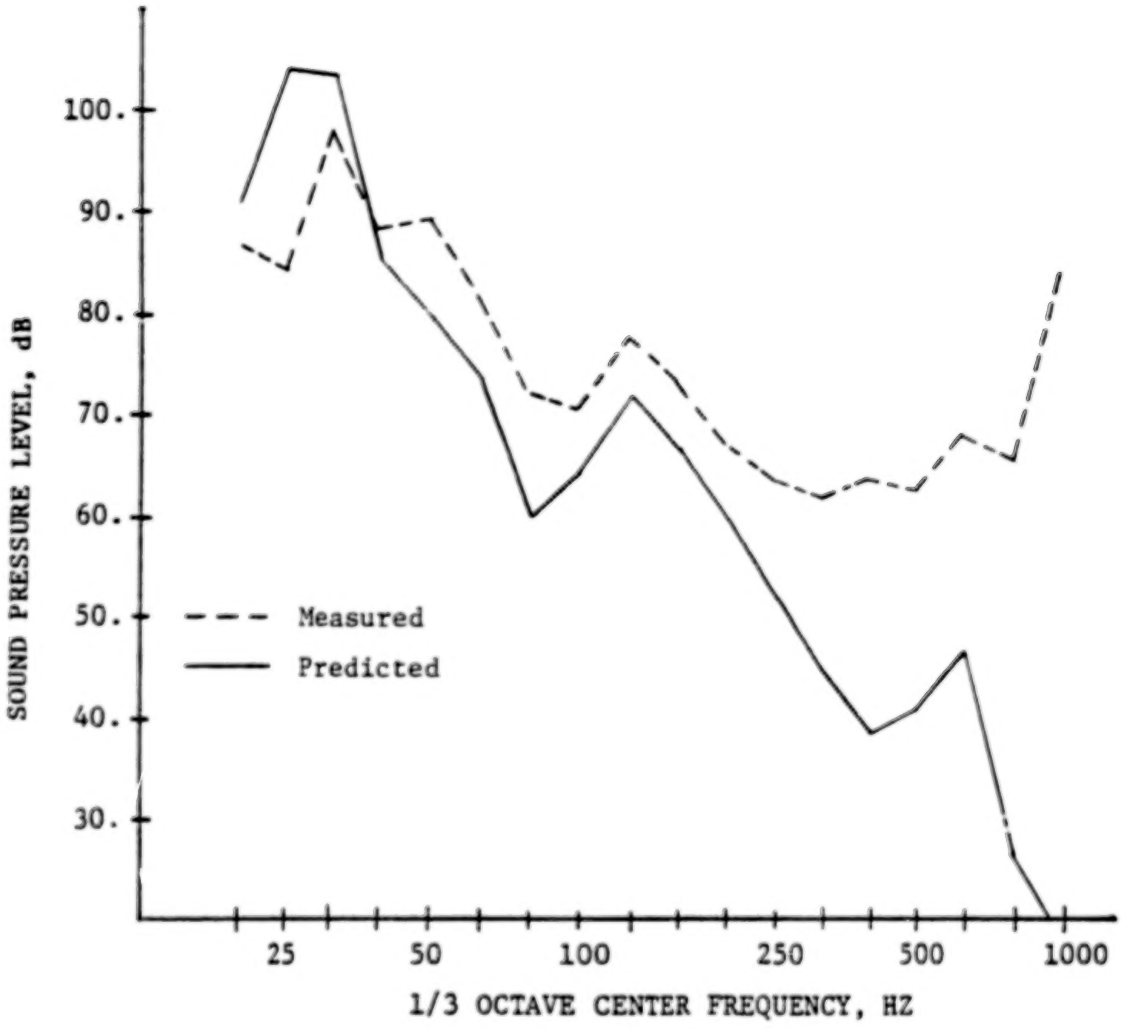

(c) Configuration AA.

FIGURE 39 (Concluded). COMPARISON OF ONE-THIRD OCTAVE PEAK SPL TRANSFER FUNCTION SPECTRA AT P1, LOAD CASE #3, REF. 89 N RMS.

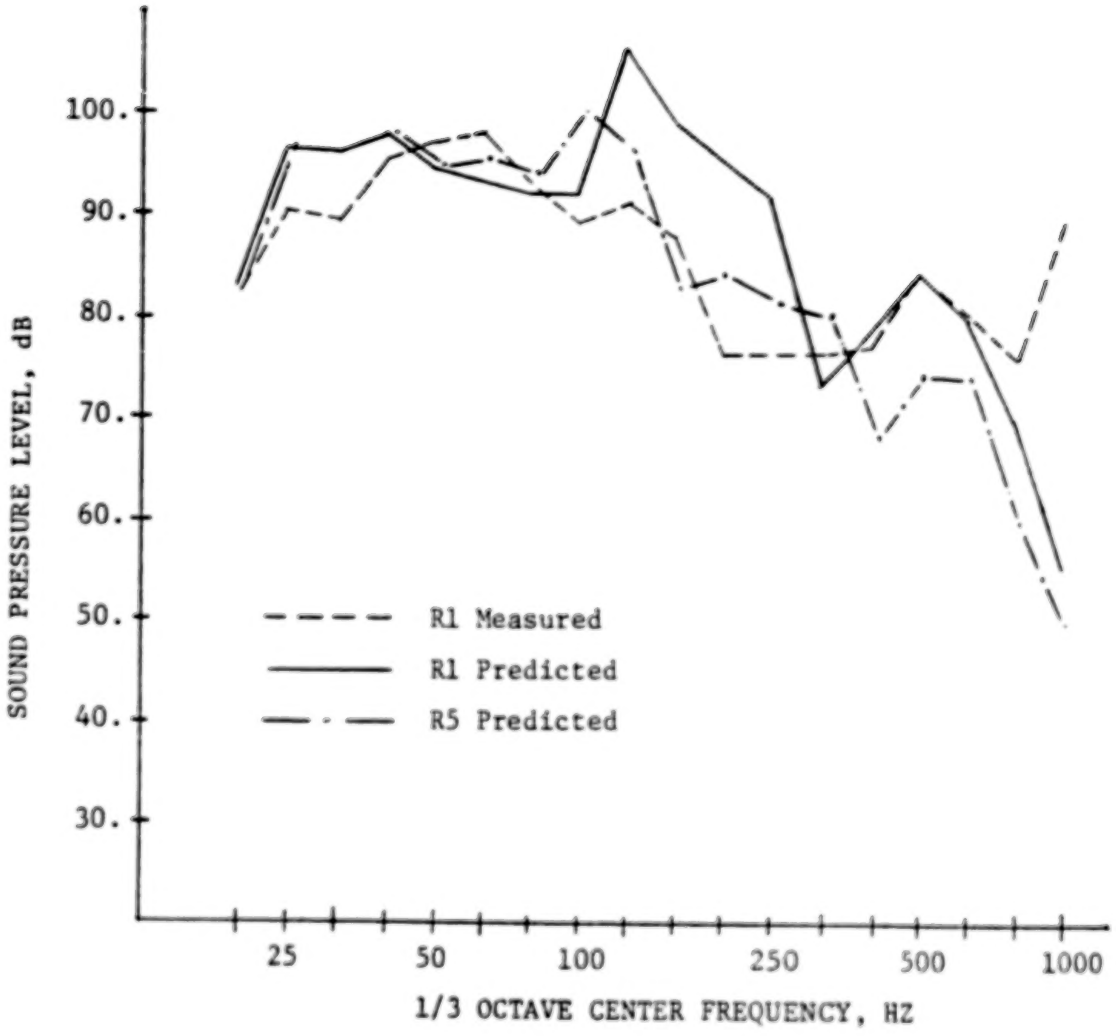

(a) Load Case #2.

FIGURE 40. EFFECT OF ENGINE MOUNT LUG STIFFNESS ON TRANSFER FUNCTION SPECTRA AT P1, REF. 89 N RMS.

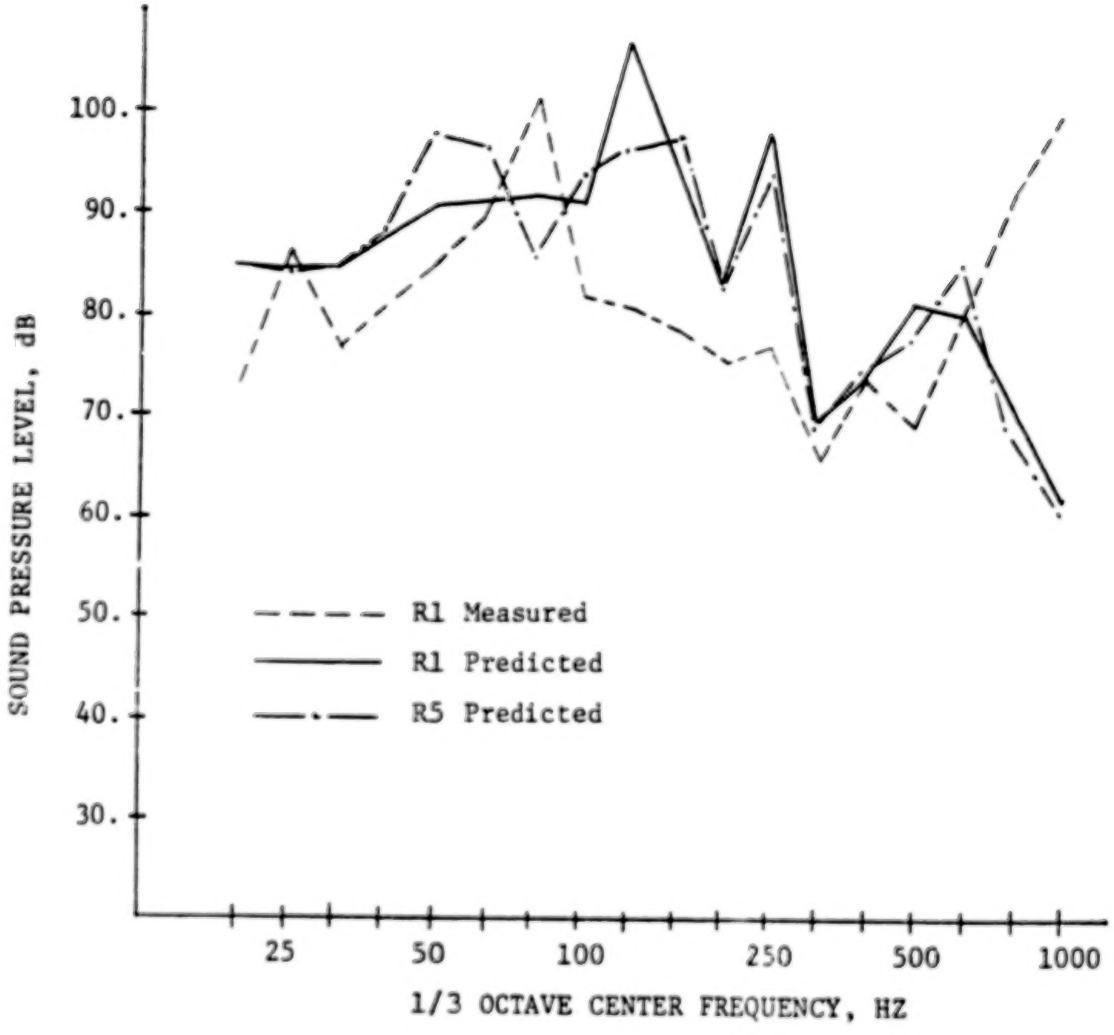

(b) Load Case #3.

FIGURE 40 (Concluded). EFFECT OF ENGINE MOUNT LUG STIFFNESS ON TRANSFER FUNCTION SPECTRA AT P1, REF. 89 N RMS.

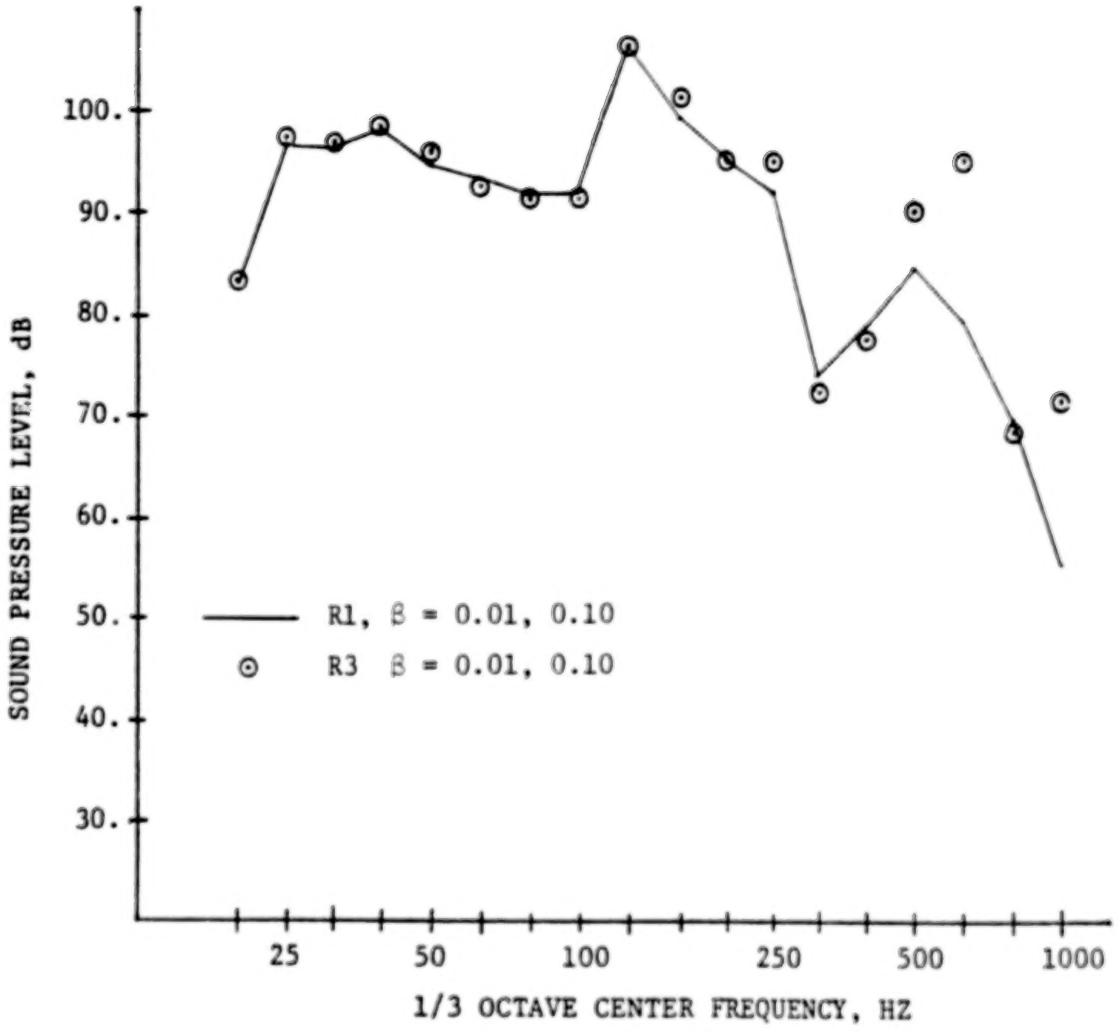

FIGURE 41. EFFECT OF VARIATION IN ENGINE MOUNT PARAMETERS ON TRANSFER FUNCTION SPECTRA AT P1, LOAD CASE #2, REF. 89 N RMS.

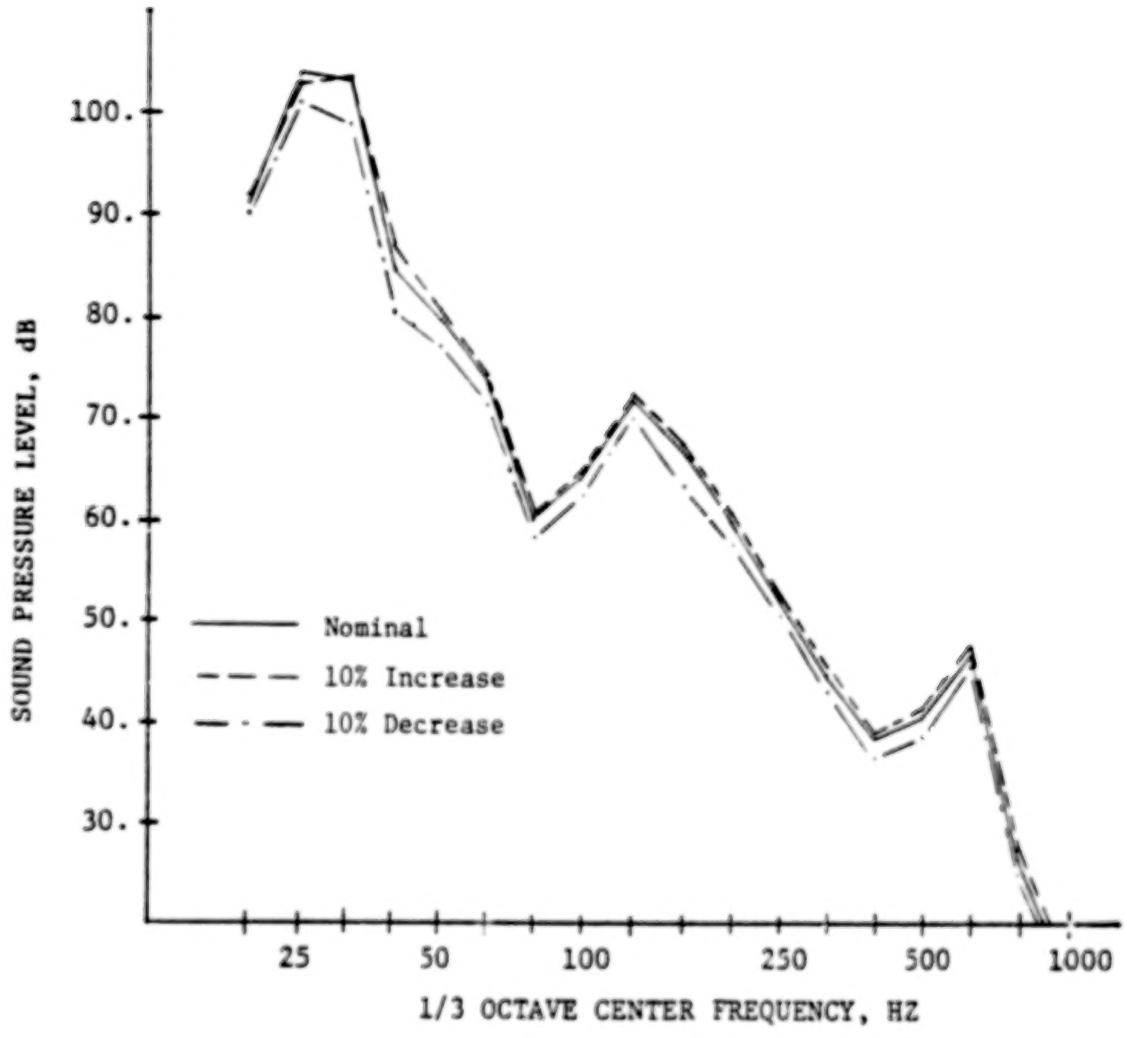

FIGURE 42. EFFECT OF ISOLATOR STIFFNESS VARIATION ON SPL TRANSFER FUNCTION SPECTRUM AT P1, LOAD CASE #2, CONFIGURATION AA, REF. 89 N RMS.

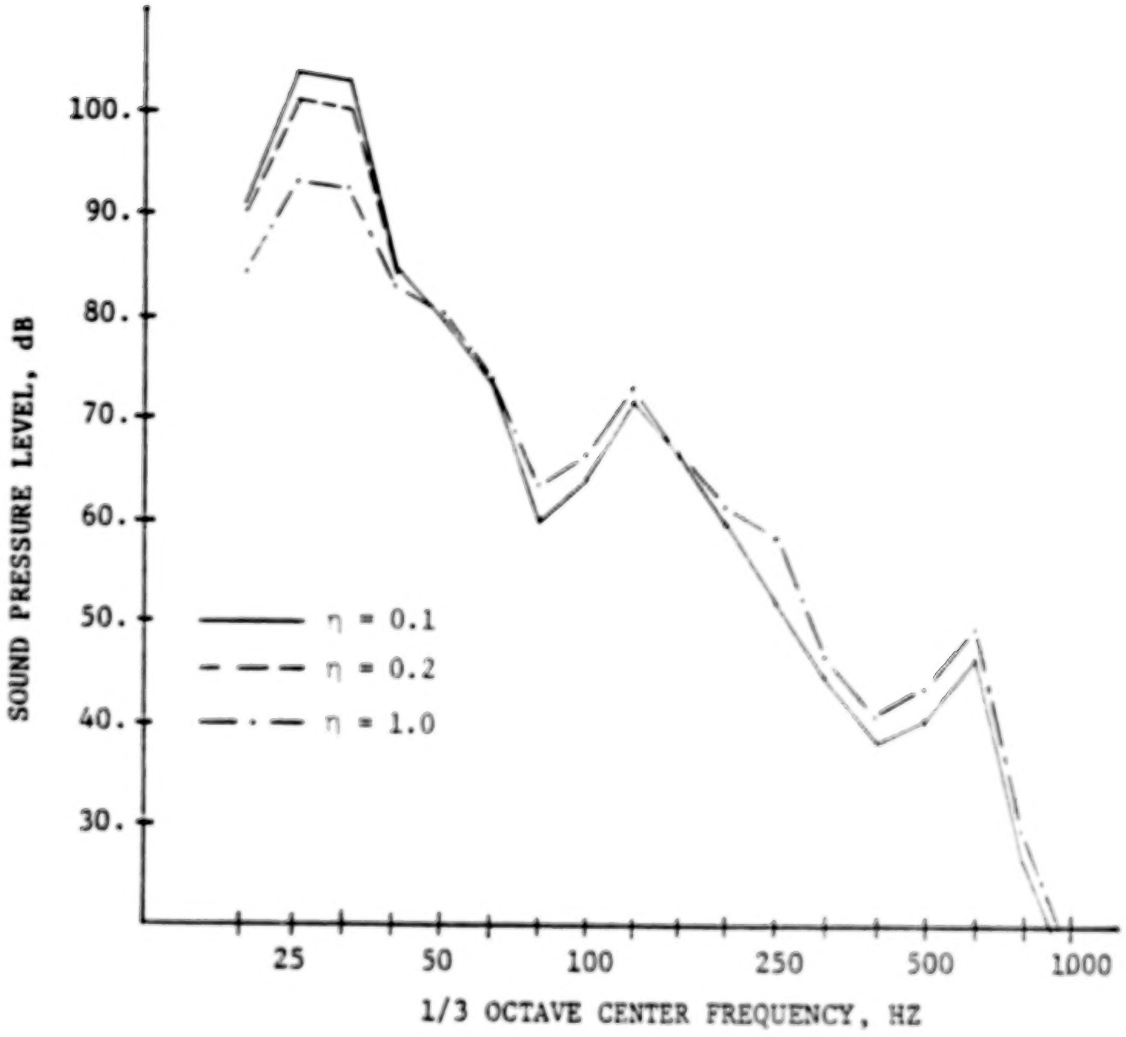

FIGURE 43. EFFECT OF ISOLATOR DAMPING VARIATION ON SPL TRANSFER FUNCTION SPECTRA P1, LOAD CASE #2, CONFIGURATION AA, REF. 89 N RMS.

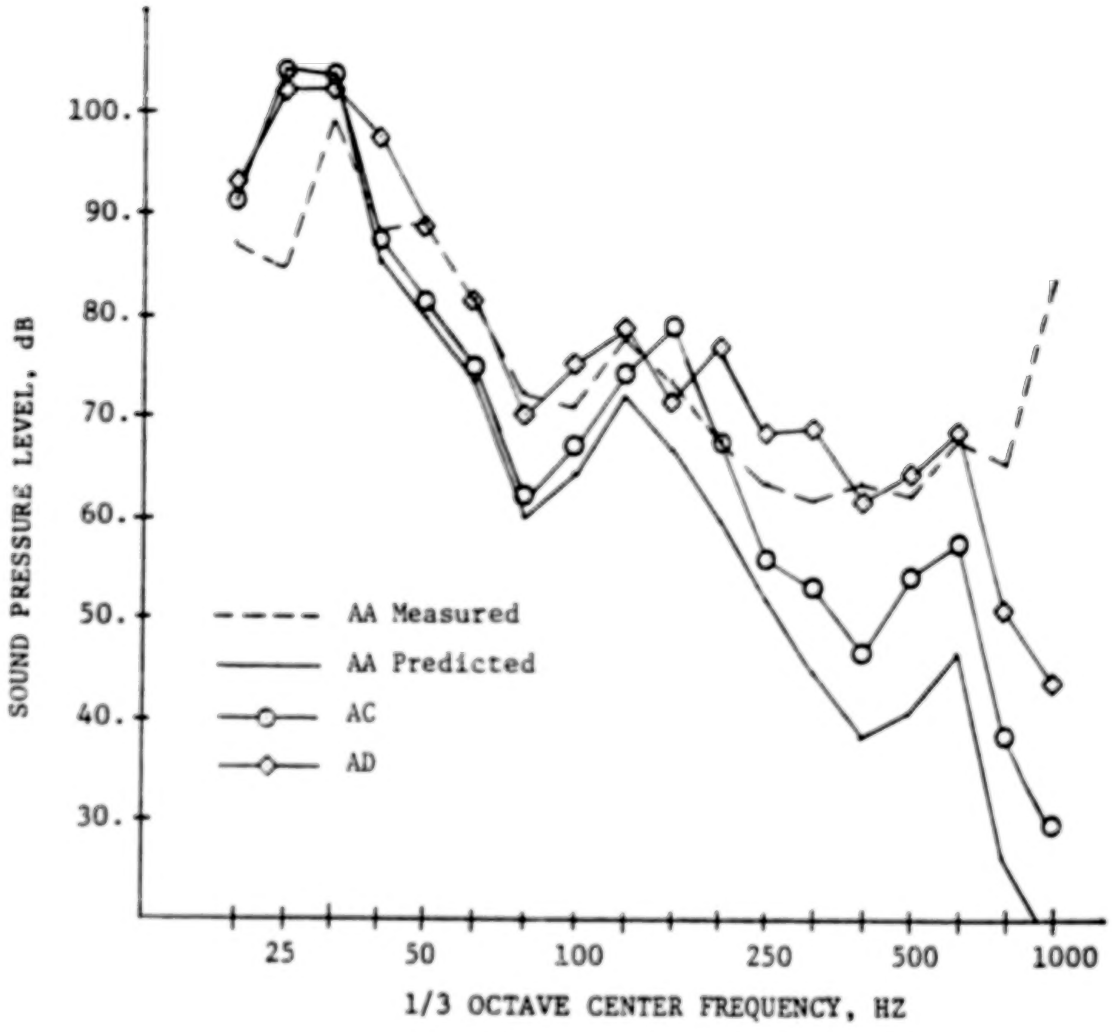

FIGURE 44. EFFECT OF ISOLATOR STIFFNESS VARIATION ON TRANSFER FUNCTION SPECTRA AT P1, LOAD CASE #2, REF. 89 N RMS.

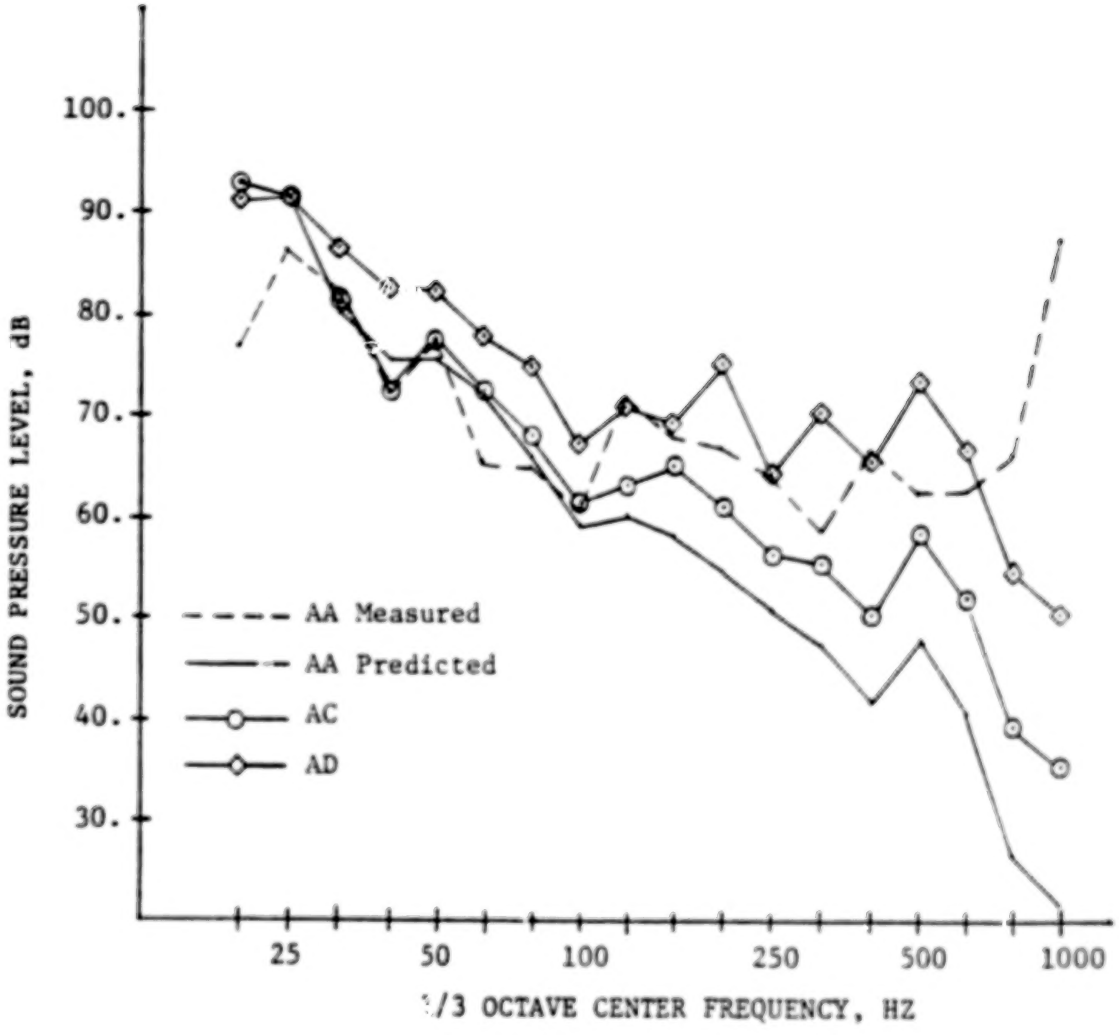

FIGURE 45. EFFECT OF ISOLATOR STIFFNESS VARIATION ON TRANSFER FUNCTION SPECTRA AT P1, LOAD CASE #3, REF. 89 N RMS.

1 Report No	2 Government Accession No	3 Recipient's Catalog No
NASA CR-3427		

4 Title and Subtitle	5 Report Date
ENGINE ISOLATION FOR STRUCTURAL-BORNE INTERIOR NOISE REDUCTION IN A GENERAL AVIATION AIRCRAFT	May 1981
	6 Performing Organization Code

7 Author(s)	8 Performing Organization Report No
James F. Unruh and Dennis C. Scheidt	02-4860
	10 Work Unit No

9 Performing Organization Name and Address	11 Contract or Grant No
Southwest Research Institute P.O.Drawer 28510 San Antonio, Texas 78284	NAS1-14861
	13 Type of Report and Period Covered
12 Sponsoring Agency Name and Address	Contractor Report
National Aeronautics & Space Administration Washington, DC 20546	14 Sponsoring Agency Code

15 Supplementary Notes

Langley Technical Monitor: John S. Mixson
Final Report

16 Abstract

An experimental and analytical study of engine vibration isolation for structural-borne interior noise reduction was carried out with the specific objectives: (1) to develop a laboratory based test procedure to simulate engine induced structure-borne noise transmission, (2) test a range of candidate isolators for relative performance data and basic data for analytical model correlations, and (3) to develop an analytical model of the transmission phenomena for isolator design evaluation. The isolator relative performance test data show that the elastomeric isolators do not appear to operate as single degree of freedom systems with respect to noise isolation. Noise isolation beyond 150 Hz levels off and begins to decrease somewhat above 600 Hz. Coupled analytical and empirical models were used to study the structure-borne noise transmission phenomena. Correlation of predicted results with measured data show that (1) the modeling procedures are reasonably accurate for isolator design evaluation, (2) the frequency dependent properties of the isolators must be included in the model if reasonably accurate noise prediction beyond 150 Hz is desired. The experimental and analytical studies reported herein were carried out in the frequency range from 10 Hz to 1000 Hz.

17 Key Words (Suggested by Author(s))	18 Distribution Statement
Interior Noise Noise Isolation General Aviation	Unclassified-Unlimited Subject Category 71

19 Security Classif (of this report)	20 Security Classif (of this page)	21 No. of Pages	22 Price
Unclassified	Unclassified	161	A08

For sale by the National Technical Information Service Springfield Virginia 22161

NASA-Langley, 1981

90%

END

10-16-81